Charles University, Faculty of Mathematics and Physics
Astronomical Institute

Thermal Effects in Physics and Dynamics of Small Bodies of the Solar System

Ph.D. Thesis

David Čapek

Supervisor: Doc. RNDr. David Vokrouhlický, DrSc.

Prague, 2007

Čapek, David

Thermal effects in physics and dynamics of small bodies of the solar system

keywords: YORP effect, Yarkovsky effect, asteroids, heat diffusion

Acknowledgements

I would like to thank my supervisor David Vokrouhlický, who is a co-autor of this research, for kind leadership, as well as for many suggestions concerning this Thesis. Furthermore, I wish to thank Miroslav Brož especially for his great help with the text of the Thesis, and Josef Ďurech for useful suggestions. I am also thankful to Martin Černý, Lukáš Hambálek, Jana Hekalová Katka Milerová and Petr Kotas for their help with English. At last, I am very grateful to my parents for their universal support during all my studies.

Contents

Chapter 1

Introduction

1.1 Motivation and aims of our work

Phenomena produced by thermal radiation forces and torques have been extensively studied during last 20 years, since they were recognized to be very important with respect to the dynamics of small Solar System bodies. A phenomenon which is known as *the Yarkovsky effect* is able to secularly change the semimajor axis of an orbit, while *the YORP effect* affects the rotation state of a body.

The Yarkovsky force and the YORP torque were previously calculated with many constraining assumptions like spherical shapes, circular orbits, small variations of the surface temperature, principal axis rotation, constant thermal parameters, etc. We developed a model of the Yarkovsky/YORP effect without such simplifications. With this model we were able to study thermal phenomena in more complex circumstances.

1.2 A brief review of our research

At first we focused on the YORP effect recently re-discovered by [Rubincam, 2000]. We studied the YORP effect on a sample of artificially generated shapes, roughly resembling Main Belt asteroids, and also on several shapes of real asteroids [Čapek and Vokrouhlický, 2002], [Vokrouhlický and Čapek, 2002]. These bodies were approximated by a polyhedral description, we assumed that their surface has a zero thermal conductivity and their orbits were circular.

We then improved our model and took into account the finite thermal conductivity and elliptical orbits. With this model we determined the Yarkovsky effect on asteroid (6489) Golevka for the purpose of the direct detection of the semimajor axis drift [Chesley et al., 2003]. The same model was used for the more general investigation of influence of the finite thermal conductivity on the YORP effect [Čapek and Vokrouhlický, 2004] and prediction of the detection of the YORP effect on asteroid (25143) Itokawa [Vokrouhlický et al., 2004]. The subsequent improvement of our model allowed to determine the Yarkovsky effect for tumbling asteroid (4179) Toutatis [Vokrouhlický et al., 2005a] and the binary system 2000 DP107 [Vokrouhlický et al., 2005b]. The last modification of the model allowed us to incorporate the temperature and spatial dependence of material parameters of an asteroid. It was used for the determination of Golevka's regolith parameters [Čapek and Vokrouhlický, 2005b].

As a result we have developed a sophisticated model which has following features: (i) It is able to describe very complicated shapes of asteroids by polyhedral representation, with several thousands surface triangular facets. (ii) It assumes arbitrary eccentric orbits. (iii) The rotation of the body can be both regular or tumbling. (iv) The insolation term (necessary for the determination of the surface temperature) is computed including mutual shadowing between

different parts of the body's surface. (In the case of binary systems it takes into account mutual eclipses between the components.) (v) The surface temperature (needed for the evaluation of the thermal force and torque) is solved numerically for each surface facet individually, using one-dimensional heat diffusion equation without any linearization. This approach assumes the body is larger than several tens of meters. (vi) Thermal parameters of the body can depend both on the temperature and the depth.

1.3 Structure of the thesis

This thesis is divided to four chapters and five appendices. Chapter 2 is devoted to the common base of the thermal effects: forces produced by a radiation. Chapter 3 deals with the YORP effect, while Chapter 4 discusses the Yarkovsky effect. There are brief summaries at the end of both chapters. In the Appendices we present details about our numerical model of the Yarkovsky/YORP effect: first, we deal with methods of solution of the heat diffusion problem (Appendix A). Then we present the polyhedral representation of the asteroidal shapes (Appendix B), the method for generation of artificial Gaussian shapes (Appendix C) and also several examples of shapes resembling real bodies (Appendix D). Finally we present a list of publications (Appendix E), with reprints of some of them (Appendix F).

Chapter 2

Radiation and corresponding forces

Let us suppose the situation in Figure 2.1, where the Sun illuminates the surface element of an asteroid. The incident direct solar radiation (D) is partially reflected (R) and partially absorbed (C). The surface with non-zero temperature emits thermal radiation (T). Here we shall derive the expressions for the forces that are applied on the surface element due to these three components of radiation.

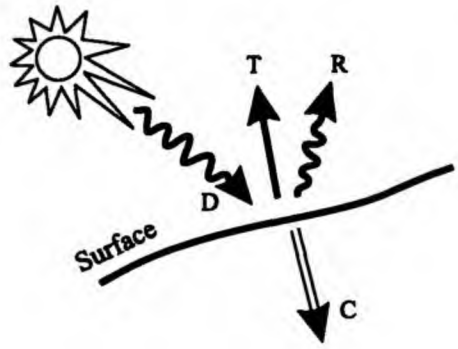

Figure 2.1: Direct (D), reflected (R) and thermally re-emitted (T) radiation from a surface element of an asteroid.

2.1 Direct solar radiation

The energy dE of the solar radiation, hitting the oriented surface element dS during the time dt can be expressed as

$$dE = \Phi\, \mathbf{s} \cdot \mathbf{n}\, dS\, dt,$$

or

$$dE = 0,$$

if the Sun is below the local horizon. Here, Φ denotes the solar energy flux (in W/m^2 units) at the given distance from the Sun, $\mathbf{s}$ the unit vector aiming towards the Sun and $\mathbf{n}$ the outer surface normal. The force $d\mathbf{f}_{\mathrm{srp}}$ produced by the solar radiation pressure[1] is

[1]Note that the relationship between the momentum and the energy of a photon is $p = E/c$, where c denotes speed of light (e.g., [Swihart, 1971]).

$$d\mathbf{f}_{\mathrm{srp}} = -\frac{\Phi}{c}\,\mathbf{s}\,\mathbf{s}\cdot\mathbf{n}\,dS\,, \tag{2.1}$$

where c is the speed of light. Integrating (2.1) over the surface Σ of a body we obtain the total force $\mathbf{f}_{\mathrm{srp}}$ produced by the solar radiation pressure:

$$\mathbf{f}_{\mathrm{srp}} = \int_{\Sigma} d\mathbf{f}_{\mathrm{srp}}\,.$$

Under normal circumstances, this force points directly from the Sun thus it is not able to secularly change the semimajor axis of an orbit. For larger bodies it only effectively weakens the solar gravitation, but it can even surpass the solar gravitation for particles with very small mass-to-area ratio. This usually occurs for $< 1\,\mu$m dust particles, e.g. [Bertotti et al., 2003]. [Vokrouhlický and Milani, 2000] showed that the direct radiation pressure (i.e., the absorbed and reflected radiation together) can produce observable long-term orbital effects for non-spherical bodies or for bodies with nontrivial albedo distribution. The total torque $\mathbf{T}_{\mathrm{srp}}$, corresponding to the direct radiation pressure, can be calculated as

$$\mathbf{T}_{\mathrm{srp}} = \int_{\Sigma} \mathbf{r}\times d\mathbf{f}_{\mathrm{srp}}\,,$$

where $\mathbf{r}$ denotes the radius vector. It is able to cause small variations of rotation during one spin period; over longer time scale it completely vanishes. [Breiter et al., 2007] showed that the torques produced by direct radiation pressure acting on spheroids are zero.

2.2 Reflected radiation

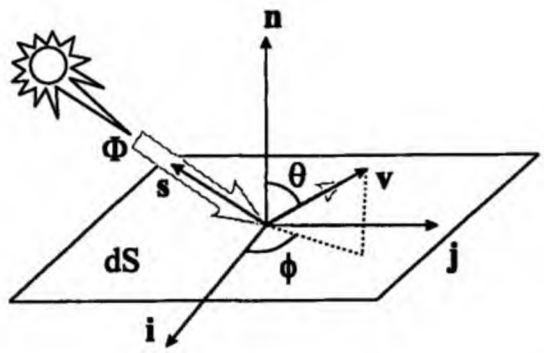

Figure 2.2: Reflection of direct solar radiation on a surface element dS. Here Φ is the flux of the solar radiation, $\mathbf{n}$ is the unit outer normal to dS, the unit vector $\mathbf{s}$ points to the Sun and the unit vector $\mathbf{v}$ parallel to the reflected radiation, is described by spherical angles θ and ϕ.

A part of incident photons is not absorbed but it is immediately reflected into the space in the optical band. Let us suppose the situation in Figure 2.2 describing geometry of the incident and reflected radiation. The direction of reflected radiation is characterized by the unit vector $\mathbf{v}$, which can be described by angles θ, ϕ with respect to the base $(\mathbf{i}, \mathbf{j}, \mathbf{n})$ as $\mathbf{v} = (\sin\theta\cos\phi, \sin\theta\sin\phi, \cos\theta)$. The intensity of the radiation reflected in the direction $\mathbf{v}$ can be expressed as

$$I_R(\mathbf{s},\mathbf{v}) = \Phi\rho(\mathbf{s},\mathbf{v}),$$

where $\rho(\mathbf{s},\mathbf{v})$ represents a reflectance (or scattering) function and Φ the incident flux. Let us introduce the hemispheric albedo A_H by the relation (see [Breiter et al., 2007]):

$$A_H(\cos\theta_0) = \frac{1}{\Phi\ \cos\theta_0} \int_{\phi=0}^{2\pi} \int_{\theta=0}^{\pi/2} I_R(\mathbf{s},\mathbf{v})\ \mathbf{v}\ \sin\theta\, d\theta\, d\phi\, dS\,, \tag{2.2}$$

where $\cos\theta_0 = \mathbf{s}\cdot\mathbf{n}$. The recoil force acting on the surface element dS is given by

$$d\mathbf{f}_R = -\frac{1}{c} \int_{\phi=0}^{2\pi} \int_{\theta=0}^{\pi/2} I_R(\mathbf{s},\mathbf{v})\ \mathbf{v}\ \cos\theta\ \sin\theta\, d\theta\, d\phi\, dS\,. \tag{2.3}$$

Assuming Lambert's law of diffuse reflection, we can express the intensity of the reflected radiation as (e.g. [Breiter et al., 2007]):

$$I_R = A\Phi\frac{\mathbf{s}\cdot\mathbf{n}}{\pi}, \tag{2.4}$$

where $A = const.$ With this approximation (which has been used in the whole text), the resulting force acting on dS reads

$$d\mathbf{f}_R = -\frac{2A\Phi}{3c}\mathbf{s}\cdot\mathbf{n}\,\mathbf{n}\,dS\,. \tag{2.5}$$

Integrating (2.5) over the surface Σ of an asteroid we obtain the whole recoil force arising from reflected radiation:

$$\mathbf{f}_R = \int_\Sigma d\mathbf{f}_R\,.$$

Under normal circumstances, this force is not able to change the orbit of a body on a long time scale (like the force caused by direct radiation). On contrary, the torque

$$\mathbf{T}_R = \int_\Sigma \mathbf{r}\times d\mathbf{f}_R \tag{2.6}$$

of this reflected-radiation force does not vanish and it is able to change the rotation of the body. In fact it is equal to the YORP with the assumption of zero thermal conductivity multiplied by a factor $A/(1-A)$. For bodies with higher albedo, such as the E-type asteroids, it is necessary to take this reflected-radiation torque into account.

2.3 Thermal radiation

Assuming isotropic emission, the intensity of a black body radiation can be expressed by Stephan-Boltzmann's law:

$$B(\mathbf{v}) = \frac{\epsilon\sigma T^4}{\pi}, \tag{2.7}$$

where $\sigma = 5.67051 \times 10^{-8}\,\mathrm{W/m^2/K^4}$ is the Stephan-Boltzmann constant, ϵ the emisivity and T is the temperature. Similarly as in Section 2.2, the recoil force due to the thermal radiation can be expressed as

$$d\mathbf{f}_{\mathrm{th}} = -\frac{1}{c}\int_{\phi=0}^{2\pi}\int_{\theta=0}^{\pi/2} B(\mathbf{v})\,\mathbf{v}\,\cos\theta\,\sin\theta\,d\theta\,d\phi\,dS\,, \tag{2.8}$$

which is equal to

$$d\mathbf{f}_{\mathrm{th}} = -\frac{2}{3}\frac{\epsilon\sigma T^4}{c}\mathbf{n}\,dS\,, \tag{2.9}$$

In the case of zero thermal conductivity ($K = 0$), all absorbed solar energy is immediately re-radiated and the resulting force on a non-shadowed facet can be expressed as

$$d\mathbf{f}_{\mathrm{th}}^{K=0} = -\frac{2(1-A)\Phi}{3c}\mathbf{s}\cdot\mathbf{n}\,\mathbf{n}\,dS\,. \tag{2.10}$$

For a shadowed facet $d\mathbf{f}_{\mathrm{th}}^{K=0} = \mathbf{0}$. In reality, even shadowed facets experience thermal recoil force because their temperature T is not zero, but this needs to be determined using heat diffusion in the body.

The total thermal force acting on the asteroid is given by an integration of (2.9) over asteroid's surface:

$$\mathbf{f}_{\mathrm{th}} = \int_{\Sigma} d\mathbf{f}_{\mathrm{th}}\,. \tag{2.11}$$

This represents the thermal (Yarkovsky) force. It is able to secularly change the semimajor axis of an asteroid's orbit. This effect arises from an anisotropic temperature distribution (due to the finite thermal inertia) across the surface[2]. The precise knowledge of the surface temperature T is necessary (see Appendix A).

The total thermal torque acting on the asteroid is given by integration over its surface:

$$\mathbf{T}_{\mathrm{th}} = \int_{\Sigma} \mathbf{r}\times d\mathbf{f}_{\mathrm{th}}\,. \tag{2.12}$$

This thermal torque (or the YORP torque, Chapter 3) is able to change the spin rate and obliquity of the body. The main difference between the YORP and the Yarkovsky effect is that the YORP is strongly dependent on the shape of an asteroid (it affects only bodies with a certain amount of "windmill" asymmetry[3]). The Yarkovsky effect is nonzero for rotating sphere but vanishes for zero thermal inertia. On the other hand, the YORP effect is nonzero even for a vanishing thermal conductivity (i.e., without any thermal lag).

[2]The thermal emission from irregularly shaped surface with zero thermal inertia is alsot able to change the orbit on a long term, but it is much smaller.

[3]For example, it does not affect spheroids [Breiter et al., 2007].

Isothermal body

Our numerical results show that $\mathbf{f}_{\mathrm{th}} = 0$ and $\mathbf{T}_{\mathrm{th}} = 0$ for an isothermal body of an arbitrary shape. This is an important limit for highly conductive small bodies which are effectively isothermal. This is in accordance with an intuition but we shall prove it in a rigorous way. Let us recall *Gauss' theorem* in vector analysis:

$$\oint_{\Sigma} \mathbf{a} \cdot d\mathbf{S} = \int_{V} \nabla \cdot \mathbf{a} \, dV \,, \tag{2.13}$$

where the first integral is over the closed surface Σ, the second over the corresponding enclosed volume V, $\mathbf{a}$ represents a general vector field. The Gauss' theorem gives rise to the following identities (e.g. [Sedlák and Štoll, 1993]):

$$\oint_{\Sigma} b \, d\mathbf{S} = \int_{V} \nabla b \, dV \,, \tag{2.14}$$

$$\oint_{\Sigma} d\mathbf{S} \times \mathbf{a} = \int_{V} \nabla \times \mathbf{a} \, dV \,, \tag{2.15}$$

where b is a general scalar field.

Let T_c be a constant temperature of the body. The total thermal force is

$$\mathbf{f}_{\mathrm{th}} = -\frac{2}{3}\frac{\epsilon\sigma}{c} \oint_{\Sigma} T_c^4 \, d\mathbf{S} = -\frac{2}{3}\frac{\epsilon\sigma}{c} \int_{V} \nabla \left(T_c^4\right) \, dV = 0 \,. \tag{2.16}$$

Here we used Equations (2.9), (2.11), (2.14) and the assumption of the constant temperature T_c (i.e., $\nabla T_c = 0$). Similarly, the thermal torque can be expressed as

$$\mathbf{T}_{\mathrm{th}} = -\frac{2}{3}\frac{\epsilon\sigma}{c} T_c^4 \oint_{\Sigma} \mathbf{r} \times d\mathbf{S} = \frac{2}{3}\frac{\epsilon\sigma}{c} T_c^4 \int_{V} \nabla \times \mathbf{r} \, dV = 0 \,. \tag{2.17}$$

Here we used Equations (2.9), (2.12), (2.15) and the well-known relation $\nabla \times \mathbf{r} = 0$. We can see clearly, that neither thermal force nor thermal torque affect a body with a constant temperature.

2.4 Example: (1620) Geographos

Here we shall demonstrate the effect of the direct, reflected and thermal radiation on the asteroid (1620) Geographos. We assumed the following orbital parameters: semimajor axis $a = 1.24547$ AU, eccentricity $e = 0.3354$, inclination $i = 13.34°$, argument of perihelion $\omega = 277.8°$, longitude of ascending node $\Omega = 337.3°$ and the pole of rotation $\lambda = 55°$, $\beta = -46°$. The rotation period is $P = 5.22484$ hours. We used the density of surface layers $\rho_s = 1.7\,\mathrm{g/cm^3}$, the bulk density $\rho_b = 2.5\,\mathrm{g/cm^3}$, the thermal conductivity $K = 0.02\,\mathrm{W/m/K}$, the thermal capacity $c = 680\,\mathrm{J/kg/K}$ and the Bond albedo 0.1. The shape was represented by a polyhedron with 4092 surface triangular facets according to [Hudson and Ostro, 1999]. (See also Appendix D.) We used a numerical one-level scheme (see Appendix A) to model forces and torques corresponding to the direct, reflected and thermal radiation.

The magnitude of radiative acceleration can be seen in Figure 2.3. The left plot shows perturbations of the semimajor axis da/dt of the orbit during first 12 hours after the perihelion

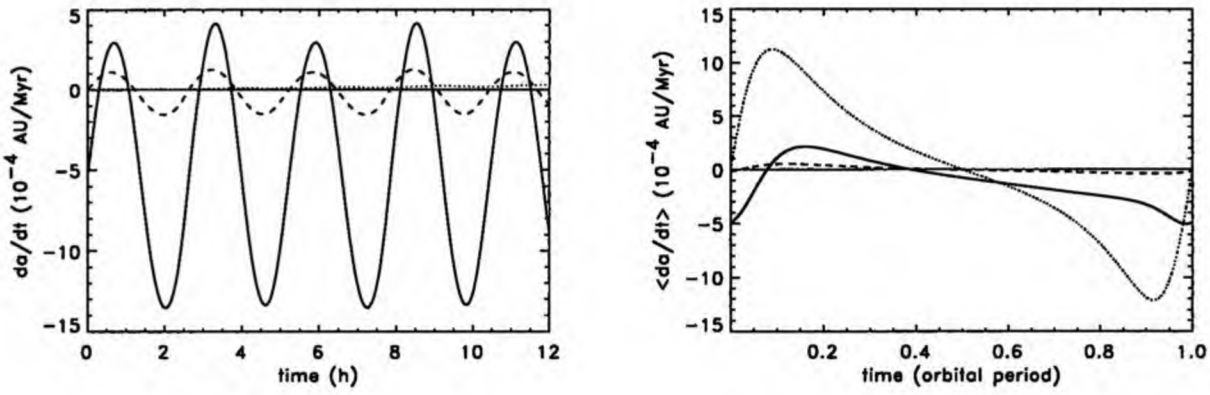

Figure 2.3: Perturbations of semimajor axis by the thermal radiation (solid curve), reflected radiation (dashed curve) and direct radiation (dotted). Left: Perturbations during the first 12 hours after passage of perihelion. Right: Perturbations averaged over spin period during one revolution about the Sun. The perihelion passage corresponds to $t = 0$. The orbit-averaged value of the semimajor axis drift $\langle da/dt \rangle$ produced by direct and reflected radiation is zero, but the thermally induced value is $\langle da/dt \rangle = -1.4 \times 10^{-4}$ AU/Myr.

passage and the right one shows these perturbations averaged over spin periods during one whole revolution about the Sun.

The thermal acceleration is able to secularly change semimajor axis by a mean (i.e. orbit-averaged) rate $\langle da/dt \rangle = -1.4 \times 10^{-4}$ AU/Myr. The variations caused by this force are shifted with respect to the variations produced by the reflected radiation due to finite thermal inertia. The reflected radiation is able to produce short-term perturbations but their orbit-averaged value is zero (the actual value $\sim 10^{-7}$ AU/Myr is due to minor numerical inaccuracies in our model). Perturbations of semimajor axis produced by direct radiation are precisely symmetric with respect to the perihelion. They can be the largest for a short term but their orbit-averaged effect is also zero ($\sim 10^{-8}$ AU/Myr due to numerical round-off errors).

We next demonstrate how the radiative torques affect the spin rate in Figure 2.4. The left plot shows perturbations of the spin rate $d\omega/dt$ during 12 hours after passage of perihelion while the right one shows the perturbations averaged over the spin period during the whole revolution about the Sun.

The thermal torque produces both short-term and long-term perturbations of the spin rate, with the orbit-averaged value $\sim 2.7 \times 10^{-19}\,\mathrm{s}^{-2}$. These perturbations are somewhat shifted with respect to the perturbations produced by reflected radiation which has a smaller amplitude. The value of the orbit-averaged perturbations of reflected radiation is $\sim 3 \times 10^{-20}\,\mathrm{s}^{-2}$. The direct radiation produces only short-term variations of the spin rate, but the orbit-averaged value is zero ($\lesssim 10^{-21}\,\mathrm{s}^{-2}$ due to numerical inaccuracies).

Note the resulting torque strongly depends on the shape model. See Section 3.4.2.

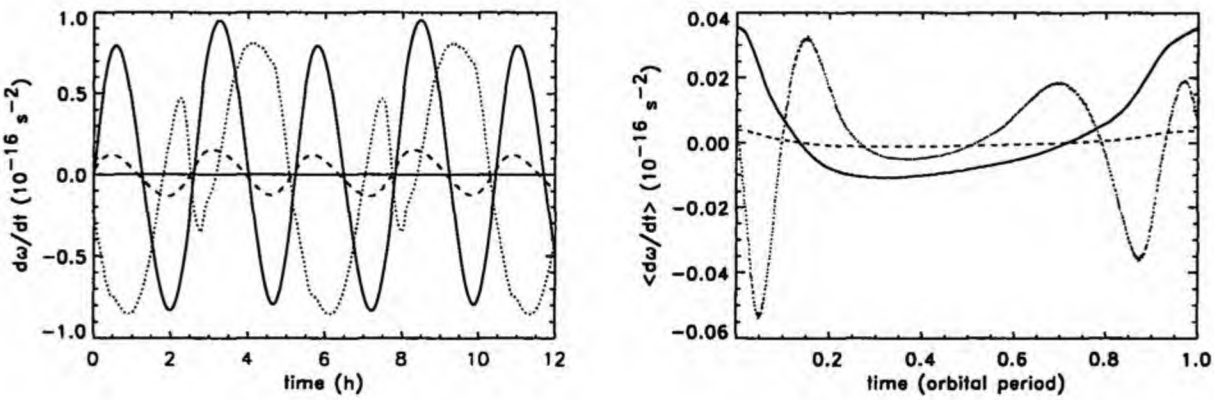

Figure 2.4: Perturbations of the spin rate $d\omega/dt$ by the thermal radiation (solid curve), reflected radiation (dashed curve) and direct radiation (dotted curve). Left: The perturbations during the first 12 hours after passage of perihelion. Right: The perturbations averaged over the spin period during one revolution about the Sun. The perihelion passage corresponds to $t = 0$. The orbit-averaged value of perturbations of spin rate $\langle d\omega/dt \rangle$ produced by direct radiation is zero, but the thermally induced value is $\langle d\omega/dt \rangle = 2.7 \times 10^{-19}$ s^{-2}.

Chapter 3

The YORP effect

3.1 Introduction

The rotation of small asteroids or meteoroids is modified especially by mutual collisions with other small solar system bodies [Farinella et al., 1992] and by solar and planetary tides. Moreover, a dissipation of free-precession energy inside larger bodies (which are larger than several hundreds of meters), which are though to be rubble piles, causes a principal-axis rotation [Burns and Safronov, 1973], [Efroimsky and Lazarian, 2000].

Aditionally, there are several non-gravitational effects caused by absorption, reflection or reemission of the solar radiation, that can also change rotation. For example [Radzievskii, 1954] showed that small ($\sim$ cm) body with a realistic albedo distribution across the surface can be spun up by solar radiation to the disruption limit on a time scale of thousand years. [Paddack, 1969] studied a possibility of destruction of small meteoroids and tektites due to the rotational fission. His "windmill effect" is due to the reflection of sunlight from surface of body with an appropriate shape. He estimated this effect is able to spin up a several cm long body, composed from tektite glass, to the bursting limit in about 60 000 years.

General properties of the YORP effect. Recently, [Rubincam, 2000] investigated spinning up and down of small asteroids due to the infrared emission from their irregularly shaped surfaces. He named this phenomenon the YORP effect as an acronym of Yarkovsky–O'Keefe–Radzievskii–Paddack (four names of planetary scientists). Rubincam computed thermal torques on bodies that were assumed to be (i) blackbodies with (ii) zero thermal conductivity on (iii) circular orbits around the Sun and (iv) rotating about the principal axis of inertia tensor. Their shapes were described by (v) spherical harmonic expansion of the shapes of real asteroids. Rubincam showed there are two important components of the YORP torque. The first one is able to change the rotation rate and the second one the obliquity of the asteroid. Both components depend on the obliquity. Rubincam's conclusions are: (a) The YORP effect is able to spin up or spin down an asteroid with 5-km radius during $\sim 10^8$ years. (b) The YORP effect dominates collisions in the inner Solar System for bodies with radius R smaller than 5 km and it dominates tidal encounters for bodies with $R < 1$ km. (c) The YORP may be responsible for the observed excess of slow and fast rotators among small asteroids. (d) Due to inevitable interplay between the torque affecting rotation rate and torque affecting obliquity, a rotational bursting due to the YORP effect actually happens very rarely. (e) The YORP effect may explain rotation states of several NEAs.

[Vokrouhlický and Čapek, 2002] studied the YORP effect on 10 shapes of real bodies (8 asteroids and Phobos and Deimos) and also on a sample of 500 automatically generated shapes

corresponding to small Solar System bodies. They assumed the Rubincam's approximation[1] but used polyhedral description of shapes of asteroids instead. They classified the bodies into four classes according to the dependance of the YORP effect on the obliquity. Most often the obliquity is slowly driven to 0°/180° or 90° and the rotation is asymptotically decelerated. Only a minority of the bodies is asymptotically accelerated. They also present several examples of the spin-state evolution due to the YORP effect where also gravitational torques due to the Sun and gravitational perturbations of the orbit by planets play an important role. They realized the YORP effect may be important for driving the rotation into resonances between the precession of the spin axis due to the solar torques and the precession of the orbital plane by planetary perturbations. In the case of small members of the Themis family, the evolution due to the YORP alone describes the evolution quite well whereas in the case of Flora family asteroids the evolution of rotation is usually much more complicated.

[Čapek and Vokrouhlický, 2004] analyzed the influence of the surface thermal conductivity K both on a sample of artificial shapes and on several real bodies for which the possibilities of the YORP detection were also discussed. They found, unlike in the zero conductivity model, the YORP effect preferentially drives the spin axis to be perpendicular to the orbital plane (i.e., the obliquity 0° or 180°) for the realistic values of K. They also found a nearly complete independence of the YORP component affecting the spin rate on surface thermal conductivity. They showed that asymptotical spinning up and down are equally likely and (unlike the results of [Rubincam, 2000]) the rotational bursting due to the YORP effect can be relatively common.

[Vokrouhlický et al., 2007] eliminated the principal axis rotation constraint used in previous studies and numerically integrated Euler's equations for several bodies. They found several new asymptotic states and analytically proved an onset of the tumbling caused by the YORP instead of slow-rotation asymptotic state.

[Scheeres, 2007] derived linearized analytical equations describing evolution of spin rate and obliquity of uniformly rotating asteroids due to YORP effect. (Non-zero thermal inertia was involved by simplified "thermal lag".) He also introduced several dimensionless parameters dependent only on the shape and mass distribution across the body, which describe the strength of YORP effect. He was able to analytically confirm a lot of results on general YORP properties obtained previously by numerical studies.

[Breiter et al., 2007] derived an analytical expression for the YORP torque acting on spheroids and proved the YORP does not contribute to the long-term evolution of their rotation.

The observation of the YORP effect in the Solar System. [Slivan, 2002] photometrically observed rotation of several Koronis family members and found a surprising anisotropy of their spin axes distribution. The prograde rotators have spin periods between 7.5 and 9.5 hours and obliquities $42° - 50°$. On the other hand, spin periods of retrograde rotators are < 5 h or > 13 h and their obliquities are $\geq 154°$. Moreover, he found the longitudes of spin axes are clustered. Such distribution can not be explained by mutual collisions.

[Vokrouhlický et al., 2003] succeded to explain the non-random distribution of the obliquities and spin periods of the Koronis family asteroids as a consequence of the YORP effect. They used a numerical model involving torques produced by reflected and thermal radiation as well as gravitational effects of the Sun and planets. With a wide range of initial conditions (shapes, spin periods and obliquities) they reproduced the observed distribution of the spin axes. [Vokrouhlický et al., 2003] found that the s_6 spin – orbit resonance is important for the prograde rotators resulting in the capture of the spin axes longitudes. Their research showed the YORP effect may be more important to changing rotation state than collisions for bodies < 40 km in diameter.

[1] Namely, asteroids are blackbodies with zero thermal conductivity on circular orbits around the Sun and rotating about the principal axis of the inertia tensor.

[Vokrouhlický et al., 2004] investigated a possibility of direct detection of the YORP effect on the asteroid (25143) Itokawa by precise measurement of its rotation period or rotation phase. They used a generalized model of the YORP effect, taking into account a finite thermal conductivity of asteroid's surface, actual elliptical orbit and proper spin axis orientation. They predicted an observable $1-3$ hr delay of the lightcurve maximum in January, 2004. Unfortunately their results were incorrect due to an inaccurate shape model and some other mistakes see Section 3.4.2).

[Scheeres et al., 2007] used a more precise shape, rotation pole and mass of Itokawa, determined by the Hayabusa mission ([Demura et al., 2006], [Gaskell et al., 2006], [Saito et al., 2006]), and calculated how the YORP affects the asteroid's rotation rate. They found Itokawa's rotation is decelerated so that doubling time is 50 000 – 90 000 years (see Equation (3.10)). They predict the detection of the YORP effect for Itokawa during future apparitions. They also discussed the distant-past rotation history of Itokawa and concluded, Itokawa's rotation was accelerated. 100 – 180 Myr ago, spin period of Itokawa reached 6.5 hours, corresponding to the bursting limit. Then the shape had been changed to the present state and it has been decelerated since that time (However, they noticed the possibility that Itokawa had a close approach with the Earth during this period, which could also change it's shape.)

Recently, the YORP effect was directly detected for small ($\sim$ 57 m) near-Earth asteroid (54509) 2000 PH5 ([Lowry et al., 2007], [Taylor et al., 2007]). The acceleration of rotation $(2.0\pm 0.2)\times 10^{-4}$ deg/day^2 was determined from radar and lightcurve data. This value corresponds to the theoretical prediction by the YORP model calculated for the shape of (54509) 2000 PH5, simultaneously determined by photometry and radar.

In the same time, [Kaasalainen et al., 2007] analyzed (1862) Apollo's photometric observations from 1980 to 2005. These authors concluded that Apollo's spin behaviour is not consistent with the assumption of a constant period of rotation. They found a change angular velocity $d\omega/dt = (5.3\pm 1.3)\times 10^{-8}$ rad/day^2. For the shape determined by photometry they calculated corresponding YORP effect and found that it is consistent with observed $d\omega/dt$, such that they interpret acceleration of Apollo's rotation rate by effects of YORP.

Here we shall present some of our results concerning the YORP effect. In Section 3.2 we derive expressions of YORP evolution of asteroid's rotational state. Basic facts concerning YORP effect are demonstrated on a simple example in Section 3.2.1. Following Section 3.3 is devoted to study of YORP effect on large sample of artificial bodies. Section 3.3.1 is based on our paper [Vokrouhlický and Čapek, 2002] and describes YORP dependence on obliquity, while 3.3.2 is based on [Čapek and Vokrouhlický, 2004] and deals with the thermal conductivity dependence of YORP. The YORP effect on the real asteroids is presented in 3.4, which is based on [Čapek and Vokrouhlický, 2004]. In the case of asteroid Itokawa we corrected our results from [Vokrouhlický et al., 2004].

3.2 Theory of the YORP effect

The YORP effect changes spin state of an irregularly shaped body due to the thermal torque. This torque is caused by a recoil force due to thermal emission from surface, heated by absorption of sunlight. The thermal torque was expressed in previous chapter by Equation (2.12). The torque arising from *the reflected radiation* also contributes to the total torque (see Section 2.2). The torque $\mathbf{T}$ changes the angular momentum $\mathbf{L}$ of the body (with respect to the inertial frame) according to the relation

$$\frac{d\mathbf{L}}{dt} = \mathbf{T}, \tag{3.1}$$

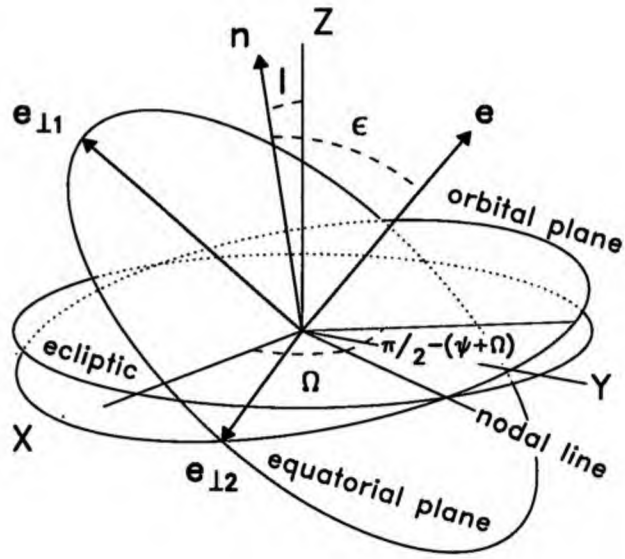

Figure 3.1: Three coordinate systems: *Ecliptical system* $(X-Y-Z)$ defined by the plane of ecliptic and the vernal equinox X, *the orbital system* defined by orbital plane and perihelion and finally *the equatorial system* defined by the base vectors $\mathbf{e}_{\perp 1}$, $\mathbf{e}_{\perp 2}$ (the intersection of the equatorial and the orbital plane) and $\mathbf{e}$ (parallel with the spin vector).

If we assume that dissipation of the rotation energy inside the body is so rapid, that any non-principal axis rotation is quickly damped and thus the body rotates around the shortest axis of the inertia tensor (corresponding the moment of inertia C), the angular momentum will be simply

$$\mathbf{L} = C\omega\mathbf{e}, \tag{3.2}$$

where ω denotes the angular velocity and $\mathbf{e}$ corresponds to the unit vector of the spin axis. This together with (3.1) leads to the expression

$$\frac{d\omega}{dt}\mathbf{e} + \frac{d\mathbf{e}}{dt}\omega = \frac{\mathbf{T}}{C}, \tag{3.3}$$

The scalar product of this equation with the vector $\mathbf{e}$ allows us to express the change of the angular velocity due to the torque[2]:

$$\frac{d\omega}{dt} = \frac{\mathbf{T}\cdot\mathbf{e}}{C} = \frac{T_\omega}{C} \tag{3.4}$$

Substituting (3.4) back into (3.3), we obtain the expression for the change of the spin axis direction:

$$\frac{d\mathbf{e}}{dt} = \frac{\mathbf{T} - (\mathbf{T}\cdot\mathbf{e})\mathbf{e}}{C\omega}. \tag{3.5}$$

The spin vector direction $\mathbf{e}$ is usually characterized by the obliquity ϵ which is the angle between the spin vector and the normal to the orbital plane, and by the precession angle in longitude

[2]Here we use that $\dot{\mathbf{e}}\cdot\mathbf{e} = 0$, because $d(\mathbf{e}\cdot\mathbf{e})/dt = 2\dot{\mathbf{e}}\,\mathbf{e}$ and $\mathbf{e}\cdot\mathbf{e} = 1$.

ψ. The components of the unit vector $\mathbf{e}$ with respect to the inertial system connected with the orbital plane of the body, where $x-$ axis corresponds to the nodal line (see Fig. 3.1), are $\mathbf{e} = (\sin\epsilon\sin(\psi+\Omega), \sin\epsilon\cos(\psi+\Omega), \cos\epsilon)$. The scalar product of (3.5) and the unit vector $\mathbf{N}$, perpendicular to the orbit of the body, leads to the expression for the change rate of the obliquity ϵ:

$$\frac{d\epsilon}{dt} = \frac{\mathbf{T}\cdot\mathbf{e}_{\perp 1}}{C\omega} = \frac{T_\epsilon}{C\omega}, \tag{3.6}$$

where

$$\mathbf{e}_{\perp 1} = \frac{(\mathbf{N}\cdot\mathbf{e})\mathbf{e} - \mathbf{N}}{\sin\epsilon}. \tag{3.7}$$

The rate of change of the precession angle ψ can be derived by a cross product of Equation (3.5) and the vector $\mathbf{N}$. After some algebra we have

$$\frac{d\psi}{dt} = \frac{\mathbf{T}\cdot\mathbf{e}_{\perp 2}}{C\omega} = \frac{T_\psi}{C\omega}, \tag{3.8}$$

where

$$\mathbf{e}_{\perp 2} = \frac{\mathbf{N}\times\mathbf{e}}{\sin\epsilon}. \tag{3.9}$$

So, the thermal torque $\mathbf{T}$ has three components $(T_\epsilon, T_\psi, T_\omega)$ with respect to the system $(\mathbf{e}_{\perp 1}, \mathbf{e}_{\perp 2}, \mathbf{e})$ which change the obliquity, the angle of precession and the angular velocity.

Useful quantities

The characteristic timescale of the YORP-driven evolution of the rotation rate can be described by the quantity called *doubling time* [Rubincam, 2000]:

$$t_d = \frac{\omega}{\langle\dot{\omega}\rangle} = \frac{C\omega}{\langle T_\omega\rangle}. \tag{3.10}$$

After the time t_d the YORP effect increases the rotation rate ω twice or decrease it to the half value. This is because $\omega(t)$ is quasilinear in time.

The quantity describing the windmill asymmetry - *windmill factor* - of the given shape can be defined as

$$\varphi_w = \frac{1}{2}\left(-1 + \sqrt{1 + \frac{2\pi(2+\sqrt{2})}{V}\,\mathbf{e}\cdot\int_{\phi=0}^{2\pi}\int_{\Sigma}\delta(\mathbf{r},\mathbf{s},\Sigma)\,\mathbf{r}\times\mathbf{s}\cdot\mathbf{n}\,dS\,d\phi}\right), \tag{3.11}$$

where V denotes volume of the body, $\mathbf{e}$ the unit vector of the spin axis, $\mathbf{r}$ the position vector of the surface element dS, $\mathbf{n}$ the outer unit normal of dS and $\mathbf{s}$ the unit vector perpendicular to spin axis. (In the body-fixed frame it can be expressed as $\mathbf{s} = (\cos\phi, \sin\phi, 0)$.) The integration is realized over the surface Σ of the body and over one revolution of $\mathbf{s}$ about the spin axis. The "mutual shadowing" function $\delta(\mathbf{r},\mathbf{s},\Sigma)$ is equal to 1 if half-line starting at $\mathbf{r}$ and propagating in the direction $\mathbf{s}$ does not intersects the surface Σ and it is equal to 0 in the opposite case.

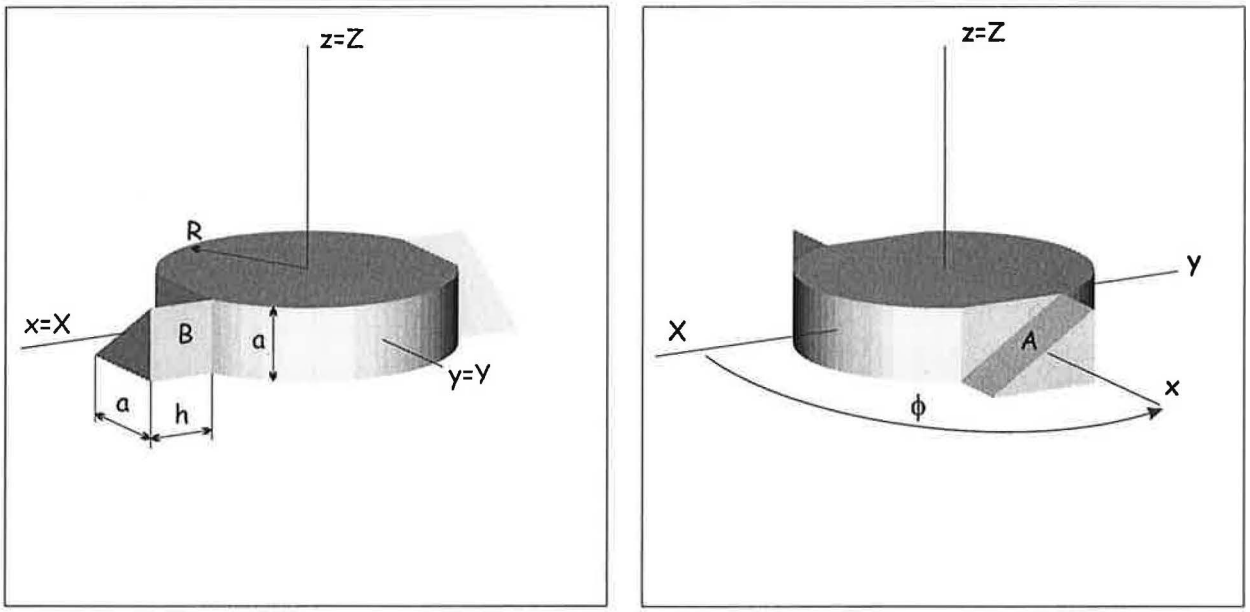

Figure 3.2: A simple test body. The small letters denote the axes of the body-fixed frame, while the capital letters the inertial frame. The facets causing the non-zero torques are denoted by "A" and "B" and ϕ represents the angle of rotation about Z-axis.

This expression is established on the basis of computing the YORP effect for a simple body composed of cylinder with two wedges, as described in following Section 3.2.1. The windmill factor is a dimensionless parameter and it depends only on the shape of the body. In reality it has value approximately from -0.15 to 0.15, but most frequently for usual asteroid-like shapes, the absolute value $|\varphi|$ is about 0.015. The positive value indicates spinning up of the body and the negative value indicates spinning down.

There is a simple relationship between the windmill factor φ_w and the mean change of the angular velocity caused by the YORP effect, under the assumption of a circular orbit, zero thermal conductivity K, zero albedo A and zero obliquity ϵ:

$$\langle \dot{\omega} \rangle = -\frac{2(2-\sqrt{2})}{3\pi c} \frac{\Phi}{d^2} \frac{\varphi_w(1+\varphi_w)}{\rho} \frac{m}{C}, \tag{3.12}$$

where Φ is the solar flux at the heliocentric distance d, ρ is the bulk density of the asteroid and m its mass.

3.2.1 The YORP effect on a windmill shape

Here we shall explain the basic YORP efect properties, using an example of the artificial body shown in Figure 3.2. It is composed from a cylinder with two wedges. This body rotates about the z-axis and the Sun shines from the $X-$axis direction. At first, we express the thermal torque acting on arbitrary surface element. Let us suppose that all incoming radiation is immediately re-radiated as a thermal radiation. This means there is no thermal conductivity of the surface material, no thermal lag. Assuming the thermal emission obeys Lambert's law, the thermal radiation pressure acting on i-th surface element $\mathbf{S}^i$ causes the force

$$\mathbf{f}^i = -\frac{2E^i}{3c}\mathbf{S}^i,$$

where E^i is the incomming solar energy (W/m^2) and c the speed of light. This force acting on the arm $\mathbf{r}^i$ results in a torque

$$\mathbf{T}^i = \mathbf{r}^i \times \mathbf{f}^i.$$

The whole thermal torque acting on the body is the sum over all its surface elements:

$$\mathbf{T} = \sum_i \mathbf{T}^i.$$

The mean change of the angular speed ω over the time is given by

$$\langle \dot{\omega} \rangle = \frac{1}{C} \langle T_z \rangle,$$

where C is the principal moment of inertia around the spin axis, $\langle T_z \rangle = \int_0^P T_z \, dt \, / \, P$ denotes mean $z-$component of the thermal torque $\mathbf{T}$ and P is the orbital period.

Let us now compute the thermal torques applied on the windmill from Figure 3.2. The jacket of the cylinder as well as its bases do not cause any torque, because any force acting on each facet has a zero arm. The only facets that can cause a thermal torque are the inclined facets denoted by A and the facets perpendicular to the $xy-$plane denoted by B. These facets have the outer normals

$$\mathbf{n}^A = \frac{1}{\sqrt{2}} \begin{pmatrix} -\sin\phi \\ \cos\phi \\ 1 \end{pmatrix}, \qquad \mathbf{n}^B = \begin{pmatrix} \sin\phi \\ -\cos\phi \\ 0 \end{pmatrix},$$

the area $S^A = ah\sqrt{2}$, $S^B = ah$ and the arms

$$\mathbf{r}^A = \mathbf{r}^B = \frac{R+h}{2} \begin{pmatrix} \cos\phi \\ \sin\phi \\ 0 \end{pmatrix}.$$

The incomming solar energy (neglecting mutual shadowing) can be expressed as

$$E^A = \begin{cases} 0, & \phi \in \langle 0, \pi \rangle \\ \Phi \, S^A \, \mathbf{n}^A \cdot \mathbf{s}, & \phi \in \langle \pi, 2\pi \rangle, \end{cases} \qquad E^B = \begin{cases} \Phi \, S^B \, \mathbf{n}^B \cdot \mathbf{s}, & \phi \in \langle 0, \pi \rangle, \\ 0, & \phi \in \langle \pi, 2\pi \rangle \end{cases}$$

where Φ is the solar flux at the asteroid's orbit and $\mathbf{s} = (1, 0, 0)$ is the direction toward the Sun. Putting all these facts together we obtain a mean torque caused by one wedge:

$$\langle \tau_z \rangle = \frac{2 - \sqrt{2}}{3c} \Phi \, ah(R + h).$$

The principal moment of inertia can be approximated by the moment of inertia of the cylinder part of the body:

$$C = \frac{1}{2} (\pi R^2 a \rho) R^2.$$

Finally, the mean change of the angular velocity caused by the two wedges can be expressed as

$$\langle \dot{\omega} \rangle = -\frac{4(2 - \sqrt{2})}{3\pi c} \frac{\Phi_0}{d^2} \frac{\varphi_w (1 + \varphi_w)}{\rho R^2}, \tag{3.13}$$

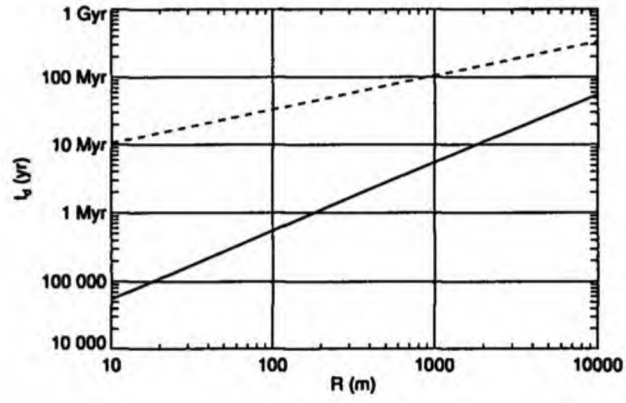

Figure 3.3: Doubling time for the body from Figure 3.2 as a function of radius of the body. The solid line corresponds to time necessary for double the rotation period due to YORP effect for body with windmill factor $\varphi_w = 0.014$, bulk density $\rho = 2.5\,\mathrm{g/cm^3}$ and orbit with semimajor axis $d = 2.5\,\mathrm{AU}$. Period of rotation is assumed $P[\mathrm{hr}] = 0.01R[\mathrm{m}]$. Dashed line describes timescale corresponding to reorientation of the spin axis due to collisions in the Main Belt.

where $\Phi_0 = 1366\,\mathrm{W/m^2}$ is the solar flux at 1 AU, d is semimajor axis of the orbit (in AU units) and φ_w the dimensional-less windmill factor, which can be expressed as $\varphi_w = h/R$ in this simple case.

Let us now estimate a characteristic timescale of the YORP acting on the body. Using (3.13) and (3.10) the doubling time is:

$$t_d = 0.05\,\mathrm{yr}\,\frac{1}{\varphi_w(1+\varphi_w)}\left(\frac{1\,\mathrm{hr}}{P}\right)\left(\frac{d}{1\,\mathrm{AU}}\right)^2\left(\frac{\rho}{1\,\mathrm{g/cm^3}}\right)\left(\frac{R}{1\,\mathrm{m}}\right)^2 \tag{3.14}$$

We can see the dependence of the doubling time on the radius of the body in Figure 3.3. We used Equation (3.14) and assumed windmill factor[3] $\varphi_w = 0.014$, period of rotation $P[\mathrm{hr}] = 0.01R[\mathrm{m}]$ and bulk density $\rho = 2.5\,\mathrm{g/cm^3}$. The solid line corresponds to the semimajor axis $d = 2.5\,\mathrm{AU}$. Dashed line denotes the timescale t_{col} corresponding to complete change of the spin axis due to collisions according to [Farinella et al., 1998]:

$$t_{col} = 3.34 \times 10^6\mathrm{yr}\left(\frac{R}{1\mathrm{m}}\right).$$

In the radius interval from 10 meters to 10 km, the YORP doubling time is smaller than typical collisional reorientation time. Then the YORP effect predominates the collisions in the evolution of spin axes for the bodies with assumed properties in the Main Belt.

Though expression (3.13) was derived for the body and situation described above, it can be generalized and we can summarize the YORP effect dependance on several parameters:

- Our first simple model (i.e., the equation describing the long term evolution of the rotation state) is valid only for bodies with sufficiently fast rotation which is strong enough to damp any deviations from principal axis rotation via inelastic dissipation of energy inside the body [Efroimsky and Lazarian, 2000]. If the spin period increases up to several hundreds hours, the asteroid begins to tumble and the approach used here is unreliable. This slow rotation limit has been studied by [Vokrouhlický et al., 2007].

[3]The main belt asteroids have $\langle|\varphi_w|\rangle \simeq 0.015$.

- The shape is the key property affecting the YORP effect. There are no thermal torques acting on spheres, triaxial ellipsoids or other bodies with lack of "windmill asymmetry" (The analytical proof can be found in [Breiter et al., 2007].) It can be roughly described by the windmill factor φ_w.
- The YORP (i.e., mean change of angular velocity) decreases with square of the size of an asteroid $\propto 1/R^2$. It is important only for bodies smaller than, say $\sim 10\,\mathrm{km}$ in diameter[4].
- The shape of the orbit, especially the semimajor axis is important. The YORP decrease with square of the distace from the Sun $\propto 1/d^2$.
- The YORP decreases with the bulk density of the body as $1/\rho$.

This simple model does not describe the dependence of the YORP effect on mutual position of the spin axis and the orbital position of the spin axis and the orbital plane, and also on thermal behaviour of the surface material. The dependence of the YORP effect on these quantities is discussed in Section 3.3.

[4]On the other hand, the dissipation of the free-rotation energy does not operate for very small bodies and moreover the temperature differences between the insolated and shadowed facets are minimal due to fast rotation and effective heat transfer through the body. These facts are not included in this simple model.

3.3 Statistical study of the YORP effect

Here we shall demonstrate the diversity of the YORP results with respect to various parameters. By computing the YORP torque on several asteroids with known shapes we can conclude that the shape of the body is the most important characteristic that determines the overall effect. Since the YORP depends sensitively on shape, we decided to study this effect on a large sample of Gaussian random spheres that sufficiently describe the shape characteristics of small asteroids in the Main Belt (see Appendix C).

We use a polyhedral description of shapes which consists of a list of surface vertices and their mutual identifications as triangular facets. This description allows us to determine the volume, inertia tensor, surface area and self-shadowing of the surface in a simple way (see Appendix B).

We are interested in the long-term evolution of the spin state. Hence we discuss the torques $\langle T_\epsilon \rangle$ and $\langle T_\omega \rangle$ averaged over rotation and revolution cycles.

3.3.1 Obliquity dependence – the YORP classification

This section is based on [Vokrouhlický and Čapek, 2002]

A study of the dependence of the YORP on obliquity was performed for 500 Gaussian random spheres orbiting on a circle with radius 2.5 AU. All bodies rotated about the shortest axis of inertia tensor with a period $P = 6$ hr. The bulk density was $\rho_{\text{bulk}} = 2.5\,\text{g/cm}^3$ and the volume corresponding to the sphere with radius 1 km. The surface thermal conductivity was assumed $K = 0$ and albedo $A = 0$. For each value of the obliquity (ϵ goes from 0° to 180° with a 30° step) the thermal force causing the YORP torque was determined according to (2.10) for all surface facets in 250 000 points during the orbital period. The final YORP torque was given by a sum over the whole body's surface (2.12) and an averaging along the orbit.

According to the dependence of the YORP component $\langle T_\epsilon \rangle$ on obliquity ϵ we can distinguish four principal types. Their description follows. We also attempt to illustrate a typical evolution of the spin axis of each type due to *the YORP effect alone*. We neglect influence of the gravitational torques due to the Sun and planets as well as meteoroid impacts. (These effects on rotation state are discussed in [Vokrouhlický and Čapek, 2002].) We use the four-order Runge-Kutta integrator with a timestep of 100 years. We compute the evolution of the spin axis for the initial rotation period of 6 hours and various initial obliquities. Each integration was stopped when the YORP effect increased the spin period to the value equal to the orbital period.

Type I. Figure 3.4a shows the averaged YORP torques $\langle T_\epsilon \rangle / C$ and $\langle T_\omega \rangle / C$ for one of Gaussian random spheres. This type is characterized by positive values of $\langle T_\epsilon \rangle / C$ in the $(0°, 90°)$ obliquity range and negative values for $\epsilon \in (90°, 180°)$. This means (see Equation (3.6)) that obliquity of such body will be driven to the "asymptotic obliquity" $\epsilon_f = 90°$, i.e., the spin axis will be parallel with the orbital plane. The torque affecting the rotation rate $\langle T_\omega \rangle / C$ is negative for $\epsilon \in (50°, 130°)$, and consequently the rotation of the asteroid is decelerated in this obliquity range and accelerated elsewhere. Type I is (together with Type II) the most probable YORP type and represents approximately 40% of all cases for the zero thermal conductivity.

Figures 3.4b and 3.4c show the evolution of obliquity and rotation rate during 50 Myr. We assumed the initial rotation period to be 6 hours. Initial obliquities were chosen with a step of 10°. For example, an obliquity with initial value $\epsilon_0 = 80°$ monotonously increases and after ~ 38.5 Myr reaches 90°. The corresponding rotation frequency monotonously decreases and after the same time reaches zero. The rotation of bodies with smaller initial obliquities evolves more slowly. If the initial obliquity is smaller than $\sim 55°$, the rotation rate initially increases until this obliquity is reached. For instance, rotation of a body with $\epsilon_0 = 10°$ is accelerated during the first ~ 24.3 Myr.

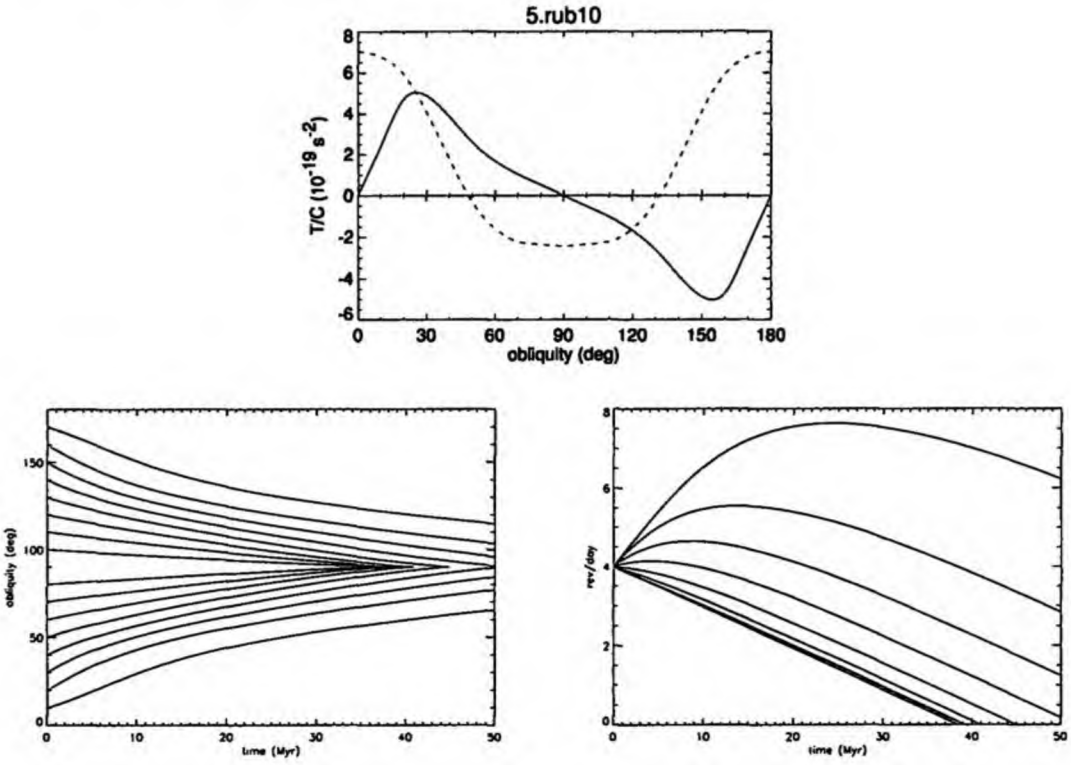

Figure 3.4: The YORP-type I: a) The dependence of $\langle T_\epsilon \rangle / C$ (solid line) and $\langle T_\omega \rangle / C$ (dashed line) on the obliquity, b) the evolution of obliquity, c) evolution of rotation rate. For explanation see the text.

The evolution of obliquities of bodies with $\epsilon_0 > 90°$ is symmetric with respect to the value of 90°. This means that obliquities monotonously decrease and finally reach 90° after the same time as bodies with initial obliquity $180° - \epsilon_0$. Nevertheless, the rotation rates evolve in the same way.

The rate of obliquity change depends also on angular velocity; if a body rotates slowly, obliquity changes faster and vice–versa.

After the obliquity of a body reaches 90°, its rotation rate falls to zero. Our model is not able to describe the YORP effect during this slow rotation limit consistently. One of the basic presumptions - principal axis rotation - is not valid in this state. [Vokrouhlický et al., 2007] studied this limit and realized onset of non-principal axis rotation of slow rotators due to the YORP effect. The non–YORP effects (solar or planetary torques or meteoroid impacts) play an important role during slow rotation state.

Type II represents just an opposite case to the Type I (see Figure 3.5b). Here, $\langle T_\epsilon \rangle / C$ is negative in $(0°, 90°)$ and positive in the $(90°, 180°)$ obliquity range. Obliquity of this body will move to $\epsilon_f = 0°$, if the initial obliquity ϵ_0 is less than 90°, or to $\epsilon_f = 180°$, if the initial obliquity ϵ_0 is larger than 90°. The spin axis becomes perpendicular to the orbital plane. The spin rate increases due to positive value of $\langle T_\omega \rangle / C$ for $\epsilon \in (55°, 125°)$ and decreases elsewhere. The Type II is (together with Type I) the most probable YORP-behaviour and represents approximately 40% of all cases for zero thermal conductivity.

Evolution of obliquity and rotation frequency can be seen in Figure 3.5b and 3.5c. The initial conditions are the same as in the case of Type I. Focusing on the curve with initial obliquity 80° we see that obliquity is decreasing to zero. Rotation rate increases during first $\sim$ 20 Myr

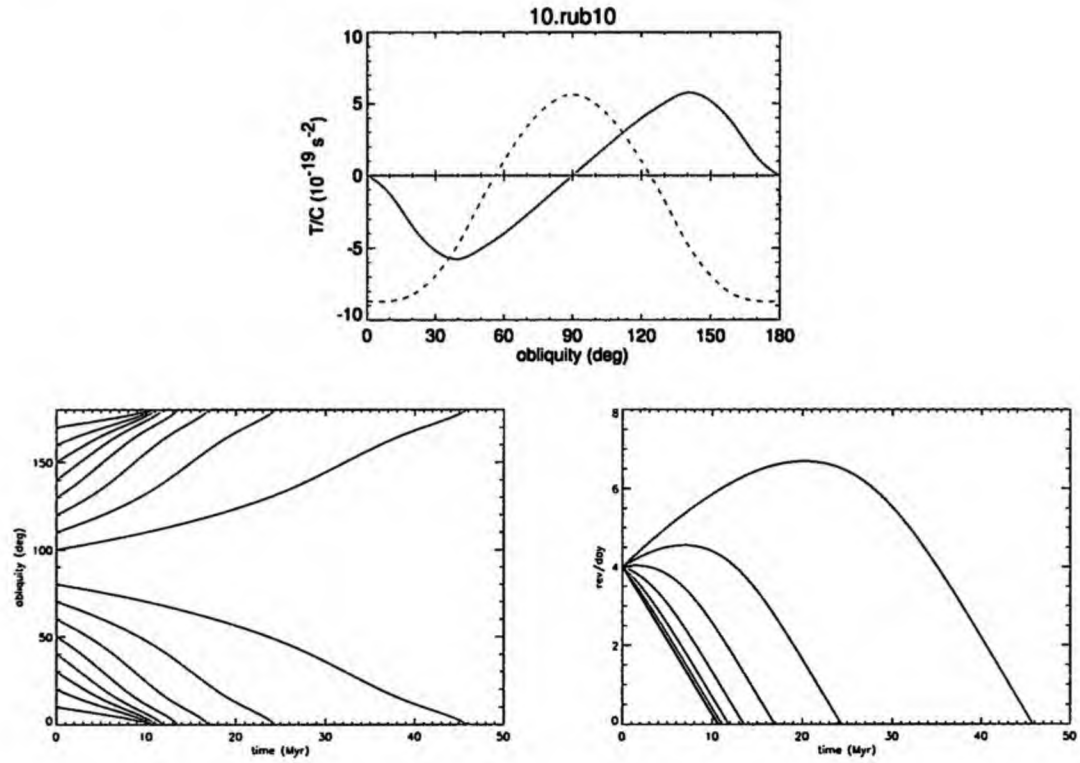

Figure 3.5: The YORP-type II: a) The dependence of $\langle T_\epsilon \rangle / C$ (solid line) and $\langle T_\omega \rangle / C$ (dashed line) on obliquity, b) the evolution of obliquity, c) evolution of rotation rate. For explanation see the text.

(obliquity is $> 55°$ and $\langle T_\omega \rangle > 0$ here) and then decreases to zero. The zero rotation rate as well as zero obliquity is reached after ~ 46 Myr.

Spin states of bodies with smaller initial obliquities evolve faster. Some of them do not undergo a phase of acceleration of rotation frequency, because their obliquity has never been larger then 55° and therefore $\langle T_\omega \rangle$ is always less than zero.

Bodies with $\epsilon_0 > 90°$ have a similar evolution. In this case the obliquity increases up to 180° and it is symmetrical to cases with ϵ_0, while the evolution of the rotation rate is the same.

For the slow rotation limit, see the discussion in the previous paragraph.

Type III represents a more complicated case than types I and II discussed above (see Figure 3.6). There are two asymptotic obliquities: the first one in $(0°, 90°)$ obliquity interval and the second one in $(90°, 180°)$. In the particular case of Figure 3.6 these asymptotic obliquities are $\epsilon_f = 44°$ and $\epsilon_f = 136°$. The spin axis will be tilt to the first one, if the initial obliquity is less than 90°, and tilt to the second one, if initial obliquity is higher then 90°. The dependence of $\langle T_\omega \rangle / C$ on ϵ differs from case to case, but in the asymptotic obliquities it is always negative. Type III represents less probable case of YORP behaviour (7%).

We can see from Figure 3.6b, that obliquities of bodies with $\epsilon_0 < 90°$ are driven to the value 44°, but they reach this obliquity after longer time than 50 Myr. Obliquities ϵ higher then 90° evolve toward value of 136°. In each case the rotational speed is finally decelerated, but some bodies undergo a phase of spinning up before deceleration (Figure 3.6c).

Type IV. There are three asymptotic obliquities for the type IV. The first one is $\epsilon_f = 0°$ and the spin axis tilt to this value if the initial obliquity is less than 42°. If ϵ_0 is more than 138°, the

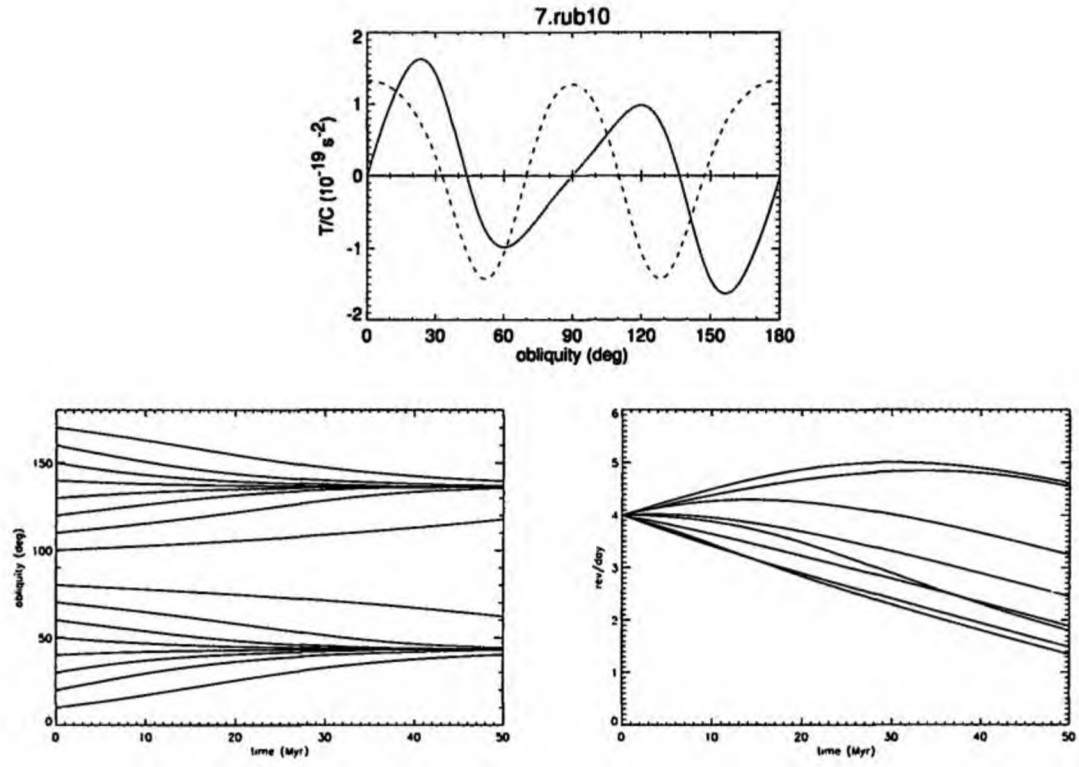

Figure 3.6: The YORP-type III: a) The dependence of $\langle T_\epsilon \rangle / C$ (solid line) and $\langle T_\omega \rangle / C$ (dashed line) on obliquity, b) the evolution of obliquity, c) the evolution of rotation rate. For explanation see the text.

spin axis is driven to $\epsilon_f = 180°$. If initial obliquity lies inside $(32°, 138°)$ range, the asymptotic obliquity will be $\epsilon_f = 90°$. The behaviour of $\langle T_\omega \rangle / C$ differs from case to case again.

The YORP effect drives obliquities of bodies with $\epsilon_0 < 45°$ to final value 0°, while initial obliquity greater than 135° is driven to $\epsilon = 180°$. If ϵ_0 is between 45° and 135°, the obliquity evolves toward 90°. The evolution of the spin rates is similar as in the previous cases. Initially some bodies undergo a spin up but finally all of them are decelerated.

Symmetries

General dependence of averaged torques on obliquity can be described by these symmetries[5]:

$$\langle T_\epsilon \rangle(\epsilon) = -\langle T_\epsilon \rangle(180 - \epsilon), \tag{3.15}$$

$$\langle T_\omega \rangle(\epsilon) = \langle T_\omega \rangle(180 - \epsilon). \tag{3.16}$$

Another symmetry stems from change of the spin axis orientation to the opposite one. This is important in the situations when a body is decelerated to zero angular velocity and then spun up in the opposite direction. Then:

$$\epsilon \longrightarrow 180 - \epsilon, \tag{3.17}$$

$$\langle T_\epsilon \rangle(\epsilon) \longrightarrow -\langle T_\epsilon \rangle(\epsilon), \tag{3.18}$$

$$\langle T_\omega \rangle(\epsilon) \longrightarrow -\langle T_\omega \rangle(\epsilon). \tag{3.19}$$

[5]Derived from the geometry of the problem.

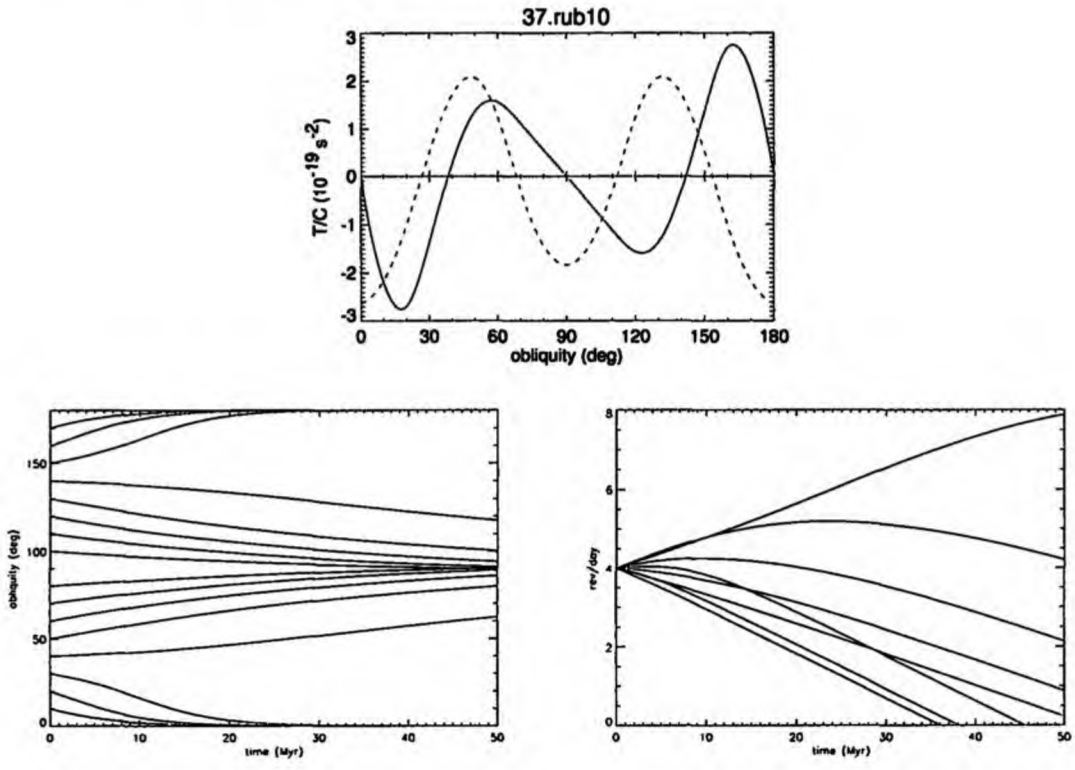

Figure 3.7: The YORP-type IV: a) The dependence of $\langle T_\epsilon \rangle / C$ (solid line) and $\langle T_\omega \rangle / C$ (dashed line) on obliquity. b) the evolution of obliquity, c) the evolution of rotation rate. For explanation see the text.

Note that all these symmetries are valid only for bodies with zero thermal conductivity on circular orbits. An elliptic orbit and non–zero thermal conductivity lead to deviations from symmetries mentioned above.

3.3.2 The non–zero conductivity of the surface material

This section is based on [Čapek and Vokrouhlický, 2004].

Here we discuss our statistical investigation of the influence of conductivity of the surface material on the orbit-averaged YORP torques $\langle T_\epsilon \rangle$ and $\langle T_\omega \rangle$ for a sample of 200 Gaussian random spheres. We assume three different values of surface conductivity: $K = 0$, 0.001 and 0.01 W/m/K. The thermal conductivity represents a very important quantity – it can vary by several orders of magnitude for different materials. This is discussed especially in Appendix A and Section 3.4.1.

We assumed that orbits are circular with $a = 2.5$ AU and period of rotation are 6 hr. The volume corresponded to a sphere with radius 1 km, the bulk density was $\rho_{bulk} = 2.5\,\mathrm{g/cm^3}$, the surface density was a bit smaller $\rho_{surf} = 1.7\,\mathrm{g/cm^3}$, the thermal capacity was $c = 680\,\mathrm{J/kg/K}$ and albedo $A = 0$.

The computation of surface temperature was performed by a one-level scheme (see Appendix A), with a non-constant spatial step, increasing as a geometrical series with quotient $q \sim 1.0725$, and a time step $\Delta t = 500\,\mathrm{s}$ (it corresponds to $\sim 8°$ of rotation). The temperature computation along the orbit was made so many times, until the temperature difference between the last two turns was less than 0.5 K. The lower boundary condition was put down in the depth $15\ell_s$,

where ℓ_s represents the penetration depth of a seasonal temperature wave. For more details see Appendix A.

We focused mainly on the following characteristics of the YORP effect:

1. An abundance of particular YORP-types.
2. A fraction of asymptotically accelerated bodies.
3. A strength of the YORP torque. An appropriate quantity describing the torque component $\langle T_\omega \rangle$ (which affects the angular velocity) is the doubling time t_d. The amplitude of $\langle T_\epsilon \rangle$ torque component (in units degrees per Myr) was chosen a description of obliquity change.

Zero conductivity. We studied this quite unrealistic limit case at the beginning of our investigation, because it is simple to evaluate – it is not necessary to solve HDE in this case. The thermal force (and torque) can be determined directly from insolation (see (2.10)). This allows to compute YORP effect for relatively large number of bodies.

Figure 3.9 shows orbit averaged rate of change of the obliquity and Figure 3.9 shows orbit averaged rate of change of the rotation speed. Among 200 Gaussian random spheres, there is roughly the same number of type I and type II objects: 40.0% and 46.5%, respectively. This means almost the same number of spin axes are driven to asymptotic obliquities 0°/180° and 90°. Among 500 Gaussian random spheres the difference between occurrences of these two types is even smaller[6] A minority of cases is represented by type III (7%) and IV (6.5%). The rotation of only 2% of all the bodies is accelerated in the asymptotic obliquity; all these cases correspond to bodies of type III or IV. Strength of the YORP torque can be characterized by a median of doubling times which is 14 Myr, and by a median of $\langle d\epsilon/dt \rangle$ amplitude, which is 3 °/Myr (see Figure 3.11a,b).

Conductivity 0.001 W/m/K. We chose this value to describe a thermal behaviour of highly particulated regolith-like surface. This is actually close to the lunar regolith value. The computation of the HDE is necessary here.

The balance between the YORP types I and II disappears completely in this case, as we can seen in Figure 3.8. A lot of types I transform to types II: only 7% of bodies remain in the type I, while 88% form type II. As a consequence the spin axes are driven with a higher likelihood to the asymptotic obliquity 0°/180°. The spin rate affecting YORP torque is almost the same as in the case of zero obliquity, as shown in Figure 3.8. This means that all types I transformed to types II will be asymptotically accelerated (40% of al the bodies).

Type III is represented by 5% of objects and there is no type IV. The median of doubling times is 13 Myr and the median of $\langle d\epsilon/dt \rangle$ amplitude is 6 °/Myr (see Figure 3.11c,d).

Conductivity 0.01 W/m/K. This thermal conductivity value was chosen to describe surface composed of a mixture of regolith and fresh rock.

The largest difference between abundance of types I (3.5%) and types II (95.5%) can be seen in Figure 3.10. The number of asymptotically accelerated bodies as well as spin axes driven to 0°/180° is even higher than in the case of $K = 0.001$ W/m/K. Abundance of types III and IV is the same - 0.5%. This corresponds to the most powerful YORP effect among among the studied conductivities: The median of doubling times is 12 Myr and the median of $\langle d\epsilon/dt \rangle$ amplitude is 9 °/Myr (see Figure 3.11e,f).

[6] Abundance of type I, II, III and IV are 39.2%, 40.4%, 10.2% and 6.2%. The remaining 4% correspond to cases with a more complicated evolution.

thermal conductivity (W/m/K)	abundance of types I	II$^-$	II$^+$	III	IV	$d\epsilon/dt$ (deg/Myr)	t_d (Myr)	# of accelerated %
0.000	40	46.5	0	7	6.5	3.33	14.3	2
0.001	7	52.5	35.5	5	0	5.94	13.1	40
0.010	3.5	52	43.5	0.5	0.5	8.60	11.9	45

Table 3.1: Influence of surface conductivity on the abundance of different YORP-types and the YORP evolution timescale among 200 (or 500 in the case of zero conductivity) gaussian random spheres. The II– (II$^+$) denotes YORP type II with the asymptotic deceleration (acceleration) of rotation.

3.3.3 Discussion

The study of the YORP effect on a large sample of artificial shapes, corresponding to small Main Belt asteroids with the assumption of zero thermal conductivity, shows that shapes can be divided according to the obliquity-affecting YORP component T_ϵ into four principal groups. The Type I is driven to the obliquity 90° and rotation is asymptotically decelerated. Type II is characterized by driving the initial spin axis to obliquity 0° or 180° and asymptotic spinning down again. Less frequent types III and IV have more complicated behaviour, but in most cases they are also asymptotically decelerated.

The statistical study of YORP effect on a sample of Gaussian random spheres shows that the surface thermal conductivity K strongly affects YORP component T_ϵ, which changes the obliquity, while spin rate affecting torque T_ω is nearly independent on the surface conductivity K. Very low value of conductivity (zero limit) results in an equal likelihood of driving the spin axes to the asymptotic obliquity 0°/180° and 90° and the rotation of the most of bodies is asymptotically decelerated. More realistic values of conductivity (0.001 and 0.01 W/m/K) lead to higher likelihood of driving spin axes to the obliquity 0°/180° and almost equal probability of accelerating and decelerating rotation in the asymptotic states. The quantitative results are summarized in Table 3.1.

We also found that the rotation of bodies with obliquity $\epsilon \simeq 55°$ and $\epsilon \simeq 125°$ is neither accelerated nor decelerated.

The YORP evolution timescales are shorter than collisional timescales. The YORP effect is then able to significantly accelerate the rotational speed (maybe up to a bursting limit) or decelerate it (to the state of very slow tumbling rotators).

Our model is not able to describe the YORP effect in these two limit states. In the case of very fast rotators it is because of very large CPU expenses and in the case of very slow rotators and also in case of bodies with size comparable to penetration depth of seasonal temperature wave – i.e. meteodoids) due to possible non-principal axis rotation of such bodies and more complicated heat diffusion inside of them.

Since the YORP component T_ω does not depend on the surface thermal conductivity K, the approximation of zero K can be used for modeling the short-time evolution of spin states due to the YORP effect. For instance, it can be used for the prediction and subsequent direct detection of the YORP effect. On the other hand, the T_ϵ depends on the thermal conductivity. The model with the finite value of the surface thermal conductivity should be used for an investigation of the long-time evolution of the spin states due to the YORP effect.

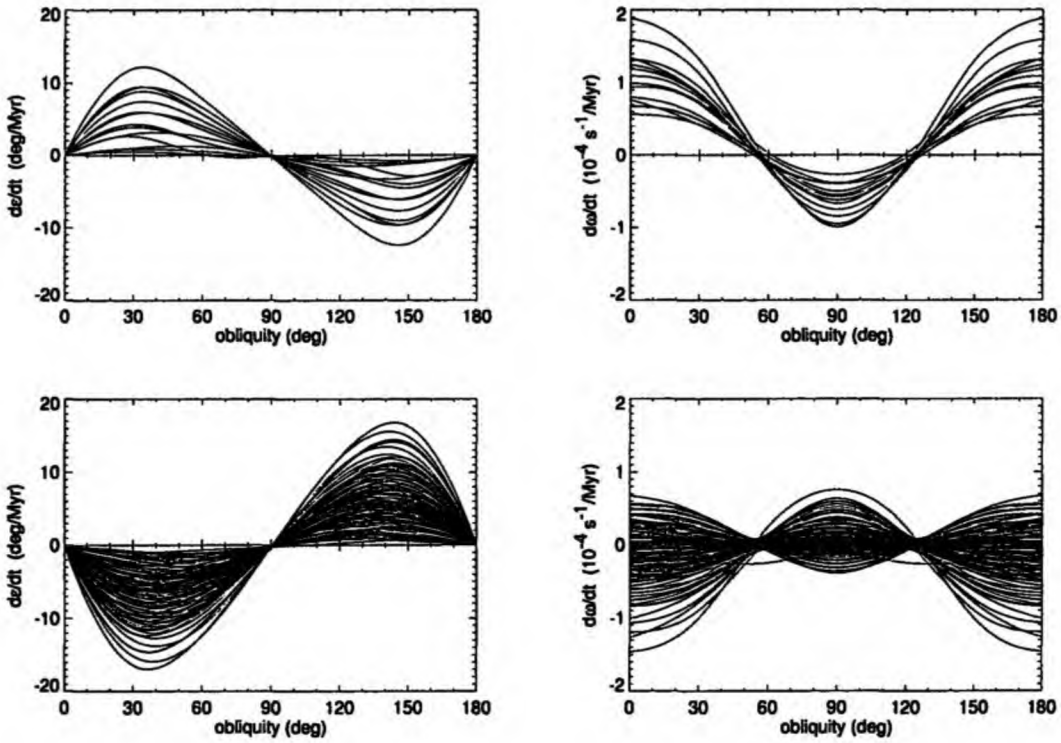

Figure 3.8: The orbit averaged YORP effect as a function of obliquity for 200 Gaussian random spheres for thermal conductivity $K = 0.001\,\mathrm{W/m/K}$. The figures in the left column represent the orbit-averaged rate of change of the obliquity $\langle d\epsilon/dt \rangle$, while the figures in the left column represent the orbit-averaged change rate of angular velocity $\langle d\omega/dt \rangle$. The upper row describes Type I objects, the lower one Type II. Here, the Type II is more likely. Type I produces asymptotic deceleration while Type II produces both deceleration and acceleration of rotation.

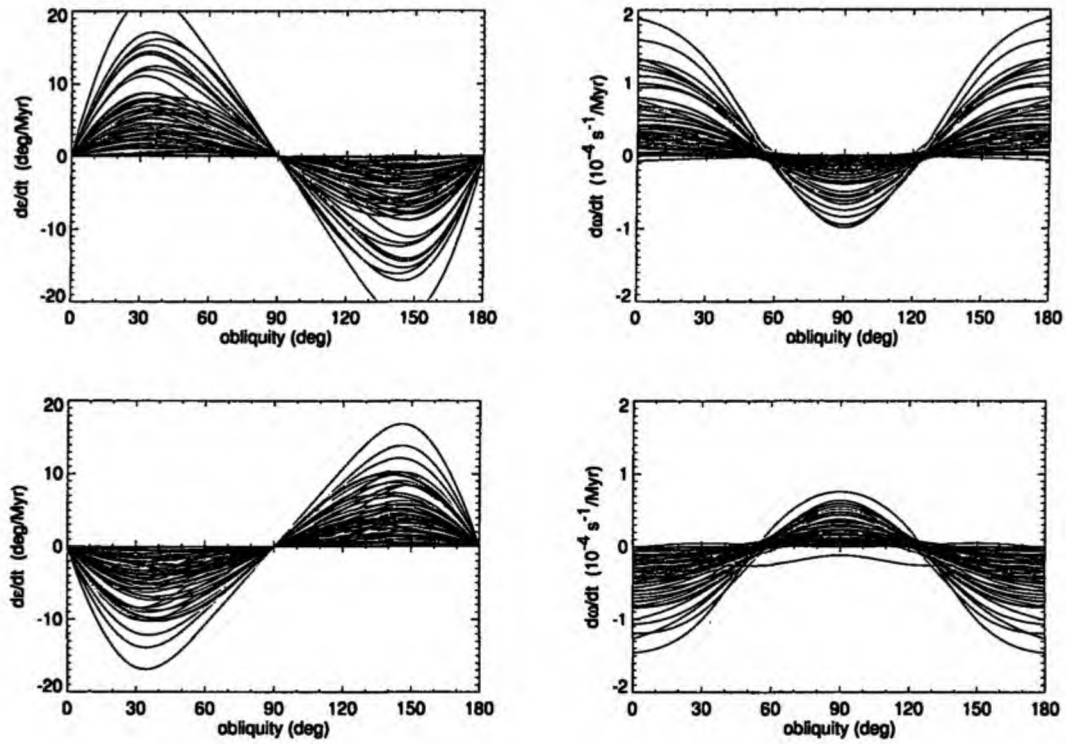

Figure 3.9: The orbit averaged YORP effect as a function of obliquity for 200 Gaussian random spheres in case of a zero conductivity limit. The figures in the left column represent the orbit-averaged rate of change of the obliquity $\langle d\epsilon/dt \rangle$, while the figures in the left column represent the orbit-averaged change rate of angular velocity $\langle d\omega/dt \rangle$. The upper row describes Type I objects, the lower one Type II. Both cases are equally likely and both produce an asymptotic deceleration of rotation.

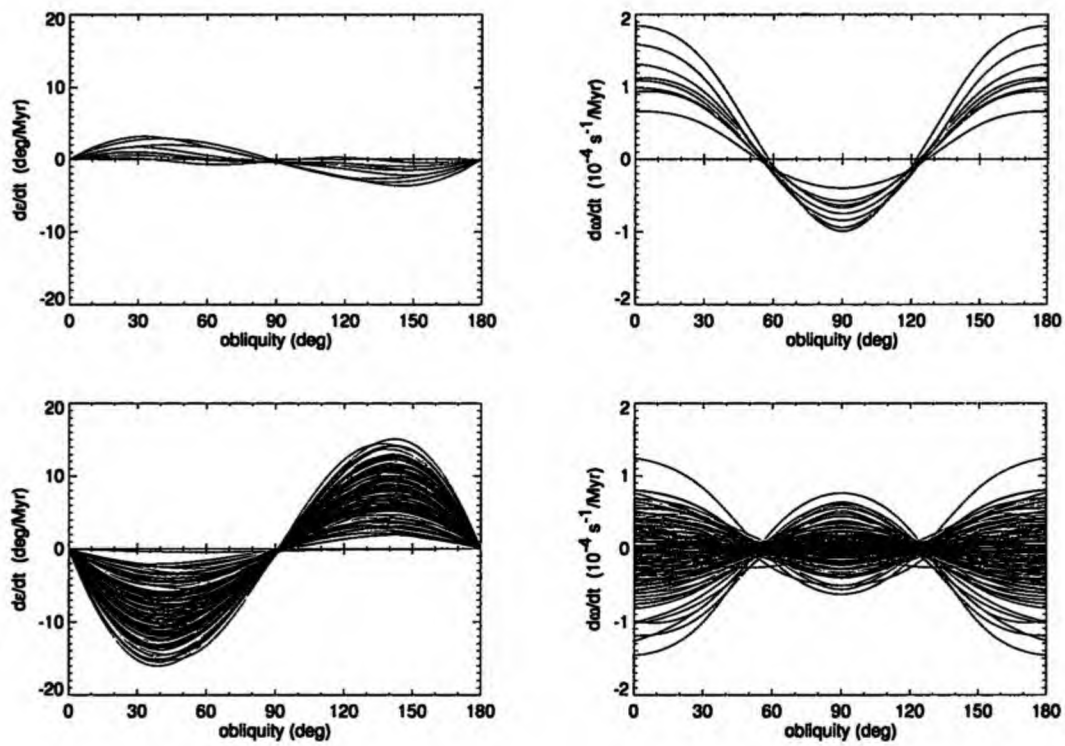

Figure 3.10: The orbit averaged YORP effect as a function of obliquity for 200 Gaussian random spheres for thermal conductivity $K = 0.01\,\mathrm{W/m/K}$. The figures in the left column represent the orbit-averaged rate of change of the obliquity $\langle d\epsilon/dt \rangle$, while the figures in the left column represent the orbit-averaged change rate of angular velocity $\langle d\omega/dt \rangle$. The upper row describes Type I objects, the lower one Type II. A great difference between the number of Type I and Type II bodies can be seen clearly. Type I produces asymptotic deceleration while Type II produces both deceleration and acceleration of rotation.

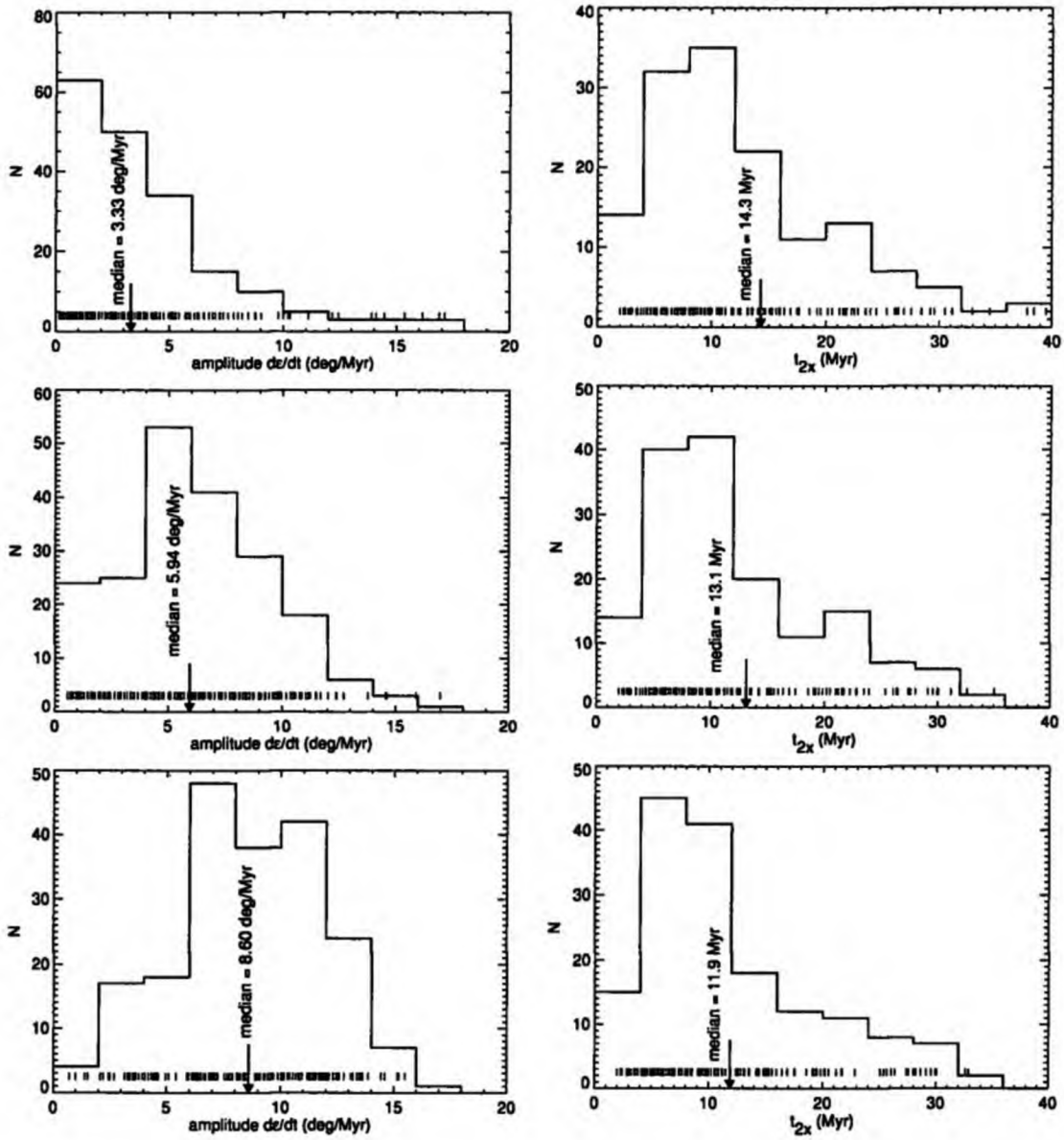

Figure 3.11: Histograms of statistical distributions of the characteristic timescales of the YORP effect acting on sample of 200 Gaussian random spheres for conductivity $K = 0\,\mathrm{W/m/K}$ (upper row, a and b), $K = 0.001\,\mathrm{W/m/K}$ (middle one, c and d) and $K = 0.01\,\mathrm{W/m/K}$ (lower row, e and f). The left column shows the distribution of maximal obliquity change rate. Small lines at the bottom of plots represent actual values and the arrow is the median value. Tn the right column we present distribution of doubling time at the asymptotic values of obliquity.

3.4 The YORP effect on individual bodies

This section is based on [Vokrouhlický and Čapek, 2002] and [Vokrouhlický et al., 2004].

We chose several asteroids with available shape models (see Appendix D) and investigated how the YORP effect acts on these bodies. We study both the YORP dependence on the thermal conductivity for bodies on circular orbits [Čapek and Vokrouhlický, 2004] and how it affects rotation rate of asteroids in actual orbital and spin configuration including possible direct detection of the YORP effect [Vokrouhlický et al., 2004].

3.4.1 The YORP dependence on the surface thermal conductivity

The material properties, like the density ρ and thermal capacity c of small Solar System bodies can be roughly determined by laboratory measurement of its meteorite analogues (e.g. [Yomogida and Matsui, 1983]). In the case of the surface thermal conductivity K the situation is more complicated. We do not know the composition and degree of porosity of surface material and then have to assume some similar material measured in laboratory, or use measurements of the lunar soil returned by Apollo missions (e.g. [Cremers, 1972])

Another way to determine K is to use data from infrared observations [Delbò et al., 2006], [Delbò et al., 2007] or measurements of non-gravitational (Yarkovsky) semimajor axis drift which is strongly dependent on asteroid's surface thermal inertia [Chesley et al., 2003]. The value of the thermal conductivity can vary by several orders of magnitude. For highly particulated regolith it can be $K \simeq 10^{-4}\,\mathrm{W/m/K}$, while for fresh iron surface $K \simeq 80\,\mathrm{W/m/K}$. Moreover, [Delbò et al., 2007] discovered a dependence of thermal inertia on asteroids diameter. So, the value of thermal conductivity of surface is the most uncertain quantity of all.

Here we present a study of the YORP effect dependence on the thermal conductivity K. We used several bodies with precisely determined shapes and assumed they are on a circular orbit about the Sun with semimajor axis $a = 2.5\,\mathrm{AU}$. Other important quantities are listed in Table 3.2. The surface thermal conductivity varies from $10^{-9}\,\mathrm{W/m/K}$ to $10\,\mathrm{W/m/K}$.

semimajor axis	2.5 AU
period of rotation	6 hours
bulk density	$2.5\,\mathrm{g/cm^3}$
surface density	$1.7\,\mathrm{g/cm^3}$
thermal capacity	680 J/kg/K
albedo	0.1
emissivity	0.9

Table 3.2: Orbital and physical parameters used for the study of the YORP K-dependence. The orbit is assumed circular and the thermal conductivity in the range $\langle 10^{-9}, 10^{1} \rangle\,\mathrm{W/m/K}$.

The computation was performed by a one-level scheme with a non-constant spatial step which is increasing as a geometrical series with a quotient $q = 1.0725$, and a time step $\Delta t = 500\,\mathrm{s}$ (it corresponds to $\sim 8°$ of rotation phase). The computation of surface temperature along the orbit was made several times, until the temperature difference between the last two turns was less than 0.5 K. The lower boundary condition was applied in the depth $15\ell_s$, where ℓ_s is the penetration depth of seasonal temperature variations. For more details see Appendix A.

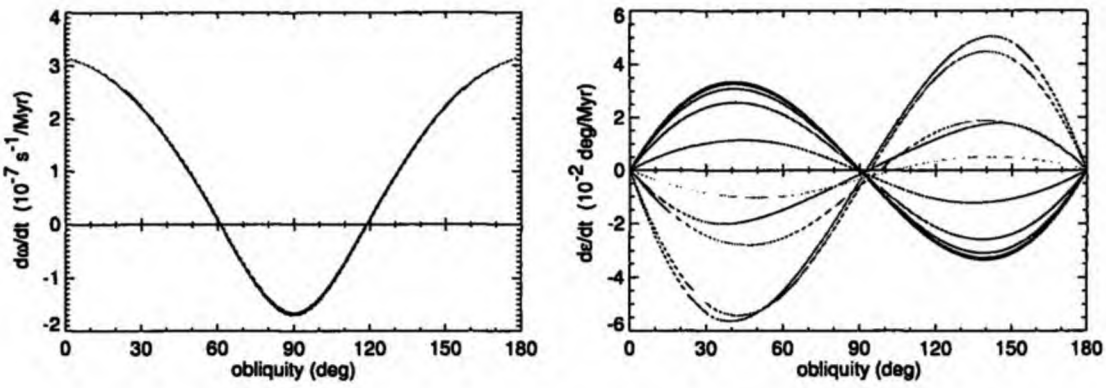

Figure 3.12: The orbit averaged rate of change of the angular velocity ω (left) and obliquity ϵ (right) due to the YORP effect for asteroid (433) Eros. Grey levels denote different surface thermal conductivities from 10^{-9} W/m/K (darkest, corresponding to the Rubincam's limit) to 10 W/m/K (lightest, corresponding to highly conductive material). For more discussion see the text.

(433) Eros

The dependence of the YORP torque on the thermal conductivity for an Eros-shaped body is shown in Figure 3.12. There is a orbit-averaged rate of change $\langle d\omega/dt \rangle$ of angular velocity and a rate of change of the obliquity $\langle d\epsilon/dt \rangle$ due to the YORP effect.

It can be seen that the component of the YORP affecting the speed of rotation ω almost does not depend on the thermal conductivity in the studied interval of K. On the other hand, the YORP-induced obliquity change depends on the thermal conductivity K very strongly. Low values of K lead to the type I of the YORP classification. This means the spin axis would evolve toward the obliquity 90° and the rotation would decelerate. As K increases, the amplitude of $\langle d\epsilon/dt \rangle$ decreases. For the conductivity $K \simeq 5 \times 10^{-4}$ W/m/K, the YORP changes to the Type II. In this case the spin axis is driven to 0° or 180° obliquity, but the rotation of the body will be accelerated in these states because $\langle d\omega/dt \rangle$ remains unaffected by the thermal conductivity. For higher K's the amplitude of $\langle d\epsilon/dt \rangle$ increases with thermal conductivity and reaches the maximal value when $K \simeq 10^{-2}$ W/m/K. Subsequently, the amplitude decreases. Note that for high conductivities the symmetry of $\langle d\epsilon/dt \rangle$ with respect to $\epsilon = 90°$ is broken.

(6489) Golevka

We can see $\langle d\omega/dt \rangle$ and $\langle d\epsilon/dt \rangle$ for Golevka in Figure 3.13. Like Eros, the component of the YORP effect changing the speed of rotation is nearly independent on the thermal conductivity in the studied interval, unlike the YORP component affecting the obliquity. Low values of K lead to the type IV of the YORP classification. As K increases, the amplitude of $d\epsilon/dt$ decreases and also the node moves slightly from $\epsilon \sim 60°$ towards zero obliquity[7]. For the conductivity $K \simeq 5 \times 10^{-4}$ W/m/K, the YORP changes to the type I. In this case, the spin axis is driven to obliquity 90° but the rotation of the body will be accelerated in this state, because $\langle d\omega/dt \rangle$ remains almost unaffected by thermal conductivity K. As K further increases, the amplitude of $\langle d\epsilon/dt \rangle$ increases, reaches the maximum value for $K \simeq 10^{-2}$ W/m/K and then falls-off a little. The symmetry of $\langle d\epsilon/dt \rangle$ with respect to obliquity $\epsilon = 90°$ is broken again for higher conductivities.

[7]The node at 120° moves towards $\epsilon = 180°$.

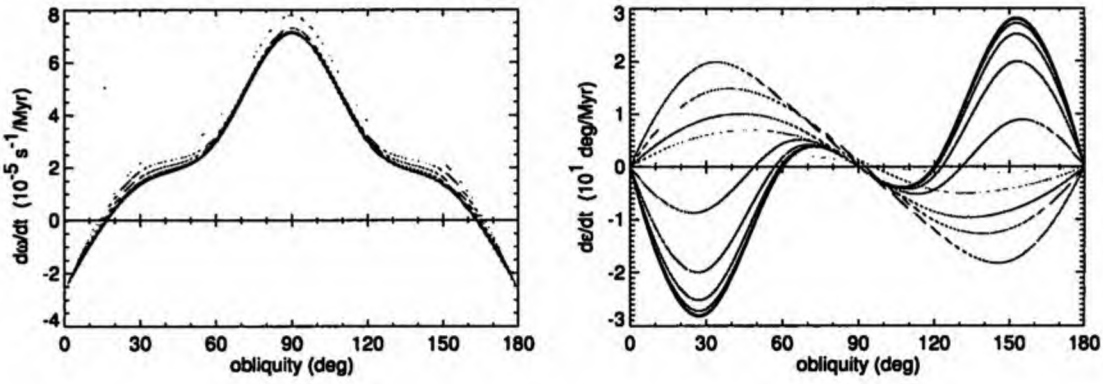

Figure 3.13: The orbit averaged rate of change of the angular velocity ω (left) and obliquity ϵ (right) due to the YORP effect for asteroid (6489) Golevka. Grey levels denote different surface thermal conductivities from 10^{-9} W/m/K (darkest, corresponding to the Rubincam's limit) to 10 W/m/K (lightest, corresponding to highly conductive material). For more discussion see the text.

(243) Ida

Figure 3.14 shows the orbit-averaged rate of change $\langle d\omega/dt \rangle$ of angular velocity and rate of change $\langle d\epsilon/dt \rangle$ of the obliquity for asteroid (243) Ida. As in previous cases, $\langle d\omega/dt \rangle$ does not depend on K, while $\langle d\epsilon/dt \rangle$ does. The YORP type is II and increasing thermal conductivity only changes its amplitude. Up to $K \simeq 10^{-2}$ W/m/K the amplitude increases and for higher conductivities decreases.

(25143) Itokawa

The dependence of the YORP effect on the surface thermal conductivity for asteroid Itokawa can be seen in Figure 3.15. This is the same case as Eros. The YORP component $\langle d\omega/dt \rangle$ is nearly independent on K, while $\langle d\epsilon/dt \rangle$ belongs to the Type I for low conductivities and to the Type II for high ones. The transition occurs for $K \simeq 5 \times 10^{-5}$ W/m/K. Note that we used the shape model derived from radar observations, see Figure D.7.

1998 KY26

Figure 3.16 shows the orbit-averaged rate of change of angular velocity $\langle d\omega/dt \rangle$ and the rate of change of obliquity $\langle d\epsilon/dt \rangle$ due to the YORP effect. Again, we can see nearly K-independent YORP component affecting the speed of rotation and the YORP component changing the obliquity strongly dependent on K. In this case increasing thermal conductivity does not change the YORP type (which is I) but only decreases the amplitude of $\langle d\epsilon/dt \rangle$.

Discussion

The study of the K-dependence of the YORP effect for several real shapes shows a strong dependence of $\langle T_\epsilon \rangle$ or $\langle d\epsilon/dt \rangle$ on thermal conductivity in the range 10^{-9} to 10^{1} W/m/K, like in the case of the artificial shapes. In most cases the YORP for realistic values of K belongs to the Type II. The YORP component $\langle T_\omega \rangle$ or $\langle d\omega/dt \rangle$ is nearly independent on K.

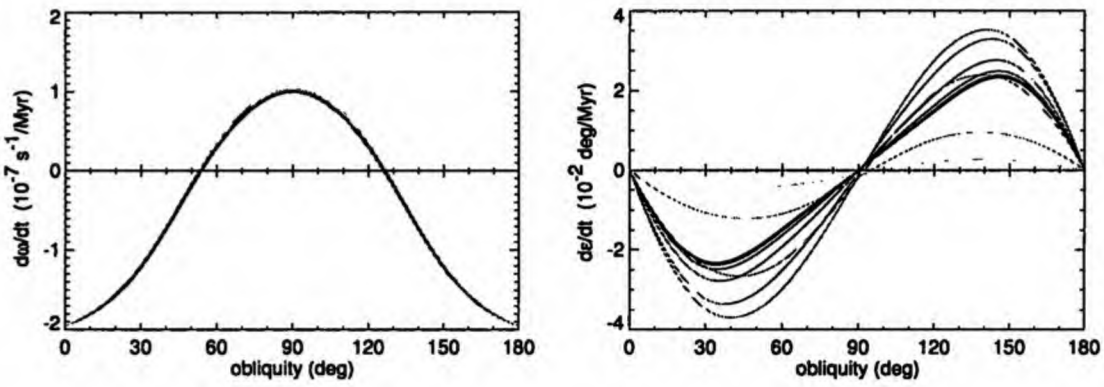

Figure 3.14: The orbit averaged rate of change of the angular velocity ω (left) and obliquity ϵ (right) due to the YORP effect for asteroid (243) Ida. Grey levels denote different surface thermal conductivities from 10^{-9} W/m/K (darkest, corresponding to the Rubincam's limit) to 10 W/m/K (lightest, corresponding to highly conductive material). For more discussion see the text.

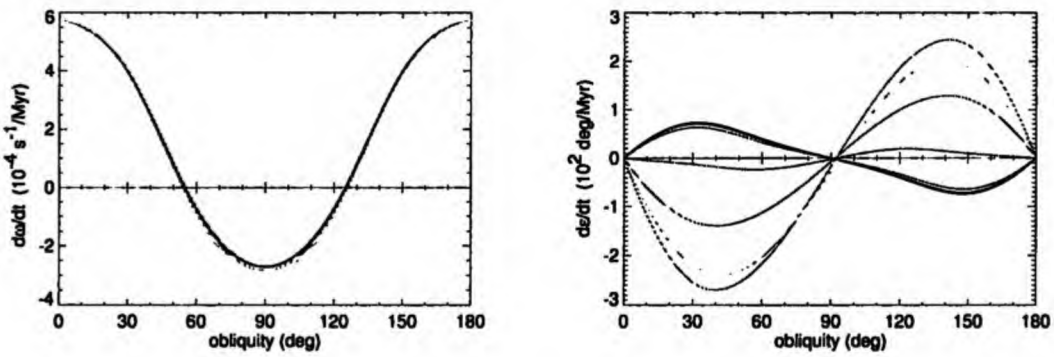

Figure 3.15: The orbit averaged rate of change of the angular velocity ω (left) and obliquity ϵ (right) due to the YORP effect for asteroid (25143) Itokawa. Grey levels denote different surface thermal conductivities from 10^{-9} W/m/K (darkest, corresponding to the Rubincam's limit) to 10 W/m/K (lightest, corresponding to highly conductive material). For more discussion see the text.

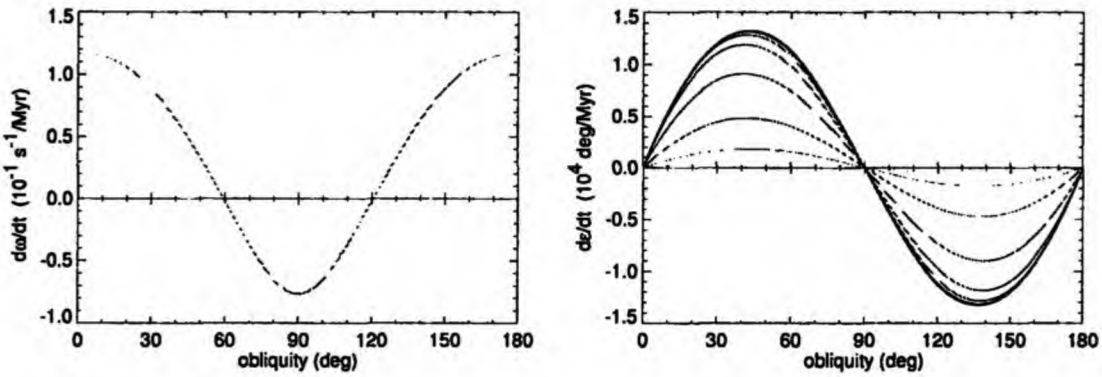

Figure 3.16: The orbit averaged rate of change of the angular velocity ω (left) and obliquity ϵ (right) due to the YORP effect for asteroid 1998 KY26. Grey levels denote different surface thermal conductivities from 10^{-9} W/m/K (darkest, corresponding to the Rubincam's limit) to 10 W/m/K (lightest, corresponding to highly conductive material). For more discussion see the text.

3.4.2 The YORP effect for real objects and their orbits

We computed the YORP effect for several asteroids with known orbits, shapes and spin parameters. The list of bodies and their orbital and physical parameters can be found in Table 3.3:

	Eros	Geographos	Golevka	Ida	Itokawa	1998KY26
semimajor axis (AU)	1.45823	1.24547	2.5065	2.816276	1.32274	1.23215
excentricity	0.222891	0.335416	0.604317	0.04616	0.279475	0.201462
inclination (°)	10.83	13.342	2.277	1.138	1.728	1.481
arg. perihel. (°)	178.645	275.8	66.06	108.55	161.021	209.181
ascend. node (°)	304.404	337.3	211.502	324.21	70.917	84.451
pole of rotation λ, β (°)	17.2, 11.3	55, -46	202, -45	262, -68	355, -84	
obliquity (°)	89.1	150	134.6	157	172.3	
period of rotation (h)	5.27	5.23	6.03	4.63	12.13	0.17837
precision of period determ. σ	1×10^{-7}	1.4×10^{-7}	1.7×10^{-5}	1.5×10^{-6}	5×10^{-4}	7×10^{-6}
thermal conductivity (W/m/K)	0.01	0.02	0.01	0.01	0.01	0.001
thermal capacity (J/kg/K)	680	680	680	680	800	680
bulk density (g/cm^3)	2.5	2.5	2.7	2.7	2.5	2.5
surface density (g/cm^3)	1.7	1.7	1.7	1.7	2.0	1.7
albedo	0.1	0.2	0.1	0.2	0.1	0.1
emisivity	0.9	0.8	0.9	0.8	0.9	0.9
Δt - first level (s)	222	87	500		192	
Δt - second level (s)	4		5		10	

Table 3.3: Orbital and physical parameters of asteroids used for our study of the YORP. Orbital data was taken mainly from NeoDyS site `http://newton.dm.unipi.it` and AstDys `http://hamilton.dm.unipi.it`. Information about the spin state was taken from [Miller et al., 2002] for Eros, [Hudson and Ostro, 1999] for Geographos, [Hudson et al., 2000] for Golevka, [Davies et al., 1996] for Ida, [Kaasalainen et al., 2003] for Itokawa and [Ostro et al., 1999b] for 1998KY26. For information about the shape models see Appendix D.

The surface temperature along the orbit was computed by a two-level scheme. The timestep was a few hundred seconds in the first level and several seconds in the second level (see Table 3.3). The initial spatial step was chosen in order to fulfill the von Neumann stability criterion. The precision of the surface temperature is typically better than 0.1 K. We computed components of the YORP torque in equally spaced right anomalies.

A possible direct detection of the YORP effect was also studied. For this purpose the most important quantity is the change of angular velocity ω and, especially, the phase of rotation ϕ. These quantities are observable (while the change of the obliquity is too small). Moreover, $\langle T_\omega \rangle$ is nearly independent on the surface thermal conductivity, which is not known accurately. The angular velocity and the phase of rotation changes due to the YORP effect can be expressed as:

$$\omega_Y(t) = \omega_0 + \int_{t_0}^{t} \frac{T_\omega}{C} dt, \qquad \phi_Y(t) = \phi_0 + \int_{t_0}^{t} \omega_Y(t)\, dt.$$

where ω_0 is the initial angular velocity at the time t_0 and the initial phase of rotation is assumed $\phi_0 = 0$. We can also express a fractional change of rotation period as $(dP/dt)/P = -(T_\omega/C)/\omega$. Using the orbit-averaged value of T_ω/C, the angular velocity will change linearly with time, whereas the phase of rotation will change as a square of time (here we neglect an eccentricity of

an orbit):

$$\omega_Y(t) = \omega_0 + \left\langle \frac{T_\omega}{C} \right\rangle t, \qquad \left\langle \frac{P - P_0}{P_0} \right\rangle_Y = -\frac{1}{\omega_0} \left\langle \frac{T_\omega}{C} \right\rangle t, \qquad \phi_Y(t) = \omega_0 t + \frac{1}{2} \left\langle \frac{T_\omega}{C} \right\rangle t^2. \tag{3.20}$$

The phase ϕ is the most easily observable quantity that can be used for a detection of the YORP effect. At least three measurements of ϕ with appropriate time delay are necessary for a discovery of the quadratic time dependence of ϕ, indicating the YORP effect. If we take into account that the period of rotation P_0 can be initially determined with an error δP, then this uncertainity propagates and causes apparent changes of ω and ϕ:

$$\omega_{\delta P}(t) = \omega_0 \pm \omega_0 \frac{\sigma}{\sigma + 1}, \qquad \left\langle \frac{P - P_0}{P_0} \right\rangle_{\delta P} = \pm\sigma, \qquad \phi_{\delta P}(t) = \omega_0 t \pm \omega_0 \frac{\sigma}{\sigma + 1} t, \tag{3.21}$$

where $\sigma = \delta P / P_0$ is a relative period error. The detection of the YORP effect via a phase shift is possible if it exceeds the effect of uncertainity. This happens after sufficient time interval:

$$t^{\phi}_{Y > \delta P} = \frac{\sigma}{\sigma + 1} \frac{2\omega_0}{\langle T_\omega / C \rangle}. \tag{3.22}$$

Moreover, the phase shift produced by an uncertainity of the rotation period must be less than 180°. In other words, $|\phi_{\delta P} - \omega_0 t| < \pi$. It corresponds to the time

$$t^{\phi}_{\pi} = \frac{P_0}{2} \frac{\sigma + 1}{\sigma}. \tag{3.23}$$

In the case of a detection by a change of the rotation period, the required time interval is

$$t^{P}_{Y > \delta P} = \frac{\omega_0 \sigma}{\langle T_\omega / C \rangle}, \tag{3.24}$$

which is shorter than (3.22) by a factor $(\sigma + 1)/2$ and moreover there is no restriction like (3.23).

(433) Eros

Figure 3.17 shows the behaviour of the T_ω / C during one orbital period of Eros. The origin of time is chosen at an instant of perihelion passage. The mean value $\langle T_\omega / C \rangle = -1.48 \times 10^{-20}\,\mathrm{s}^{-2}$ corresponds to a doubling time 709 Myr. Eros's rotation is decelerated.

With this YORP torque and NEAR/Shoemaker data, rotation period $P = 5.27025547$ hr, $\sigma = 1 \times 10^{-7}$ ([Miller et al., 2002]), we have determined the change of rotational period and the phase from 1900 to 2020 as can be seen in Figure 3.18. The origin was chosen on Jan 1, 2001. The phase of rotation changed due to YORP effect by $\sim 4°$ in 100 years, while the uncertainity in rotation period makes phase shift $\sim 7°$ after the same time. In terms of the period, the YORP leads to a relative change of period $(P - P_0)/P_0 \simeq -1.5 \times 10^{-7}$ in 1900, which is slightly higher than uncertainity σ.

[Ďurech, 2005] compared photometric data of Eros from years 1901 – 1931 with a synthetic lightcurve derived from shape and rotation state obtained by NEAR/Shoemaker space probe. He found that $\langle d\omega/dt \rangle$ cannot be higher than $\sim 5 \times 10^{-20}\,\mathrm{s}^{-2}$. It is interesting, that the formal fit gives the value $\langle d\omega/dt \rangle = -1.4 \times 10^{-20}\,\mathrm{s}^{-2}$, which corresponds well to the value predicted by us, but the case is not statistically conclusive.

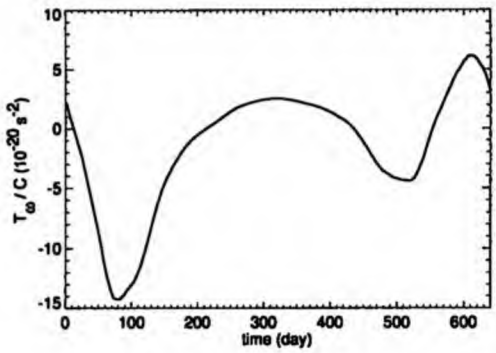

Figure 3.17: The YORP component affecting the angular velocity of (433) Eros during one revolution about the Sun. This was computed using data from Table 3.3.

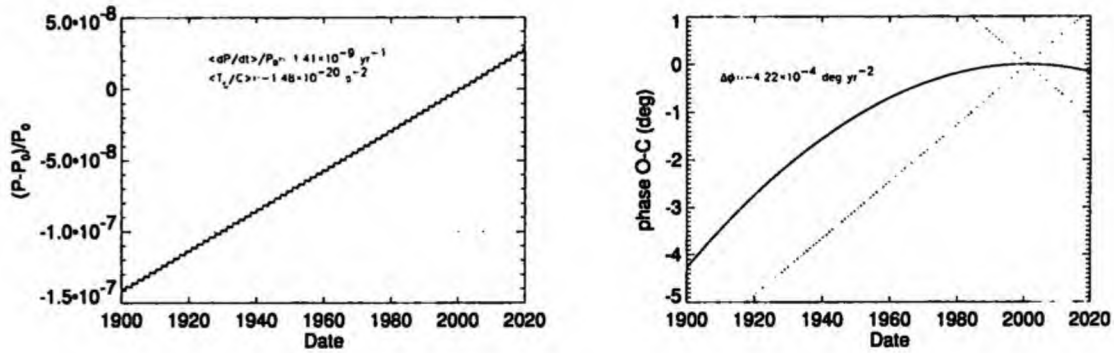

Figure 3.18: Left: The relative change of rotation period of Eros. Right: The corresponding change of the rotation phase. The results are referred to the value P_0 =5.27 hr on Jan 1, 2001. The dotted line corresponds to a change of period or phase of rotation due to an uncertain determination of the initial period P_0. The relative uncertainity is $\sigma = 1 \times 10^{-7}$. The solid one corresponds to the orbit-averaged YORP effect. Note a linear growth of $(P - P_0)/P_0$ and the corresponding quadratic dependence of phase $O - C$.

(6489) Golevka

The time dependence of the YORP component T_ω/C that affects angular velocity of Golevka can be seen in Figure 3.19. The orbit-averaged value is $\langle T_\omega/C \rangle = 2.04 \times 10^{-18}$ s. This corresponds to a doubling time of only 4.5 Myr, the asteroid's rotation is accelerated in this state.

A possibility of a successful direct detection of the YORP can be seen in Figure 3.20: The mean value of the fractional change of rotation period is $\langle (dP/dt)/P \rangle = -2.2 \times 10^{-7}\,\mathrm{yr}^{-1}$. We used data obtained during the close encounter with the Earth in 1995 from [Hudson et al., 2000]: $P = 6.0289$, $\sigma = 1.7 \times 10^{-5}$, and chose an origin of integration on Jan 2, 1995. It can be seen, that the YORP (though relatively strong) does not exceed the effect of uncertainity of rotation period. Unfortunately, no usable photometric data were recorded during the close approach in 2003. Next opportunities will be in 2007, 2011, 2015 and 2019. Due to the large YORP effect on Golevka, the data from these future encounters may lead to a successful detection of the YORP.

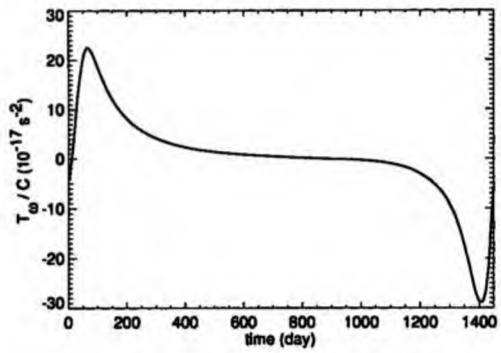

Figure 3.19: The YORP component T_ω/C affecting the angular velocity for (6489) Golevka during one revolution about the Sun. This was computed using data from Table 3.3.

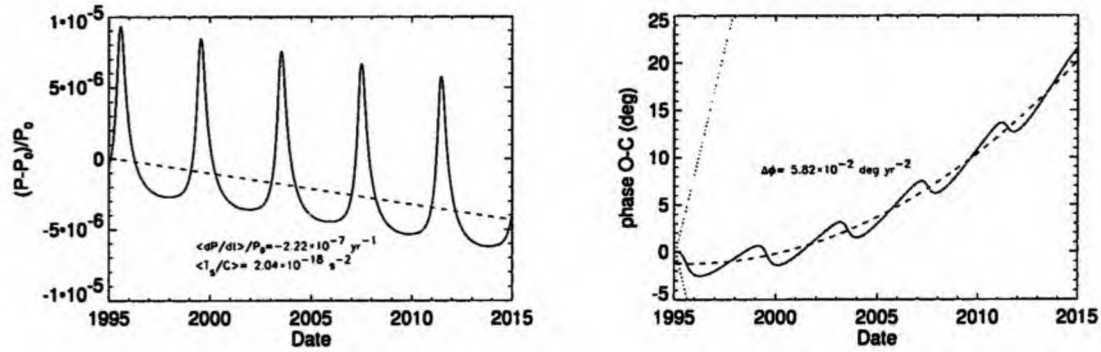

Figure 3.20: The same plots as in Figure 3.18 but for Golevka. The results are referred to the value P_0 =6.02667 hr on Jan 2, 1995. Note the large variations of $(P_0 - P)/P_0$ due to high eccentricity of Golevka's orbit $e \simeq 0.6$.

1998 KY26

The asteroid 1998 KY26 has an unknown orientation of the spin axis. We can only scale the results obtained in the previous section. We assumed values listed in Table 3.3 and zero obliquity. Then the orbit-averaged YORP component changing the angular velocity is $\langle T_\omega/C\rangle = 1.52 \times 10^{-14}$ and the doubling time $t_d = 20\,400$ yr. This corresponds to a mean fractional change of rotation period $\langle (dP/dt)/P\rangle = 5\times10^{-5}\,\mathrm{yr}^{-1}$. Thus, we expect the possible successful detection of the YORP effect for this body during its next apparition is September 2013. (The determination of the pole orientation is also probable during this apparition.) Even more probable YORP effect detection will be during the close-Earth encounter in June 2024.

(243) Ida

We do not compute YORP effect for the actual orbital configuration as listed in Table 3.3, but scaling the results from previous section, the orbit averaged component of YORP is $\langle T_\epsilon/C\rangle \simeq 3.5\times10^{-21}\ \mathrm{s}^{-2}$ and the doubling time $t_d \simeq 3.4$ Gyr. This is comparable to the age of the Koronis asteroid family and might have caused the evolution of spins discussed by [Vokrouhlický et al., 2003]. Nevertheless, for direct short-term detection, the YORP is too weak.

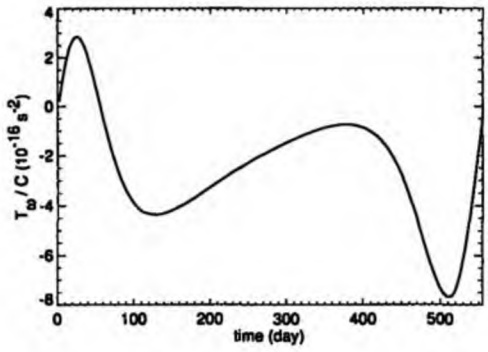

Figure 3.21: The YORP component affecting the angular velocity of (25143) Itokawa during one revolution about the Sun. This was computed using data from Table 3.3.

(25143) Itokawa

[Vokrouhlický et al., 2004] computed the YORP effect strength for this asteroid and predicted the possible detection of the YORP effect by an observation of the ligtcurve maximum shift during its close encounter in 2004. Unfortunately, this conclusion was incorrect: (i) we underestimated the uncertainity of the rotation period by a factor 2π and (ii) we used an incorrect component of the YORP torque (T_ϵ or T_ψ instead of T_ω) . This led to conclusion that the rotation of Itokawa is accelerated and a fractional change of Itokawa's rotation is $(dP/dt)/P \simeq 1.5 - 3 \times 10^{-4}\,\mathrm{yr}^{-1}$. An attempt to detect failed.

Using the correct data (see Table 3.3) and the same shape model as [Vokrouhlický et al., 2004], based on radar and optical Earth-based observations (see Figure D.7), we found that Itokawa's rotation is accelerated due to the YORP torque $\langle T_\epsilon/C\rangle = 6.6 \times 10^{-17}\,\mathrm{s}^{-2}$ and the value of the fractional change of spin period is $(dP/dt)/P = -1.45 \times 10^{-5}\,\mathrm{yr}^{-1}$. This corresponds to the doubling time $t_d \simeq 69\,000$ years. The phase shift due to the YORP effect then increases as $\Delta\phi = 1.89° \left(\frac{t}{\mathrm{yr}}\right)^2$ and after three years it is $\sim 17°$.

We also used the shape model determined by Hayabusa mission [Gaskell et al., 2006], see Figure D.8. The shape model with 2000 surface elements leads to the deceleration of Itokawa's rotation: $\langle T_\epsilon/C\rangle = -10^{-17}\,\mathrm{s}^{-2}$ and $(dP/dt)/P = 2 \times 10^{-6}\,\mathrm{yr}^{-1}$. The shape models with higher number of the surface elements give even $\sim 3\times$ higher values of the YORP effect (D. Vokrouhlický, personal communication).

[Nesvorný and Vokrouhlický, 2007] found that intermediate and small-surface-area features are important for the overall YORP torque on Itokawa. This fact can explain the difference between YORP effect computed for low-resolution shape models (e.g. [Ostro et al., 2004]) and detailed shape models determined by Hayabusa mission.

Recently, [Scheeres et al., 2007] have used data of shape and rotation of Itokawa from Hayabusa mission to Itokawa and with aid of semianalytical theory of YORP effect they found Itokawa's spin rate deceleration $-(2.5 - 4.5) \times 10^{-17}\,\mathrm{s}^{-2}$, depending on the shape model used. They also discussed strong dependence of strength and sense of YORP on the shape model. Itokawa seems to be an exemplary case in this sense.

(1620) Geographos

Using data from Table 3.3 we computed the YORP effect on the asteroid (1620) Geographos. In this case we faced a problem with the choice of the right shape model. Using the shape model derived from combination of the radar and optical observations (available at the website

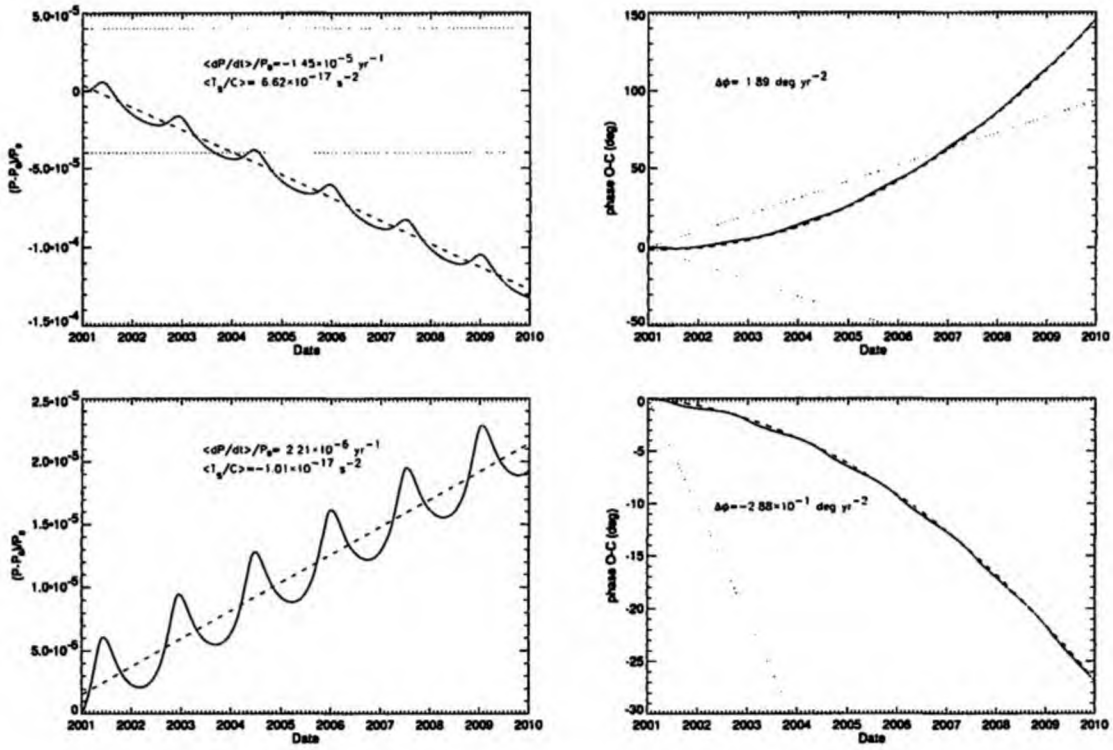

Figure 3.22: The same as 3.18 but for Itokawa. The results are referred to the value 12.134 hr on Jan 1. 2001. The upper row corresponds to the shape mode determined from radar observations and the lower one corresponds to the Hayabusa shape model (2000 surface elements). See Appendix D.

`http://www.psi.edu/pds/asteroid/`), we obtained the YORP torque (produced by thermal and reflected radiation) changing the spin rate $d\omega/dt = T_\omega/C = -4.4 \times 10^{-18}\,\mathrm{s}^{-2}$. In this model, the $z-$axis does not correspond to the axis of the maximal moment of inertia.

Then we made rotation of the body-fixed frame (90° about the $x-$axis) to the system of proper axes and achieved an agreement of $z-$axis orientation with the axis of maximal moment of inertia and also with the position of "north pole" in [Hudson and Ostro, 1999] (see Figure D.1). In this case, the change of spin rate is $d\omega/dt = 3 \times 10^{-19}\,\mathrm{s}^{-2}$.

Another shape model derived by J. Ďurech (personal communication) from ligtcurve analysis (see Figure D.2) gives a value $d\omega/dt = 2.4 \times 10^{-18}\,\mathrm{s}^{-2}$. Here we used the pole of the spin axis derived by Ďurech: $\lambda = 51.5°$, $\beta = -57.3°$. The volume of Ďurech's model was scaled to the same volume as model of [Hudson and Ostro, 1999]. We also made rotation of body-fixed frame to the system of principal axis of inertia tensor.

The possibility of detection of the YORP effect on (1620) Geographos is shown in Figure 3.23. Here we used the shape model of Ďurech. The next opportunity to observe Geographos during its approach will be in 2008. The YORP effect produces a phase lag $\sim 13°$ between 1994 and 2008. Thus, if the shape derived by Ďurech is the correct one[8], we can expect the successful detection in 2008.

[8]The shape of [Hudson and Ostro, 1999] leads to phase lag $\sim 1.3°$ between 1994 and 2008. This is not enough to successful detection in 2008.

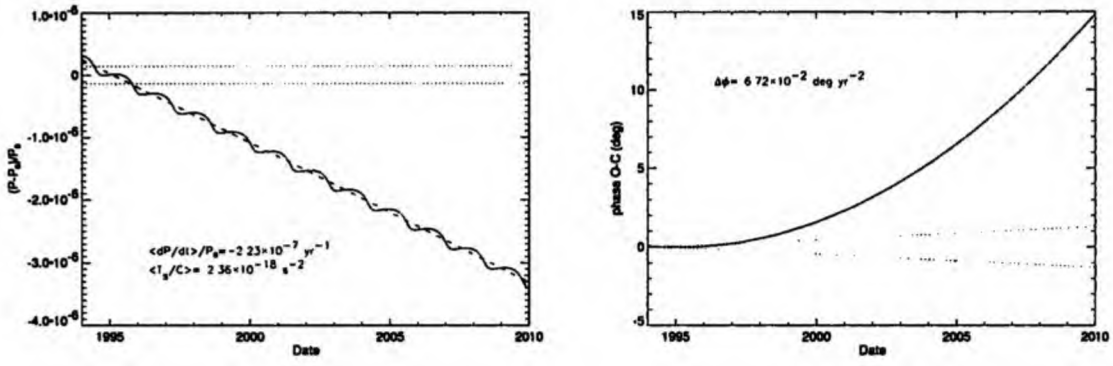

Figure 3.23: Left: Relative change of rotation period of (1620) Geographos. Right: Change of the rotation phase. The results are referred to the value P_0 =5.23 hr on September 15, 1994. The dotted line corresponds to the change of period or phase of rotation due to uncertain determination of the initial period P_0. The uncertainity of the spin period is $\sigma = 1.4 \times 10^{-7}$ (according to [Hudson and Ostro, 1999]). The dashed one corresponds to the orbit-averaged YORP effect. Note linear growth of $(P - P_0)/P_0$ and corresponding quadratic dependence of phase $O - C$.

Discussion

We have shown that the YORP component T_ω causes the changes of the angular velocity $d\omega/dt$ (or the phase shift), which can be measured directly. Moreover, the YORP component T_ω does not depend on thermal conductivity K. Thus the principal moment C of inertia and the bulk density ρ_b of the asteroid can be determined by measured $d\omega/dt$ together with the YORP effect model.

3.5 Summary

- The YORP effect affects both the spin period and the obliquity of the asteroids with certain amount of the windmill asymmetry. The shape and obliquity are the key quantities affecting the YORP effect.
- A typical YORP evolution timescales are shorter than collisional timescales (for asteroids smaller than several tens of kilometers in the Main Belt). The YORP effect can double the rotation period of 2 km Main Belt asteroid in ≈12 Myr.
- The obliquity-affecting YORP component T_ϵ depends on the thermal conductivity K of surface material, while the component T_ω, affecting the angular velocity, is almost K-independent.
- There is a wide variety of possible YORP evolution paths of the spin states. In the most likely case, the spin axis is driven to be perpendicular with respect to the orbital plane.
- The spin period can be both accelerated (maybe up to a bursting limit and possible formation of binary asteroids) or decelerated (to the state of very slow tumbling rotators).
- The spin period of bodies with obliquity $\epsilon \simeq 55°$ and $\epsilon \simeq 125°$ is not affected by the YORP effect.

- We computed the YORP effect for several asteroids, assuming their actual shape and orbital, rotational and physical configuration, and showed possibilities of a successful YORP effect detection via change of the rotation period or a phase shift of the lightcurve. We predict the successful direct detection of the YORP effect for (6489) Golevka, 1998 KY26, (25143) Itokawa and (1620) Geographos in the near future.

Chapter 4

The Yarkovsky effect

4.1 Introduction

4.1.1 The principle of the Yarkovsky effect

The Yarkovsky effect is a relatively weak non-gravitational force arising from anisotropic thermal emission from the surface of a body, which is heated by the absorption of the solar radiation. The principle of the effect can be explained as follows: Let us assume an asteroid orbiting about the Sun and rotating about the spin axis perpendicular to the orbital plane. The surface of the body absorbs solar radiation[1] which heats it up. Due to the finite thermal inertia of the surface material the temperature follows the insolation with some delay, as can be seen in Figure 4.1. This causes the "morning" hemisphere is cooler and the "evening" one is warmer. The surface emits thermal radiation which takes certain amount of momentum away. This causes a repulsive *thermal force*, which direction is somewhat shifted from the direction opposite to the Sun due to disbalance of temperature between the morning and evening hemispheres. The transverse component of this force, parallel to the velocity vector of the asteroid, then causes (according to the laws of celestial mechanics) a change of the semimajor axis of the orbit. If the body's rotation is prograde, its semimajor axis increases, if it is retrograde the semimajor axis decreases. (The body spirals inwards or outwards.) The above described effect is called the *Yarkovsky diurnal effect* (see Figure 4.2a). The strength of this effect depends on the distance from the Sun, the diameter of the body, its mass, thermal parameters of the surface (the thermal conductivity K, thermal capacity c, surface density ρ_s), the speed of rotation and the obliquity.

Another component of the Yarkovsky effect is connected with the orbital motion about the Sun and, consequently, it is called *seasonal*. It is independent on the rotation speed and always leads to the semimajor axis decay. It is caused by the effect of thermal inertia during the revolution about the Sun. The necessary condition is the obliquity not equal 0° or 180°. Let us expect the Sun is shining on the northern hemisphere during the summer (see Figure 4.2b). In the autumn equinox the Sun illuminates both hemispheres equally, but due to the thermal inertia the northern one is warmer and then the resulting thermal force is shifted from the direction opposite to the Sun and against the direction of motion. A similar situation occurs in the spring equinox: The southern hemisphere is warmer than northern one and the thermal force again aims against the velocity vector. In real situations, the Yarkovsky effect is a combination of the above mentioned components.

[1]The momentum of this absorbed radiation together with the radiation reflected due to non-zero albedo give rise to the solar radiation pressure. But this force has direction opposite to the direction towards the Sun and its effect overall averaged over orbital period only decreases the solar gravitation force.

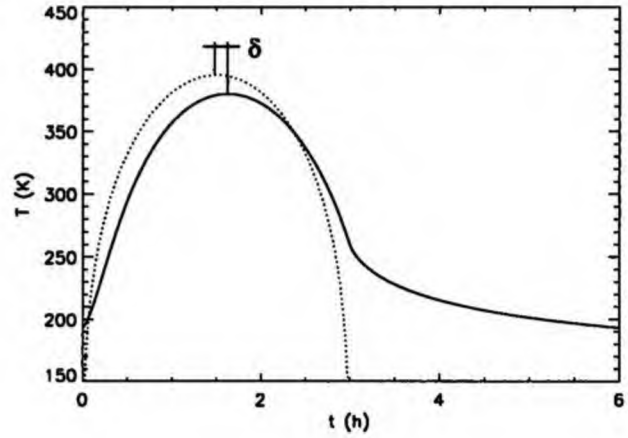

Figure 4.1: The delay δ between the maximal insolation (dotted line) and the maximal temperature (solid line) due to the thermal inertia of the surface material. The figure corresponds to an equatorial surface element during one rotation cycle lasting 6 hours.

4.1.2 The Yarkovsky effect in the Solar System

The Yarkovsky effect plays an important role in the dynamics of meter to multi-kilometer sized bodies in the Solar System. It helps us to explain many observed (and previously puzzling) facts. Some of them we shall briefly mention here.

Delivery of meteorites to the Earth. The first application of the Yarkovsky effect was an explanation of the meteorite transport from the Main Belt to the Earth's vicinity (e.g., [Öpik, 1951], [Peterson, 1976]). Recently the subject was studied for example by [Farinella et al., 1998] and [Vokrouhlický and Farinella, 2000]. According to the model of [Vokrouhlický and Farinella, 2000], the asteroidal fragments, ejected after the disruption of parent body, slowly spiral due to the Yarkovsky effect. A typical semimajor axis drift rate da/dt is from $\sim 10^{-4}$ to $\sim 10^{-2}$ AU/Myr. It depends mainly on diameters of fragments, densities and thermal parameters of the surface. The obliquity also affects the strength and direction of Yarkovsky effect. During this stage (that can take from several Myr up to several 10 Myr) the fragments may undergo secondary collisions, causing changes of their spin axes or even further fragmentation. Finally the fragments reach a powerful gravitational resonance (3:1 mean motion resonance with Jupiter or ν_6 secular resonance), where they are captured and their excentricity rapidly increases up to 1. This stage lasts only a few Myr. Most bodies then fall directly into the Sun and only less than 1% hit the Earth. There is a good agreement between the calculated transport timescales and the observed cosmic ray exposure times of various meteorite types (they differ for various materials), and it is also possible to explain the observed total meteorite flux.

Delivery of small asteroids to the near Earth space. It was recognized that most of the near-Earth asteroids originate in the Main Belt from where they are delivered to the Earth's vicinity via powerful resonances. [Bottke et al., 2002] estimated that approximately 220 objects per Myr with absolute magnitude $H < 18$ (i.e., with diameter $D \gtrsim 1$ km) must escape from the inner Main Belt in order the population of NEAs to be in steady state. Refilling of new asteroids to the resonances can be explained by a semimajor axis drift caused by the Yarkovsky effect. [Morbidelli and Vokrouhlický, 2003] studied the transfer of bodies towards 3 : 1 and ν_6 resonances, assuming random reorientation of spin axes due to collisions and the YORP effect. Their model gives the same flux as derived by [Bottke et al., 2002]. Moreover, due to the

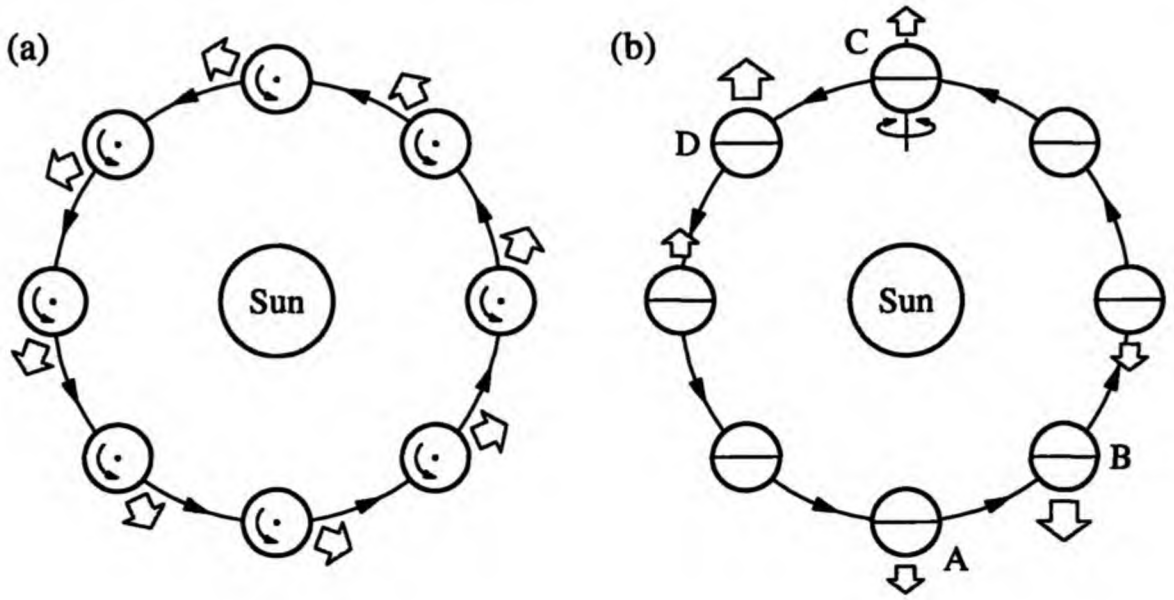

Figure 4.2: The principle of Yarkovsky effect: (a) diurnal and (b) seasonal component. More explanation in the text. (The autor of this figure is M. Brož)

Yarkovsky effect sensitivity on size, they are able to explain the difference between the cumulative size distribution of main belt asteroids $N(>D) \propto D^{-1.3}$ and thet of the near-Earth asteroids $N(>D) \propto D^{-1.75}$. [La Spina et al., 2004] also noticed the dominance of the Yarkovsky effect over collisions in injecting the bodies into resonances. They found that retrograde rotators[2] among NEA's are more numerous than the prograde ones. This is most probably caused by the fact that the ν_6 resonance transport route is more effective than the 3 : 1, and because the ν_6 is located inside the Main Belt, the bodies have to drift inwards (and thus have retrograde spins).

Evolution of asteroid families due to the Yarkovsky effect. Asteroid families originate from a catastrophic collisions or cratering event of a parent body that produced fragments, which we can observed today as clusters in the space of proper elements a_p, e_p, $\sin i_p$; they also exhibit similar spectral properties. Subsequent evolution is driven by the Yarkovsky effect, mutual collisions of the fragments and planetary perturbations.

For example [Bottke et al., 2001] investigated the evolution of the Koronis family. They explain the observed shape in $(a, e, \sin i)$ space evolution in three steps. Firstly, the catastrophic disruption produces multi-kilometer fragments with random orientation of spin axes. Next, their semimajor axes evolve due to the Yarkovsky effect. The fragments also interact with numerous weak resonances, which results in the changes in eccentricity. The most important of them is the secular resonance $g + 2g_5 - 3g_6$, located at 2.92 AU, that typically increases the eccentricity of passing asteroids, producing the separation of Koronis family into two parts. Finally, if the body reaches the powerful resonances 5:2 or 7:3, its eccentricity and inclination rapidly increases, causing an ejection from the Solar System, an impact on the Sun or a planet.

[Vokrouhlický et al., 2006b] studied the structure of the Eos family. They found that after the primary collision, a compact family arose and it consequently have evolved by the Yarkovsky effect and by planetary perturbations. The fragments, which were driven by the Yarkovsky effect to the smaller semimajor axes and encounter 7 : 3 mean motion resonance with Jupiter were

[2] 15 from 21 bodies with known obliquity rotates in a retrograde sense.

removed. This explains the sharp boundary of the family located exactly at the above mentioned resonance. On the other side the fragments driven outward from the Sun meet a bit weaker 9:4 resonance and only some of them pass it. By this scenario they are able to explain the asymmetric distribution of the family members with respect to the 9:4 mean motion resonance with Jupiter. They also estimated the age of this family to be $1.3^{+0.15}_{-0.2}$ Gyr.

[Vokrouhlický et al., 2006a] developed a method for determination of ages of asteroidal families on the basis of the Yarkovsky/YORP maturity. They determined the ages for families Astrid, Erigone, Massalia and Merxia, as well as their initial dispersion velocities of fragments after the primary collision.

Detection of the Yarkovsky effect. The first measurement of the Yarkovsky force was achieved by observations of the drag of satellite Lageos from 1976 to 1987 (e.g., [Rubincam, 1990]).

[Vokrouhlický et al., 2000] studied a possibility of direct detection of the Yarkovsky effect via precise orbit determination of near-Earth asteroids. Since the Yarkovsky perturbation accumulates quadratically with time, they predicted a successful detection on several asteroids (namely (6489) Golevka, (1620) Geographos, (1566) Icarus) with orbits determined by radar ranging during their next apparitions. In May 2003 the radar ranging of (6489) Golevka was made during its close encounter with the Earth and non-gravitational perturbation was detected [Chesley et al., 2003]. This perturbation corresponds to the predicted shift due to the Yarkovsky effect and allows to estimate the bulk density of Golevka as $2.7^{+0.4}_{-0.6}$ g/cm^3 and thermal conductivity as 0.01 W/m/K.

Further detections of the Yarkovsky effect for more near-Earth asteroids are expected in the near future [Vokrouhlický et al., 2005a]. An interesting opportunity to detect the Yarkovsky effect (both on the motion of centre of mass and on relative motion of components) appears in the case of near-Earth binary asteroids [Vokrouhlický et al., 2005b].

[Nesvorný and Bottke, 2004] studied the young Karin family, with age only 5.8±0.2 Myr, and on the basis of convergence of orbits they determined the Yarkovsky effect for its $\sim$ 70 members. The magnitude of the measured Yarkovsky orbital drift agreed with the theoretical predictions. They also determine the surface conductivity of asteroidal fragments as $\sim$ 0.1 W/m/K.

[Chesley et al., 2006] focused on the small near-Earth asteroid 1992 BF. Orbital calculations based on the observations from 1992–2005 poorly fit the pre-discovery observations from 1953, but with the Yarkovsky effect included into the force model they were able to fit the complete observational arc 1953–2002. The resulting semimajor axis drift is $da/dt = -(11 \pm 2) \times 10^{-4}$ AU/Myr, which corresponds to the Yarkovsky effect with a retrograde spin axis orientation with obliquity 120° – 180°.

4.1.3 The theory of the Yarkovsky effect

The computation of the Yarkovsky effect usually consists of the determination of asteroid's surface temperature, the computation of the corresponding thermal force and the determination of its effect on asteroid's orbit. The surface temperature T is calculated from the heat diffusion equation (HDE for short) inside the body (see Appendix A)

$$\rho c \frac{\partial T}{\partial t} = \nabla(K \cdot \nabla T), \tag{4.1}$$

where the density ρ, the thermal capacity c and the thermal conductivity K describe the thermal properties of asteroid material. The HDE is connected with the surface boundary condition:

$$K \nabla T \cdot \mathbf{n} + \epsilon\sigma T^4 = (1 - A)\mathcal{E}. \tag{4.2}$$

Here, $\mathbf{n}$ denotes the outer normal to the surface, ϵ the emisivity, σ the Stephan–Boltzmann constant, A the albedo and $\mathcal{E}$ incident solar flux. This equation is essentially the energy conservation law: The first term represents the energy conducted from the surface to the interior of the body, the second one is the energy taken away by thermal radiation and the right hand side term represents the absorbed solar energy.

The thermal force $\mathbf{f}_{\mathrm{th}}(t)$ acting on a body can be determined by Equation (2.11). Knowing the force we can obtain the change of the semimajor axis a of asteroid's orbit due to the Yarkovsky effect by Gauss equation

$$\frac{da}{dt} = \frac{2}{n^2 a\, m}\, \mathbf{f}_{\mathrm{th}}(t) \cdot \mathbf{v}(t), \tag{4.3}$$

where $\mathbf{v}(t)$ denotes the velocity vector of the asteroid, m its mass and n the mean motion.

As mentioned in Section 4.1, the key phenomenon controlling the strength of Yarkovsky effect is an anisotropic thermal radiation from asteroid's surface caused by thermal lag due to non-zero thermal inertia of the asteroid's surface material. As we shall see, the Yarkovsky effect is not so sensitive to the asteroid's shape as the YORP effect.

The heat diffusion problem can be solved analytically or numerically. In analytical theories the boundary condition is often linearized (e.g. [Vokrouhlický, 1998a], [Vokrouhlický, 1999]). Moreover, the analytical theories assume (i) spherical objects, (ii) circular orbits, (iii) uniform rotation, (iv) constant thermal parameters. Several attempts to remove these constraints were made. For example [Vokrouhlický, 1998b] took into account the effects of non-sphericity for the Yarkovsky diurnal effect, [Vokrouhlický and Brož, 1999] computed the seasonal effect assuming a regolith layer above the higher conductive core and [Vokrouhlický and Farinella, 1999] presented a semianalytical theory of seasonal effect which is able to involve elliptical orbits.

The numerical approach allows to eliminate all the above mentioned constraints, but it may be very time-consuming (it depends on the precision and complexity of the model). The numerical model was used for prediction of Yarkovsky orbital drift of (6489) Golevka [Chesley et al., 2003]. In [Vokrouhlický et al., 2005a] the Yarkovsky effect on irregularly shaped (1620) Geographos and tumbling (4179) Toutatis was also computed numerically, as well as in the case of binary asteroid 2000 DP107 [Vokrouhlický et al., 2005b].

4.2 Yarkovsky diurnal effect on irregularly shaped objects

This section is based on the poster [Čapek and Vokrouhlický, 2002] presented at the ACM conference 2002 in Berlin.

Analytical theories of the Yarkovsky effect usually assume spherical objects and rely on linearized surface boundary condition of the HDE. Our goal is to remove both simplifying assumptions by solving the heat diffusion problem numerically for an arbitrarily shaped body. Here we present the comparison of results obtained by an analytic theory and those of numerical model. We proved that (i) the Yarkovsky effect is not very sensitive to the exact asteroid's shape and (ii) the linearized analytical theory is a good approximation.

4.2.1 Numerical model

Our approach can be briefly described in the following four steps:

1. For a body described by a polyhedron, with typically several thousands of triangular surface facets, we determine the insolation of a given surface element, including effects of self-shadowing between different surface elements (see Appendix B). The time step is 1 s, which corresponds to only 1′ of rotation phase.

2. With this insolation, we solve the one-dimensional HDE during one rotation cycle from surface to depth of $15\ell_d$ (see Appendix A). The initial condition is derived from the mean insolation.

3. We repeat the previous scheme (with the initial condition corresponding to the temperature determined in the previous turn), until the convergence of the HDE solution is attained. Usually, we require the uncertainty of the surface temperature is less than 0.1 K.

4. With the converged solution we compute the corresponding mean Yarkovsky force acting on each surface element according to Equation (2.9). The Yarkovsky force is then given by a sum over all surface elements. The mean rate of change of the semimajor axis is given by the corresponding Gauss' equation (assuming circular orbit):

$$\frac{da}{dt} = \frac{2}{n}\,\mathbf{f}_{\rm th}\cdot\mathbf{e}_t \tag{4.4}$$

Note that because of the assumption of zero eccentricity and obliquity, it is sufficient to evaluate the Yarkovsky effect at a single point only during its revolution around the Sun. Here, n denotes mean motion, $\mathbf{e}_t$ the along-track vector of the orbit $\mathbf{f}_{\rm th}$ the Yarkovsky force per unit mass.

4.2.2 Analytical vs. numerical approach for a sphere

As a test of our method, we first computed the diurnal Yarkovsky drift on a sphere, both analytically and numerically. We assume a circular orbit with semimajor axis $a = 2.5$ AU, the rotation period 6 h, the radius 1 km, the bulk and surface density $\rho = 2500\,\mathrm{kg/m^3}$, thermal capacity $c = 680\,\mathrm{J/kg/K}$ and zero obliquity. Thermal conductivity of the surface regolith was varied from 10^{-9} to $10^{2}\,\mathrm{W/m/K}$. Analytical model was adopted from [Vokrouhlický, 1999]. Numerical approach uses a "sphere" consisting of 1004 surface triangular facets.

The resulting Yarkovsky orbital drift as a function of the thermal conductivity, computed by the analytical and numerical theory, can be seen in Figure 4.3. The most likely values of K (as well as the peak of da/dt) inferred from infrared observations of small NEA's are in the interval

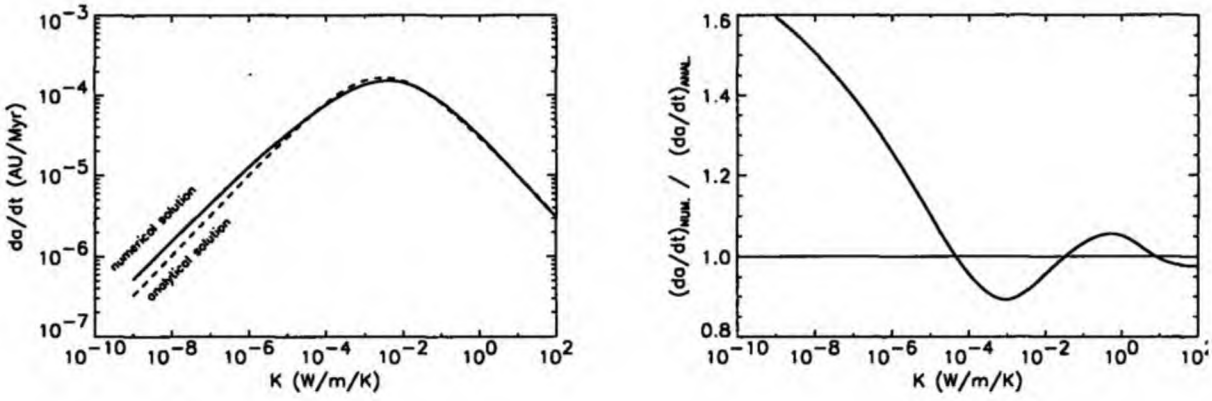

Figure 4.3: Left: The diurnal Yarkovsky orbital drift da/dt as a function of the thermal conductivity K for a sphere with radius 1 km and zero obliquity. The solid line corresponds to the numerical solution of the HDE and the dashed line to the analytical one. Right: The ratio between the Yarkovsky orbital drift computed numerically and analytically as a function of the thermal conductivity for the same sphere.

$0.001 - 0.1$ W/m/K [Delbò et al., 2006]. The results of numerical and analytical model is shown in Table 4.1.

A comparison of Yarkovsky orbital drift da/dt computed numerically and analytically is shown in Figure 4.3 right. It can be seen that the amplitude of ratio of numerical and analytical results is decreasing with increasing thermal conductivity. This is caused by the fact, that due to great thermal variations in the case of low conductivity, the analytical linearization of HDE fails and produces incorrect results. Nevertheless, the analytical results are only 1.6 times smaller for conductivity 10^{-9} W/m/K. For the realistic values of thermal conductivity ($K > 10^{-4}$ W/m/K) the difference is less than 10%.

4.2.3 Irregularly shaped bodies vs. sphere

We tested the calculations of the Yarkovsky effect for irregular bodies on a sample of 100 Gaussian random spheres (see Appendix), all having the same mass as a sphere with radius 1 km and density 2500 kg/m^3. We computed the Yarkovsky orbital drift assuming the thermal conductivity 10^{-3} and 10^{-2} W/m/K, keeping other parameters as above for the spherical body. The resulting distributions of da/dt are shown in Figure 4.4.

The analytical result systematically overestimates the semimajor axis drift, both with respect to the numerical solution for a sphere and with respect to the mean value over the Gaussian spheres sample. Quantitative results are summarized in Table 4.1.

The analytical theory thus gives higher values by a factor of 1.25 or 1.19. Overall, however,

K (W/m/K)	10^{-3}	10^{-2}
numerical model (the mean value for GRS)	1.23×10^{-4}	1.27×10^{-4}
numerical model (sphere)	1.36×10^{-4}	1.45×10^{-4}
analytical model (sphere)	1.53×10^{-4}	1.52×10^{-4}

Table 4.1: The diurnal Yarkovsky semimajor axis drift da/dt in the units of (AU/Myr) computed by numerical and analytical model. See the text.

this difference is comfortably small so that the results of the linearized analytical theory can be used for modelling statistical parameters of the meteorite transport, the origin of NEAs, evolution of asteroid families and for simillar applications.

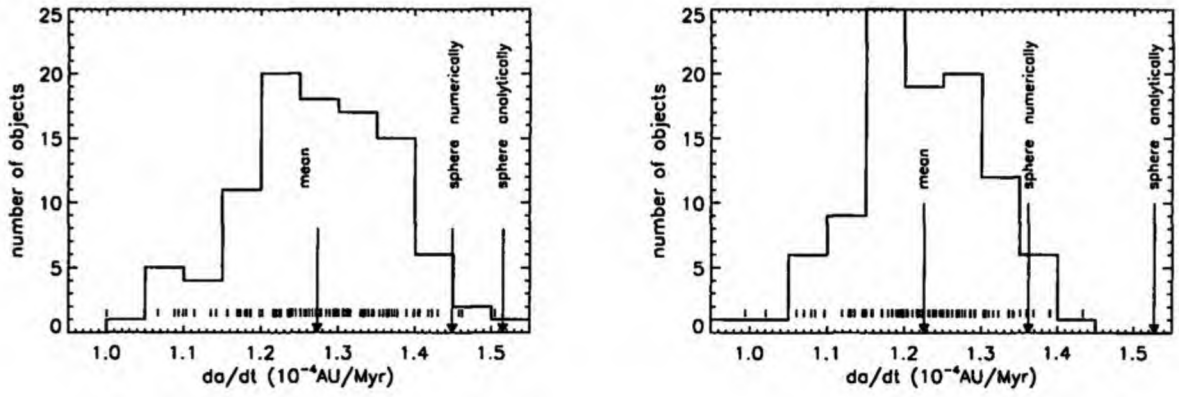

Figure 4.4: The distribution of the diurnal Yarkovsky orbital drift computed for 100 Gaussian random spheres with zero obliquity. Left plot corresponds to the thermal conductivity 0.01 W/m/K and right one to 0.001 W/m/K. The symbols at the bottom of the plot represent actual individual values of da/dt.

4.3 Yarkovsky effect on individual bodies

4.3.1 (6489) Golevka – the direct detection of the Yarkovsky effect

In the following text we describe our computations which were used for the prediction and detection of the Yarkovsky effect on asteroid (6489) Golevka ([Chesley et al., 2003]).

(6489) Golevka (1991 JX) is a $\sim$ 500 m size Apollo-type object with an orbit close to the 3 : 1 mean motion resonance with Jupiter and also near to the 1 : 4 resonance with the Earth. It was discovered during a close encounter with the Earth on May 10, 1991 [Helin et al., 1991]. A large international observing campaign during its apparition in 1995 allowed to determine the spin vector, period of rotation, shape model and other physical properties, as well as precise orbit [Mottola et al., 1997], [Hudson et al., 2000].

[Vokrouhlický et al., 2000] investigated a possibility of detecting of the Yarkovsky effect via precise orbit determination of near-Earth asteroids. They showed that such a detection is possible only using an accurate radar astrometry at several apparitions. The radar observations must cover sufficiently long time span to accumulate Yarkovsky perturbations, which depend quadratically on the time. In the case of Golevka they predicted the Yarkovsky orbital drift $da/dt \simeq -6\times10^{-4}$ AU/Myr (assuming thermal conductivity $K = 0.01$ W/m/K) and corresponding displacement of 15.2 km, with respect to the purely gravitational model of orbital evolution, during time interval between apparition in 1991 and 2003. On the basis of known astrometric observations they determined the initial state vector and its uncertainity. Then they propagated it using the pure gravity model and also the model that included the Yarkovsky force. For the time of the close encounter in 2003 they determined 3σ uncertainity ellipses in the range (R) vs. range-rate (dR/dt) plane. (These quantities are directly observable by radar.) They showed that the ellipsoids corresponding to standard and Yarkovsky-included model are shifted by $\sim$ 15 km and are well separated. They concluded that the Yarkovsky effect could be dected by radar ranging during 2003 approach.

On the basis of this prediction, Golevka was observed by radar facility of Arecibo on May 24, 26 and 27 2003 and the Yarkovsky semimajor axis drift effect was successfully detected [Chesley et al., 2003]. In this case the Yarkovsky effect was modeled by our numerical method for various thermal parameters as is described below. In the propagation of the uncertainity ellipses, they took into account uncertainities of astrometric measurements, planetary and small bodies masses and Yarkovsky modeling. The resulting 3σ uncertainity ellipses were well separated again. With the best fitting values of the surface conductivity and bulk density[3] $K = 0.01$ W/m/K, $\rho_b = 2.7$ g/cm^3, the actual Arecibo astrometry of Golevka falls into the ellipse corresponding to Yarkovsky model (the offset of $\sim$ 15 km in R and $\sim 5\times10^{-6}$ km/s in dR/dt). In what follows we give some more details about the Yarkovsky model used in [Chesley et al., 2003].

The model

Unlike [Vokrouhlický et al., 2000], we have used fully numerical model which is able to take into account eccentric orbit, irregularly shaped surface of a body and precise solution of heat diffusion problem without any linearization [Chesley et al., 2003]. Some specific features of our model are described in detail in Appendices.

The shape model of Golevka represented by a 4092-hedron (see Appendix D) was taken from [Hudson et al., 2000]. We determined the insolation of all surface elements along whole elliptical orbit, including effects of self-shadowing between different surface elements (see Appendix B).

[3] K and ρ are fully correlated.

With this insolation, we solved the one-dimensional HDE by a two-level scheme, during one orbital period, from surface to depth of $15\ell_s$ (see Appendix A). We usually made several iterations until the surface temperature precision was better than 0.1 K. The timestep in the first level was ~ 500 s while in the second one only ~ 5 s. The spatial steps increase with the depth according to $\Delta x_k = \Delta x_0 \exp(0.1\,k)$. The initial spatial step was $\sim 0.76\,\ell_d$ in the first level and $\sim 0.0076\,\ell_d$ in the second one. Here ℓ_d represents penetration depth of diurnal temperature variations.

K (W/m/K)	10^{-4}	10^{-3}	10^{-2}	10^{-1}
ℓ_s (cm)	4.2	13.1	41.5	131.3
ℓ_d (mm)	0.5	1.7	5.4	17.3

Table 4.2: Penetration depths of seasonal (ℓ_s) and diurnal (ℓ_d) temperature waves as functions of the thermal conductivity K. The surface density was assumed 1.7 g/cm^3, the thermal capacity 680 J/kg/K and the period of rotation 6 h.

With the converged solution of surface temperature we computed the corresponding Yarkovsky force acting on each surface element according to Equation (2.9). The total Yarkovsky force $\mathbf{f}_{\rm th}$ is then given by a sum over all surface elements (Eq. 2.11). The mean rate of change of the semimajor axis is given by the corresponding Gauss' equation (4.3).

We used the following orbital parameters: semimajor axis $a = 2.5065$ AU, excentricity $e = 0.604317$, inclination $i = 2.277°$, argument of perihelion $\omega = 66.06°$, longitude of ascending node $\Omega = 211.502°$. The pole of rotation was $l = 202°$, $b = -45°$ (ecliptical coordinates) and corresponding obliquity $\epsilon = 134°$. Period of rotation $P_{rev} = 6.0264$ h was slightly modified to $P_{rev} \simeq 6.02666$ h in order the fraction P_{rev}/P_{orb} to be an integer number[4]. The thermal capacity was $c = 680$ J/kg/K, the surface density[5] $\rho_s = 1.7$ g/cm^3, the bulk density $\rho_b = 2.5$ g/cm^3, Bond albedo $A = 0.1$ and emisivity $\epsilon = 0.9$. We assumed the thermal conductivity K from 10^{-4} to 10^{-1} W/m/K.

Results

For the given material parameters K, c and ρ_s we computed components of the Yarkovsky thermal force with respect to the inertial frame and corresponding semimajor axis drift da/dt. Figure 4.5 shows an example of da/dt behaviour during one orbital period for $K = 0.01$ W/m/K. The orbit-averaged da/dt as a function of surface thermal conductivity is shown in Figure 4.6. We also present results obtained by an analytical theory [Vokrouhlický, 1999]. We can see that both numerical and analytical approaches lead to almost the same averaged value of the Yarkovsky orbital drift for Golevka.

Due to a priori unknown thermal conductivity of the surface material, we had to compute the Yarkovsky orbital drift for a wide range of possible K's from 10^{-4} to 10^{-1} W/m/K (see the discussion in Section 3.4.1).

[4] In this case $P_{rev}/P_{orb} = 5772$. Such change of the period do not affect the results, but it allows to use a impler approach.

[5] We also made a few computation assuming the surface density 1 g/cm^3 and 2.5 g/cm^3.

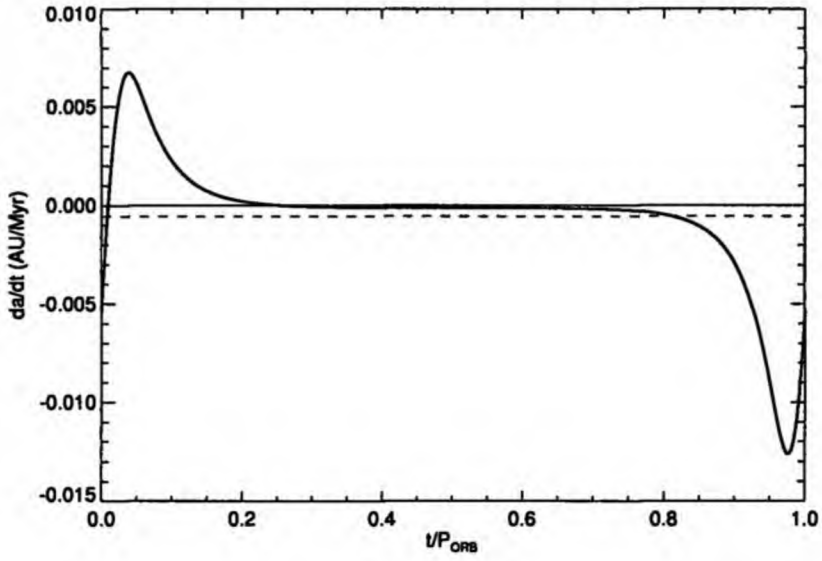

Figure 4.5: The Yarkovsky orbital drift as a function of the orbital phase (t/P_{orb}). The origin of time is chosen at the perihelion passage. The solid curve was computed for $K = 0.01\,\mathrm{W/m/K}$, $c = 680\,\mathrm{J/kg/K}$, $\rho_b = 1.7\,\mathrm{g/cm^3}$. The dashed one represents the average value $\langle da/dt \rangle = -5.5 \times 10^{-4}\,\mathrm{AU/Myr}$.

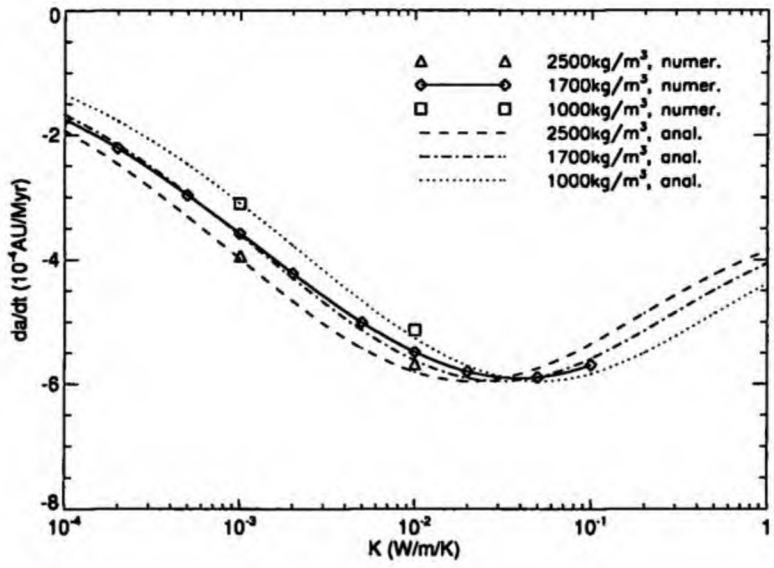

Figure 4.6: The Yarkovsky semimajor axis drift da/dt according to the numerical and analytical theory as a function of the surface conductivity K. The solid line (with diamond symbols indicating the actually determined values) represents da/dt determined by the numerical method, expecting the density of the surface material $1.7\,\mathrm{g/cm^3}$. The dash-dotted line is computed by the analytical theory, with the same density assumed. The dotted and dashed curves were computed analytically, assuming the surface density $1\,\mathrm{g/cm^3}$ and $2.5\,\mathrm{g/cm^3}$ respectively. The square and triangle symbols denote numerical results for densities $1\,\mathrm{g/cm^3}$ and $2.5\,\mathrm{g/cm^3}$ respectively.

4.3.2 (6489) Golevka – plausible constraints on its surface layer

This section is based on the poster [Čapek and Vokrouhlický, 2005b] presented at the conference ACM 2005 in Búzios, Brazil.

We improved our numerical model of Yarkovsky/YORP effect (which was used for example in [Chesley et al., 2003]) by taking into account spatial and temperature dependence of the thermal capacity c and thermal conductivity K. As a result we can derive constraints on the surface properties such as regolith thickness for this asteroid.

The model

We assumed the same spin, orbital and shape parameters of Golevka as in Section 4.3.1. The main differences are in the thermal parameters: we assumed a the high-conductive core, composed from fresh basalt covered by a layer with low thermal conductivity ("regolith"). Moreover, we allow for temperature dependence of thermal parameters. This is discussed in detail in Section A.1.3. We adopt the temperature dependence of the thermal capacity c from [Urquhart and Jakosky, 1997] as

$$c = (-0.037 + 1.19 \times 10^{-3} T - 1.96 \times 10^{-6} T^2 + 1.24 \times 10^{-9} T^3) \times 4186.05 \quad \text{(J/kg/K)},$$

where T (in Kelvins) is the temperature. The thermal capacity for a given temperature is almost the same for a wide range of stony materials. But due to the temperature dependence it can vary from ~ 400 to ~ 800 J/kg/K at aphelion and perihelion of Golevka, respectively.

The temperature dependence of the thermal conductivity K was assumed as

$$K = A + BT^3, \tag{4.5}$$

where the term A corresponds to a heat transfer by conduction and BT^3 represents a radiative heat transfer. The second term is important in materials like regolith containing voids. In the case of Golevka, the second term plays only a minor role.

The density is not affected by temperature variations. The thermal conductivity and density of the core and regolith used in our model are summarized in Table 4.3.

	A (W/m/K)	B (W/m/K^4)	ρ_s (g/cm^3)
regolith	$0.001 - 0.1$	2×10^{-11}	1.7
core	2.5	0	2.5

Table 4.3: The thermal parameters used in our model of Golevka. The B term of regolith corresponds to the lunar regolith (Table 1 in [Cremers, 1972]).

The solution of the heat diffusion equation was more difficult due to the dependence of thermal parameters on the temperature. We had to modify the Crank-Nicolson scheme and find an appropriate combination of spatial and time steps (see Appendix A). This scheme is much more time consuming. We computed the Yarkovsky effect only for regolith depths $h = 1$ mm, 1 cm, 10 cm and for conductivities $A = 0.001$, 0.01, 0.1 W/m/K. We again assumed exponentially increasing spatial step (the initial one was 0.01 mm) and timestep 300 s and used polyhedral shape of Golevka (4092 surface elements).

Results

Our results are summarized in Figures 4.7 and 4.8. Figure 4.7 shows the dependence of da/dt on the regolith depth for three values of its conductivity[6] ($K = 0.1, 0.01, 0.001\,\mathrm{W/m/K}$). Focusing on the right side panel we can see the Yarkovsky effect is similar for the three conductivity values. For large regolith thickness ($h > 10\,\ell_d$) the semimajor axis drift approaches the value corresponding to infinite regolith depth, while for h small (compared to ℓ_d) it approaches the zero regolith depth limit ($-3 \times 10^{-4}\,\mathrm{AU/Myr}$ corresponding to uniform composition with $K = 2.5\,\mathrm{W/m/K}$). There is transition zone between these two limit cases, characterized by a peak of da/dt for $h \simeq 4\,\ell_d$ and local minimum at $h \simeq 1/2\,\ell_d$. The left panel shows the same dependence, but the $x-$axis is in the metric units. We can notice the horizontal line corresponding to measured orbital drift $\langle da/dt \rangle \simeq 5.5 \times 10^{-4}\,\mathrm{AU/Myr}$. This measurement is consistent with our model only for some particular combinations of the regolith depth h and the thermal conductivity K: 1.3 cm or 3 cm for $K = 0.01\,\mathrm{W/m/K}$ and 3 cm or 13 cm for $K = 0.1\,\mathrm{W/m/K}$.

More complex constraints on combination's of the regolith's depth h and the thermal conductivity K can be inferred from Figure 4.8, where we plot a 2D function $da/dt(h, K)$.

The measured value of da/dt for Golevka is $-5.5 \times 10^{-4}\,\mathrm{AU/Myr}$ ([Chesley et al., 2003]). We assumed 10% uncertainity of this value (or our model) and marked the corresponding area (upper right part of the figure) by dots. This area denotes plausible combinations of the regolith depth h and its thermal conductivity K, which are consistent both with our model and with measured value of non gravitational da/dt. We can conclude:

- If Golevka has a high-conductive (basalt) core, the thickness of the low-conductive surface layer is larger than 1 cm and its thermal conductivity is larger then $0.004\,\mathrm{W/m/K}$.
- The radiative term BT^3 in the thermal conductivity (Eq. 4.5) has a negligible effect on the resulting da/dt for Golevka.

Future improvements

In reality, many asteroids seem to be covered by both regolith and fresh rock. Recently we took this fact into account and developed a model with thermal parameters dependent both on depth under the surface and on the position on the asteroid's surface. Only facets with the slope[7] smaller than the angle of repose of regolith have a regolith layer above the fresh rock core; others are assumed to be regolith-free fresh rock. (See Figure 4.9.)

For example, we assumed the angle of repose 30°. Regolith parameters were: depth h =1 mm, thermal conductivity $K_{\mathrm{regolith}} = (0.1 + 2 \times 10^{-11}\,T^3)\,\mathrm{W/m/K}$ and density $\rho_{\mathrm{regolith}} = 1.7\,\mathrm{g/cm^3}$ and fresh rock parameters were: $K_{\mathrm{rock}} = 2.5\,\mathrm{W/m/K}$, $\rho_{\mathrm{rock}} = 2.5\,\mathrm{g/cm^3}$ Other quantities were the same as in [Čapek and Vokrouhlický, 2005b]. We obtained the semimajor axis drift $-3.2 \times 10^{-4}\,\mathrm{AU/Myr}$. If we chose the regolith depth 100 times larger (0.1 m), we obtained the semimajor axis drift $\langle da/dt \rangle = -5.4 \times 10^{-4}\,\mathrm{AU/Myr}$. Details of this model need to be developed in the future work.

[6] In fact, it is the conductivity parameter A in Equation (4.5).

[7] Defined as the angle between outer normal and vector of local gravity + centrifugal acceleration.

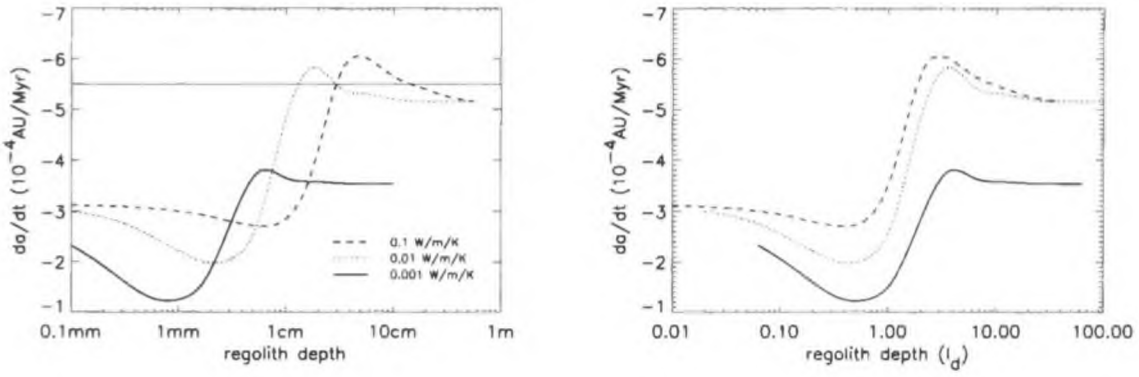

Figure 4.7: The Yarkovsky semimajor axis drift dependence on regolith depth for three values of thermal conductivity. The dashed curve corresponds to $K = 0.1\,\mathrm{W/m/K}$, dotted one to $0.01\,\mathrm{W/m/K}$ and solid one to $0.001\,\mathrm{W/m/K}$. The x-axis in the left panel represents the depth of regolith in metric units and horizontal line indicates the actually measured da/dt on Golevka by [Chesley et al., 2003]. The right panel has x-axis in the units of penetration depth of diurnal temperature variations ℓ_d. See the text for discussion.

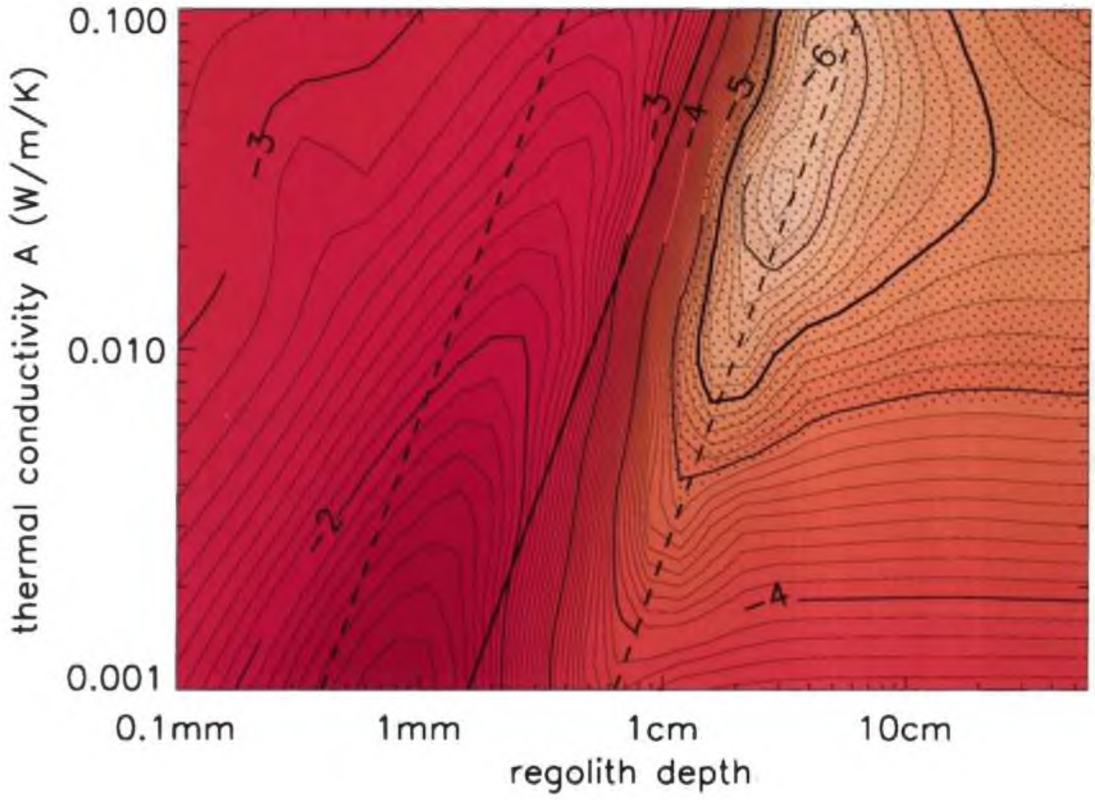

Figure 4.8: The dependence of the Yarkovsky semimajor axis drift on the depth of the regolith layer (x-axis) and its thermal conductivity (y-axis). The thick solid straight line represents the penetration depth of diurnal temperature variations ℓ_d, while dashed ones correspond to $1/4\,\ell_d$ and $4\,\ell_d$. The thick contour corresponds to a value -5.5×10^{-4} AU/Myr and dotted area indicates a 10% interval of its uncertainity.

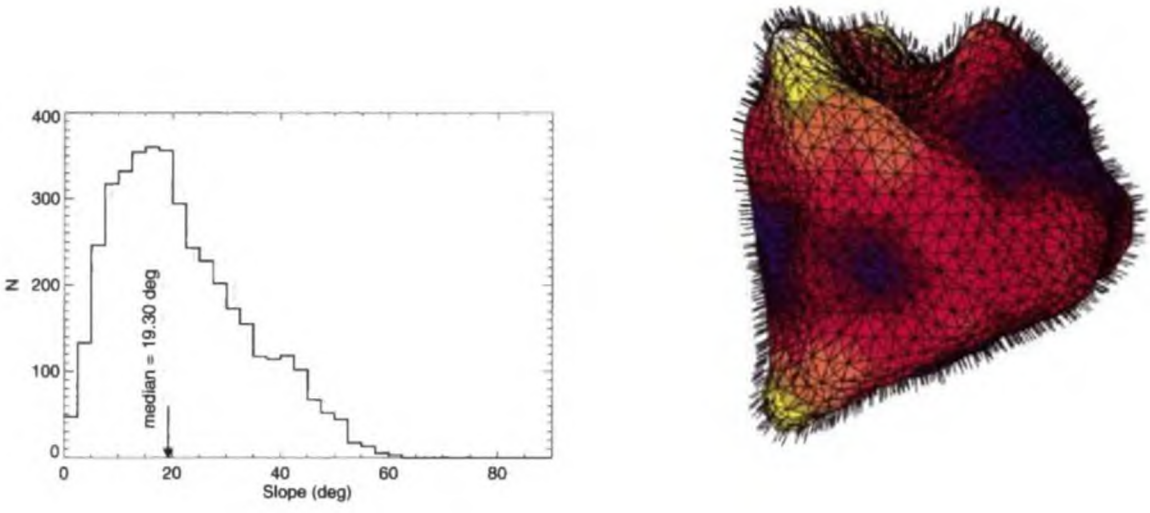

Figure 4.9: Left: The abundance of slopes for the asteroid (6489) Golevka. Right: The distribution of gravitational plus rotational acceleration across the surface of asteroid Golevka. The short lines correspond to directions and the colors to magnitudes of accelerations on the surface. (White color corresponds to the lowest value ($g_{\min} = 1.35 \times 10^{-4}\,\mathrm{m/s^2}$) and blue color to the highest value ($g_{\max} = 1.86 \times 10^{-4}\,\mathrm{m/s^2}$).)

4.3.3 (4179) Toutatis - an asteroid with non-principal axis rotation

This section is based on the investigation presented in [Čapek and Vokrouhlický, 2005a] and [Vokrouhlický et al., 2005a].

(4179) Toutatis, a body with dimensions $\sim 4.6\times2.4\times1.9$ km, is an Apollo-type asteroid in the 3:1 mean motion resonance with Jupiter and in the 1:4 mean motion resonance with the Earth. During its frequent close encounters to the Earth, radar observations revealed its irregularly elongated shape [Hudson et al., 2003], non-principal axis spin state [Hudson and Ostro, 1995] and precisely determined its orbit.

[Vokrouhlický et al., 2000] studied a possibility of the Yarkovsky effect detection on this body, but several mistakes occurred in their calculations. [Vokrouhlický et al., 2005a] corrected the older results, taking into account the right shape, dimensions, the non-principal axis rotation, and solved the HDE numerically. In the following text we shall briefly describe our method used in [Vokrouhlický et al., 2005a].

The model

We have used a reduced shape model determined by [Hudson et al., 2000]. This model consists of 12796 surface facets (see Appendix D).

The main problem, we faced in this case, was the non-principal axis rotation of Toutatis. In the body-fixed frame, the spin axis wobbles about the long principal axis with a period of 5.367 days and this axis precedes about the angular momentum axis with period 7.420 days [Ostro et al., 1999a]. The orientation of such a freely rotating body never exactly reaches the initial orientation. It can pose a problem for the HDE solution, since we do not dispose with a condition of its exact periodicity.

We first determined the orientation of Toutatis by a numerical solution of Euler equations (see [Kryszczyńska et al., 1999]):

$$A\dot{\omega}_A + (C-B)\,\omega_B\,\omega_C = 0, \tag{4.6}$$
$$B\dot{\omega}_B + (A-C)\,\omega_C\,\omega_A = 0, \tag{4.7}$$
$$C\dot{\omega}_C + (B-A)\,\omega_A\,\omega_B = 0, \tag{4.8}$$

$$\dot{\phi} = \frac{\omega_A \sin\psi + \omega_B \cos\psi}{\sin\theta}, \tag{4.9}$$
$$\dot{\psi} = \omega_C - \frac{\cos\theta}{\sin\theta}(\omega_A \sin\psi + \omega_B \cos\psi), \tag{4.10}$$
$$\dot{\theta} = \omega_A \cos\psi - \omega_B \sin\psi, \tag{4.11}$$

where ϕ, ψ and θ denote Euler's angles, $A < B < C$ principal moments of inertia and ω_A, ω_B and ω_C are projections of spin vector to the principal axes (A is the longest axis and C the shortest one). The first set of equations solves for the spin axis vector with respect to the body frame whereas the second one solves for the orientation of the body with respect to the inertial frame.

We used the initial conditions listed in Table 4.4 and propagated them for one orbital period[8]. Then we determined deviations of the body axes from the initial position as a function of time and searched for the best agreement with the initial orientation. We found that Toutatis reaches

[8]The angles had been transformed due to a different orientation of our shape model.

ϕ_0	$-103°$	ω_A	$20.7°$/day
ψ_0	$-134°$	ω_B	$31.3°$/day
θ_0	$97°$	ω_C	$98.0°$/day

Table 4.4: Initial conditions of the Toutatis's rotation taken from [Ostro et al., 1999a], Table VII. The data corresponds to the date Dec 11, 1992, 9:21 UTC.

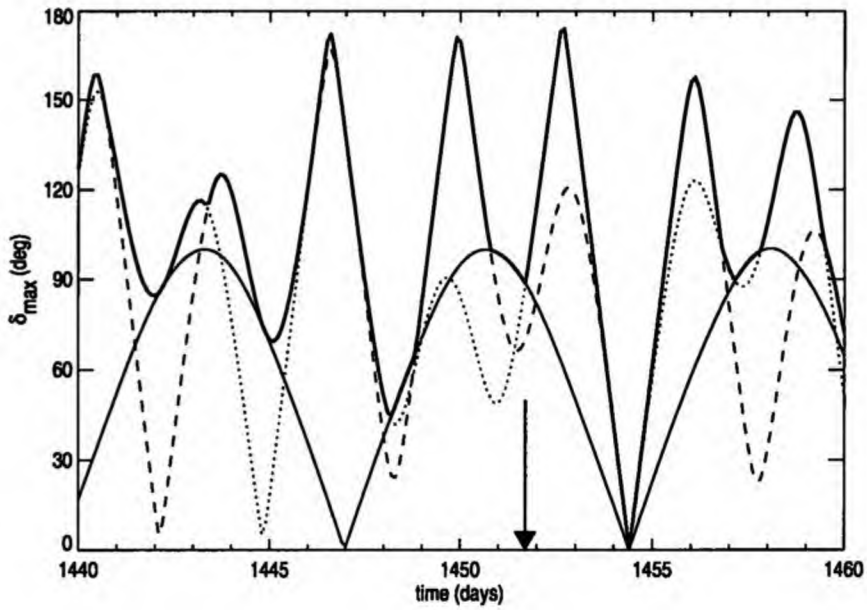

Figure 4.10: Angular deviations of the x (thin solid curve), y (dotted curve), and $z-$axis (dashed curve) from initial orientation in space as a function of time for asteroid (4179) Toutatis. Here we show only a short segment of 20 days near one revolution period of the asteroid. The thick solid curve denotes the maximal angular deviation. Almost the same orientation as the initial one is reached after 1454.4 days, which is very close to the orbital period 1451.7 days, denoted by the arrow.

a nearly identical orientation in the space with a period 1454.4 days, which is close to the orbital period $P_{orb} = 1451.7$ days (see Figure 4.10). This result is very surprising and we have no explanation for this fact yet. In any case, this circumstance greatly helps the HDE solution because we may use the near periodicity of Toutatis' orientation in space as a boundary condition in the time coordinate.

The semimajor axis of Toutatis' orbit was then slightly changed in order the orbital period to be exactly 1454.4 d (due to the periodic initial condition). We assumed these orbital parameters: semimajor axis $a = 2.5123$ AU, excentricity $e = 0.64038$, inclination $i = 0.466°$, argument of perihelion $\omega = 276.2°$ and ascending node $\Omega = 126.6°$.

With known orientation in space, we determined the insolation of each facet. (Including effects of self-shadowing between different surface elements – see Appendix B.) For the surface temperature determination we chose the following thermal parameters: thermal capacity $c = 800$ J/kg/K, surface density $\rho_s = 2\,\mathrm{g/cm^3}$, bulk density $\rho_b = 2.6\,\mathrm{g/cm^3}$, Bond albedo $A = 0.08$ and the emisivity $\epsilon = 0.92$. We assumed values of the thermal conductivity K from 5×10^{-4} to 5×10^{-1} W/m/K.

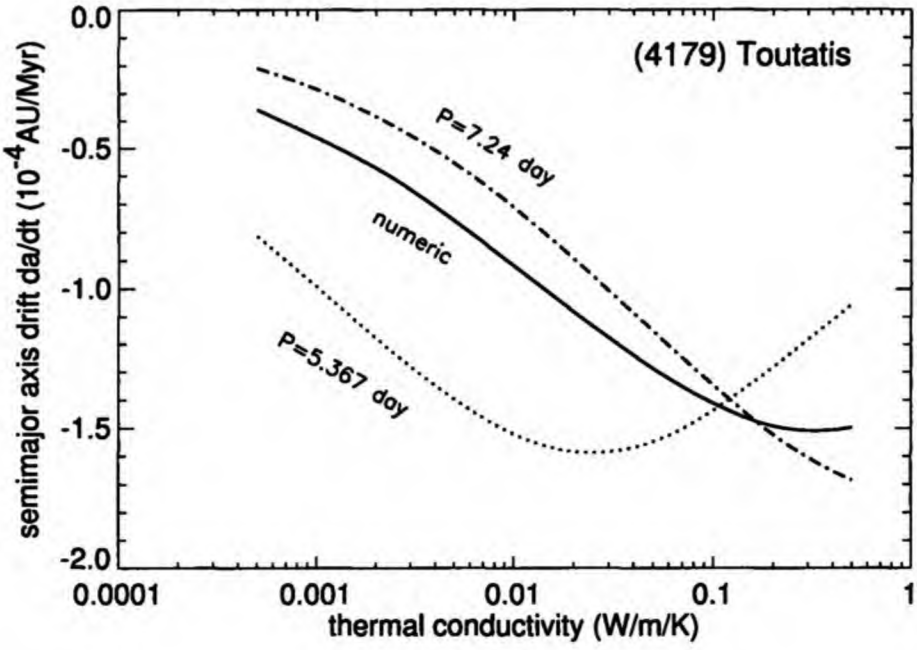

Figure 4.11: The orbit averaged semimajor axis drift for asteroid (4179) Toutatis as a function of the thermal conductivity. The thick solid line represents the result obtained by a precise numerical method, while the other two curves correspond to simplified analytical approaches. For more information see the text.

Thanks to Toutatis' slow rotation, we can solve the one-dimensional HDE by a one-level scheme, during orbital period, from the surface to the depth of $15\ell_s$ (see Appendix A). We made 5 iterations, leading to the temperature precision better than $0.009 - 0.04$ K, depending on the thermal conductivity. The timestep was 125 s (62 s in the case of $K = 5 \times 10^{-4}$ W/m/K). The spatial steps increased with the depth according to $\Delta x_k = \Delta x_0 \exp(0.1\,k)$, where the initial spatial step was $1/200\,\ell_s$.

With the converged solution of the surface temperature and the known orientation of the body we computed the corresponding Yarkovsky effect by the same way as in the case of Golevka (Section 4.3.1).

Results

The resulting orbit-averaged semimajor axis drift can bee seen in Figure 4.11. We compared this result with an estimation by a simplified analytical method (solving the linearized HDE). In the analytical approach, Toutatis was represented by a sphere of the same mass as real asteroid. Moreover, we assumed regular rotation about the vector of Toutatis angular momentum which has the pole $\ell = 180°$, $b = -52°$ in ecliptical coordinates. We chose two periods: 7.24 d and 5.367 d. The result of the analytical method (solving linearized HDE) with the period 7.24 d is in a surprisingly good agreement with the more sophisticated numerical theory.

We predicted the range[9] offset $+40\,\mu$s between Yarkovsky and non-Yarkovsky orbit during its encounter with Earth in October 2004, giving a good perspective of a second direct detection of the Yarkovsky effect.

Unfortunately, the detection failed so far. The measurement of the range offset led to the

[9]The Range means the quantity $2\Delta R/c$, where ΔR is the distance from the Earth (radar) to the asteroid, and c is the speed of light.

value $(-23.5 \pm 4)\,\mu$s. According to [Vokrouhlický and Chesley, personal communication], this was caused by several facts: (i) the Yarkovsky force was badly incorporated into the software computing the orbit. The correct value of the Yarkovsky range offset should have been $(+16 \pm 5)\,\mu$s (instead of $+40\,\mu$s) on October 7th 2004. (ii) More importantly, the effects of asteroid perturbers, and their poorly known masses, were not taken into account, though they are very important. Thus the combination of the Yarkovsky and asteroidal perturbations leads to the range offset $(-41 \pm 18)\,\mu$s. Then the observation $(-23.5 \pm 4)\,\mu$s fits into the predicition but the difference between the "Yarkovsky" and "non-Yarkovsky" models is not statistically significant yet (due to the large uncertainities). It is yet to be determined if data from the 2008 radar ranging will allow a clear detection of the non-gravitational signal.

4.3.4 2000 DP107 – a binary system

The section is based on the investigation presented in [Čapek and Vokrouhlický, 2005a] and [Vokrouhlický et al., 2005b].

Radar observations of 2000 DP107 ([Margot et al., 2002]) revealed this object is a binary system consisting of a primary with diameter ~ 800 m and a secondary with diameter ~ 300 m. The orbital period of the pair is $P_2 = 1.755$ day, the rotation period of the primary is $P_1 = 2.77536$ h, while the secondary has a synchronous rotation. [Margot et al., 2002] also estimated the parameters of the relative orbit: semimajor axis $a = 2622$ m, excentricity $e = 0.01$, inclination $i = 17°$, argument of perihelion $\omega = 7°$ and ascending node $\Omega = 10°$ with a large error in ω due to almost circular orbit. Binary nature of this body helped to determine the mass of the system $M = 4.6 \times 10^{11}$ kg and corresponding bulk density of the primary component as $1.7\,\mathrm{g/cm^3}$ (we expected the same density of the secondary). The heliocentric orbit of the whole system is characterized by the semimajor axis $a = 1.3662$ AU, excentricity $e = 0.376863$, inclination $i = 8.663°$, argument of perihelion $\omega = 289.687°$ and ascending node $\Omega = 358.829°$.

We studied this system [Čapek and Vokrouhlický, 2005a], [Vokrouhlický et al., 2005b] as an example of the Yarkovsky effect influence on binary asteroid. In this cases the Yarkovsky force affects both the motion of the center of mass (COM for short) of the system and the relative motion of the components.

The model

Most parameters of the relative orbit and orbit of the COM were taken as above. The only exception was the semimajor axis of the COM and primary's rotation period that were changed[10] slightly, in order to the ratios between orbital period P_{orb} of COM, rotation period of secondary P_2 and rotation period of primary P_1 were integers: $P_{orb} : P_2 = 332 : 1$ and $P_{orb} : P_1 = 5034 : 1$.

Next we expected the spin axes of both components are perpendicular to the plane of mutual motion. The corresponding pole in ecliptical coordinates is $\ell = 280°$ and $b = 73°$. We modeled both components as spheres with appropriate diameters, which were approximated by regular polyhedrons with 1004 triangular facets. In contrast to other studied bodies, the self shadowing of the asteroid's surfaces plays only a minor role here, but the mutual shadowing of both components during the revolution about the COM is very important and we had to incorporate this phenomenon into our model.

The thermal capacity was assumed $c = 800\,\mathrm{J/kg/K}$, the bulk and surface density $\rho_b = \rho_s = 1.7\,\mathrm{g/cm^3}$, the albedo $A = 0.1$ and emisivity $\epsilon = 0.9$. We computed the Yarkovsky effect for thermal conductivities in the range from $0.001\,\mathrm{W/m/K}$ to $1\,\mathrm{W/m/K}$.

We solved the HDE by a one-level scheme (see Appendix A) with an exponentially increasing spatial step. The exponent was 0.1 and the initial step $\Delta x_0 = 0.36\,\ell_d$ for the primary, and $\Delta x_0 = 0.18\,\ell_d$ for the secondary, where ℓ_d represents the penetration depth of diurnal temperature variations. The lower boundary condition lied in the depth $15\ell_s$, where ℓ_s is penetration depth of the seasonal temperature variations. The time step was 50 s for the primary and 200 s for the secondary. We determined the Yarkovsky acceleration $\mathbf{f}_1$ for primary and $\mathbf{f}_2$ for the secondary separately. The Yarkovsky acceleration of the whole system (COM) is given by

$$\mathbf{f}_{\mathrm{COM}} = \frac{\mathbf{f}_1 M_1 + \mathbf{f}_2 M_2}{M_1 + M_2} \tag{4.12}$$

and the Yarkovsky perturbation of the relative motion is given by:

[10] To the values $a = 1.365264$ AU and $P_1 \simeq 2.7779$ h.

$$\delta \mathbf{f} = \mathbf{f}_2 - \mathbf{f}_1. \tag{4.13}$$

Results

Firstly, we focus on Yarkovsky perturbations of the COM motion. Figure 4.12 shows the orbit averaged semimajor axis drift due to the Yarkovsky effect. We also computed the Yarkovsky effect only for primary - both analytically and numerically. We can see that the contribution of the secondary to the whole effect is negligible for low conductivities and its significance increases with thermal conductivity. This can be explained by the fact that the Yarkovsky effect for the primary decreases with increasing K more quickly than for the secondary due to the rapid rotation of the primary, and thus vanishing diurnal temperature variations for high K. We can also see the disagreement of the linearised analytical solution with the numerical one for low K, due to higher temperature variations, causing the HDE linearization to fail.

The time dependence of the absolute value of Yarkovsky acceleration is shown in Figure 4.13. We can see deep minima of the secondary's acceleration due to its eclipses. The eclipses are total near the perihelion and apohelion and they are partial near the quadratures. Eclipses of the primary are only partial and minima of the acceleration of this component are smaller. After the main minimum we can observe oscillations with decreasing amplitude and a period equal to the rotational period of the primary. This phenomenon is caused by the rotation of a cold spot arose from the passage of the secondary's shadow and its subsequent warming.

The Yarkovsky perturbation of the relative motion is caused by $\delta \mathbf{f}$. The most important is the component parallel to the relative motion δf_τ. In the long time scales this component produces a linear increase of the mutual distance and a quadratic advance of the longitude in the relative orbit. The orbit averaged $\langle \delta f_\tau \rangle$ as a function of the surface thermal conductivity is shown in Figure 4.14.

The time dependence of the along-track component is shown in Figure 4.15. During a shadowing of the secondary, δf_τ temporarily increases. This is because the shadow at first reaches the morning side of the secondary and then this side is colder than the evening one, causing an increase of the along-track component of the Yarkovsky force. An opposite situation occurs during an emersion from the shadow. Due to thermal relaxation after occulations, the along-track component δf_τ does not average to zero (like the solar radiation pressure) and can produce observable effects [Vokrouhlický et al., 2005b].

We demonstrated the Yarkovsky effect is able to produce both perturbations of a heliocentric orbit of the COM and perturbations of a relative orbit of components about the common COM. Both these effects can serve to a detection of the Yarkovsky effect, but in the case of 2000 DP107, the effect on the relative motion is too small to be detected. Detection of Yarkovsky effect via its influence on the COM motion can be successful in 2016 if radar observations in 2008 are successful.

Our model is able to describe the Yarkovsky effect on binary asteroids but in this particular case, the approach is very simplified. This is mainly due to unknown orientation of spin axes, unknown shapes and due to an uncertain evolution of the rotational states and the relative orbit by tides. In the future we plan an application to better characterized systems, such as (66 391) 1999 KW4 [Ostro et al., 2006].

4.3.5 Discussion

We are able to determine the Yarkovsky effect for a wide variety of asteroids: simple cases of spherical bodies with semimajor axis rotation, as well as irregularly shaped bodies, tumbling

asteroids or binaries. Our model realistically describes the thermal behaviour of the surface material (the temperature and spatial dependence of the thermal parameters).

The knowledge of the Yarkovsky effect is necessary for the prediction of the asteroid's orbit. For instance, the precise knowledge of the orbit is important in the case of potential Earth impactors [Giorgini et al., 2002].

The Yarkovsky and YORP effect can be also used for determination of the thermal conductivity of the asteroid's surface and its bulk density ρ_b and consequently the mass, porosity and type of the surface material (the fresh rock, regolith or mixture of them).

The independent measurement of the bulk density via direct detection of the Yarkovsky effect alone is not possible, because bulk density is coupled with the surface thermal conductivity K as $\rho_b K$. However, if the Yakrovsky and the YORP effect are measured together, the independent determination of ρ_b and K is possible. (See Chapter 3.)

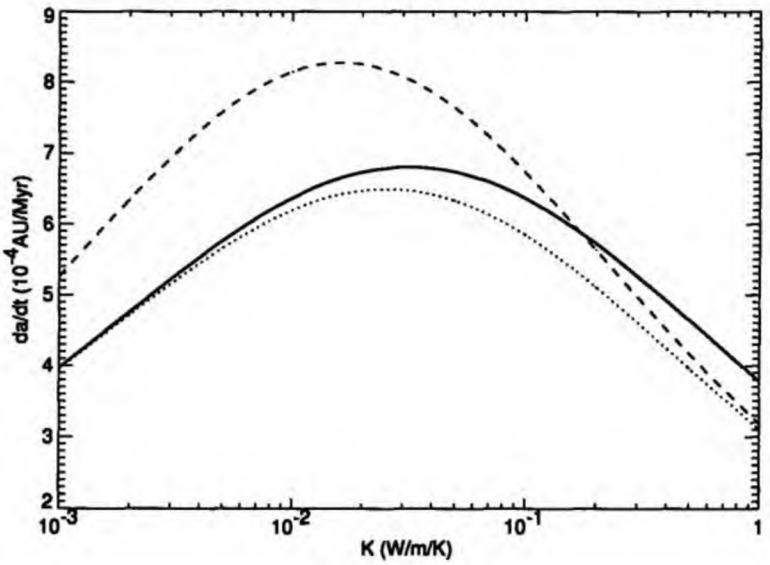

Figure 4.12: The orbit averaged semimajor axis drift da/dt for 2000 DP107. The solid line represents numerical results for the whole system, while the dashed one is computed for the primary alone. The dotted line corresponds to the analytical results for a solitary primary.

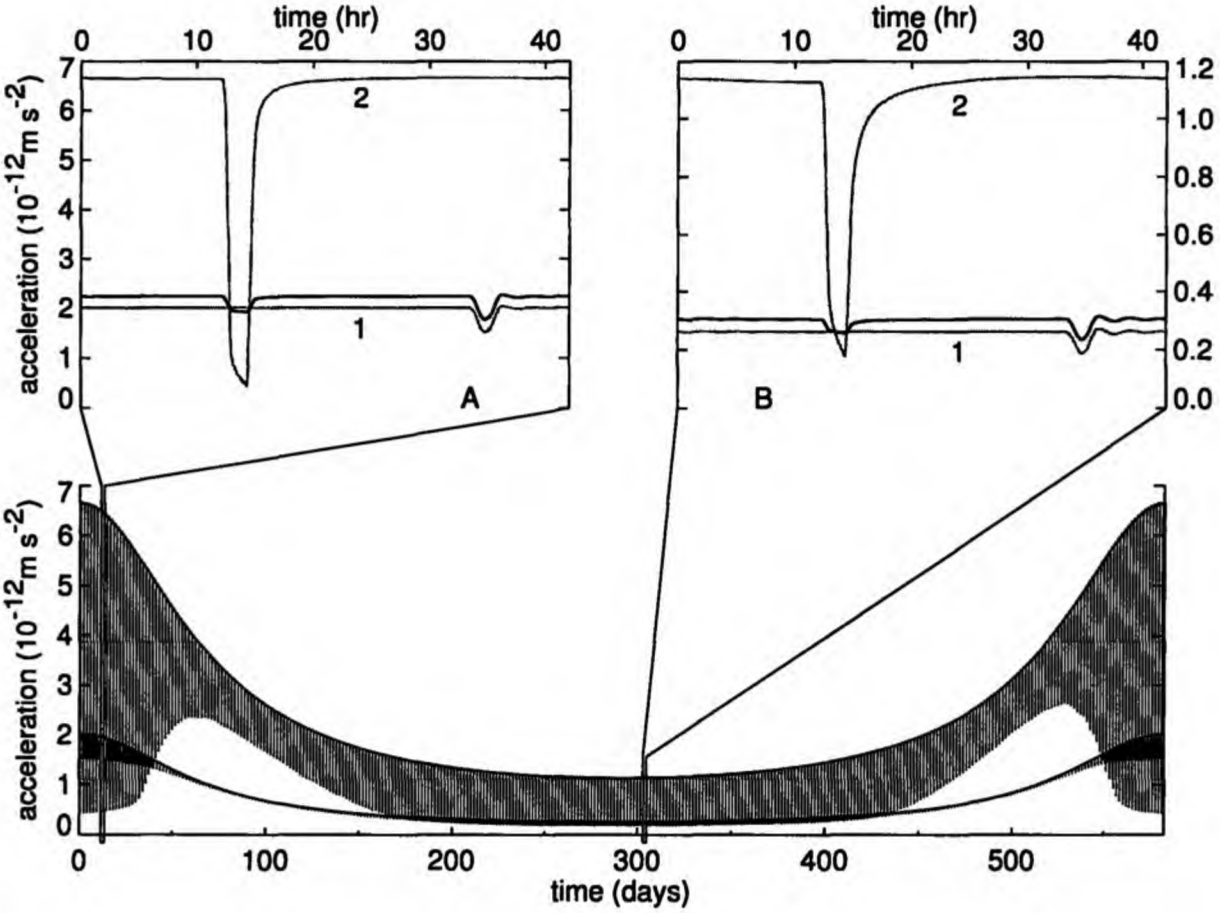

Figure 4.13: The absolute value of the Yarkovsky acceleration of 2000 PD107 as a function of time for the thermal conductivity $K = 0.01$ W/m/K. Lower figure shows the acceleration of the primary (the curve with a smaller amplitude) and the secondary (the larger amplitude) during one revolution about the Sun. Upper figures show in detail the situation near the perihelion (left) and aphelion (right) during one revolution of the components about the COM. Here the upper grey curve denoted by "2" represents the secondary, the lower denoted by "1" the primary and the black curve corresponds to the acceleration of the COM (according to Equation (4.12)). More explanation in the text.

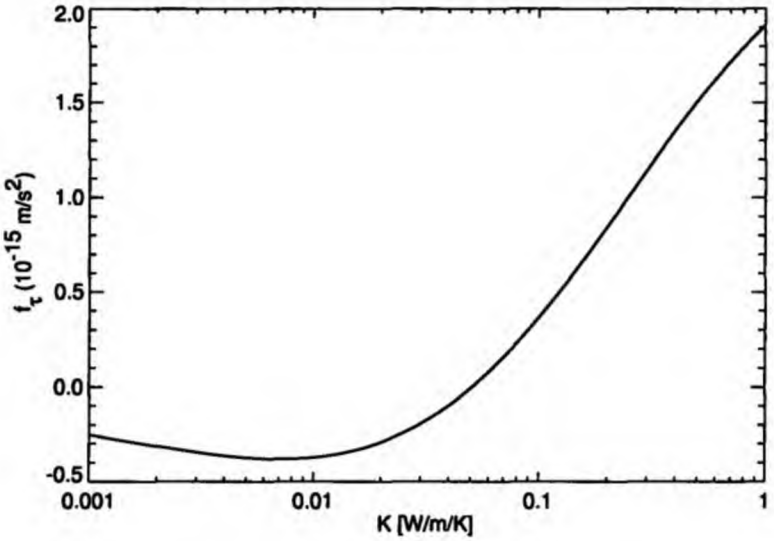

Figure 4.14: The orbit averaged along-track component f_T as a function of the surface thermal conductivity K.

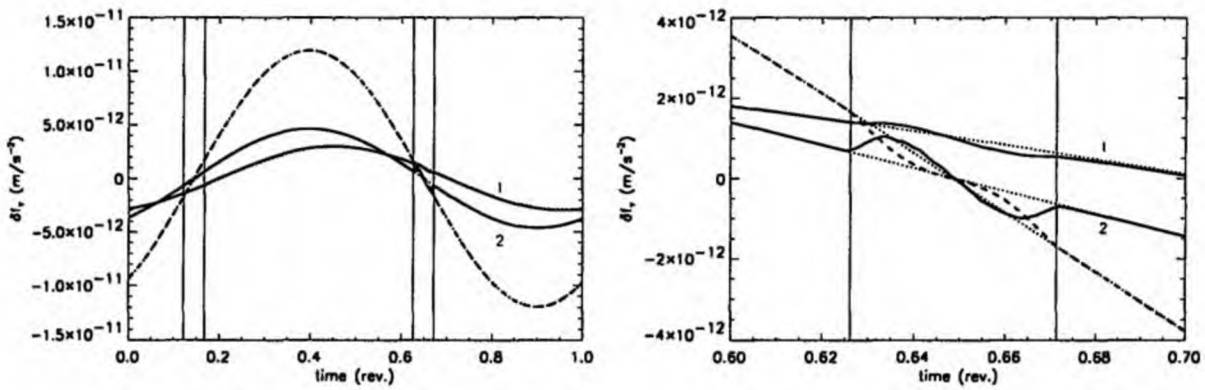

Figure 4.15: The long-track component of $\delta \mathbf{f}$ as a function of time. Left plot shows the dependence during one revolution about the COM. The vertical lines correspond to the entry and exit of occulations. The first is the occulation of the primary and the second the partial occulation of the secondary. The dashed line denotes an effect of the solar radiation pressure, the solid curve denoted by "1" corresponds to the thermal conductivity $K = 1\,\mathrm{W/m/K}$ and the solid curve denoted by "2" to $K = 0.001\,\mathrm{W/m/K}$. Right plot zooms the occulation of the secondary. Dotted curves correspond to a situation when no occulations occur.

4.4 Summary

- Our numerical model was used succesfully for the prediction and the following detection of the Yarkovsky effect on asteroid (6489) Golevka. It was the first direct detection of this phenomenon effect on a natural body.
- We also computed the Yarkovsky effect and estimated possibilities of the detection for several other asteroids. We are able to describe highly eccentric orbits, non-principal axis rotation (e.g., (4179) Toutatis), or mutual shadowing in components of binary systems (e.g., 2000 DP107).
- On the basis of the detected Yarkovsky orbital drift for (6489) Golevka and our model involving depth and temperature dependence of thermal parameters, we estimated the depth and thermal conductivity of the surface regolith layer.
- We compared the results of the analytical theory with our sophisticated numerical model and concluded that the analytical model mostly gives very similar results as the numerical one.
- In contrast to the YORP effect, where the shape plays a key role, we showed near complete independence of the Yarkovsky effect on the detailed shape of the body.
- As a by-product, we revealed an interesting agreement between the orbital period of the tumbling asteroid (4179) Toutatis and the period needed to its return to the initial orientation with respect to the inertial system (i.e., its "rotational" period).

Appendix A

The heat diffusion equation

This chapter deals with a problem of the determination of the asteroid's surface temperature, which is necessary for the calculation of the Yarkovsky force and the YORP torque. We will assume that the asteroid is thermally relaxed, this means the temperature variations are caused by insolation only. Neither radiogenic nor other sources of heat are taken into account.

A.1 Introduction

A.1.1 Derivation of the Heat Diffusion Equation

Any gradient of the temperature ∇T inside a body is connected with the heat flow $\mathbf{q}$ according to Fourier's law:

$$\mathbf{q} = -K\,\nabla T, \tag{A.1}$$

where K [$\mathrm{W\,m^{-1}\,s^{-1}}$] is the thermal conductivity. This heat flow through the closed surface S increases an energy of the enclosed volume V of a body after time dt by

$$\delta Q = -\oint_S \mathbf{q}\cdot d\mathbf{S}\,dt = \int_V \nabla\cdot(K\,\nabla T)\,dV\,dt, \tag{A.2}$$

The second law of thermodynamics is[1] (e.g. [Svoboda and Bakule, 1992]):

$$\delta Q = T\,ds = T\frac{\partial s}{\partial t}\,dt,$$

and for the volume V:

$$\delta Q = \int_V T\frac{\partial s}{\partial t}\,dt\,dV, \tag{A.3}$$

where s is density of entropy. Together with equation (A.2) we have (assuming there is no deformation):

$$T\frac{\partial s}{\partial t} = \nabla\cdot(K\,\nabla T). \tag{A.4}$$

If there are no heat sources, as a decay of radioactive elements, and no deformations (i.e., constant volume) we can write

$$\frac{\partial s(T)}{\partial t} = \frac{\partial s}{\partial T}\frac{\partial T}{\partial t} = \rho\frac{c_v}{T}\frac{\partial T}{\partial t},$$

[1] We use the notation δQ instead of dQ, because Q depends on the integration path between initial and final state, i.e., δQ is not a total differential.

where c_v [$\mathrm{J\,kg^{-1}\,K^{-1}}$] is the specific heat capacity[2] for constant volume. Finally, together with (A.4) we can obtain the heat diffusion equation (HDE for short)

$$\rho c_v \frac{\partial T}{\partial t} = \nabla \cdot (K \nabla T), \tag{A.5}$$

which is a second order partial differential equation of parabolic type for the temperature $T(\mathbf{r}, t)$ as a function of position $\mathbf{r}$ and time t. Due to simplicity, we are using the notation "c", but it always means "c_v".

A.1.2 Initial and boundary conditions

The uniqueness of the solution of the HDE requires additional equations constraining the temperature field. These are called initial and boundary conditions.

An initial condition defines temperature field in a given time τ: $T(t = \tau, \mathbf{r}) = f_1(\mathbf{r})$; alternately, the initial condition can be sometimes replaced by periodic boundary condition $T(t, \mathbf{r}) = T(t + P, \mathbf{r})$, where P is the constant period.

An boundary condition describes the behavior of the temperature at the boundaries of the body. Here we list a few examples of the most common boundary conditions (e.g., [Isachenko et al., 196[illegible] [Vitásek, 1987]).

- If the temperature is predefined at the boundary as a function of time, $T(t, \mathbf{r}) = f_2(t, \mathbf{r})$ for $\mathbf{r} \in \Sigma$, then it is called *the Dirichlet condition.*
- *The Neumann condition* specifies the gradient of the temperature at the boundary: $\nabla T(t, \mathbf{r}) = f_3(t, \mathbf{r})$ for $\mathbf{r} \in \Sigma$ and actually represents a contact with a defined thermal flux.
- Another type of boundary condition describes a cooling or heating of the body by a surrounding reservoir. Then the heat flux is proportional to heat-transfer coefficient α ($\mathrm{W/m^2}$) and the difference between the temperature of the body's surface $T(t, \mathbf{r} \in \Sigma)$ and temperature of the reservoir T_ρ: $-K\nabla T(t, \mathbf{r} \in \Sigma) = \alpha(T(t, \mathbf{r} \in \Sigma) - T_\rho)$. In fact, this is a combination of Dirichlet and Neumann boundary condition.

All these boundary conditions are linear in the temperature. In the following sections we face a more complicated non-linear boundary condition, which stems from the energy conservation law on the surface, where the heat transfer by the radiation and the conduction occurs.

A.1.3 Thermophysical parameters

In a solid material with a non-zero porosity the heat is transferred by the conduction and by the thermal radiation in the voids. The thermal conductivity K can be divided into the conduction term K_a and temperature-dependent radiative term $K_b T^3$:

$$K = K_a + K_b T^3. \tag{A.6}$$

The typical values of both terms for various materials are shown in Table A.1.

The thermal capacity c also depends on temperature. This dependence is often approximated by a power law. [Winter and Saari, 1969] derived a model, that is appropriate for a wide range of materials (Ca-feldspar, magnesium silicate, quartz, basalt, diorite, granite) and for temperatures from few tens to $\sim 500\,\mathrm{K}$:

$$c(T) = -0.034\,T^{1/2} + 0.008\,T - 0.0002\,T^{3/2}. \tag{A.7}$$

[2]Sometimes called *thermal capacity.*

Material	K_a (W/m/K)	K_b (W/m/K^3)
Moon's regolith	$0.001 - 0.002$	$\sim 2 \times 10^{-11}$
Basalt powder	$0.002 - 0.005$	$\sim 4 \times 10^{-12}$
Fresh basalt	2.56	0

Table A.1: Typical thermal conductivities ([Urquhart and Jakosky, 1997])

[Urquhart and Jakosky, 1997] use another model for lunar materials in the range from 70 K to 400 K:

$$c(T) = -0.037 + 4.98 \times 10^{-3} T - 8.21 \times 10^{-6} T^2 + 5.19 \times 10^{-9} T^3. \quad \text{(A.8)}$$

The thermal capacity $c(T)$ for both models can be seen in Figure A.1.

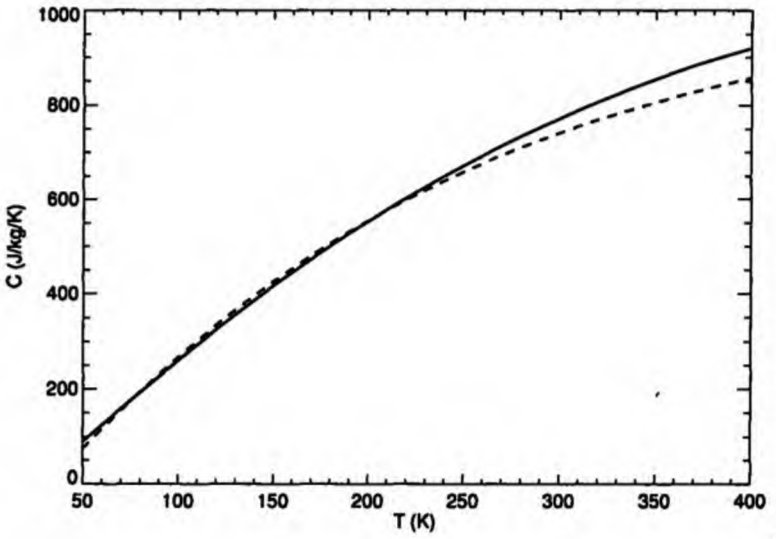

Figure A.1: Dependance of the thermal conductivity c on the temperature according to [Winter and Saari, 1969] (solid) and [Urquhart and Jakosky, 1997] (dashed).

We shall demonstrate the importance of these variable thermal parameters on the example of asteroid (6489) Golevka. In the perihelion (0.99 AU), the mean temperature at the equator (for zero albedo) is approximately 297 K and the corresponding thermal capacity $c \sim 800$ J/kg/K. The mean temperature in the aphelion (4.01 AU) is 148 K, which corresponds to $c \sim 400$ J/kg/K. The value of the thermal capacity does not depend on the chemical composition of the material and it changes solely due to temperature dependence by $\sim \pm 33\%$.

If we turn our attention to the thermal conductivity, we can see that its value depends especially on the type of material, rather then on temperature. Material like Moon's regolith has $K \sim 0.00106$ W/m/K and 0.0015 W/m/K at the aphelion and perihelion respectively. For different materials the value of K may differ by 3 orders of magnitude (see Table A.1).

We can conclude that the material dependence of the thermal conductivity is the most important. The knowledge of surface material and especially its K is a crucial factor for correct determination of the temperature and consequently the Yarkovsky/YORP effect.

Except for the laboratory measurements of lunar or terrestrial materials ([Cremers, 1972], [Winter and Saari, 1969], [Urquhart and Jakosky, 1997]), we mention several more ways how to estimate surface thermal properties of asteroids: laboratory studies of their meteorite equivalents

[Yomogida and Matsui, 1983], direct measurements of the Yarkovsky effect [Chesley et al., 2003], or infrared observations of asteroids [Delbò et al., 2007].

For the purpose of this section we shall to introduce very useful quantity describing the thermal wave propagation, which is *penetration depth of the temperature variations*

$$\ell = \sqrt{\frac{K}{\rho c \omega}}. \tag{A.9}$$

Here ω denotes a frequency of variations of the temperature[3]. In fact, this represents a depth, where the amplitude of the surface temperature variations decreases by a factor $1/e$.

A.2 One dimensional approach

[Vokrouhlický, 1999] presented an analytical solution of the linearized HDE in three dimensions for a spherical body. Unfortunately, the analytical solution of the HDE for irregularly shaped objects is not known. Moreover, the numerical solution of the HDE in three dimensions is unacceptably time-consuming (and computer's memory-intensive) in our applications. Fortunately, there are possibilities how to avoid the solution of the complete HDE (A.5).

If several conditions are fulfilled, the surface temperature of irregularly shaped asteroids can be determined by separate solutions of one dimensional-HDE for each surface element individually. We assume the surface of an asteroid is approximated by a polyhedron composed of a large number of triangular facets. Next we assume that

- the temparature of each surface element does not significantly affect its neighbouring elements,
- depth of the layer thermally affected by solar radiation is much smaller than size of the asteroid.

If this is fulfilled, we can determine the temperature of any surface elements separately, using one-dimensional form of the HDE:

$$\rho c \frac{\partial T}{\partial t} = \frac{\partial}{\partial z}\left(K \frac{\partial}{\partial z} T\right), \tag{A.10}$$

where z coordinate represents depth below the surface[4]. This approach can be quantitatively tested by means of penetration depth of seasonal temperature variations ℓ_n, which corresponds to Equation (A.9) with frequency equal to the mean motion n. The thermal variations must occur only in a relatively thin layer close to the surface, which is thin compared to the dimension of the asteroid.

Figure A.2 shows, how the depth ℓ_n depends on surface thermal conductivity K. If a main belt body ($a = 2.5\,\mathrm{AU}$) has a regolith layer with $K = 0.001 - 0.01\,\mathrm{W/m/K}$, then this depth is several tens of cm. For s body with a fresh surface ($K = 1 - 10\,\mathrm{W/m/K}$), ℓ_n may be several meters. The penetration depth of the diurnal temperature wave (assuming rotational period 6 hours) is about 100 times smaller than seasonal. So, our one-dimensional approach can be used for regolith covered bodies larger than several meters and regolith free bodies larger than several tens of meters.

The two boundary conditions complement the HDE. The first one arises from the energy conservation at the surface ($z = 0$):

[3]Usually diurnal and seasonal frequency, i.e., rotation frequency or the mean motion about the Sun.

[4]Its value increases from the surface into the centre of the body.

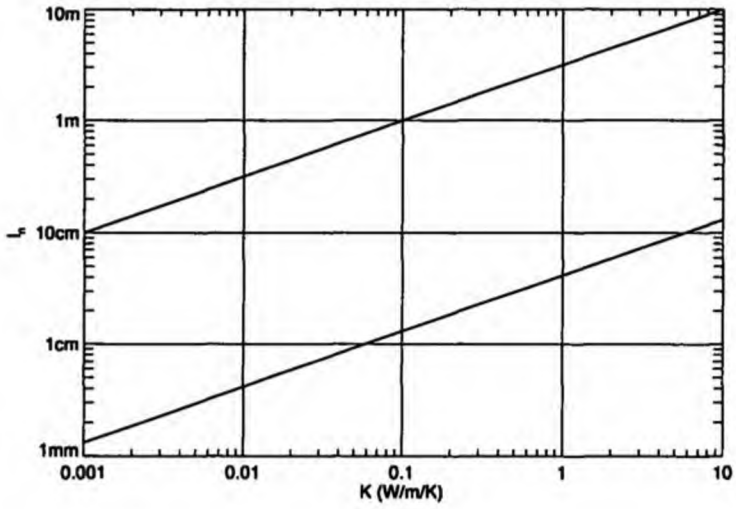

Figure A.2: The dependence of the seasonal temperature penetration depth on the thermal conductivity. The upper line corresponds to the orbital period 3.95 yr, that is appropriate for bodies with the semimajor axis $a = 2.5$ AU. The lower one denotes the penetration depth of daily temperature variations ($P = 6$ hr). The thermal capacity is assumed 800 J/kg/K and the density 2500 kg/m^3.

$$-K\frac{\partial T(t,0)}{\partial z} + \epsilon\sigma T^4(t,0) = (1-A)\mathcal{E}(t)\,. \tag{A.11}$$

Here $\sigma = 5.6697 \times 10^{-8}\mathrm{JK}^{-4}$ is the Stephan–Boltzmann constant, ϵ the infrared emisivity, A the Bond albedo and $\mathcal{E}(t)$ the insolation of the surface element. The first term on the left hand side represents the energy conducted into core, the second term (which is usually linearized in analytical theories) is the energy thermally radiated into space and the right hand side term describes the absorbed solar energy. The second boundary condition corresponds to the assumption of the isothermal core of the asteroid

$$\lim_{z\to\infty}\frac{\partial T(t,z)}{\partial z} = 0\,. \tag{A.12}$$

We also use the periodic initial condition arising from the assumption that the body is thermally relaxed:

$$T(t,z) = T(t+P,z), \tag{A.13}$$

where P is usually the orbital period.

A.3 Linearized analytical solutions

A.3.1 Infinite regolith depth

In this section we shall assume the case of material parameters K, c, ρ which depend neither on depth nor temperature. Then the heat diffusion Equation (A.10) reads

$$\rho c\frac{\partial T}{\partial t} = K\frac{\partial^2 T}{\partial z^2}. \tag{A.14}$$

According to [Vokrouhlický, 1998a], we introduce new variables which are appropriate for solving this equation. Instead of time t we use $\zeta = \exp(int)$, where n is a mean motion, and the depth is replaced by $x = z/\ell$. Next we assume the temperature can be split into constant and variable component and we express it in terms of mean temperature $T_\star$ as $T = T_\star(1 + \delta T')$. The mean temperature $T_\star$ follows from the balance between the emmited and the absorbed energy,

$$\epsilon\sigma T_\star^4 = (1 - A)\mathcal{E}_\star,$$

where $\mathcal{E}_\star = \langle \mathcal{E}(t) \rangle$ is the mean value of the insolation at the given surface element. With these variables, the heat diffusion equation (A.14) has a form

$$i\zeta \frac{\partial}{\partial \zeta} \delta T'(\zeta, x) = \frac{\partial^2}{\partial x^2} \delta T'(\zeta, x). \tag{A.15}$$

If $\delta T' \ll 1$ then $T^4 = T_\star^4(1+4\delta T' + \mathcal{O}(\delta T'^2))$ and we can linearize the surface boundary condition (A.11), which now reads:

$$-\theta \frac{\partial}{\partial x} \delta T' + 4\delta T' + 1 = \mathcal{E}', \tag{A.16}$$

where $\mathcal{E}' = \mathcal{E}/\mathcal{E}_\star$ and

$$\theta = \frac{\sqrt{\rho c K n}}{\epsilon\sigma T_\star^3}. \tag{A.17}$$

Note, that θ is the only dimensional-less quantity left in the heat diffusion problem; it is often called *the thermal parameter* (e.g. [Spencer et al., 1989]). The boundary condition (A.12) in the core of an asteroid reads

$$\lim_{x \to \infty} \frac{\partial}{\partial x} \delta T' = 0\,. \tag{A.18}$$

If the insolation term can be written as a sum of Fourier coefficients

$$\mathcal{E}' = \sum_{k=-\infty}^{+\infty} f_k \zeta^k, \tag{A.19}$$

and consequently the temperature variations will have simillar form

$$\delta T'(\zeta, x) = \sum_{k=-\infty}^{+\infty} a_k(x) \zeta^k. \tag{A.20}$$

Substitution these expressions to (A.15) and comparison of terms with the same power of ζ leads to a set of second order linear differential equations

$$\frac{d^2}{dx^2} a_k(x) - ika_k(x) = 0, \tag{A.21}$$

which has general solution

$$a_k(x) = A_k \exp(\sqrt{ik}x) + B_k \exp(-\sqrt{ik}x).$$

Since $\sqrt{\pm i\,|k|} = \sqrt{|k|/2}\,(i \pm 1)$, we have

$$\begin{aligned} a_0 &= A_0 + B_0 x \\ a_{k>0}(x) &= A'_k \exp\left(\sqrt{|k|/2}\,(i+1)\,x\right) + B'_k \exp\left(-\sqrt{|k|/2}\,(i+1)\,x\right), \\ a_{k<0}(x) &= A'_k \exp\left(\sqrt{|k|/2}\,(i-1)\,x\right) + B'_k \exp\left(-\sqrt{|k|/2}\,(i-1)\,x\right). \end{aligned}$$

The cases with $k \neq 0$ can be collected into a single expression

$$a_{k\neq 0}(x) = A_k \exp(-\psi_k x) + B_k \exp(\psi_k x), \tag{A.22}$$

where

$$\psi_k = \sqrt{|k|/2}\,(1 + i \operatorname{sgn} k). \tag{A.23}$$

The B_k coefficients must be zero due to the constant temperature in the large depth (A.18). The A_k coefficients can be expressed by the substitution (A.22) and (A.20) into to surface boundary condition (A.16):

$$-\theta \sum_{k=-\infty}^{+\infty} A_k \psi_k \exp(-\psi_k x)\,\zeta^k + 4 \sum_{k=-\infty}^{+\infty} A_k \exp(-\psi_k x)\,\zeta^k + 1 = \sum_{k=-\infty}^{+\infty} f_k \zeta^k.$$

Comparison of the terms with the same power of ζ leads to

$$A_k = \frac{f_k}{4 + \theta \psi_k}$$

for $k \neq 0$. Since $A_0 = (f_0 - 1)/4$ and $f_0 = 1$ the coefficient $A_0 = 0$. Finally, we have

$$T(t,z) = T_\star \left(1 + \sum_{k=-\infty}^{+\infty} \frac{f_k}{4 + \theta \psi_k} \exp(-\psi_k \frac{z}{\ell} + iknt)\right). \tag{A.24}$$

Since $\mathcal{E}'$ is a periodic real function then $f_k = f_{-k}$ for $k = 2l$ and $f_k = -f_{-k}$ for $k = 2l+1$. Moreover f_{2l} is a real number, while f_{2l+1} is an imaginary number. After a little algebra we end up with the expression for the temperature:

$$\begin{aligned} T = \quad T_\star \Bigg[& 1 + \frac{1}{2} \sum_{k=2,4,\ldots}^{\infty} f_k \exp\left(-\sqrt{\frac{k}{2}}\,x\right) \left[(1+\lambda_k)\cos\phi_k + \lambda_k \sin\phi_k\right] \\ & + \frac{1}{2} \sum_{k=1,3,\ldots}^{\infty} i\, f_k \exp\left(-\sqrt{\frac{k}{2}}\,x\right) \left[\lambda_k \cos\phi_k - (1+\lambda_k)\sin\phi_k\right] \Bigg], \end{aligned} \tag{A.25}$$

where $\lambda_k = \theta\sqrt{k/32}$ and $\phi_k = -\sqrt{k/2}\,x + knt$. From this expression we can conclude, that the amplitude of the temperature variations decreases with increasing depth below the surface as $e^{-\sqrt{k/2}x}$. There is also a thermal lag (given by the combination of trigonometric functions in (A.25)).

A.3.2 Finite regolith depth

Here we assume a more general model for a body which surface is covered by a regolith layer of depth h, with the density ρ_1, thermal capacity c_1 and thermal conductivity K_1, while the core has the material parameters ρ_2, c_2, K_2. We also assume these constants do not depend on temperature. (A similar model for a spherical body was derived by [Vokrouhlický and Brož, 1999].) Similarly as in the previous section we introduce new variables. In the regolith layer $x_1 = z/\ell_1$, $\ell_1 = \sqrt{K_1/(\rho_1 c_1 n)}$ and temperature $T_1 = T_\star(1+\delta T_1')$, in the core $x_2 = z/\ell_2$, $\ell_2 = \sqrt{K_2/(\rho_2 c_2 n)}$ and $T_2 = T_\star(1 + \delta T_2')$. Then the heat diffusion Equation (A.14) has a form

$$i\zeta \frac{\partial}{\partial \zeta} \delta T_1'(\zeta, x_1) = \frac{\partial^2}{\partial x_1^2} \delta T_1'(\zeta, x_1) \tag{A.26}$$

in the regolith layer and

$$i\zeta \frac{\partial}{\partial \zeta} \delta T_2'(\zeta, x_2) = \frac{\partial^2}{\partial x_2^2} \delta T_2'(\zeta, x_2) \tag{A.27}$$

in the core. The surface boundary condition is similar to (A.16)

$$-\theta \frac{\partial}{\partial x_1} \delta T_1' + 4\delta T_1' + 1 = \mathcal{E}', \tag{A.28}$$

as well as the requirement of the constant temperature in large depth, corresponding to (A.18)

$$\lim_{x_2 \to \infty} \frac{\partial}{\partial x_2} \delta T_2' = 0\,. \tag{A.29}$$

Compared to the case of homogeneous material, discussed in the previous section, here we have two additional conditions on the regolith-core boundary. The first stems from the assumption of the temperature continuity[5]

$$\lim_{x_1 \to h_1^-} \delta T_1' = \lim_{x_2 \to h_2^+} \delta T_2', \tag{A.30}$$

and the second one corresponds to the thermal flux continuity

$$\lim_{x_1 \to h_1^-} \theta_1 \frac{\partial}{\partial x_1} \delta T_1' = \lim_{x_2 \to h_2^+} \theta_2 \frac{\partial}{\partial x_2} \delta T_2'. \tag{A.31}$$

Here $h_1 = h/\ell_1$ and $h_2 = h/\ell_2$. Using the same technique as in the case of homogeneous material, we obtain the temperature in the regolith layer as

$$\delta T_1'(\zeta, x_1) = \sum_{k=-\infty}^{+\infty} a_k(x_1) \zeta^k, \tag{A.32}$$

where

[5]Note that $x_1 \to h_1^-$ means that x_1 approaches h_1 from lower values of x_1 and $x_1 \to h_1^+$ means that x_1 approaches h_1 from higher values of x_1.

$$a_{k\neq 0}(x_1) = A_k \exp(-\psi_k x_1) + B_k \exp(\psi_k x_1) \tag{A.33}$$

and $a_0 = A_0 + B_0 x_1$. Let us recall that ψ_k is defined by Equation (A.23). Temperature in the core is

$$\delta T_2'(\zeta, x_2) = \sum_{k=-\infty}^{+\infty} b_k(x_2)\zeta^k, \tag{A.34}$$

where

$$b_{k\neq 0}(x_b) = C_k \exp(-\psi_k x_2) + D_k \exp(\psi_k x_2) \tag{A.35}$$

and $b_0 = C_0 + D_0 x_2$. The four boundary conditions mentioned above can be used to express the coefficients A_k, B_k, C_k and D_k. The assumption of constant temperature in the large depth (A.29) can be satisfied only if $D_k = 0$ (but note that $B_k \neq 0$). At first, we discuss coefficients with $k \neq 0$. The energy balance on the surface (A.28) leads to

$$(\theta_1\psi_k + 4)A_k - (\theta_1\psi_k - 4)B_k = f_k. \tag{A.36}$$

The temperature continuity on the regolith-core boundary (A.30) reads

$$\exp(-\psi_k h_1)\, A_k + \exp(\psi_k h_1)\, B_k - \exp(-\psi_k h_2)\, C_k = 0, \tag{A.37}$$

and the thermal flux continuity on the same boundary (A.31) reads

$$-\exp(-\psi_k h_1)\, A_k + \exp(\psi_k h_1)\, B_k + \frac{\theta_2}{\theta_1}\exp(-\psi_k h_2)\, C_k = 0. \tag{A.38}$$

Putting these results together we obtain

$$A_k = \frac{f_k}{\Xi_k}\left(\frac{\theta_2}{\theta_1} + 1\right), \tag{A.39}$$

$$B_k = -\frac{f_k}{\Xi_k}\left(\frac{\theta_2}{\theta_1} - 1\right)\exp(-2\psi_k h_1), \tag{A.40}$$

$$C_k = 2\frac{f_k}{\Xi_k}\frac{\theta_2}{\theta_1}\exp\left[\psi_k(h_2 - h_1)\right], \tag{A.41}$$

where

$$\begin{aligned}\Xi_k = {} & \frac{\theta_2}{\theta_1}\left[\theta_1\psi_k\left(1 + e^{-2\psi_k h_1}\right) + 4\left(1 - e^{-2\psi_k h_1}\right)\right] \\ & + \left[\theta_1\psi_k\left(1 - e^{-2\psi_k h_1}\right) + 4\left(1 + e^{-2\psi_k h_1}\right)\right].\end{aligned} \tag{A.42}$$

For $k = 0$, the conditions (A.28), (A.30) and (A.31) lead to

$$-\theta_1 B_0 + 4A_0 + 4B_0 + 1 = f_0,$$

$$A_0 + B_0 h_1 = C_0 + D_0 h_2,$$

$$\theta_1 B_0 = \theta_2 D_0 = 0,$$

and consequently

$$A_0 = B_0 = C_0 = D_0 = 0.$$

Finally, in the regolith layer ($z < h$) we have

$$T = T_\star \left\{ 1 + \sum_k \frac{f_k \exp(iknt)}{\Xi_k} \left[\left(\frac{\theta_2}{\theta_1} + 1 \right) \exp(-\psi_k x_1) - \left(\frac{\theta_2}{\theta_1} - 1 \right) \exp(\psi_k x_1 - 2\psi_k h_1) \right] \right\}, \tag{A.43}$$

and in the core ($z > h$)

$$T = T_\star \left\{ 1 + 2\frac{\theta_2}{\theta_1} \sum_k \frac{f_k}{\Xi_k} \exp[\psi_k (h_2 - h_1 - x_2) + iknt] \right\}. \tag{A.44}$$

All the sumations are made from $k = -\infty$ to $k = \infty$, without $k = 0$.

We can see, that these expressions for temperature inside a two-layered body approach the expression (A.24), describing the temperature in a homogeneous body. In particular, (A.43) approaches (A.24) when $h \to \infty$, (A.43) approaches (A.24) when $h \to 0$ and both (A.43) and (A.44) approach (A.24) when $c_1 \to c_2$ and $K_1 \to K_2$ and $\rho_1 \to \rho_2$.

A.4 A numerical method for constant material parameters

The linear analytical theories are valid when the temperature variations are relatively small; for larger variations the linearization fails. Moreover, present analytical theories are derived on the basis of several simplifications (e.g., the temperature independence of thermal parameters). In this section we shall derive a numerical model that uses non-linearized boundary condition. This model can be used even for cases with large temperature variations.

If the depth z is scaled by ℓ_n and time by orbital period P, then the heat diffusion equation (A.14) has a form

$$\frac{\partial T}{\partial t} = \frac{\partial^2 T}{\partial x^2}, \tag{A.45}$$

where $t \in (0, 1)$ and $x = z/\ell_n$. The energy conservation law on the surface (A.11) reads

$$-\theta \frac{\partial T(t,0)}{\partial x} + \epsilon\sigma T^4(0,t) = (1 - A)\mathcal{E}(t) \tag{A.46}$$

and the lower boundary condition (A.12)

$$\lim_{x \to \infty} \frac{\partial T(t,x)}{\partial x} = 0. \tag{A.47}$$

Derivatives must be expressed in terms of finite differences. We suppose constant time step $\Delta t = 1/L$, where L is the number of time intervals. Time will be denoted by an upper index $l = 1 \ldots L$. Since analytical theory predicts exponential decrease of amplitude of temperature variations, we chose exponentially spatial step exponentially increasing with depth (like [Hamilton and Matson, 1987]) as $\Delta x_j = x_{j+1} - x_j = \Delta x_0 \exp(\alpha j)$ with $j = 0 \ldots h_{max} - 1$. Lower index will denotes spatial coordinate. Then partial derivatives of the temperature according to time or depth are

$$\left(\frac{\partial T}{\partial t}\right)_j^l = \frac{T_j^{l+1} - T_j^l}{\Delta t}, \qquad \left(\frac{\partial T}{\partial x}\right)_j^l = \frac{T_{j+1}^l - T_j^l}{\Delta x_j}, \tag{A.48}$$

$$\frac{\partial^2 T}{\partial x^2} = \frac{1}{\Delta x_j}\left[\left(\frac{\partial T}{\partial x}\right)_j^l - \left(\frac{\partial T}{\partial x}\right)_{j-1}^l\right] = \frac{1}{\Delta x_j}\left[\frac{T_{j+1}^l - T_j^l}{\Delta x_j} - \frac{T_j^l - T_{j-1}^l}{\Delta x_{j-1}}\right]. \tag{A.49}$$

Using these expressions, the HDE (A.45) reads

$$T_j^{l+1} = T_j^l + \frac{\Delta t}{\Delta x_j}\left(\frac{T_{j+1}^l - T_j^l}{\Delta x_j} - \frac{T_j^l - T_{j-1}^l}{\Delta x_{j-1}}\right), \tag{A.50}$$

which represents an explicit formula for the temperature at time l. Here $j = 1 \ldots J-1$ and $l = 1 \ldots L$. Selection of the time step and initial spatial step is restricted by von Newmann stability criterion[6]

$$\Delta t/(\Delta x_0)^2 < 1/2.$$

The surface boundary condition (A.46) in terms of finite differencies is

$$\left(T_0^l\right)^4 + \frac{\sqrt{\rho c K n}}{\sigma\epsilon}\frac{1}{\Delta x_0}T_0^l - \left(\frac{1-A}{\sigma\epsilon}\mathcal{E}^l + \frac{\sqrt{\rho c K n}}{\sigma\epsilon}\frac{1}{\Delta x_0}T_1^l\right) = 0. \tag{A.51}$$

This equation needs to be solved numerically, for instance by the method of Laguerre (e.g. [Press et al., 1992], online version `http://www.nrbook.com/a/bookfpdf.php`). Finally, lower boundary condition reads

$$T_N^l = T_{N-1}^l. \tag{A.52}$$

These equations together with some suitable initial temperature allow to determine the temperature in any time t^l and any depth x_j.

Now we will briefly describe the algorithm how to compute the surface temperature of a single facet of an asteroid.

1. Determine the insolation function $\mathcal{E}$ of the given facet. This is discussed in (Appendix B).
2. Chose the initial temperature so that $T_j^0 = \sqrt[4]{(1-A)\langle\mathcal{E}\rangle/(\epsilon\sigma)}$.
3. Chose the appropriate time step Δt and the spatial step Δx in order the von Neumann criterion of stability is satisfied: $\Delta x_0 = 2\sqrt{\Delta t}$.
4. Find the temperatures T_j^l using Equations (A.50), (A.51) and (A.52) for $j = 0, \ldots, J$, $l = 1, \ldots, L$, i.e., during the whole orbital period.
5. The second choice of the initial temperature T_j^0 is done by averaging of the surface temperature T_0^l over the whole orbit (i.e., for $l = 1, \ldots, L$): $T_j^0 = \langle T_0^l\rangle$. The temperature is computed again according to 4.

[6] Since $\Delta x_i > \Delta x_0$ for $i > 0$, then von Neumann stability criterion is fulfilled in all depths.

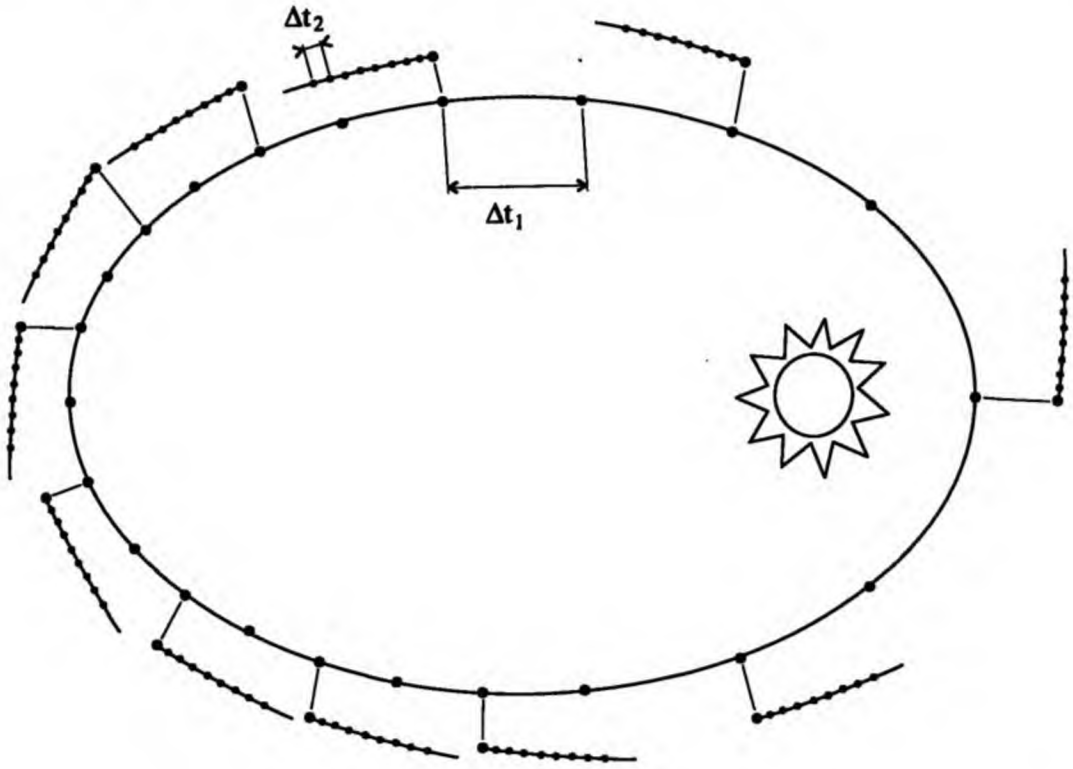

Figure A.3: A "two-level scheme": In the first level we solve the HDE with a longer timestep Δt_1 along the orbit and save the temperature profiles. In the second level we choose an appropriate amount of time instants and solve the HDE with a shorter timestep Δt_2 for several tens of rotational periods. Here we use initial temperature profile determined in the first level.

6. The third and following choices of initial temperature are done by $T_j^0 = T_j^L$ and new temperature is again computed according to 4. This is repeated until the required relaxation of temperature is reached.

The time step Δt must be chosen small enough, in order the time delay between the maximal temperature and the "noon" is sufficiently covered.

A problem arises, when the rotational period is small compared to the orbital period. In this case, the necessary number of time steps is so high, that the requirements on computer's memory and computational time are unacceptable. We begin with a longer timestep and save the temperature (their depth profiles) in an appropriate amount of time instants (usually 100). Than we integrate temperature during several tens of rotational periods after these time instants and we use the saved temperatures as the initial ones. The integration with the rough timestep gives a sufficient determination of the sesonal temperature profile, whereas the integration with the fine time step gives a precise diurnal temperature variations. We call this technique a "two–level scheme", whereas the former a "one–level scheme". See Figure A.3.

A.5 Numerical method for non-constant material perameters

In this section we will deal with the case, when material parameters depend both on depth and temperature. The dependance on depth follows namely from a possible existence of surface regolith layer, which has several orders of magnitude lower thermal conductivity than a fresh rock beneath.

A.5.1 Modification of the Crank-Nicholson scheme

We can not use the explicit numerical scheme (A.50) here, because it would be very difficult to fulfill the von Neumann stability criterion due to thermal dependence of material parameters. So, we have to modify implicit Crank-Nicholson method which is unconditionally stable and moreover it is of second order in Δt. The one-dimensional heat diffusion Equation (A.10) for non-constant material parameters is

$$\rho c \frac{\partial T}{\partial t} = \frac{\partial K}{\partial z}\frac{\partial T}{\partial z} + K\frac{\partial^2 T}{\partial z^2}.$$

Expressing the partial derivatives in the terms of finite differencies, we obtain

$$T_j^{l+1} - T_j^l = \frac{\Delta t}{\Delta x_j \rho_j^l c_j^l}\left[\frac{K_{j+1}^l}{\Delta x_j}T_{j+1}^l - \left(\frac{K_{j+1}^l}{\Delta x_j} + \frac{K_j^l}{\Delta x_{j-1}}\right)T_j^l + \frac{K_j^l}{\Delta x_{j-1}}T_{j-1}^l\right], \tag{A.53}$$

which allows to solve the HDE explicitely with non-constant material parameters. If the partial derivatives with respect the time are expressed in the time $n+1$, instead of n, then we obtain purely implicit scheme:

$$T_j^{l+1} - T_j^l = \frac{\Delta t}{\Delta x_j \rho_j^{l+1} c_j^{l+1}}\left[\frac{K_{j+1}^{l+1}}{\Delta x_j}T_{j+1}^{l+1} - \left(\frac{K_{j+1}^{l+1}}{\Delta x_j} + \frac{K_j^{l+1}}{\Delta x_{j-1}}\right)T_j^{l+1} + \frac{K_j^{l+1}}{\Delta x_{j-1}}T_{j-1}^{l+1}\right]. \tag{A.54}$$

The sum of (A.53) and (A.54) gives

$$\begin{aligned} &T_{j+1}^{l+1}[b_j^{l+1}a_j^{l+1}] + T_j^{l+1}[-2 - a_j^{l+1}(b_j^{l+1} + b_{j-1}^{l+1})] + T_{j-1}^{l+1}[a_j^{l+1}b_{j-1}^{l+1}] = \\ &= -2T_j^l - a_j^l[b_j^l T_{j+1}^l - (b_j^l + b_{j-1}^l)T_j^l + b_{j-1}^l T_{j-1}^l], \end{aligned} \tag{A.55}$$

where

$$a_j^l = \frac{\Delta t}{\Delta x_j \rho_j^l c_j^l}, \qquad b_j^l = \frac{K_{j+1}^l}{\Delta x_j}$$

for $j = 0 \ldots J-1$. This, together with the lower boundary condition (bottom row), can be expressed in the matrix notation

$$\mathbb{D}\mathbf{T}^{l+1} = \mathbf{R},$$

or

$$\begin{pmatrix} B_1^{l+1} & C_1^{l+1} & & & & \\ A_2^{l+1} & B_2^{l+1} & C_2^{l+1} & & & \\ & A_3^{l+1} & B_3^{l+1} & C_3^{l+1} & & \\ & & \cdots & \cdots & \cdots & \\ & & & A_{J-1}^{l+1} & B_{J-1}^{l+1} & C_{J-1}^{l+1} \\ & & & & 1 & -1 \end{pmatrix} \begin{pmatrix} T_1^{l+1} \\ T_2^{l+1} \\ T_3^{l+1} \\ \cdots \\ T_{J-1}^{l+1} \\ T_J^{l+1} \end{pmatrix} = \begin{pmatrix} R_1^l - A_1^{l+1}T_0^{l+1} \\ R_2^l \\ R_3^l \\ \cdots \\ R_{J-1}^l \\ 0 \end{pmatrix}, \tag{A.56}$$

where

$$\begin{aligned} &A_j^l = a_j^l b_{j-1}^l, \quad B_j^l = -2 - a_j^l b_j^l - a_j^l b_{j-1}^l, \quad C_j^l = a_j^l b_j^l, \\ &R_j^l = -C_j^l T_{j+1}^l + (-4 - B_j^l)T_j^l - A_j^l T_{j-1}^l \end{aligned}$$

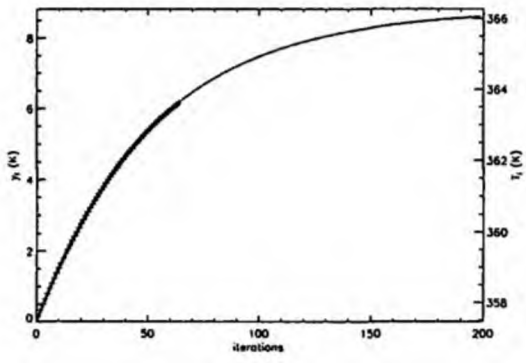

Figure A.4: A typical example of slow convergence of surface temperature. The cross symbols denote iterated temperatures (65 iterations), the solid curve is temperature computed analytically from the first four iterations. The limit temperature T_∞ is represented by the top margin of the $y-$axis. It can be seen, that more than 200 iterations would be necessary for good relaxation of the right value. Here, the analytical estimation of T_∞ is needed.

for $j = 1 \dots J-1$. ($A_J^l = 1$, $B_J^l = -1$.) The temperature in the time $l+1$ can be expressed from the equation system (A.56) and the surface boundary condition:

$$(T_0^{l+1})^4 + \frac{K_0^{l+1}}{\epsilon\sigma\Delta x_0} T_0^{l+1} - \frac{1}{\epsilon\sigma}\left[(1-A)\mathcal{E}^{n+1} + \frac{K_0^{l+1}}{\Delta x_0} T_1^{l+1}\right] = 0. \qquad \text{(A.57)}$$

System (A.56) represents a modified Crank-Nicholson scheme, which is unconditionally stable and thus there are no restrictions on spatial or time step from the stability point of view.

A.5.2 Improvement of the convergence

The main trouble is that the matrix $\mathbb{D}$ as well as the right hand side $\mathbf{R}$ depends non-linearly on the unknown temperature $\mathbf{T}^{l+1}$. (Matrix $\mathbb{D}$ is expressed in the time $l+1$ and contains coefficients A_i^{l+1}, B_i^{l+1} and C_i^{l+1} which are functions of the temperature dependent material parameters K and c. The same situation is in the case of right hand side $\mathbf{R}$.) This problem can be solved iteratively so that initially we determine $\mathbb{D}$ and $\mathbf{R}$ using $\mathbf{T}^l$ instead of $\mathbf{T}^{l+1}$. Then we obtain the first iteration $\mathbf{T}^{l+1}|_0$ and use it again instead of $\mathbf{T}^{l+1}$. This would be repeated until a difference between i-th and $(i+1)$-th iteration will be smaller than a given precision. However, our experience shows that sometimes a huge number of iterations is necessary to reach a right value of $\mathbf{T}^{l+1}$. Thus we had to develop a technique which accelerates the convergence of $\mathbf{T}^{l+1}$, and we describe it below.

Let T_i denotes the i-th iteration of the temperature $\mathbf{T}^{l+1}$. We expect that iterations exponentially approach a limit T_∞ which means that $T_\infty - T_i = y_\infty a^{-i}$. We shall try to estimate this limit from the first few iterations. (See Figure A.4.)

A difference between the zeroth and i-th iteration is $y_i = T_i - T_0$. Then $y_i = y_\infty(1-a^{-i})$ and $y_j = y_\infty(1-a^{-j})$. After some algebra we obtain $y_i - y_j = y_i a^{-j} - y_j a^{-i}$. Assuming $j = ki$ and substituting $t = a^{-i}$ we have

$$y_i t^k - y_j t + (y_j - y_i) = 0.$$

For $k = 2$ the solution is

$$t_{1,2} = \frac{y_j \pm |y_j - 2y_i|}{y_i},$$

which leads to the single value[7] $t = (y_j - y_i)/y_i$. This means that[8] $a = \left(\frac{y_i}{y_j - y_i}\right)^{\frac{1}{i}}$ and $y_\infty = \frac{y_i^2}{2y_i - y_j}$, or by means of the temperature iterations

$$a = \left(\frac{T_i - T_0}{T_{2i} - T_i}\right)^{\frac{1}{i}}, \qquad y_\infty = \frac{(T_i - T_0)^2}{2T_i + T_0 - T_{2i}}.$$

The limit temperature is then

$$T_\infty = T_0 + \frac{(T_i - T_0)^2}{2T_i + T_0 - T_{2i}}. \tag{A.58}$$

If $i = 2$, the limit temperature can be determined from four iterations as

$$T_\infty = T_0 + \frac{(T_2 - T_0)^2}{2T_2 + T_0 - T_4}.$$

Here, a special care must be taken if the denominator is zero or nearly zero. This indicates, that temperature iterations converge too slowly and due to small differences between them they seem to change linearly and not exponentially. In this case, we substitue $i = 4$, 8, 16, etc. until the exponential convergence (or large number of iterations) is reached. Finally, we substitute the limit temperature T_∞ into (A.56) and verify it does not differ from $\mathbf{T}^{l+1}$.

Let us to estimate the number of iterations necessary to reach a good approximation of y_∞. Let $p = y_i/y_\infty$. Then $a^{-i} = 1 - p$ and $i = -\ln(1-p)/\ln(a)$. For example, if we want y_i to be 99% of y_∞, we need roughly $-\ln(0.01)/\ln(a)$ iterations.

A.5.3 The algorithm

Our algorithm for the computation of the surface temperature on a facet of an asteroid is the following:

1. Determine the insolation function $\mathcal{E}(t)$ for the given facet. This is discussed in (B).
2. Chose the initial temperature so that $T_j^0 = \sqrt[4]{(1-A)\langle\mathcal{E}\rangle/(\epsilon\sigma)}$.
3. Chose appropriate initial time step Δt_0 and spatial steps Δx_i. (See the example in Section A.6.)
4. Solve the temperature T_j^l, during the whole orbital period, by equations (A.56), (A.57) using method described in Section A.5.2.
5. The second choice of initial temperature T_j^0 is given by the averaging of the surface temperatures T_0^l over the whole orbit (i.e., for $l = 1, \ldots, L$): $T_j^0 = \langle T_0^l \rangle$, and the temperature is further computed[9] according to 4.
6. The third and following choices of the initial temperature are performed simply by $T_j^0 = T_j^L$ and the temperature is again computed according to 4. The time step can be smaller and smaller in the subsequent turns. This is repeated until a satisfactory relaxation of temperature is reached.

[7] rejecting the solution $t = 2$

[8] The fraction is always positive because if $y_j > y_i$ then $y_i > 0$ and if $y_j < y_i$ then $y_i < 0$

[9] Optionally, with a smaller time step Δt_1

A.6 A simple example of temperature behaviour

Here we shall present an example of the temperature behaviour computed by different techniques described before. Let us suppose the situation described in Figure A.5. The body is at a circular orbit, 1 AU from the Sun. We shall focus on surface element dS at the equator. Its insolation $\mathcal{E}(t)$ can be express as

$$\mathcal{E}(t) = \begin{cases} A \sin 2\pi t/P, & t < P/2 \\ 0, & t \geq P/2, \end{cases}$$

with the amplitude $A = 1366\,\mathrm{W/m^2}$ (corresponding to the flux at 1 AU distance from the Sun) and period $P = 6\,\mathrm{hr}$. The along-track component of the thermal force corresponding to the temperature T is

$$f_T(t) = \frac{2\epsilon\sigma}{3c} T^4(t) \sin(2\pi t/P).$$

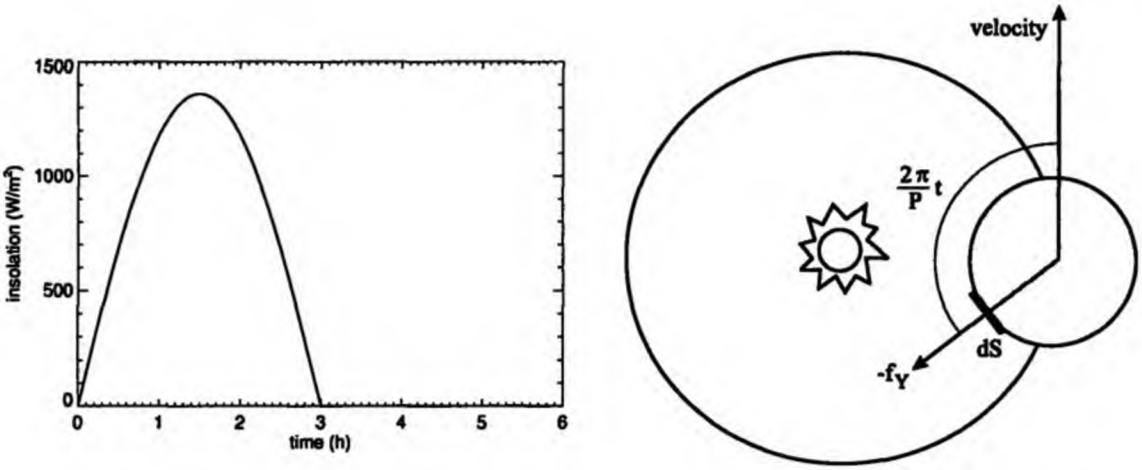

Figure A.5: Left: The insolation as a function of time. An amplitude is $1366\,\mathrm{W/m^2}$. Right: geometry of the problem. More explanation in the text.

In the following figures A.6–A.8 we present the solution of the surface temperature corresponding to the insolation $\mathcal{E}(t)$,depicted in Figure A.5. A detailed discussion can be found in the figure captions of particular figures.

In Figure A.6 we deal with a problem of the right choice of spatial and time steps (for homogeneous body). We found that the results (temperature and the Yarkovsky force) are almost independent on the time step (6 s – 600 s). If the initial spatial step is less than $\Delta x_0 \simeq 0.1\ell_d$, the results do not depend neither on the spatial step.

In A.7 we show the dependence of temperature and the Yarkovsky force on the spatial step and the regolith depth. We found the results are nearly independent on spatial step.

Finally, in Figure A.8, we compare the results (time dependence of the temperature, thermal lag and the Yarkovsky force) of the analytical and numerical model.

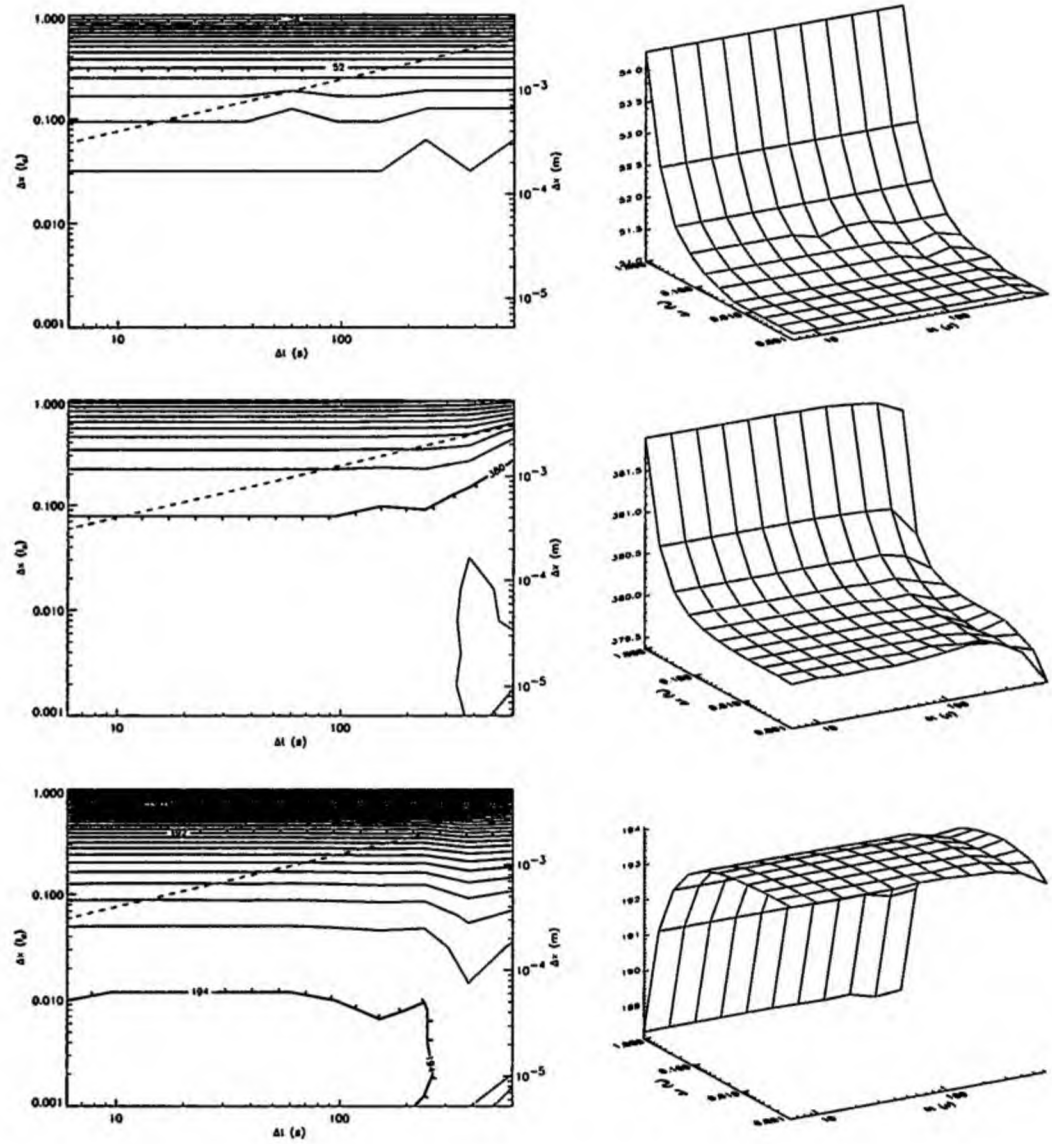

Figure A.6: The dependence of the numerically (modified Crank-Nicolson scheme) computed Yarkovsky force and the surface temperature on chosen initial spatial step Δx_0 and time step Δt. The **upper row** represents the resulting spin-averaged along-track component of the thermal force in 10^{-8} N/m units. The **middle row** corresponds to the maximal surface temperature and the **lower one** to minimal surface temperature in K. The left column is a countour plot (here, the dashed line divides the figure to upper-left area, where the von Neumann criterion is fulfilled and lower-right one where it is not fulfilled) while the right one is a surface plot. These results correspond to the insolation from Figure A.5. Here, we assume the thermal parameters to be independent both on temperature and spatial coordinates (but the results with temperature dependent material parameters are quite similar). The thermal conductivity is assumed $K = 0.01$ W/m/K, the thermal capacity $c = 735$ J/kg/K and the density $\rho = 1.7\,\mathrm{g/cm^3}$. We can see a near independence on time step in the range from 6 to 600 s. However, the initial spatial step is more important quantity. We found that Δx_0 should be smaller than $\sim 0.1\,\ell_d$ or $0.01\,\ell_d$. We can also see that the usage of the modified Crank-Nicolson scheme allows us to prevent a very short time step < 6 s which should be used in an explicit scheme together with $\Delta x_0 < 0.1\,\ell_d$ (due to von Neuman criterion of stability).

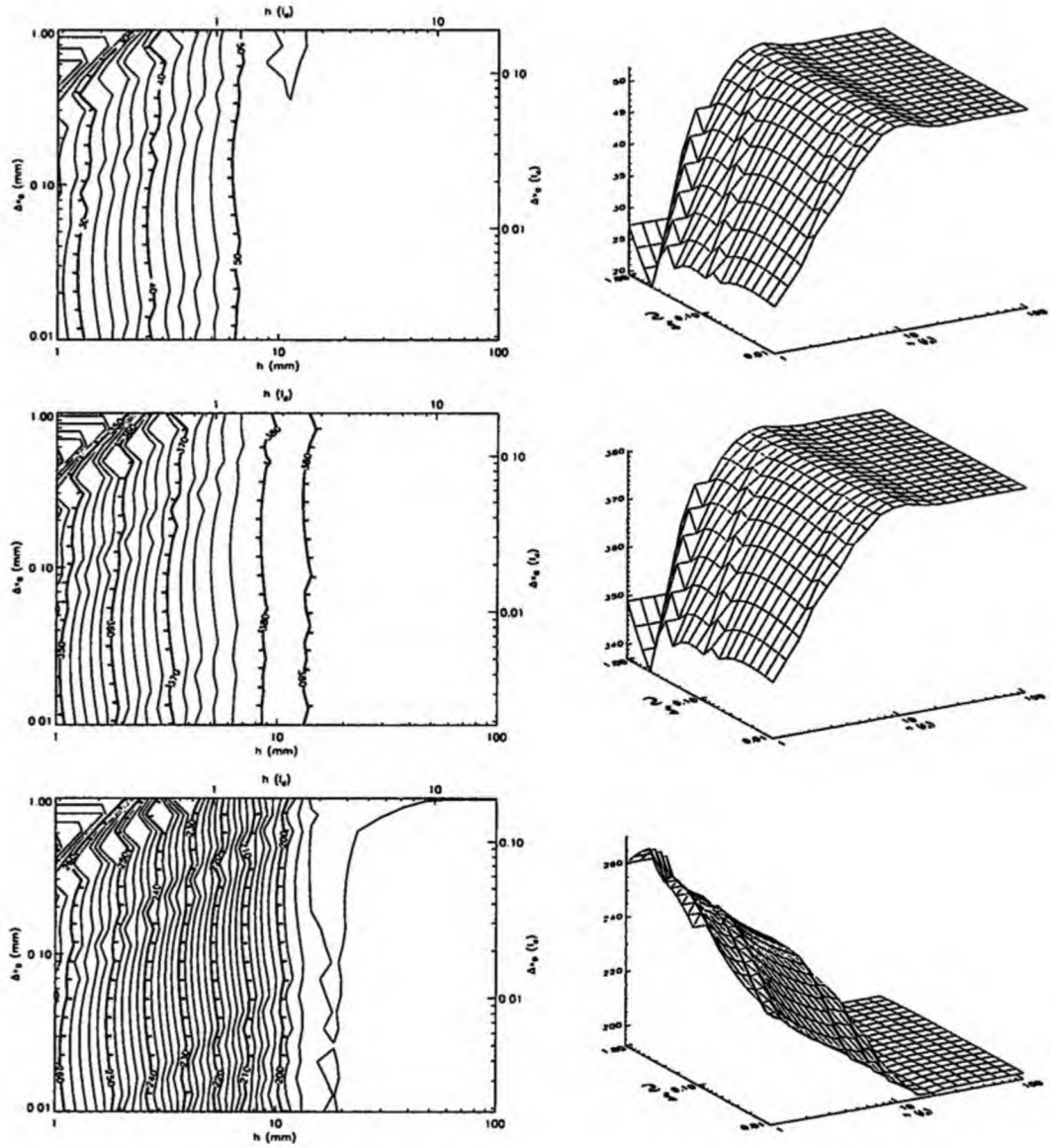

Figure A.7: The dependence of the numerically computed Yarkovsky force and the surface temperature on the chosen initial spatial step Δx_0 for various regolith depths. As in Figure A.6, the **upper row** represents the resulting spin-averaged along track component of the thermal force in 10^{-8} N/m. The **middle row** corresponds to the maximal and the **lower one** to the minimal surface temperature in K. The left column is a countour plot while the right one is a surface plot. These results correspond to the insolation from Figure A.5. Here we assume (unlike in Figure A.6) the thermal parameters dependent both on temperature and space: The regolith layer is characterized by the thermal conductivity $K = 0.01 + 2 \times 10^{-11} (T/\mathrm{K})^3\,\mathrm{W/m/K}$ and the thickness from 1 to 100 mm, while the core has $K = 2.6\,\mathrm{W/m/K}$. The thermal capacity (A.8) and the density $\rho = 1.7\,\mathrm{g/cm^3}$ are the same for regolith and core. The results are again nearly independent on a timestep. The dependence on Δx_0 is fortunately also weak, though it is better to use $\Delta x_0 < 0.1\,\ell_d$ again.

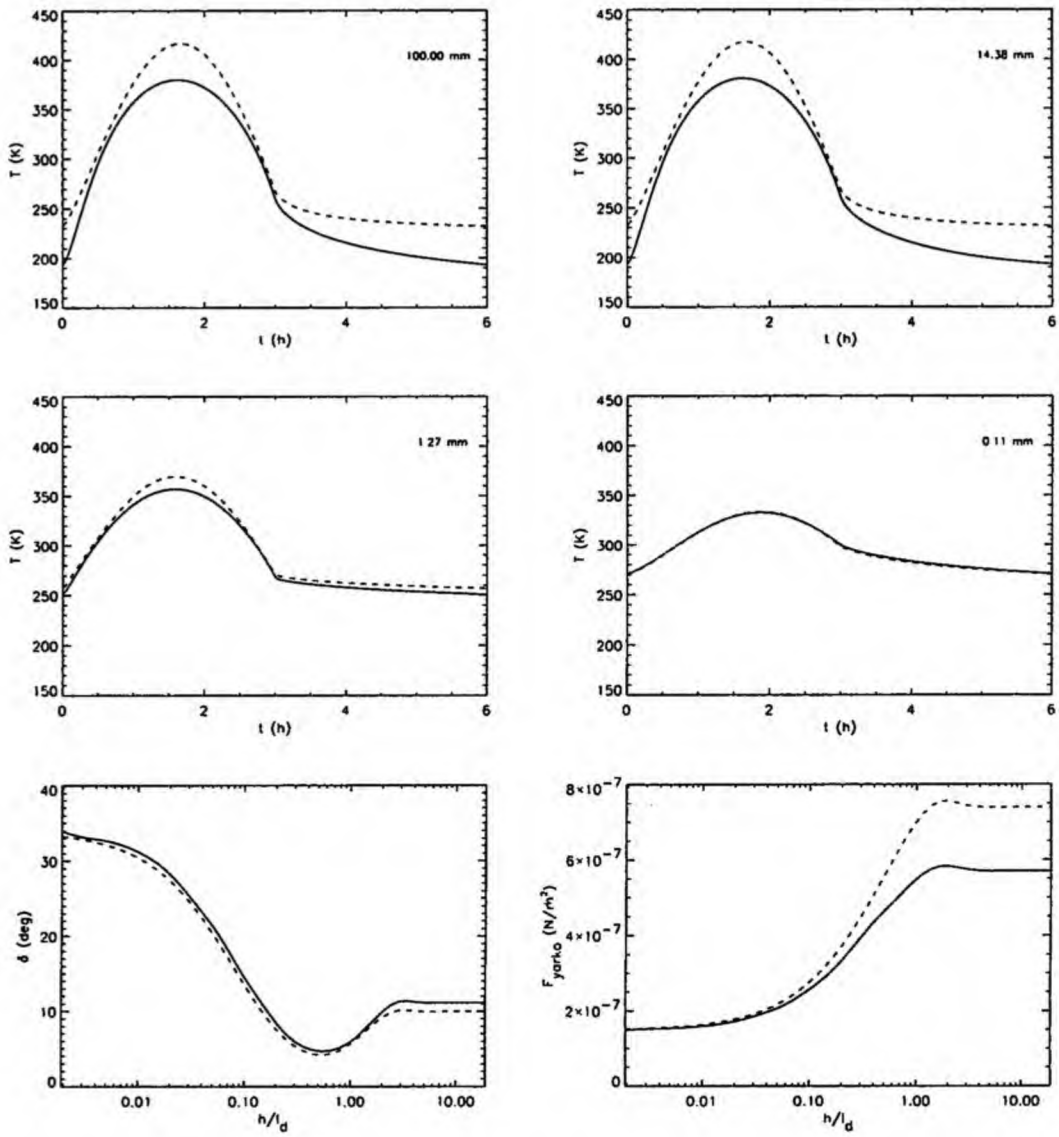

Figure A.8: A comparison of results of the numerical theories (solid curves) and the analytical theories (dashed curves, according to A.43) for various depths for regolith layer. **Upper two rows** show the time dependence of the temperature for regolith thickness denoted in upper right corner of each plot. It can be seen that there is quite well agreement between the numerical and the analytical theory for small regolith depths. In this case the amplitude of the temperature variations are small (due to highly conductive core) and the linearization in analytical theory works well. The **lower left figure** shows the dependence of the angle δ, between the direction opposite to the Sun and the thermal Yarkovsky force. The **lower right figure** shows the dependence of the along-track component of the thermal force on regolith depth. These results again correspond to the insolation from Figure A.5. Here we assume thermal parameters dependent both on the temperature and space: The regolith layer is characterized by the thermal conductivity $K = 0.013\,\mathrm{W/m/K}$ and the thickness from 0.01 to 100 mm, while the core has $K = 1\,\mathrm{W/m/K}$. The thermal capacity c is the same for the core and the regolith layer. It is (A.8) for the numerical method and $750\,\mathrm{J/kg/K}$ for the analytical method. The density of the core and regolith is $\rho = 1.7\,\mathrm{g/cm^3}$.

Appendix B

Shape representation

In our work, the shapes of all bodies (both artificial and real) are modeled by polyhedrons with thousands of triangular facets. The bodies are represented by a list of vectors, describing the vertices, and by a list of mutual identification (which of the vectors form a triangle). This representation is able to describe complicated irregular shapes of small solar system bodies, including craters, mountains or valleys on the surface (e.g., [Simonelli et al., 1993]).

For each polyhedron we need to know the volume V (mass), inertia tensor $\mathbf{I}$ (principal moments A, B, C, eigenvectors of $\mathbf{I}$) as well as centers $\mathbf{r}_i$, outer normal $\mathbf{n}_i$ and areas S_i for each surface facet.

Moreover, we need to transform the coordinate system into the one having the origin in the center of mass and with axes corresponding to the eigenvectors of inertia tensor (x-axis corresponding to the longest axis of $\mathbf{I}$, z-axis to the shorter one).

Here we present a procedure, how to determine these quantities and insolation (including self-shadowing of the surface) of such a body.

Fortunately, any polyhedron (with triangular facets) can be divided into tetrahedrons (surface triangular facet forms the base and some point inside the polyhedron represents vertex). We use the procedure published by [Dobrovolskis, 1996] and generalize it slightly, in order to describe the case of non-convex bodies (with respect to the origin of coordinate system). We call the body as "non-convex with respect to the origin", if there exist such a half-line going from the origin, which intersects the surface in more than one point (see Figure B.1).

B.1 Basic characteristics of the polyhedron and its facets

Consider the vertices of tetrahedron, which can be described by four position vectors $\mathbf{E}_i$, $\mathbf{F}_i$, $\mathbf{G}_i$ and $\mathbf{0}$, which coincides with the origin of coordinate system (see Figure B.1 left). The center of the surface triangular facet i, defined by the vectors $\mathbf{E}_i$, $\mathbf{F}_i$ and $\mathbf{G}_i$, is

$$\mathbf{t}_i = \frac{1}{3}(\mathbf{F}_i + \mathbf{E}_i + \mathbf{G}_i). \tag{B.1}$$

The center of mass of the tetrahedron is

$$\mathbf{r}_i = \frac{1}{4}(\mathbf{E}_i + \mathbf{F}_i + \mathbf{G}_i). \tag{B.2}$$

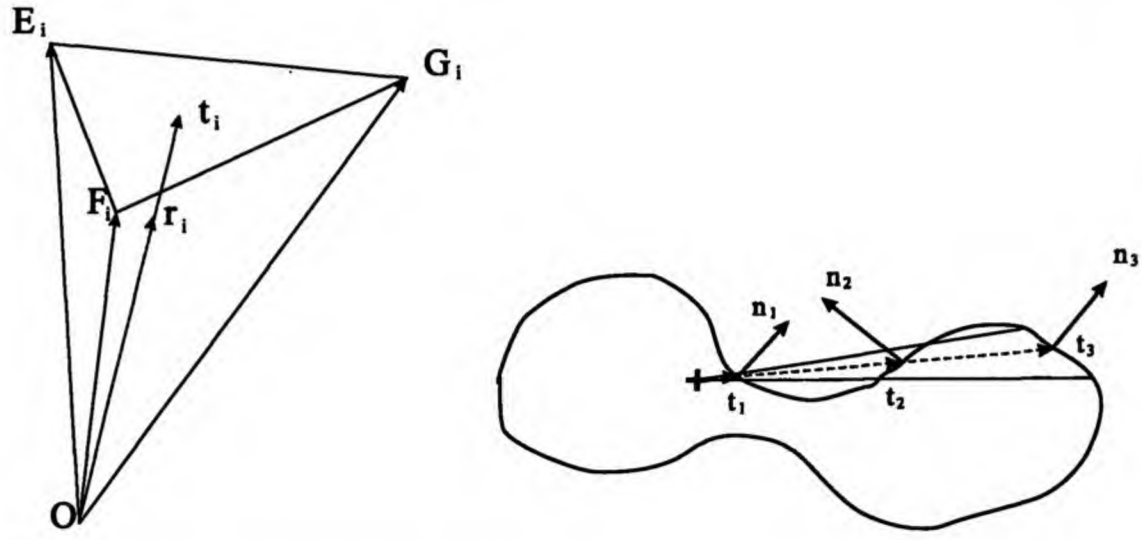

Figure B.1: Left: The tetrahedron with the position vectors $\mathbf{E}_i$, $\mathbf{F}_i$, $\mathbf{G}_i$ of the vertices, vector pointing to the center of surface facet $\mathbf{t}_i$ and the center of mass $\mathbf{r}_i$. Right: a body which is non-convex with respect to the center of mass (denoted by the cross). This plot illustrates how the sign of $\mathbf{n}_i \cdot \mathbf{t}_i$ depends on the number of intersections of $\mathbf{t}_i$ with the surface (if the number is odd, the dot product is negative).

Then we determine the number of intersections[1] of the line $\mathbf{0} - \mathbf{t}_i$ with the surface. We denote this number as ν_i. In the case of a body convex with respect to the origin, $\nu_i = 0$.

The outer normal to the triangular facet is given by

$$\mathbf{n}_i = \frac{1}{2}(\mathbf{F}_i - \mathbf{E}_i) \times (\mathbf{G}_i - \mathbf{E}_i) \tag{B.3}$$

and $\mathbf{n}_i \cdot \mathbf{t}_i > 0$ must be fulfilled if ν_i is even while $\mathbf{n}_i \cdot \mathbf{t}_i < 0$ if ν_i is odd (see Figure B.1 right). The area of the facet can be expressed as $S_i = |\mathbf{n}_i|$ and the whole area of a body is

$$S = \sum_i S_i = \sum_i |\mathbf{n}_i| \tag{B.4}$$

The volume of the tetrahedron is given by

$$V_i = \frac{1}{3}(-1)^{\nu_i} |\mathbf{E}_i \cdot \mathbf{n}_i|. \tag{B.5}$$

Note that for ν_i odd the volume V_i is negative. The whole volume can be expressed as

$$V = \sum_i V_i, \tag{B.6}$$

[1] In other words, we have to find a number of facets $j \neq i$ which are intersected by the vector $\mathbf{t}_i$. This means we solve the equation

$$\mathbf{E}_j\, a + \mathbf{F}_j\, b + \mathbf{G}_j\, c = \mathbf{t}_i,$$

where the vectors $\mathbf{E}_j$, $\mathbf{F}_j$, $\mathbf{G}_j$ describe the j–th facet. If $\min(a, b, c) > 0$, then the vector $\mathbf{t}_i$ intersects the facet j.

where the summation is made over all the tetrahedron volumes (both positive and negative). Assuming a uniform density ρ, the center of mass of the whole polyhedron is given by

$$\mathbf{r} = \frac{1}{V}\sum_i V_i \mathbf{r}_i. \tag{B.7}$$

Finally, the tensor of inertia of the tetrahedron can be expressed in cartesian coordinates as (according to [Dobrovolskis, 1996]):

$$I_{xx} = P_{yy} + P_{zz}, \qquad I_{yz} = -P_{yz} \tag{B.8}$$
$$I_{yy} = P_{zz} + P_{xx}, \qquad I_{xz} = -P_{xz} \tag{B.9}$$
$$I_{zz} = P_{xx} + P_{yy}, \qquad I_{xy} = -P_{xy}, \tag{B.10}$$

where

$$P_{jk} = \frac{\rho V}{20}(2E_jE_k + 2F_jF_k + 2G_jG_k + E_jF_k + E_kF_j + E_jG_k + E_kG_j + F_jG_k + F_kG_j). \tag{B.11}$$

For simplicity we do not write the index i of the tetrahedron. The inertia tensor of the whole polyhedron is given by

$$\mathbf{I} = \sum_i \mathbf{I}_i. \tag{B.12}$$

After the translation of the coordinate system into the center of mass ($\mathbf{r} = 0$), we can proceed with the determination of the principal moments of inertia $A \leq B \leq C$ and the corresponding eigenvectors according to [Dobrovolskis, 1996].

B.2 Insolation and shadowing

Next we shall describe a procedure we use to determine the insolation $\mathcal{E}$ (W/m^2) of a facet. There are three possible cases:

Facet pointing away from the Sun. The facet i is in the shadow and the insolation is zero when the outer normal $\mathbf{n}_i$ and the direction to the Sun $\mathbf{s}$ fulfills the relation

$$\mathbf{s} \cdot \mathbf{n}_i < 0. \tag{B.13}$$

Sunward facet shadowed by another facet. The facet i is pointing towards the Sun, if

$$\mathbf{s} \cdot \mathbf{n}_i > 0. \tag{B.14}$$

However, even this sunward facet can be shadowed in case of non-convex shape of polyhedron. We must test every surface facet $j \neq i$ whether it casts shadow on the facet[2] i: The facet i is shadowed by another facet j if the ray[3], defined by the center of facet $\mathbf{t}_i$ and the vector $\mathbf{s}$, lies inside a tetrahedron defined by vertices $\mathbf{r}_i$, $\mathbf{E}_j - \mathbf{r}_i$, $\mathbf{F}_j - \mathbf{r}_i$ and $\mathbf{G}_j - \mathbf{r}_i$. This means that we solve the set of 3 linear equations

[2]It is necessary for sunward facets only.

[3]This ray can be described as $\mathbf{r}_i + q\mathbf{s}$, where q is positive.

$$(\mathbf{E}_j - \mathbf{r}_i)\, a + (\mathbf{F}_j - \mathbf{r}_i)\, b + (\mathbf{G}_j - \mathbf{r}_i)\, c = \mathbf{s}, \tag{B.15}$$

for three unknowns a, b, c. The facet i is shadowed by the facet j if

$$\min(a, b, c) > 0. \tag{B.16}$$

Again, the insolation of this facet is $\mathcal{E} = 0$.

Non-shadowed sunward facet. If the facet i obeys (B.14) and moreover there is no facet $j \neq i$ that obeys (B.15) with (B.16), we can say the facet i is insolated and its insolation is

$$\mathcal{E} = \Phi\, \mathbf{s} \cdot \mathbf{n}_i, \tag{B.17}$$

where Φ is the solar flux.

This procedure is very CPU time consuming so we had to accelerate it somehow. We describe vector $\mathbf{s}$ by spherical coordinates φ and ϑ, conected with body-frame. For any $\varphi = 0 \ldots 360°$ and $\vartheta = +90 \cdots -90$ (with a 1° step) we determined all sunward facets which are self-shadowed and stored their indices into a file.

The computation of the insolation of a polyhedron along its orbit about the Sun is made in several steps. At first we determine the position of the Sun $\mathbf{s}$ with respect to the body frame. Then the insolation (B.17) is calculated for sunward facets (B.14). Finally, the insolation of shadowed sunward facets corresponding to the vector $\mathbf{s}$ (described by φ, ϑ), whose indices has been stored in the file, is set to zero.

Appendix C

Gaussian random spheres

Due to a limited number of precisely determined shapes of asteroids we turn our attention to artificially generated shapes by the technique of Muinonen (e.g., [Muinonen, 1996], [Muinonen, 1998], [Muinonen and Lagerros, 1998]). These shapes are called Gaussian random spheres. The radius of such a body in the direction given by spherical angles θ and ϕ may be expressed as

$$r(\theta,\phi) = \frac{a}{\sqrt{1+\sigma^2}} \exp\left[s\left(\theta,\phi\right)\right] , \tag{C.1}$$

where a is the scaling factor and σ is the variance of r. The "logradius" $s(\theta,\phi)$ is given by a spherical harmonic development

$$s(\theta,\phi) = \sum_{\ell=0}^{\infty} \sum_{m=0}^{\ell} P_\ell^m(\cos\theta) \left(a_{\ell m} \cos m\phi + b_{\ell m} \sin m\phi\right) . \tag{C.2}$$

Here the coefficients $a_{\ell m}$ and $b_{\ell m}$ are independent Gaussian random variables with zero mean, and variance reading

$$\beta_{\ell m}^2 = (2-\delta_{\ell 0}) \frac{(\ell-m)!}{(\ell+m)!} c_\ell \beta^2 , \tag{C.3}$$

where $\beta^2 = \ln(1+\sigma^2)$ and $\delta_{\ell 0}$ is the Kronecker symbol. The model then depends on the scaling factor a, the variance σ of the distribution of surface heights, and a set of parameters c_ℓ from Equation (C.3).

[Muinonen and Lagerros, 1998] analysed accurately known shapes of 14 asteroids and they obtained best estimates of the parameters σ and c_ℓ for their sample of asteroids. These parameters, determined for 7 smallest and 7 largest bodies, slightly differ. The most useful data for our purpose are those for smallest bodies[1]. The standard deviation σ of radius is then 0.245 and the coefficients c_ℓ are listed in Table C.1.

We used these parameters to generate a set of 1000 Gaussian random spheres. These bodies are scaled to have the same volume as the sphere with radius 10 km. Figure C.1 shows the distribution of the dynamical ellipticity $(C-(A-B)/2)/C$ and triaxiality parameter A/B for the set of 1000 Gaussian random spheres. The quantities $A < B < C$ denote the principal moments of inertia. Diamond symbols in the figure denote the values for several real objects (not used in Muinonen and Lagerros' analysis).

[1]Namely: (4769) Castalia, (4179) Toutatis, (1620) Geographos, (915) Gaspra, Phobos, Deimos, (243) Ida.

ℓ	c_ℓ	ℓ	c_ℓ
0	9.5431×10^{-3}	6	6.7379×10^{-3}
1	2.1972×10^{-1}	7	2.6938×10^{-3}
2	6.2665×10^{-1}	8	2.8687×10^{-3}
3	8.3670×10^{-2}	9	5.6931×10^{-4}
4	3.1648×10^{-2}	10	3.9023×10^{-4}
5	1.5512×10^{-2}		

Table C.1: The coefficients c_ℓ from Equation (C.3). Adapted from table 5, column "Small" in [Muinonen and Lagerros, 1998], computed for seven smallest bodies under study (see the text).

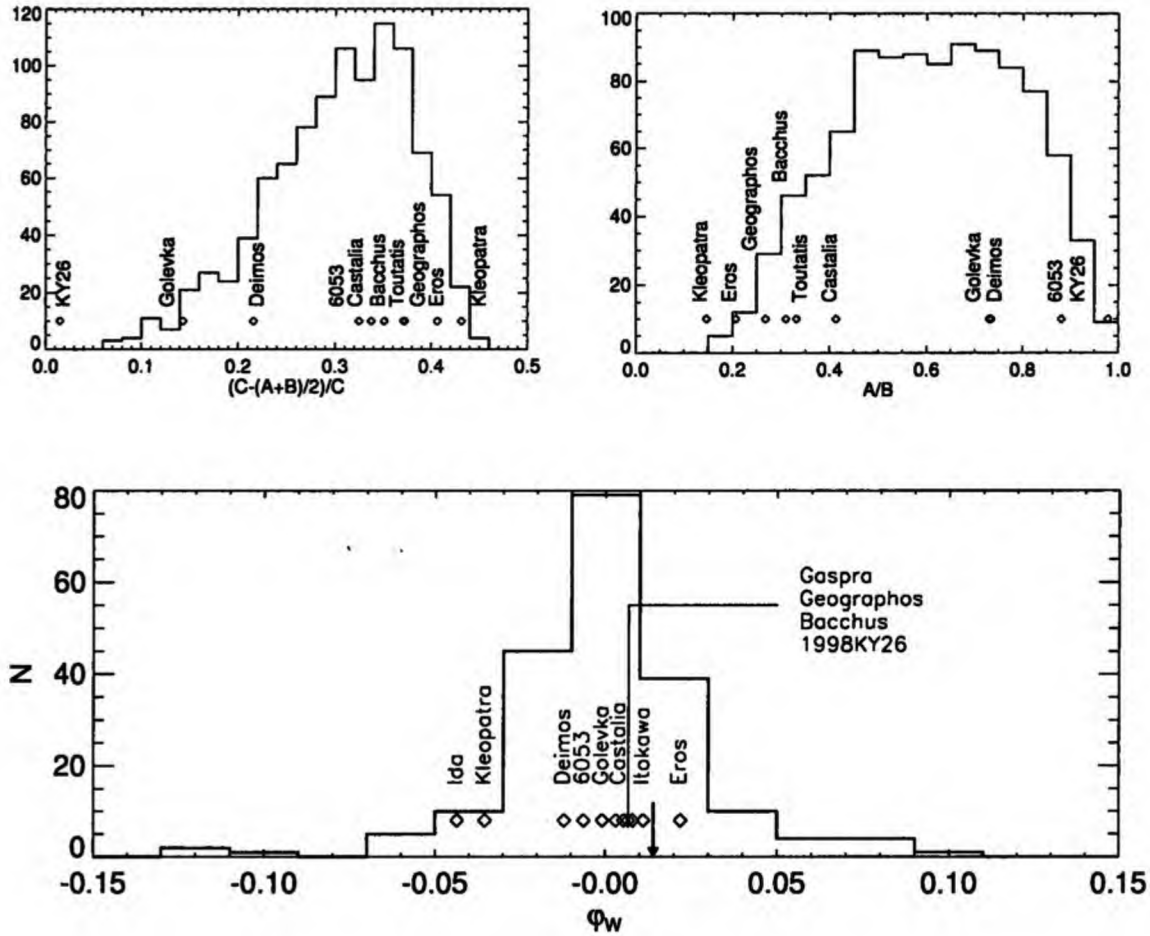

Figure C.1: Shape characteristics for 1000 artificially generated Gaussian random spheres. Upper left (a): Distribution of the dynamical elipticity $(C-(A+B)/2)/C$. Upper right (b): triaxiality parameter A/B. Lower figure (c): the windmill factor φ_w. The arrow denotes the median of absolute values, which is 0.014, and the diamond symbols indicate the values of these parameters calculated for real objects.

Figure C.1c depicts the distribution of the absolute value of windmill factor (φ_w) defined by Equation 3.11 within the set of 1000 Gaussian random spheres. (The windmill factor corresponds to the strength of YORP effect and depends on the shape of body.) There are also values for several real asteroids in the plot. The median of windmill factor is the value 0.014. The shapes of 200 Gaussian random spheres can be seen in Figures C.2 - C.7.

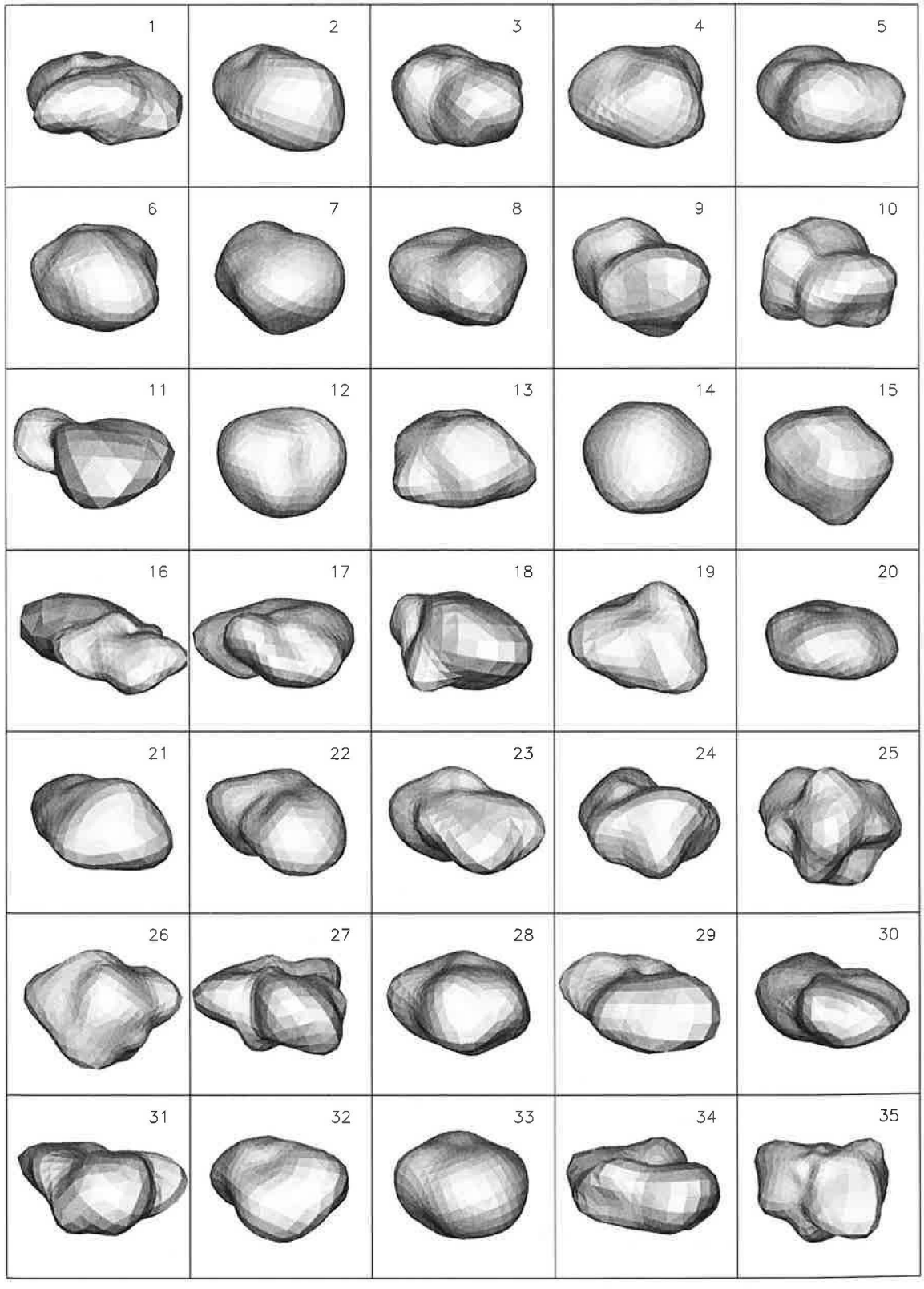

Figure C.2: Gaussian random spheres no. 1 ... 35

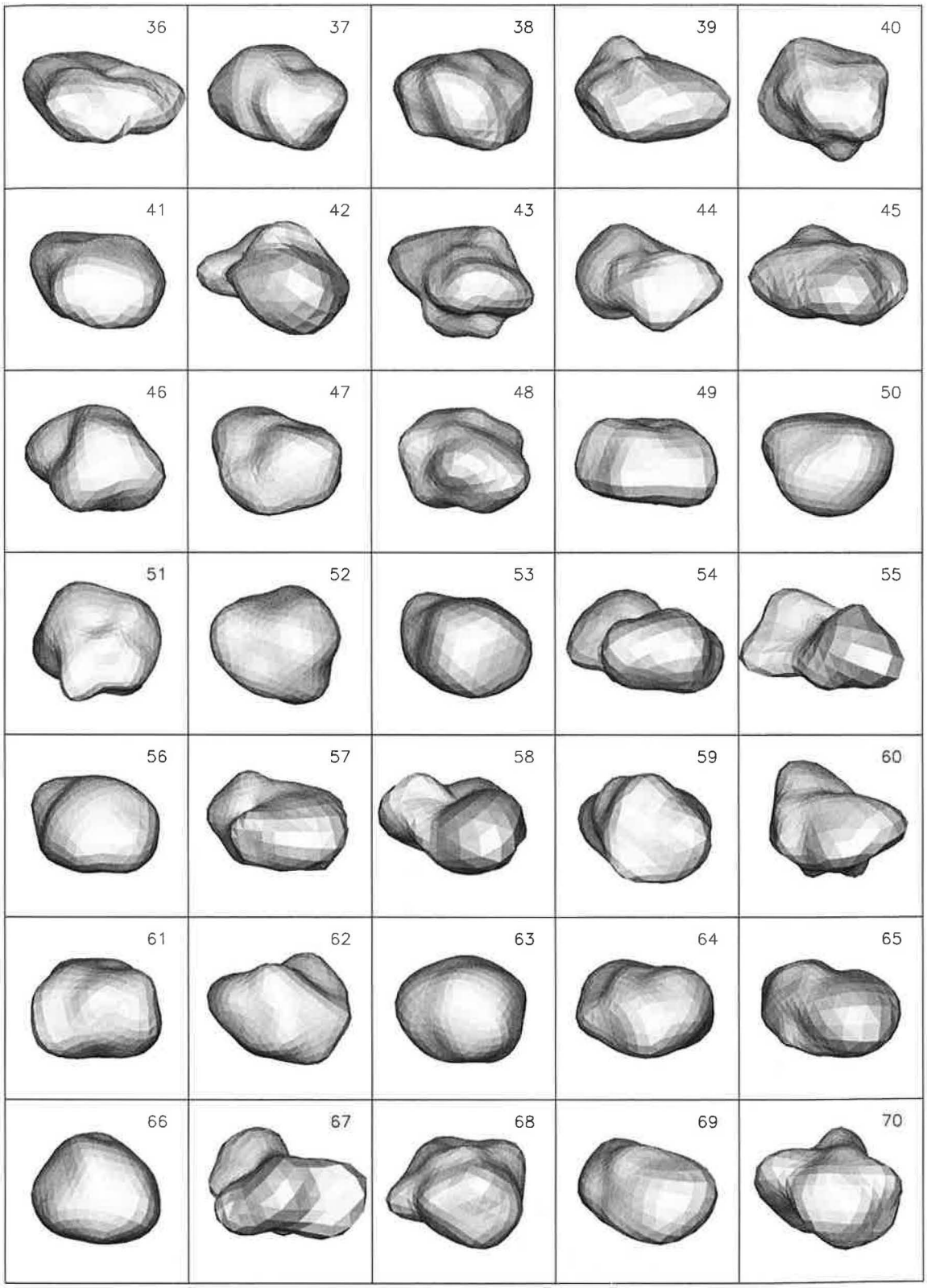

Figure C.3: Gaussian random spheres no. 36 ... 70

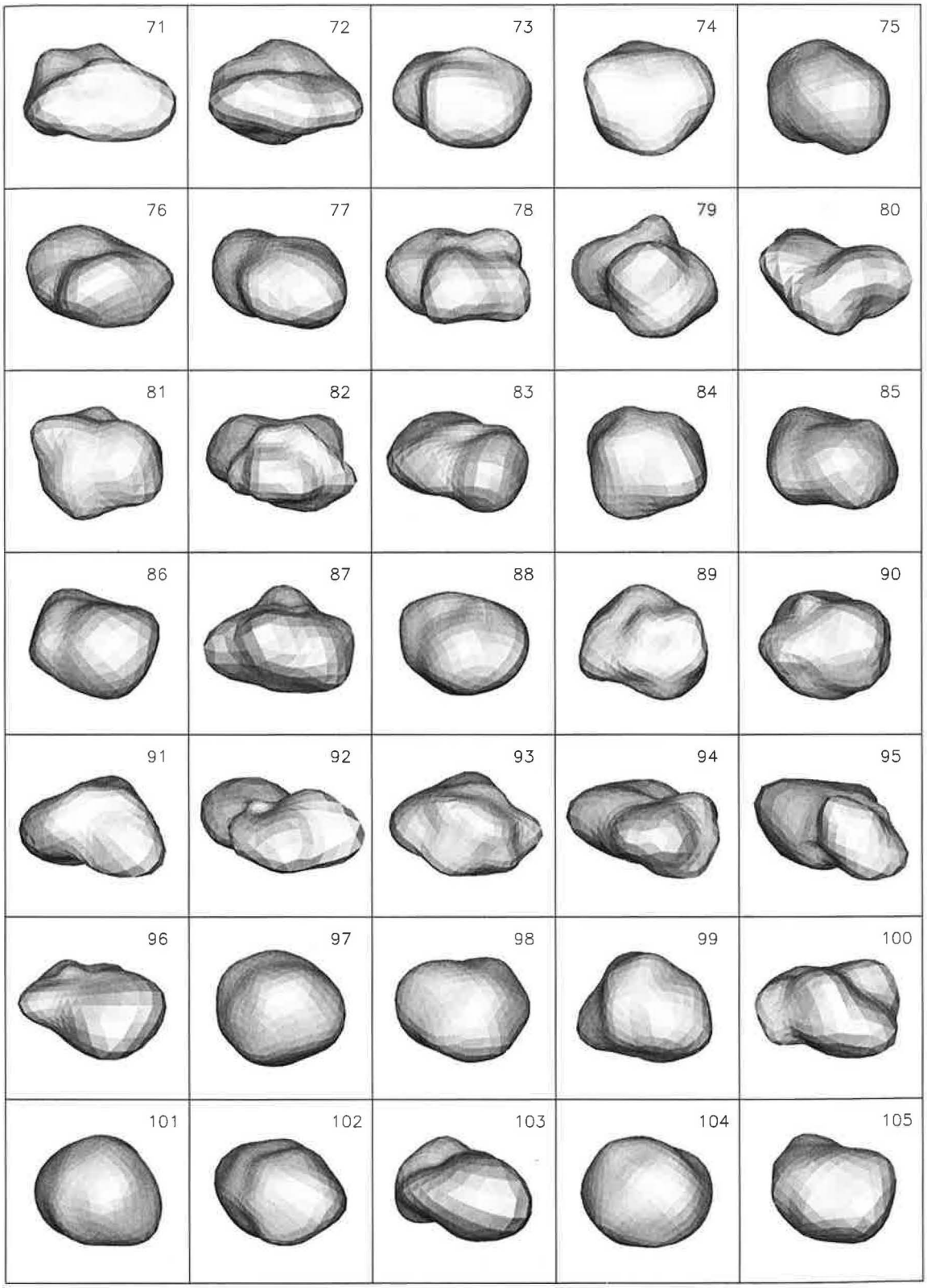

Figure C.4: Gaussian random spheres no. 71 ... 105

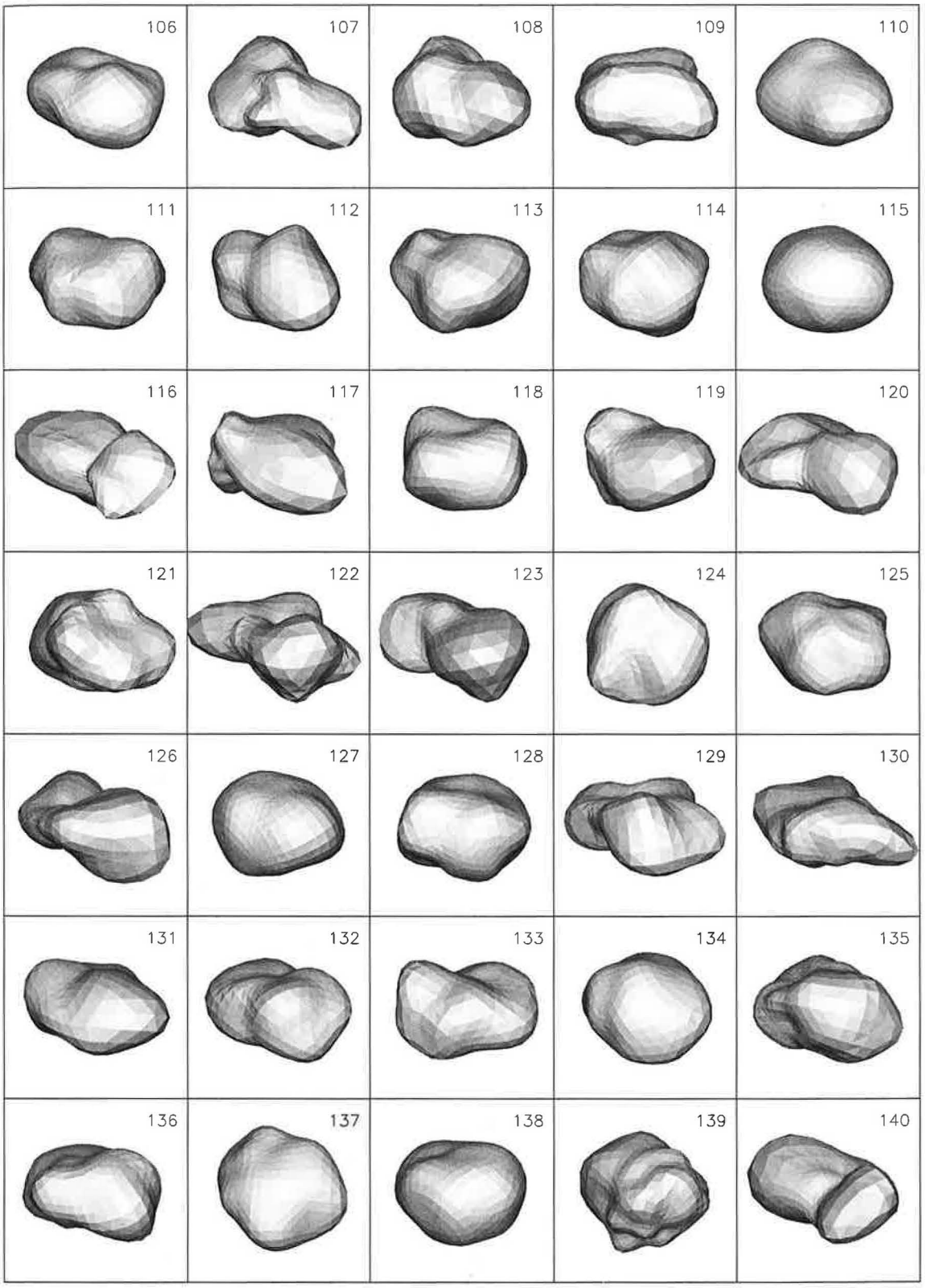

Figure C.5: Gaussian random spheres no. 106 ... 140

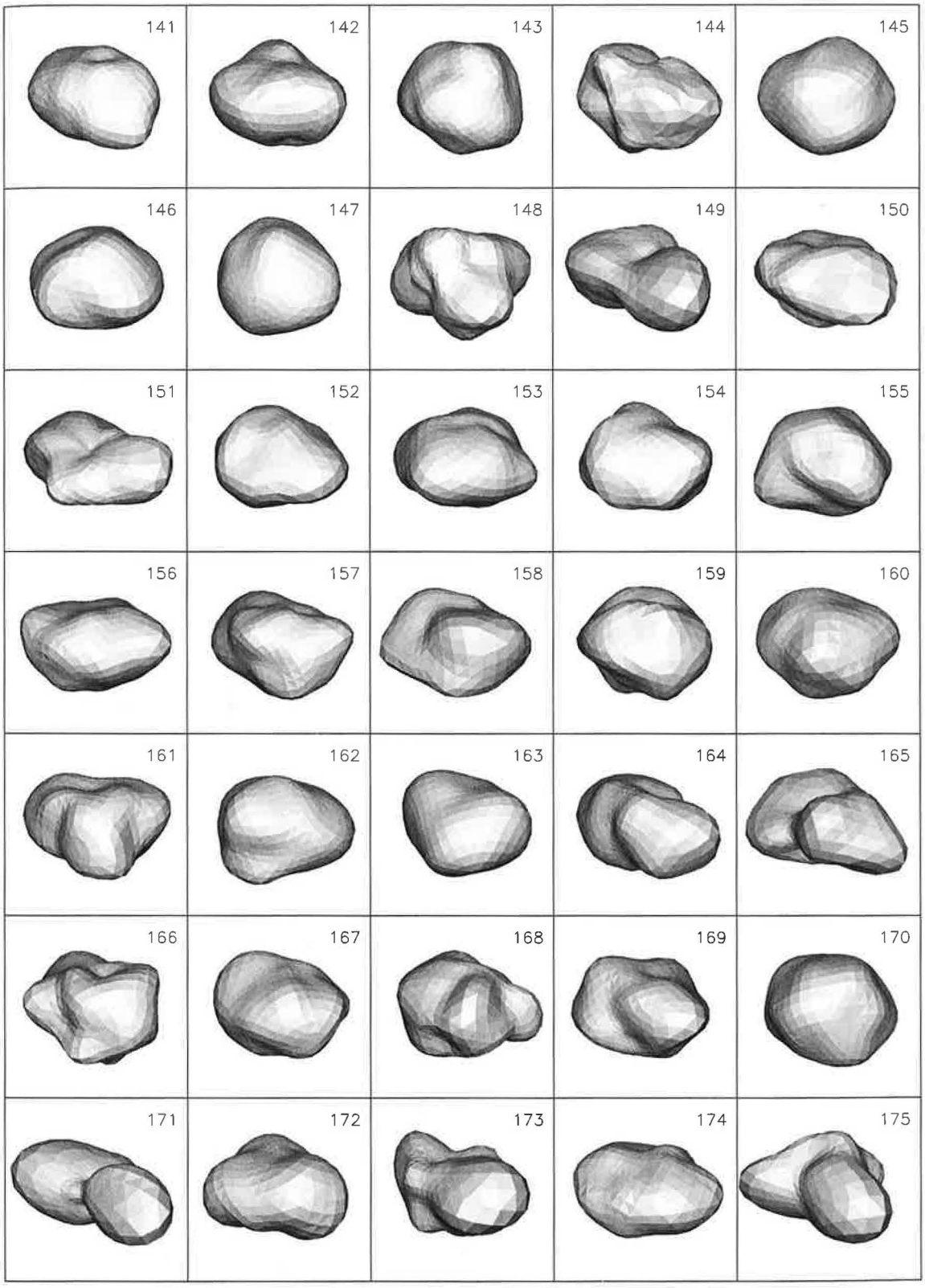

Figure C.6: Gaussian random spheres no. 141 ... 175

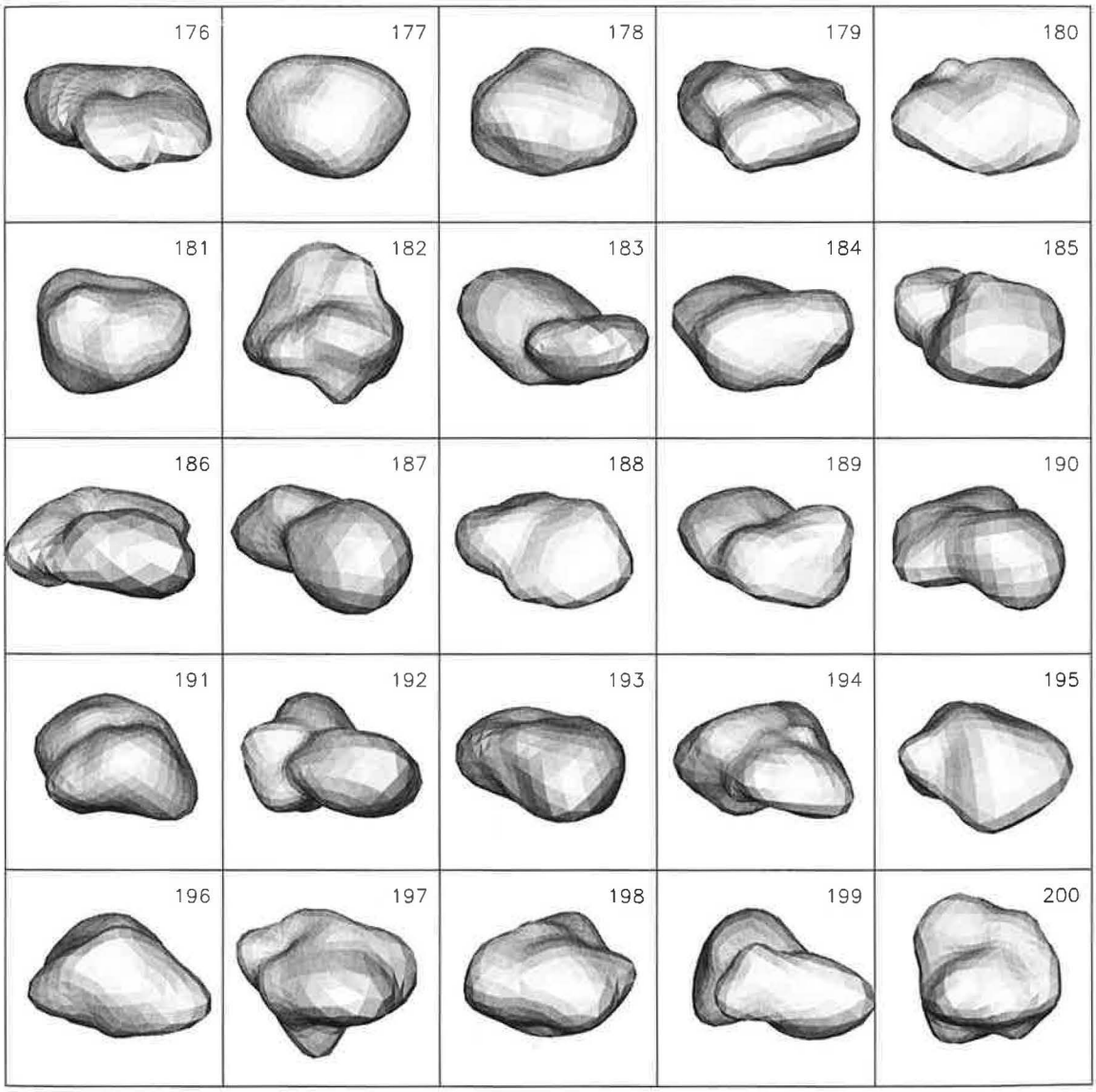

Figure C.7: Gaussian random spheres no. 176 ... 200

Appendix D

Shape models of real asteroids

Here we shall to present the shape models of asteroids that were used for our study of the YORP and Yarkovsky effect. All the bodies are represented by polyhedrons with typically several thousands of surface triangular facets. Their axes coincide with the main axis of inertia tensor and the origin is considered in the center of mass (assuming an uniform density). The shape models of the following asteroids are available from `http://www.psi.edu/pds/asteroid/`: (433) Eros, (1620) Geographos, (6489) Golevka, (25143) Itokawa, (243) Ida, 1998KY26, (4197) Toutatis.

For each asteroid there is a file with the following format:

```
v   x1 y1 z1
v   x2 y2 z2
v   x3 y3 z3
...
f   i1 j1 k1
f   i2 j2 k2
f   i3 j3 k3
...
```

The first part of the file represents a vertex table, each row starts with the letter `v` and contains x, y, z coordinates of one vertex. The second part is a facet table, containing the linkages the vertices into facets. Each triangular facet begins with the letter `f`. Note the relationship between the number of facets n_f and the number of vertices n_v is $n_f = 2\,n_v - 4$ for the body consisting of triangular facets. All important quantities, like volume, inertia tensor, area of facets, etc., were determined by the technique described in Appendix B.

For all the bodies, which were used in our research of the Yarkovsky/YORP effect, we computed the parameter φ_w, describing the windmill asymmetry, see (Equation 3.11). (The windmill factor is dimensionalless quantity which depends only on the shape of the body and corresponds to the strength and "sense" of YORP effect.) The values for particular bodies can be found in Table D.1. The shape models can be seen in Figures D.2 – D.9.

Golevka	-0.0009	6053	-0.0064	Deimos	-0.0121
Castalia	0.0031	Bacchus	0.0067	Eros	0.0219
Gaspra	0.0054	1998KY26	0.0080	Kleopatra	-0.0354
Geographos	0.0054	Itokawa	0.0111	Ida	-0.0436

Table D.1: Windmill factors φ_w for 11 asteroids and Deimos.

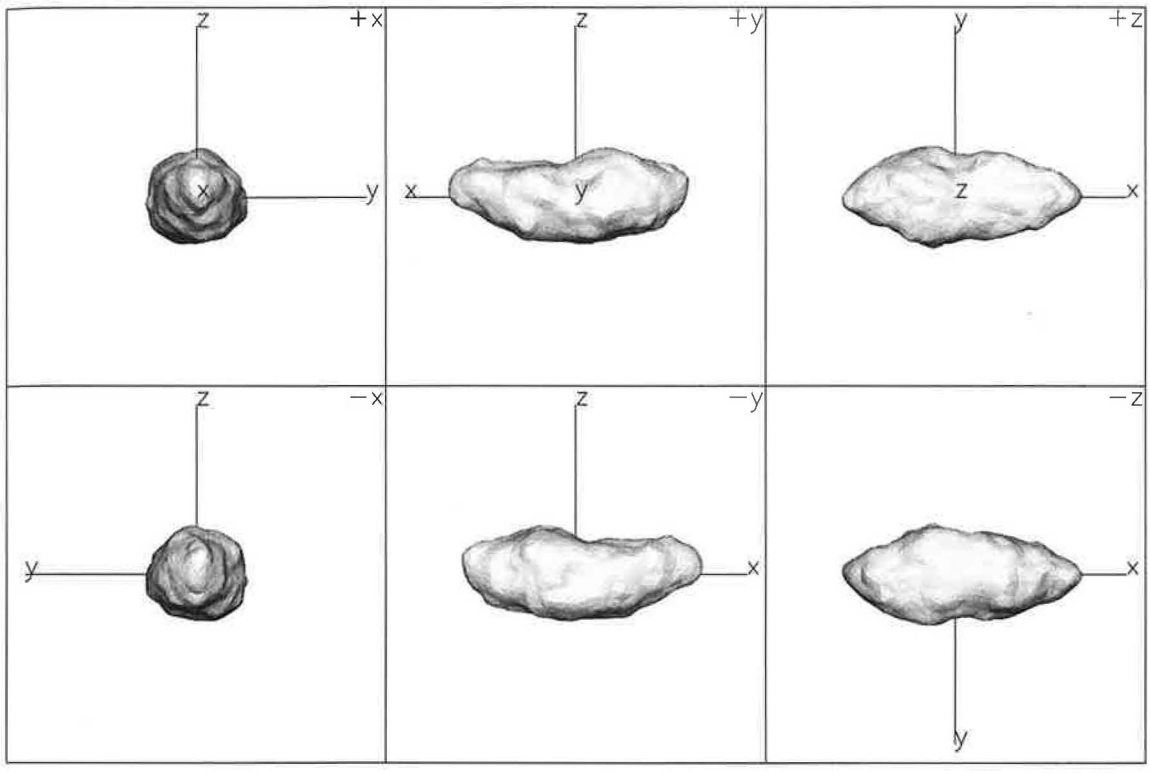

Figure D.1: The shape model of (1620) Geographos based on radar and optical observations. Dimension of each box is 8000 m. ([Hudson and Ostro, 1999]).

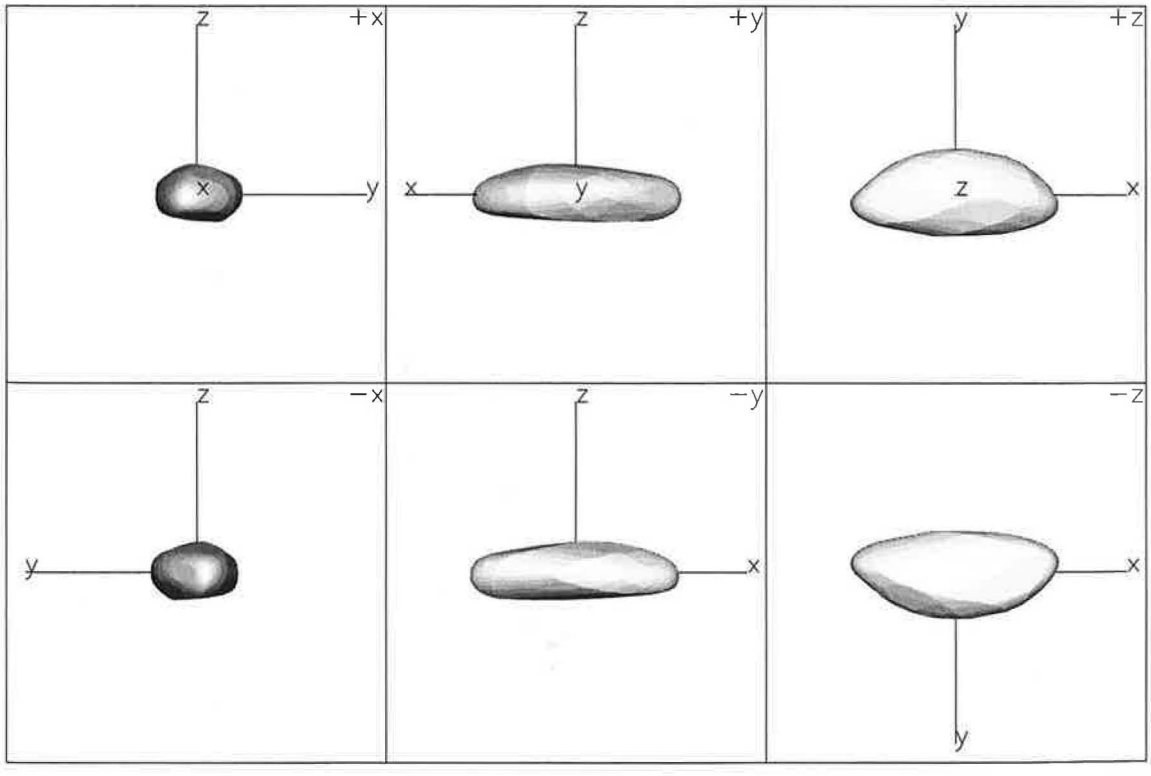

Figure D.2: Another shape model of (1620) Geographos determined by the lightcurve inversion method. Dimension of each box is 8000 m. (J. Ďurech, personal communication).

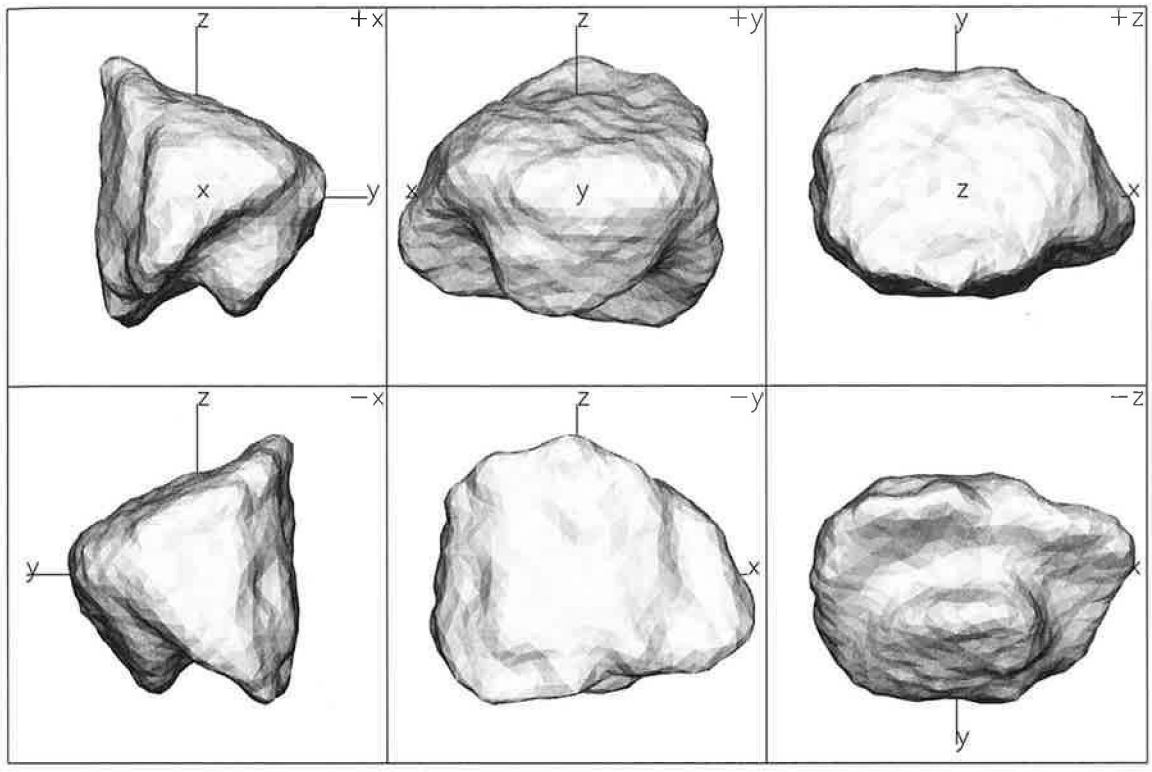

Figure D.3: The 4092-facets model of (6489) Golevka. The dimension of each box is 800 m. ([Hudson et al., 2000])

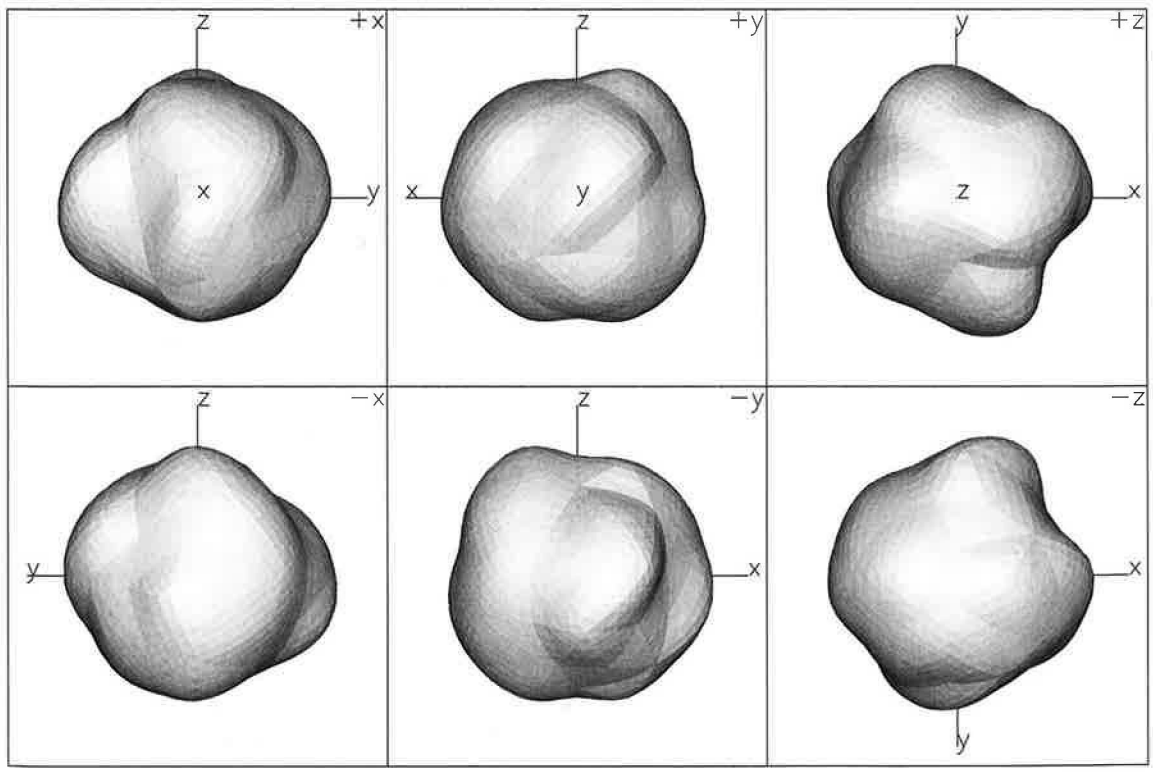

Figure D.4: The 4092-facets model of 1998 KY26. The dimension of each box is 30 m. ([Ostro et al., 1999b])

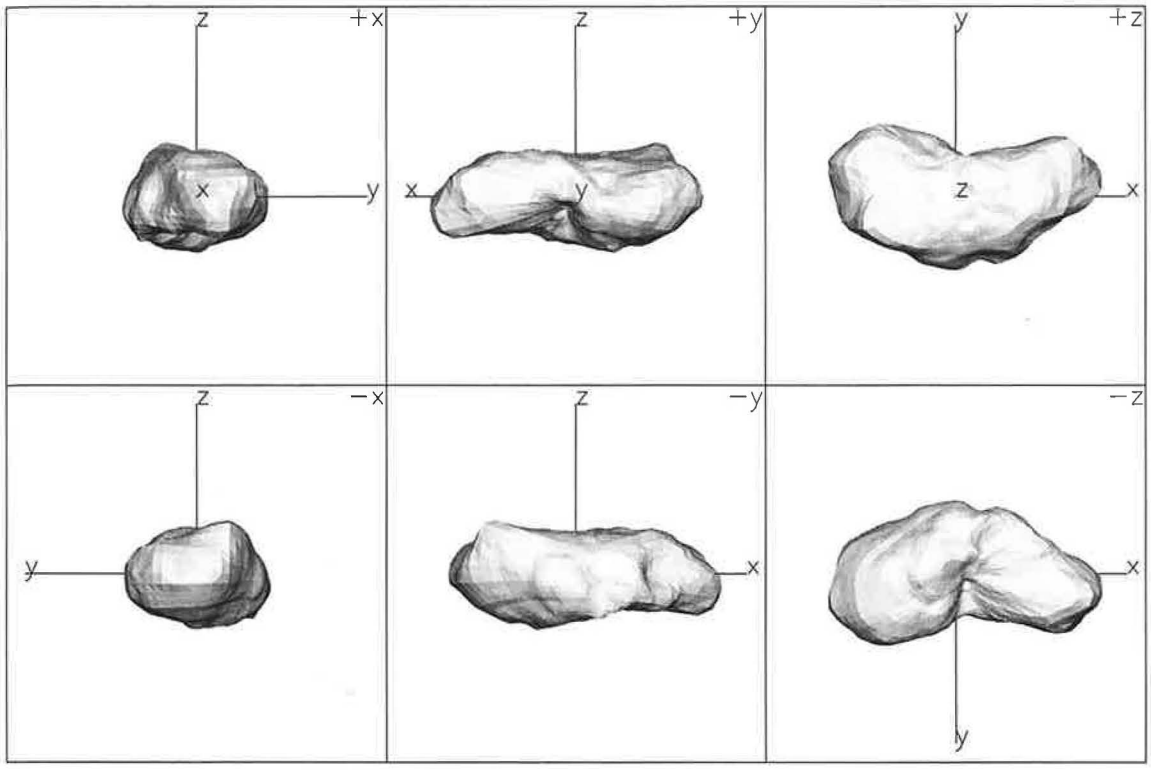

Figure D.5: The model of (243) Ida composed from 4036 surface triangular facets. The dimension of each box is 40 km. ([Thomas et al., 1996])

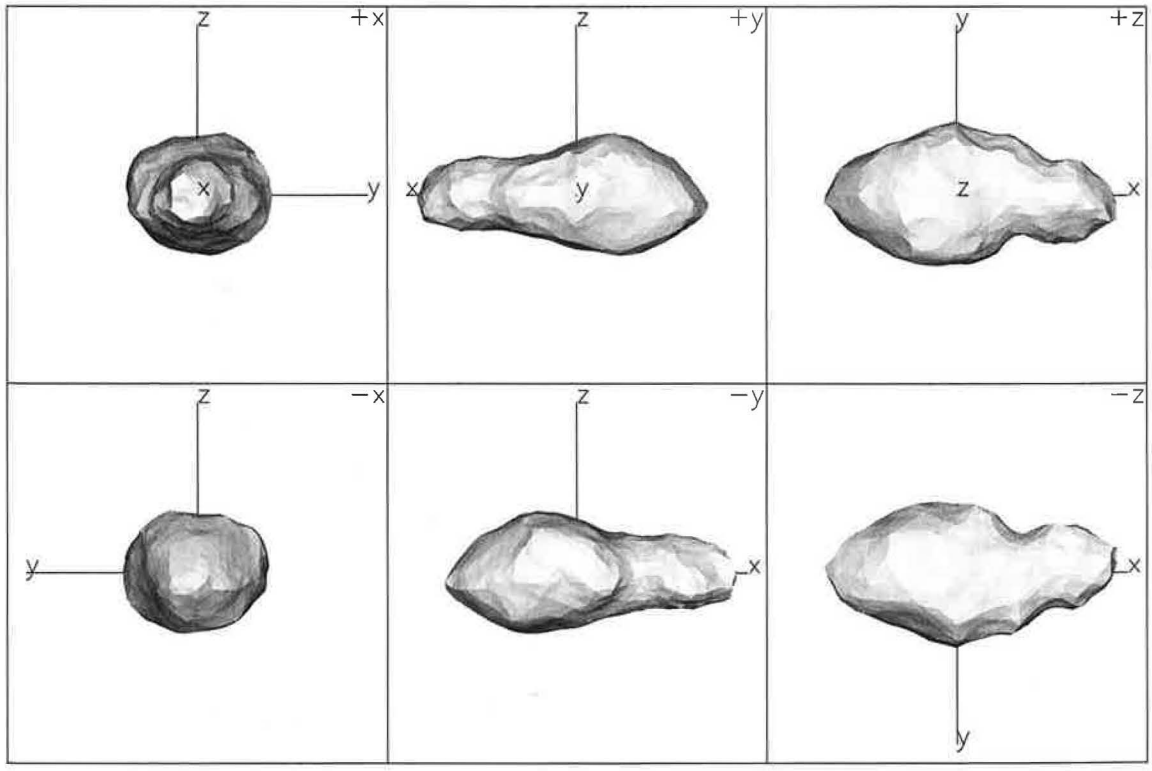

Figure D.6: The 12796-facet model of the asteroid (4179) Toutatis. The dimension of each box is 6 km. ([Hudson et al., 2003])

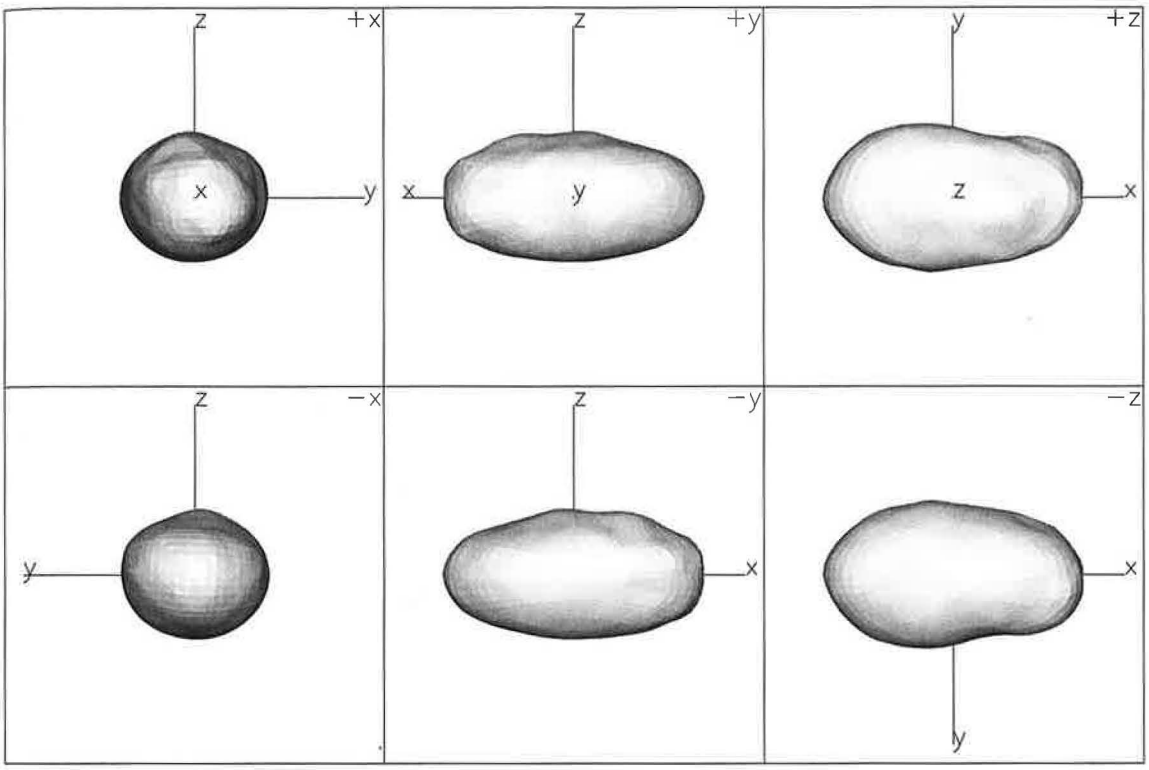

Figure D.7: The model of (25143) Itokawa, derived by radar observations [Ostro et al., 2004]. The dimension of each box is 800 m.

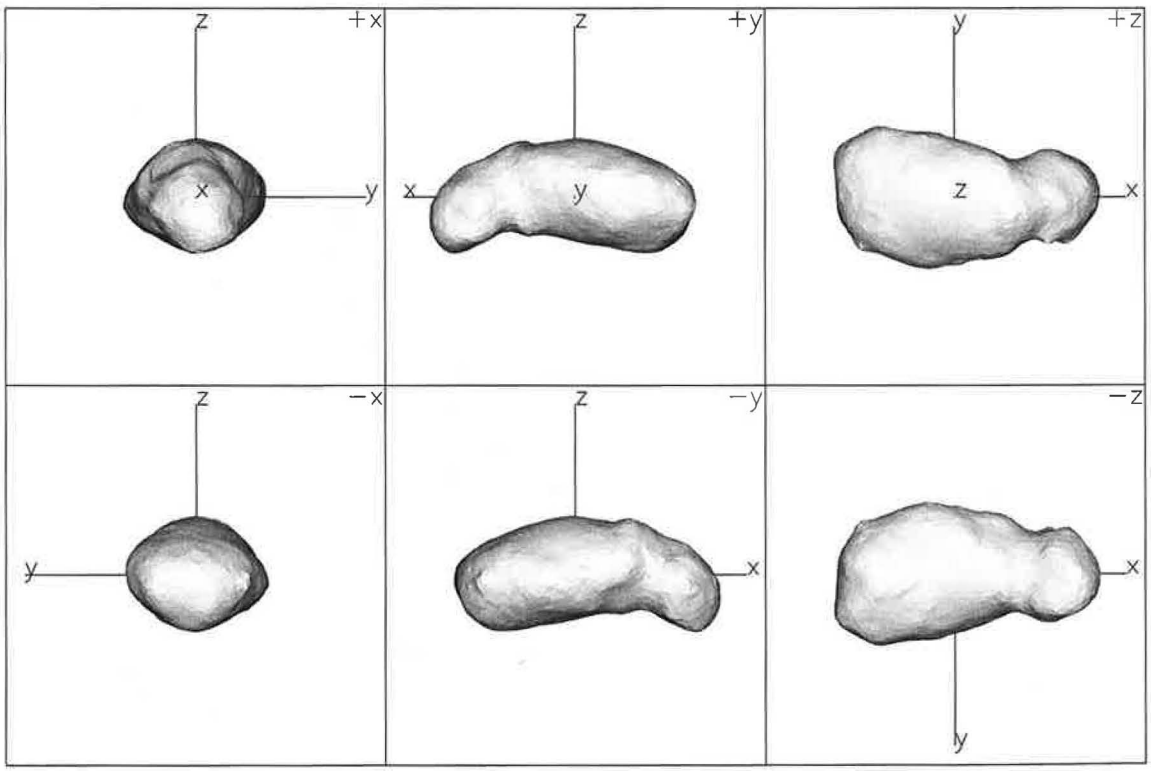

Figure D.8: The model of (25143) Itokawa derived from measurements of the Hayabusa mission (e.g. [Demura et al., 2006], [Gaskell et al., 2006]).

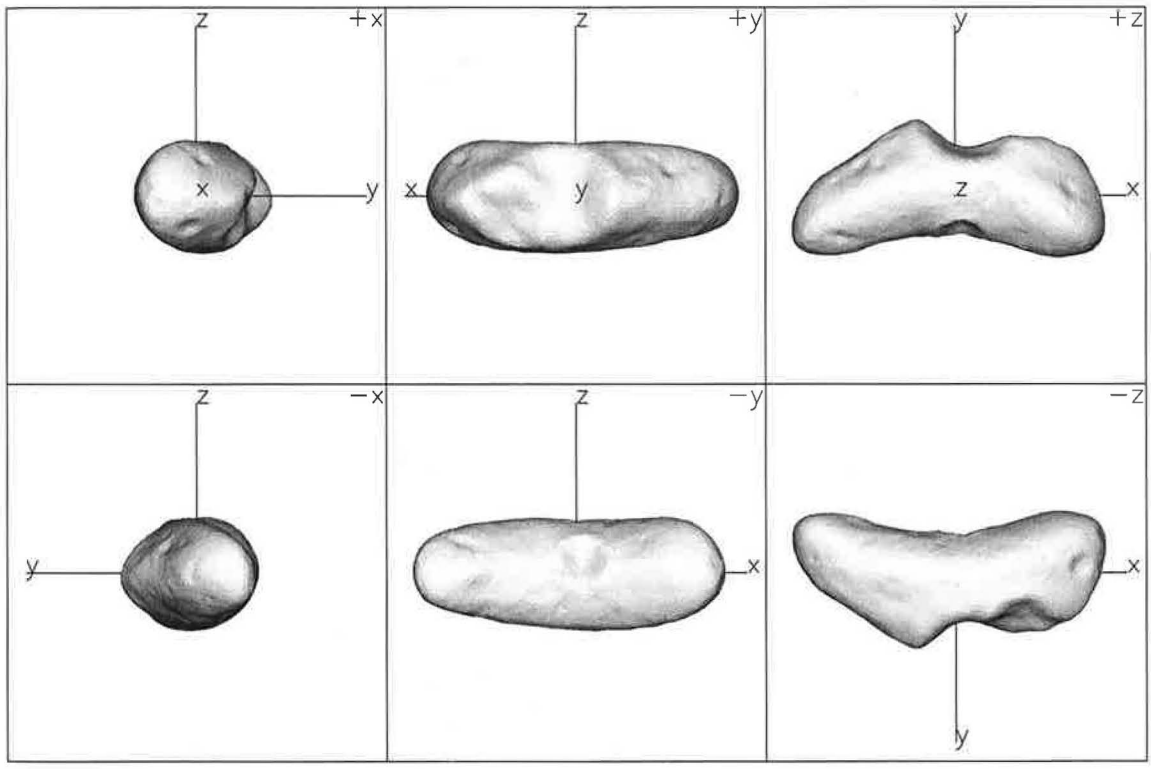

Figure D.9: The 7790-facets model of (433) Eros. The same model with reduced number of facets (1708 facets) was used for the study of the K influence on the YORP effect. The dimension of each box is 40 km. ([Miller et al., 2002])

Appendix E

Publications

We list recorded independent citations below each publication.

Refereed papers

- Vokrouhlický, D. and **Čapek, D.** (2002). YORP-Induced Long-Term Evolution of the Spin State of Small Asteroids and Meteoroids: Rubincam's Approximation. *Icarus*, **159**, 449-467.

  1. J.N. Spitale and R. Greenberg, Numerical evaluation of the general Yarkovsky effect: Effects on eccentricity, inclination and longitude of periapse, *Icarus*, **156**, 211, 2002.
  2. D.P. O'Brien and R. Greenberg, Steady-state size distributions for collisional populations: analytical solution with size-dependent strength, *Icarus* **164**, 334, 2003.
  3. M. Kaasalainen et al., Photometry and models of 8 near-Earth asteroids, *Icarus* **167**, 178, 2004.
  4. H. Hsieh, D.C. Jewitt and Y.R. Fernandez, The strange case of 133P/Elst-Pizarro: A comet among the asteroids, *Astron. J.* **127**, 2997, 2004.
  5. P. Pravec et al., Tumbling asteroids, *Icarus* **173**, 108, 2005.
  6. D. Nesvorný and W.F. Bottke, Direct detection of the Yarkovsky effect for main-belt asteroids, *Icarus* **170**, 324, 2004.
  7. D.P. O'Brien, *The Collisional and Dynamical Evolution of the Main-Belt, NEA, and TNO Populations*, PhD Dissertation, University of Arizona, 2004.
  8. A.W. Harris, YORP alteration of asteroid spins: Why are slow rotators tumbling and not synchronized?, *BAAS* **36**, 1185 (also http://www.aas.org/publications/baas/v36n4/dps2004/137.htm).
  9. D.P. O'Brien and R. Greenberg, Collisional and dynamical evolution of the main-belt and NEA size distributions, *Icarus* **178**, 179, 2005.
  10. J. Ďurech, 433 Eros – comparison of lightcurve extrema from 1901-1931 with the actual rotation state, *Astron. Astrophys.* **431**, 381, 2005.
  11. M. Ćuk and J.A. Burns, Effects of thermal radiation on the dynamics of binary NEAs, *Icarus* **176**, 418, 2005.
  12. D.C. Richardson and K.J. Walsh, Binary minor planets, *Ann. Rev. Earth Planet. Sci.* **34**, 47, 2006.
  13. M. Makuch, N.V. Brilliantov, M. Sremčević, F. Spahn and A.V. Krivov, Stochastic circumplanetary dynamics of rotating non-spherical dust particles, *Planet. Sp. Sci.* **54**, 855, 2006.
  14. D.J. Scheeres, The dynamical evolution of uniformly rotating asteroids subject to YORP, *Icarus*, in press, 2007.

15. E. Mysen, Canonical rotation variables and non-Hamiltonian forces: solar radiation pressure effects on asteroid rotation, *Mon. Not. R. Astr. Soc.* **372**, 1345, 2006.
16. P. Jenniskens, Meteor Showers and their Parent Comets (Cambridge, Cambridge University Press, 2006) p. 536.
17. M. Delbó, A. dell'Oro, A.W. Harris, S. Mottola and M. Mueller, Thermal inertia of near-Earth asteroids and implications for the magnitude of the Yarkovsky effect, *Icarus*, in press, 2007.
18. V. Carruba, F. Roig, T.A. Michtchenko, S. Ferraz-Mello and D. Nesvorný, Modeling close encounters with massive asteroids: a Markovian approach, *Astron. Astrophys.*, in press, 2007.
19. D.J. Scheeres, Rotational fission of contact binary asteroids, *Icarus* **188**, 430, 2007.
20. M. Kaasalainen, J. Ďurech, B.D. Warner, Y.N. Krugly and N.M. Gaftonyuk, Acceleration of the rotation rate of asteroid 1862 Apollo by radiation torques, *Nature* **446**, 420, 2007.
21. M. Ćuk, Formation and destruction of small binary asteroids, *Astrophys. J.* **659**, L57, 2007.
22. V. Carruba and T.A. Michtchenko, A frequency approach to asteroid families' identification, *Astron. Astrophys.*, in press, 2007.

- Chesley, S. R., Ostro, S. J., Vokrouhlický, D., **Čapek, D.**, Giorgini, J. D., Nolan, M. C., Margot, J.-L., Hine, A. A., Benner, L. A. M., and Chamberlin, A. B. (2003). Direct Detection of the Yarkovsky Effect by Radar Ranging to Asteroid 6489 Golevka. *Science*, **302**, 1739–1742.

1. E.S. Reich, Sunlight's gentle nudge on asteroids detected, http://www.newscientist.com/news/.
2. S. Ives, Will discovery help repel asteroids headed for Earth?, Science and Technology section of *NationalGeographic.Com*, December 11, 2003.
   (also http://news.nationalgeographic.com/news/science.html)
3. S. Hurtley and P. Szuromi, A nudge from Yarkovsky, *Science* **302**, 1621, 2003.
4. D. Morrison, Precision NEO Orbits and the Yarkovsky Effect, http://nai.arc.nasa.gov/impact/news_detail.cfm?ID= 132
5. D. Tytell, The Asteroid and the Pea, *Sky & Telescope*
   (also http://skyandtelescope.com/news/article_1126_1.asp)
6. B. Dumé, Radar reveals asteroid force, *Physics Web*, http://physicsweb.org/article/news/7/12/3
7. D. Tytell, Sunlight makes asteroids spin in harmony, *Sky & Telescope*, p. 26, January 2004.
8. C. Schreiber, Kann der Yarkovsky-Effekt die Asteroiden neu gruppieren?, *Telepolis*, http://www.heise.de/tp/r4/artikel/16/16261/1.html
9. http://www.masterliness.com/a/Yarkovsky.effect.htm
10. http://www.absoluteastronomy.com/encyclopedia/Y/Ya/Yarkovsky_effect.htm
11. http://www.economicexpert.com/a/Yarkovsky:effect.html
12. *Yarkovsky effect* in Wikipedia http://en.wikipedia.org/wiki/Yarkovsky_effect
13. U. Penco, A. Dell'Oro, P. Paolicchi et al., Yarkovsky depletion and asteroid collisional evolution, *Planet. Sp. Science* **52**, 1087, 2004.
14. R.D. Lorentz and J.N. Spitale, The Yarkovsky effect as a heat engine, *Icarus* **170**, 229, 2004.
15. R. Michelsen, Near-Earth Asteroids from discovery to characterization, *PhD Thesis*, N. Bohr Institute for Astronomy, Physics and Geophysics, University of Copenhagen, 2004.
16. V. Carruba, Dynamics of asteroid families and irregular satellites of jovian planets, *PhD Thesis*, Cornell University, 2004 (http://www.astro.iag.usp.br/~valerio/PUB/thesis.pdf).
17. A. Cellino, A. Dell'Oro and V. Zappalà, Asteroid families: open problems, *Planet. Sp. Sci.* **52**, 1075, 2004.
18. A. Dell'Oro, G. Bigongiari, P. Paolicchi and A. Cellino, Asteroid families: evidence of ageing of the proper elements, *Icarus* **169**, 341, 2004.

19. B.J. Butler, D.B. Campbell, I. de Pater, et al., Solar system science with SKA, *New Astronomy Revs.* **48**, 1511, 2004.

20. A. Lemaitre, Asteroid family classification from very large catalogs, in: *Dynamics of Populations of Planetary Systems*, IAU Colloquium 197, Cambridge University Press, 2005, p. 135.

21. D. Nesvorný, R. Jedicke, R.J. Whiteley and Z. Ivezić, Evidence for asteroids space weathering from the Sloan Digital Sky Survey, *Icarus* **173**, 132, 2005.

22. S.R. Valluri, P. Yu, G.E. Smith, et al., An extension of Newton's apsidal precession theorem, *Mon. Not. R. Astron. Soc.* **358**, 1273, 2005.

23. V. Trimble and M. Aschwanden, Astrophysics in 2004, *Publ. Astron. Soc. Pacific* **117**, 311, 2005.

24. R. Kippenhahn, Der sanfte druck des lichtes, *Sterne und Weltraum*, Sep 2005, p. 46.

25. P. Tanga, Impact of Gaia on dynamics and evolution of the Solar System, in *The Three-Dimensional Universe with Gaia*, C. Turon, K.S. O'Flaherty, M.A.C. Perryman (Eds.), p. 243, 2005.

26. F. Yoshida and T. Nakamura, Size distribution of faint Jovian L4 Trojan asteroids, *Astron. J.* **130**, 2900, 2005.

27. J.R. Gott, Lagrange L-4/L-5 points and the origin of our Moon and Saturn's Moons and rings, *Ann. New York Acad. Sci.* **1065**, 325, 2005.

28. G. Wurm and O. Krauss, Concentration and sorting of chondrules and CAIs in the late Solar Nebula, *Icarus* **180**, 487, 2006.

29. K.J. Walsh and D.C. Richardson, Binary near-Earth asteroid formation: Rubble pile model of tidal distortions, *Icarus* **180**, 201, 2006.

30. S. Marchi, P. Paolicchi, M. Lazzarin and S. Magrin, A general spectral slope-exposure relation for S-type main belt and near-Earth asteroids, *Astron. J.* **131**, 1138, 2006.

31. G. Beekman, I.O. Yarkovsky and the discovery of his effect, *J. History of Astronomy* **37**, 71, 2006.

32. G. Cheng, J. Duan, S. Zhang and Y. Chen, Inverse thinking and problems for light scattering, *Progress in Physics* **26**, 51, 2006 (in chinese).

33. D.C. Richardson and K.J. Walsh, Binary minor planets, *Ann. Rev. Earth Planet. Sci.* **34**, 47, 2006.

34. G.B. Valsecchi, A. Milani, A. Rossi and G. Tommei, The SRT, Near-Earth objects, and space debris, *Mem. Soc. Astron. Italiana* **10**, 186, 2006.

35. M. Delbó, A. dell'Oro, A.W. Harris, S. Mottola and M. Mueller, Thermal inertia of near-Earth asteroids and implications for the magnitude of the Yarkovsky effect, *Icarus*, in press, 2007.

36. D.F. Lupishko, M. Di Martino and R.P. Binzel, Near-Earth objects as principal impactors on the Earth, in: *Near Earth Objects, our Celestial Neighbors: Opportunity and Risk*, A. Milani, G.B. Valsecchi and D. Vokrouhlický, Eds., Cambridge Univ. Press, 2007, in press.

37. P. Michel and K.A. Holsapple, Tidal disturbances of small cohesionless bodies: limit planetary distances and applications, in: *Near Earth Objects, our Celestial Neighbors: Opportunity and Risk*, A. Milani, G.B. Valsecchi and D. Vokrouhlický, Eds., Cambridge Univ. Press, 2007, in press.

38. M. Delbò, P. Tanga and F. Mignard, On the detection of the Yarkovsky effect on near-Earth asteroids by means of Gaia, *Planet. Sp. Sci.*, in press, 2007.

39. W.F. Bottke, Spun in the sun, *Nature* **446**, 382-383, 2007.

40. M. Kaasalainen, J. Ďurech, B.D. Warner, Y.N. Krugly and N.M. Gaftonyuk, Acceleration of the rotation rate of asteroid 1862 Apollo by radiation torques, *Nature* **446**, 420, 2007.

- Vokrouhlický, D., **Čapek, D.**, Kaasalainen, M., and Ostro, S. J. (2004). Detectability of YORP rotational slowing of asteroid 25143 Itokawa. *Astronomy and Astrophysics*, 414:L21–L24.

  1. A.W. Harris and P. Pravec, Rotational properties of asteroids, comets and TNOs, in: *Asteroids, Comets and Meteors*, eds. D. Lazzaro, S. Ferraz-Mello and J.A. Fernandez, Cambridge University Press, p. 439, 2006.
  2. D.J. Scheeres, M. Abe, R. Nakamura, R.W. Gaskell, P.A. Abell, Predicted rotational deceleration of asteroid Itokawa due to YORP, abstract COSPAR2006-A-02665 at COSPAR meeting, Beijing, 2006. (http://www.cosis.net/abstracts/COSPAR2006/02665/COSPAR2006-A-02665.pdf)
  3. D.J. Scheeres, The dynamical evolution of uniformly rotating asteroids subject to YORP, *Icarus* **188**, 430, 2007.
  4. D.J. Scheeres, M. Abe, M. Yoshikawa, R. Nakamura, R.W. Gaskell, P.A. Abell, The effect of YORP on Itokawa, *Icarus* **188**, 425, 2007.
  5. T.G. Müller, T. Sekiguchi, M. Kaasalainen, M. Abe and S. Hagesawa, Itokawa: The power of ground-based mid-infrared observations, in: *Near Earth Objects, our Celestial Neighbors: Opportunity and Risk*, A. Milani, G.B. Valsecchi and D. Vokrouhlický, Eds., Cambridge Univ. Press, 2007, in press.

- **Čapek, D.** and Vokrouhlický, D. (2004). The YORP effect with finite thermal conductivity. *Icarus*, 172:526–536.

  1. J. Ďurech, 433 Eros – comparison of lightcurve extrema from 1901-1931 with the actual rotation state, *Astron. Astrophys.* **431**, 381, 2005.
  2. V. Carruba, T.A. Michtchenko, F. Roig, S. Ferraz-Mello and D. Nesvorný, On the V-type asteroids outside the Vesta family. I. Interplay ..., *Astron. Astrophys.* **441**, 819, 2005.
  3. D.J. Scheeres, The dynamical evolution of uniformly rotating asteroids subject to YORP, *Icarus*, in press, 2007.
  4. E. Mysen, Canonical rotation variables and non-Hamiltonian forces: solar radiation pressure effects on asteroid rotation, *Mon. Not. R. Astr. Soc.* **372**, 1345, 2006.
  5. P. Jenniskens, Meteor Showers and their Parent Comets (Cambridge, Cambridge University Press, 2006) p. 536.
  6. M. Kaasalainen, J. Ďurech, B.D. Warner, Y.N. Krugly, N.M. Gaftonyuk, Acceleration of the rotation of asteroid 1862 Apollo by radiation torques, *Nature*, **446**, 420, 2007.
  7. M. Delbó, A. dell'Oro, A.W. Harris, S. Mottola and M. Mueller, Thermal inertia of near-Earth asteroids and implications for the magnitude of the Yarkovsky effect, *Icarus*, in press, 2007.
  8. M. Delbò, P. Tanga and F. Mignard, On the detection of the Yarkovsky effect on near-Earth asteroids by means of Gaia, *Planet. Sp. Sci.*, in press, 2007.
  9. V. Carruba, F. Roig, T.A. Michtchenko, S. Ferraz-Mello and D. Nesvorný, Modeling close encounters with massive asteroids: a Markovian approach, *Astron. Astrophys.*, in press, 2007.
  10. M. Ćuk, Formation and destruction of small binary asteroids, *Astrophys. J.* **659**, L57, 2007.
  11. A. Kryszczyńska, A. La Spina, P. Paolicchi, A.W. Harris, S. Breiter and P. Pravec, New findings on the asteroid spin-vector distributions, *Icarus*, in press, 2007.

- Vokrouhlický, D., **Čapek, D.**, Chesley, S. R., and Ostro, S. J. (2005a). Yarkovsky detection opportunities. I. Solitary asteroids. *Icarus*, 173:166–184.

  1. D. Nesvorný and W.F. Bottke, Direct detection of the Yarkovsky effect for main-belt asteroids, *Icarus* **170**, 324, 2004.

2. T.G. Müller, T. Sekiguchi, M. Kaasalainen, M. Abe and S. Hagesawa, Itokawa: The power of ground-based mid-infrared observations, in: *Near Earth Objects, our Celestial Neighbors: Opportunity and Risk*, A. Milani, G.B. Valsecchi and D. Vokrouhlický, Eds., Cambridge Univ. Press, 2007, in press.
3. M. Delbò, P. Tanga and F. Mignard, On the detection of the Yarkovsky effect on near-Earth asteroids by means of Gaia, *Planet. Sp. Sci.*, in press, 2007.

- Vokrouhlický, D., **Čapek, D.**, Chesley, S. R., and Ostro, S. J. (2005b). Yarkovsky detection opportunities II. Binary asteroids.. *Icarus*, 179:128–138.

1. A. Morbidelli, H.F. Levison and W.F. Bottke, Formation of the binary near-Earth object 1996 FG(3): Can binary NEOs be the source of short-CRE meteorites? *Meteor. Planet. Sci.* **41**, 875, 2006.
2. D.J. Scheeres, The dynamics of NEO binary asteroids, in: *Near Earth Objects, our Celestial Neighbors: Opportunity and Risk*, A. Milani, G.B. Valsecchi and D. Vokrouhlický, Eds., Cambridge Univ. Press, 2007, in press.

Proceedings

- **Čapek, D.** and Vokrouhlický, D. (2005). Accurate model for the Yarkovsky effect. In Knezevic, Z. and Milani, A., editors, *IAU Colloq. 197: Dynamics of Populations of Planetary Systems*, p. 171–178.
- Brož, M. and Vokrouhlický, D. and Bottke, W. F. and Nesvorný, D. and Morbidelli, A. and **Čapek, D.** (2006), Non-gravitational forces acting on small bodies. *IAU Symp. 229: Asteroids, Comets, and Meteors*, p. 351-365.

Abstracts

- **Čapek, D.** and Vokrouhlický, D. (2002). Yarkovsky force and torque on Gaussian random spheres. Poster at *Asteroids, Comets and Meteors*, Berlin, Germany.
- S.R. Chesley, D. Vokrouhlický, D. **Čapek** and S. Ostro (2003). Test of the Yarkovsky effect using radar ranging to Golevka: Place your bets, *BAAS* **35**, 1033.
- D. Vokrouhlický, **D. Čapek**, S.R. Chesley and S. Ostro (2004). Next Yarkovsky candidates, *New trends in near-Earth asteroids research*, Arecibo, Puerto Rico.
- S.R. Chesley, S.J. Ostro, D. Vokrouhlický, J.D. Giorgini, **D. Čapek**, L.A.M. Benner, M.C. Nolan and J.-L. Margot (2005). Direct detection of the Yarkovsky effect: Progress and prognostications, *BAAS* **37**, 521.
- **Čapek, D.** and Vokrouhlický, D. (2005). Plausible constraint on Golevka's regolith from an accurate Yarkovsky/YORP effect model. Poster at *Asteroids, Comets and Meteors*, Búzios, Rio de Janeiro, Brazil.

Appendix F

Reprints

1. Vokrouhlický, D. and Čapek, D. (2002). YORP-Induced Long-Term Evolution of the Spin State of Small Asteroids and Meteoroids: Rubincam's Approximation. *Icarus*, **159**, 449-467.

2. Chesley, S. R., Ostro, S. J., Vokrouhlický, D., Čapek, D., Giorgini, J. D., Nolan, M. C., Margot, J.-L., Hine, A. A., Benner, L. A. M., and Chamberlin, A. B. (2003). Direct Detection of the Yarkovsky Effect by Radar Ranging to Asteroid 6489 Golevka. *Science*, **302**, 1739–1742.

3. Vokrouhlický, D., Čapek, D., Kaasalainen, M., and Ostro, S. J. (2004). Detectability of YORP rotational slowing of asteroid 25143 Itokawa. *Astronomy and Astrophysics*, 414:L21–L24.

4. Čapek, D. and Vokrouhlický, D. (2004). The YORP effect with finite thermal conductivity. *Icarus*, 172:526–536.

5. Vokrouhlický, D., Čapek, D., Chesley, S. R., and Ostro, S. J. (2005). Yarkovsky detection opportunities. I. Solitary asteroids. *Icarus*, 173:166–184.

6. Vokrouhlický, D., Čapek, D., Chesley, S. R., and Ostro, S. J. (2005). Yarkovsky detection opportunities II. Binary asteroids.. *Icarus*, 179:128–138.

7. Čapek, D. and Vokrouhlický, D. (2005). Accurate model for the Yarkovsky effect. In Knezevic, Z. and Milani, A., editors, *IAU Colloq. 197: Dynamics of Populations of Planetary Systems*, p. 171–178.

8. Čapek, D. and Vokrouhlický, D. (2005). Plausible constraint on Golevka's regolith from an accurate Yarkovsky/YORP effect model. Poster at *Asteroids, Comets and Meteors*, Búzios, Rio de Janeiro, Brazil.

Icarus 159, 449–467 (2002)
doi:10.1006/icar.2002.6918

YORP-Induced Long-Term Evolution of the Spin State of Small Asteroids and Meteoroids: Rubincam's Approximation

D. Vokrouhlický and D. Čapek

Institute of Astronomy, Charles University, V Holešovičkách 2, CZ-18000 Prague 8, Czech Republic
E-mail: vokrouhl@mbox.cesnet.cz

Received September 15, 2001; revised May 10, 2002

The rotation states of small asteroids and meteoroids are determined primarily by their collisions, gravitational torques due to the Sun and planets (in the case of close encounters), and internal dissipative effects (that relax the free-precession energy toward the fundamental state of principal-axis rotation). Rubincam has recently pointed out that thermal reemission on irregular-shaped bodies also results in a torque that may secularly change both the rotation rate and the orientation of the spin axis (the so-called YORP effect). Here we pursue investigation of this effect. Keeping the zero thermal-relaxation approximation of Rubincam and the assumption of the principal-axis rotation, we study the YORP effect both for precisely determined shapes of near-Earth asteroids and also for a large statistical sample of automatically generated shapes by the Gaussian-sphere technique of Muinonen. We find that the asymptotic state of the YORP evolution is characterized by an arbitrary value of the obliquity, with higher but nearly equal likelihood of 0°/180° and 90° states. At the adopted approximation, the most typical feature of this end state of the YORP evolution is secular deceleration of the rotation rate, which means that at some instant collisions will randomize the rotation state. In a minority of cases, the final state of the obliquity evolution leads to a permanent acceleration of the body's rotation, eventually resulting in rotational fission. The YORP-induced slow evolution may also play an important role in driving the rotation state of small asteroids toward the resonances between the forced precession due to the solar torque and perturbations of the orbital node and inclination. We find that for small Themis asteroids these resonances are isolated in the relevant range of frequencies, and the YORP evolving rotation may be either temporarily captured or rapidly jump across these resonances. In contrast, the possible values of the forced precession for small Flora asteroids may be resonant with clustered, nonisolated lines of the orbital perturbation. The individual rotation histories of small Flora asteroids may be thus very complicated and basically unpredictable. We comment on possible astronomical consequences of these results.

Key Words: minor planets; asteroids; meteors; meteoroids; rotation.

1. INTRODUCTION

Small asteroids and meteoroids acquire their rotation states at the instant of their birth as ejecta from a parent body (e.g., Love and Ahrens 1997, Giblin and Farinella 1997). At later stages, mutual collisions keep modifying the rotation state, which means that the size–distribution collisional model needs to be consistently coupled with the rotation rate–distribution model (e.g., Harris 1979, Farinella *et al.* 1992). Thus, none of the small Solar System bodies have primordial rotation states that are steady over a billion year timespan.

Though collisions represent the most extensively studied aspect of the long-term evolution of the small bodies' rotation state, other effects may be also involved. Recently, Rubincam (2000) pointed out that the thermal radiation by a surface of an irregular-shaped object results in a torque which may secularly affect both the rotation frequency and the obliquity of the spin axis. Following Rubincam's suggestion we shall speak about the YORP effect (named after Yarkovsky–O'Keefe–Radzievskii–Paddack, scientists who all contributed to this topic in the past). The corresponding time scale to change the rotation rate or obliquity is unrealistically long for asteroids larger than ≈20 km in size, but it becomes short enough for kilometer-sized (or smaller) bodies. The YORP effect may require a timespan comparable, or even shorter than, the collision time scale to significantly change the rotation state (≈tens or hundreds of Myr) in this size range. For decameter-sized meteoroid precursors, the YORP time scale may even become so short that this effect would dominate over collisions (Rubincam 2000). We note in advance that this conclusion may not be certain because the strength of the YORP effect could be diminished by the finite conductivity of the meteoroid surface. This, as yet unaccounted for fact in the YORP determination will be removed in the second paper of this series. However, the YORP effect certainly continues to be an important factor for modifying the rotation state of meteoroids.

The previous "YORP facts" are important as such, since they may have interesting implications on the statistical distribution

0019-1035/02 $35.00

of the rotation periods of small asteroids, occurrence of close binaries produced by rotational fission, etc. However, there is an additional and very important implication of the YORP effect related to the Yarkovsky orbital effect. Actually, both effects—the Yarkovsky effect and YORP effect—have a common physical origin, namely, the surface recoil force due to the thermal radiation of the body. The Yarkovsky effect has been studied extensively over the past few years with a number of new applications related to the transport of meteorites toward the Earth (e.g., Farinella *et al.* 1998, Hartmann *et al.* 1999, Bottke *et al.* 2000, Vokrouhlický and Farinella 2000), origin and transport of large near-Earth asteroids (e.g., Farinella and Vokrouhlický 1999, Bottke *et al.* 2001a), processes in the asteroid families (e.g., Vokrouhlický *et al.* 2001, Nesvorný *et al.* 2002, Bottke *et al.* 2001b), or the possibility of directly detecting the Yarkovsky orbital perturbations of the near-Earth asteroids (e.g., Vokrouhlický *et al.* 2000). It is well known that the Yarkovsky effect sensitively depends on the orientation of the spin axis (e.g., Rubincam 1995, 1998, Vokrouhlický 1998, 1999). This mainly applies to the diurnal variant of the Yarkovsky effect, which leads to an opposite orbital effect when the prograde rotation of the body is changed by the retrograde rotation. Frequent variations of the spin axis orientation thus diminish the resulting (accumulated) Yarkovsky orbital perturbation, and this may have important implications on the relevance of the Yarkovsky effect as described here. Note that thus far most of the developed applications of the Yarkovsky effect do not include any (or just very simplified) evolution of the spin axis orientation. We thus need to understand whether some of the past investigations of the Yarkovsky effect have to be modified if the YORP-induced evolution of the spin axis is taken into account.

In this paper we investigate in a more quantitative detail the YORP effect in Rubincam's approximation. The major restriction of this approach is that of zero thermal inertia of the surface material. Following Rubincam (2000) we shall thus assume effectively immediate thermal reemission of the absorbed energy. This assumption applies rather well for small asteroids, possibly down to hundreds of meters across, that are likely covered with a thin regolith layer. Our results for the YORP evolution of several small asteroids, for which we use a very precise shape model (mostly from the analysis of the radar ranging data), are therefore justified. We shall demonstrate that the individual YORP results, such as the asymptotic values of the obliquity and the rotation rate, depend sensitively on the shape of the asteroid so that there is "no generic YORP result." To obtain information about "average YORP results" we need a larger statistical sample of objects than the few real asteroids with accurately known shapes. To that end, we analyze YORP results for a sample of small (synthetic) asteroids generated by the Gaussian-sphere technique introduced by Muinonen (e.g., Muinonen 1996, 1998). Motivated by the analysis of the proper element dispersion in the asteroid families (e.g., Nesvorný *et al.* 2002), we shall determine the characteristic YORP results (relevant time scales, etc.) for small members of the Flora and Themis families.

As already mentioned, the YORP effect is certainly not alone in affecting the rotation state of small asteroids. Of major importance are mutual collisions and, under certain circumstances, gravitational torques due to the Sun or planets. In this paper we neglect the collisional influence on rotation, since this appears to be a complicated and, to some degree, separate problem, and we focus on the long-term dynamical effects that influence the rotation state of small asteroids. Apart from the YORP effect, we pay attention to the role of the gravitational torque due to the Sun. We show that the rate of the forced precession due to this effect may resonantly beat with planetary perturbations of the orbit. Obliquity may then undergo rapid jumps or periods of random wandering on a large scale. The possible past histories of the rotation of terrestrial planets, especially Mars, Venus, and Mercury, may give an idea about the degree of chaotic effects that are predicted here for small asteroids (e.g., Laskar and Robutel 1993). The YORP effect may be instrumental in driving the rotation state of small asteroids toward these resonant phenomena. Our analysis thus indicates that the rotation state evolution of small asteroids on a Myr time scale (or longer) may be very complicated and it that may sensitively depend on the asteroid shape (and its history, which may be sculpted by collisions).

The assumption of zero thermal inertia, used throughout this paper, is most likely violated for smaller bodies, such as decameter- or meter-sized meteoroids, for the following two reasons: (i) these bodies likely rotate fast, and (ii) their surface is likely not insulated by regolith layer but characterized by much higher thermal conductivity (affected possibly by porosity only). We thus relegate a more detailed discussion of the YORP effect on meteoroids to the second paper in this series. In particular, we shall generalize the current YORP model by including the thermal relaxation between the absorption of the solar radiation and thermal reemission, there by relaxing the restrictive assumption of the Rubincam approximation.

In the final paper of this series, we shall investigate the YORP effect within a full-fledged formulation. This means that we shall solve numerically the complete Euler's equations for the rotation state of the body on a secularly evolving orbit in the Solar System. Gravitational torque due to the Sun, as well as the thermophysical model of the YORP effect, will be included. Initial rotation will not necessarily be constrained to the principal-axis mode.

2. THEORY

Given a skin force $d\mathbf{f}$ acting on a body at the oriented surface element $d\mathbf{S}$ with a position vector $\mathbf{r}$, referred to the center of mass system, we can evaluate the total torque on the whole body as

$$\mathbf{T} = \int \mathbf{r} \times d\mathbf{f}, \tag{1}$$

where the integration is assumed over the whole surface. The

recoil force $d\mathbf{f}$ due to the thermally emitted radiation is given by $d\mathbf{f} \simeq -2\varepsilon\sigma T^4 d\mathbf{S}/3$, where ε is the thermal emissivity, σ is the Stefan–Boltzmann constant, and T is the temperature. Note the minus sign due to the recoil property of the radiation effect. This formula holds for an isotropic (Lambertian) thermal emission law. Certainly this law only approximates the directional properties of thermal emission of real objects, but a more complex approach goes beyond the scope of this paper. However, an even cruder simplification, which we are going to accept, follows an estimation of the surface temperature T. In principle we need a thermophysical model for its determination. Only at the limit of zero thermal relaxation, satisfied when the surface is highly insulating, can we further approximate from energy conservation $\varepsilon\sigma T^4 \simeq (1 - A)\Phi(\mathbf{n}\cdot\mathbf{n}_0)$, if $(\mathbf{n}\cdot\mathbf{n}_0) > 0$ and the element is not shadowed by another surface element; otherwise $\varepsilon\sigma T^4 \simeq 0$. $\varepsilon\sigma T^4 \simeq (1 - A)\Phi(\mathbf{n}\cdot\mathbf{n}_0)$, if $(\mathbf{n}\cdot\mathbf{n}_0) > 0$ element, $\mathbf{n}_0$ is the direction toward the Sun, Φ is the solar flux at the distance of the body from the Sun, and A is the hemispheric albedo (Vokrouhlický and Bottke 2001). Moreover, since albedo A is typically small, and additionally a part of the radiation in the optical band is also diffusely reflected (the same directional characteristics as we assume for the thermal emission), we further approximate $(1 - A) \simeq 1$. Combining the previous results we have

$$d\mathbf{f} \simeq -\frac{2\Phi}{3c}(\mathbf{n}\cdot\mathbf{n}_0)\,d\mathbf{S} \tag{2}$$

(here again we set formally $(\mathbf{n}\cdot\mathbf{n}_0) = 0$ when the surface element is not illuminated or shadowed). Following the suggestion of Rubincam (2000) we additionally multiply $d\mathbf{f}$ from (2) by a "fudge factor" 2/3 to accommodate at a very rough approximation the effect of the surface thermal inertia. Though we shall see in the next paper of this series that this approximation rather weakly expresses the inertia effect, we keep the Rubincam formulation in this paper.

The formula (2) for the infinitesimal surface force $d\mathbf{f}$ is then used in (1) to obtain the total radiative torque $\mathbf{T}$. For a spherical body we would have $\mathbf{r} \propto \mathbf{n}$, which together with $d\mathbf{f} \propto \mathbf{n}$ leads trivially to the conclusion that the YORP torque vanishes. However, for a body of a generically irregular shape the torque $\mathbf{T}$ does not vanish. After we specify the way that the body's shape is modeled, the integral in (1) is computed numerically as a sum over infinitesimal surface facets.

Assuming then the principal-axis rotation of the body, we obtain (e.g., Rubincam 2000)

$$\frac{d\omega}{dt} = \frac{T_s}{C}, \qquad \frac{d\epsilon}{dt} = \frac{T_\epsilon}{C\omega} \tag{3}$$

for the rate of change of the rotation angular velocity ω and the obliquity ϵ (hence $\cos\epsilon = \mathbf{N}\cdot\mathbf{s}$, with $\mathbf{N}$ normal to the orbital plane and $\mathbf{s}$ the spin axis). Here C is the principal moment of inertia around the spin axis and we define

$$T_s = \mathbf{T}\cdot\mathbf{s}, \qquad T_\epsilon = \mathbf{T}\cdot\mathbf{e}_\perp, \tag{4}$$

and $\mathbf{e}_\perp = (\mathbf{s}\cos\epsilon - \mathbf{N})/\sin\epsilon$. Note a difference between our variables and those used by Rubincam (2000). Namely, we systematically refer the projections T_s and T_ϵ of the YORP torque $\mathbf{T}$ to the *spin vector* (a unit vector of the rotational angular momentum) and not to the body axis $\mathbf{e}_z$ (hence we prefer the notation T_s instead of T_z used by Rubincam). When the sense of rotation is changed, or in other words the spin axis is inverted with respect to the body ($\mathbf{s} \to -\mathbf{s}$), the YORP torque $\mathbf{T}$ and the projection T_ϵ do not change their sign but the projection T_s does change sign. With Eqs. (3) this means that when the spin axis is inverted with respect to the body the rotation is accelerated in one case and decelerated in the other; the effect on obliquity is also reversed, since the axis inversion means the obliquity transformation $\epsilon \to 180 - \epsilon$. Another symmetry, involving averaging over a circular orbit, will be discussed in the following.

Let us emphasize our *assumption* that the internal processes resulting in dissipation of the free-wobble energy are strong enough to maintain the shortest axis rotation state. In Section 3.3 we shall summarize the current knowledge of the strength of these dissipative effects and we shall give the corresponding time scale to align the generic rotation state toward the lowest energy state. Note, however, that the YORP effect tends to destroy the principal-axis rotation, since the projection of YORP torque on all axes in the body frame are of comparable magnitude. This is still true for the averaged quantities discussed in the following. Only if the YORP evolution time scale were (much) longer than the estimated time scale for the wobble dissipation would principal-axis rotation be justified. We shall see that this is true for multikilometer-sized asteroids, but it becomes questionable for kilometer-sized objects. A thorough analysis of the YORP effect in the non-principal-axis rotation state, with the YORP contribution used to trigger this state, is beyond the scope of this introductory paper. The third paper in this series will be devoted to this problem.

Since we are interested in the long-term evolution of the rotation state, it is appropriate to average T_s and T_ϵ in the right-hand sides of (3) over both rotation and revolution cycles. This procedure may require care in the case of a very slow rotation, but in the majority of cases of interest the rotation period is several orders of magnitude smaller than the revolution period. The double averaging can therefore be performed in rotation and revolution phase angles independently. Unlike in the case of the torque due to the direct (absorbed) solar radiation pressure, the YORP torque does not average to zero. For circular orbits, assumed throughout this paper, the resulting averaged torques $\bar{T}_s$ and $\bar{T}_\epsilon$ depend on the obliquity ϵ. In the case of an eccentric orbit the phase angle of the spin axis projection onto the orbital plane would appear as a second parameter of the $(\bar{T}_s, \bar{T}_\epsilon)$ torques.

In assuming a circular orbit, we should notice another "symmetry" related to the spin axis inversion (not identical, however,

to that just discussed). For a *conserved* sense of rotation, or in other words a conserved position of the spin axis in the body-fixed frame, we may be willing to investigate how the *averaged* torques $\bar{T}_z$ and $\bar{T}_\epsilon$ change at the inversion of the spin axis in space. For a given instant of the revolution around the Sun, this operation results in a different value of the YORP torque, since a different part of the body's surface is illuminated. However, there is a symmetric configuration, as far as the surface illumination is concerned, after half revolution on the circular orbit. The YORP torque projected onto the body-fixed axes is the same, and thus so is the T_z quantity, but the T_ϵ variable changes its sign. As a result, the obliquity transformation $\epsilon \to 180 - \epsilon$, with the conserved orientation of the spin axis in the body-fixed frame, results in the following (anti)symmetry of the averaged YORP torques: $\bar{T}_z(180 - \epsilon) = \bar{T}_z(\epsilon)$ and $\bar{T}_\epsilon(180 - \epsilon) = -\bar{T}_\epsilon(\epsilon)$. Note also the fine difference between this symmetry and the one accompanied by the spin axis inversion in the body-fixed frame. In the latter case both $\bar{T}_z(\epsilon)$ and $\bar{T}_\epsilon(\epsilon)$ change their sign.

Throughout the text we assume that the averaging approach is applicable. In the real astronomical situations we have in mind, this constrains the rotation period to be smaller than a few months (a constraint that is essentially always satisfied). We shall see in the following that the YORP evolution may result in an asymptotic phase characterized by a permanent despinning of the rotation. We should thus keep in mind that the adopted approximation, based on the averaging technique, does not allow us to extrapolate this asymptotic phase too long. However, such long periods are probably not relevant because of collisional evolution, which is also neglected in this paper.

Adopting the preceding physical approximations we realize that the appropriate modeling of the irregular shape of the body is the most important issue. In the next two sections we briefly explain our approach in this respect. We investigate about a dozen cases of small asteroids for which the shapes are accurately known. Unfortunately, this represents too small a sample for characterizing statistically the YORP effect on the long-term spin dynamics of asteroids. Therefore, in Section 2.2 we recall a powerful technique for generating irregular-shaped (synthetic) objects with mean characteristics fitting small asteroids. This will allow us to produce a larger sample of objects for which we may determine the "mean YORP effect" on their rotation state.

2.1. Polyhedral Model of the Asteroid Shape

Though the ellipsoidal shape model for small asteroids is by far the most common and was thus used for computing their lightcurves in majority of cases, real asteroids typically indicate a much higher degree of irregularity. In addition, the fact that the YORP effect depends sensitively on the asteroid shape, as already noted by Rubincam (2000), prompts us to use a more accurate shape model.

There are basically two approaches that are often used for describing of an arbitrarily shaped body: (i) spherical harmonics development of the distance $r(\theta, \phi)$ toward the surface along the direction characterized by the spherical angles θ and ϕ, and (ii) polyhedral model consisting of a list of surface vertexes and their identification as infinitesimal surface elements (facets). Both methods have been used for shape modeling of planetary satellites and small asteroids. The polyhedral model is clearly a more general tool (e.g., Simonelli *et al.* 1993). First, fine surface structures (such as crater morphology or linear faults) are difficult to accommodate into a "reasonable-degree" spherical model; yet they may have influence on the exact value of the YORP torque. Second, the most irregular shapes cannot even be described by a single series within the spherical harmonic approach, since there might be several surface facets seen along a given direction from the center of mass. This situation occurs, for instance, in the case of the asteroids Kleopatra and Geographos. These reasons led us to use the polyhedral model description of the asteroid shape in this paper. A practical bonus is the fact that the best-determined shapes of the near-Earth asteroids (except Eros), acquired by radar ranging, are directly exported in this format. We thus use data of six detailed asteroidal shapes available from http://echo.jpl.nasa.gov/links.html (their polyhedral approximation contains typically 4092 surface elements; the finest model of Toutatis has 12,796 surface elements). The polyhedral model of asteroid 6053 (1993BW3) is taken from Ďurech (2002). Additionally, we use data on asteroids and martian satellites acquired through satellite observations and available as spherical harmonics models [e.g., 24-degree Eros data are available from http://near.jhuapl.edu/(see also Yeomans *et al.* 2000) and a six-degree Deimos model is taken from Rubincam *et al.* 1995]. In each of these cases we have transformed the original data to a polyhedral model with typically 4000 surface elements. We started with nodes given by even coverage of a sphere in latitude and longitude but then iterated nodal positions so that the surface elements have approximately the same area.

Given the goal of our study, we need to compute a number of physical parameters of the studied objects: total mass (volume), surface area, inertia tensor, etc. For that purpose we basically follow the paper by Dobrovolskis (1996), generalizing it for a few complicated cases with several surface facets in a given (single) direction in the center of mass system.

A particular problem we faced when computing the YORP torque is that of illumination of a given surface facet. Given a frequent concave shape of small objects, there exists a possibility that some surface elements may produce a shadow which prevents illumination of other surface elements. Interestingly, a similar problem is encountered in satellite geodesy, in particular for accurate determination of the atmospheric and radiation drag on irregular-shaped artificial satellites. The most precise approach, notably the individual ray-tracing technique (e.g., Klinkrad *et al.* 1990), is typically a rather time-consuming procedure. We have thus chosen a compromise between the computational accuracy and computer-time demands. For all surface elements we precomputed a list of other, potentially shadowing facets. The minimum local zenith angle is also precomputed and

stored in computer memory. A special test is then performed when a potentially shadowing situation is detected in the course of computing the YORP effect. Notably, we investigate whether centers of the potentially shadowing facets are projected onto the given surface element (as seen from the solar direction).

At a still higher degree of precision one should take into account self-irradiation of the irregular shape (i.e., thermal radiation from one surface facet can illuminate another facet and thus produce a corresponding radiation pressure). The ray-tracing technique can tackle complexities of this kind, but we neglect this effect in this study.

The precision with which we can compute the averaged values of the YORP torques $\bar{T}_z$ and $\bar{T}_\epsilon$ is limited mainly due to finite area of the surface facets (modeled as planar). However, we have verified that by taking more than 1000 facets, as we always do, the YORP torques can be computed with at least 1% precision in all our cases. The fact that the computed quantities are averaged over the rotation and revolution cycles helps to diminish the error of numerical evaluation of the resulting torques.

2.2. Gaussian Random Spheres

Muinonen (1996, 1998), following previous studies of the Finish school dealing with light scattering on small, irregular dust particles, pointed out that the Gaussian-sphere model is a robust scheme for describing shapes of small Solar System objects (asteroids and comets). Within this model, radii of a large sample of the objects satisfy log-normal statistics with a variance σ and a characteristic dimensional factor a (if properly scaled). In the center of mass system the radius $r(\theta, \phi)$ in a direction given by spherical angles θ and ϕ may be expressed as

$$r(\theta, \phi) = \frac{a}{\sqrt{1+\sigma^2}} \exp[s(\theta, \phi)], \tag{5}$$

where the $s(\theta, \phi)$ function obeys spherical harmonic development,

$$s(\theta, \phi) = \sum_{\ell=0}^{\infty} \sum_{m=0}^{\ell} P_\ell^m(\cos\theta)(a_{\ell m} \cos m\phi + b_{\ell m} \sin m\phi). \tag{6}$$

The coefficients $(a_{\ell m}, b_{\ell m})$ of these series are independent Gaussian random variables with zero mean and variance reading

$$\beta_{\ell m}^2 = (2 - \delta_{\ell 0}) \frac{(\ell - m)!}{(\ell + m)!} c_\ell \beta^2, \tag{7}$$

with $\beta^2 = \ln(1 + \sigma^2)$ and $\delta_{\ell 0}$ the Kronecker symbol. The model then depends on the variance σ of the distribution of surface heights and on a set of parameters c_ℓ from (7). These latter parameters describe how the height anomalies fluctuate over the sphere, or more precisely they describe autocorrelation of the log radii for a given angular distance of two surface elements. A convenient single parametric choice for this autocorrelation function was suggested by Muinonen (1996); the second Gaussian-sphere model parameter is then Γ, the correlation angle of the surface fluctuations. This model was later generalized by Muinonen (1998), who constructed the autocorrelation function of surface heights at given angular distance by a linear combination of two different functions of Γ (the weighting factor represents then an additional parameter of the model).

The most relevant, in our context, is then the work by Muinonen and Lagerros (1998). These authors analyzed accurately known shapes of 14 asteroids to verify whether they satisfy the Gaussian-shape hypothesis. They obtained the best estimates of the parameters (σ, Γ) for their sample of asteroids, and also for a subset of 7 small asteroids (with sizes smaller than 10 km). In what follows we generate a large sample of "synthetic" shapes of small asteroids, represented by the Gaussian spheres with the previously mentioned parameters determined by Muinonen and Lagerros (1998) for small asteroids. Notably, we have $\sigma = 0.274$ and $\Gamma = 30.9°$; in fact we consider directly the values of c_ℓ as determined by Muinonen and Lagerros (1998) and accept a cutoff at $\ell = 10$ (see Table 5 of this reference). The scale parameter a, in Eq. (5), is obviously arbitrary and we typically fix its value at 1 km. As already indicated, we then convert each of the generated objects in the finite-element triangulation of the surface (polyhedral model); for the sake of statistical tests that follow we use 1004 surface elements. Figure 1 shows four typical synthetic asteroids in our sample.

Figures 2 and 3 show distribution of the dynamical ellipticity $(C - (A + B)/2)/C$ and the triaxiality factor A/B for a sample of 1000 Gaussian random spheres generated by this procedure. Symbols indicate the values of the same parameter for the few real asteroids (and Deimos) with accurately known shape. Figure 2 confirms that the small Solar System objects are significantly different from spheres with a typical dynamical

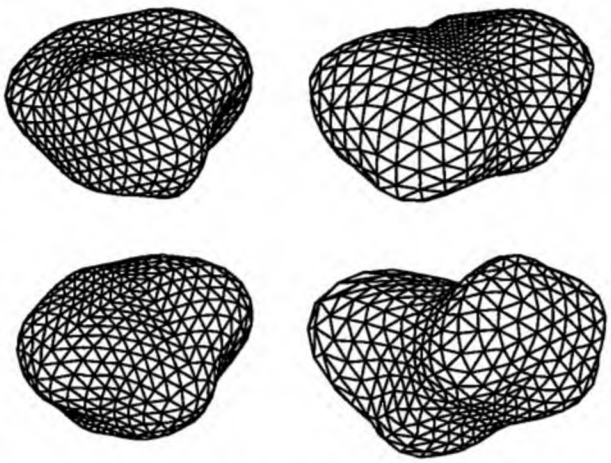

FIG. 1. Typical shapes of four synthetic asteroids generated by the Gaussian-sphere method; statistical parameters of the model correspond to those determined for small asteroids by Muinonen and Lagerros (1998). Each of the objects is represented by a polyhedral model with 1004 surface elements.

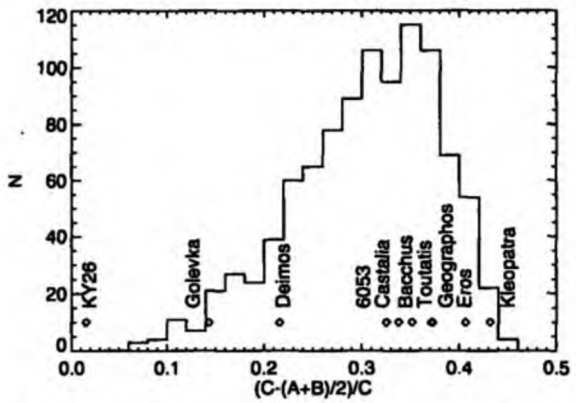

FIG. 2. Distribution of the dynamical ellipticity $(C-(A+B)/2)/C$ for a set of 1000 generated artificial objects by the technique described in the text. The peak value is at about 0.3; symbols denote values of this parameter for the nine asteroids and Deimos, for which we have precise shape models from the inversion of the radar data or satellite observations.

ellipticity value of ≈0.3. The distribution of both variables for the synthetic Gaussian spheres represents relatively well the density determined from real asteroid data. This confirms that our synthetic asteroids describe the asteroid population realistically. A curious exception is the ≈30-m-sized asteroid 1998KY26 (Ostro *et al.* 1999b).

3. RESULTS AND DISCUSSION

Hereafter we shall demonstrate the possible diversity of the YORP results through the parameter dependence of the averaged torques $\bar{T}_s$ and $\bar{T}_\epsilon$ [see Eqs. (4)]. In particular, we find that the YORP effect on these few asteroids, which basically differ just by their shape, may span all possible combinations of results.

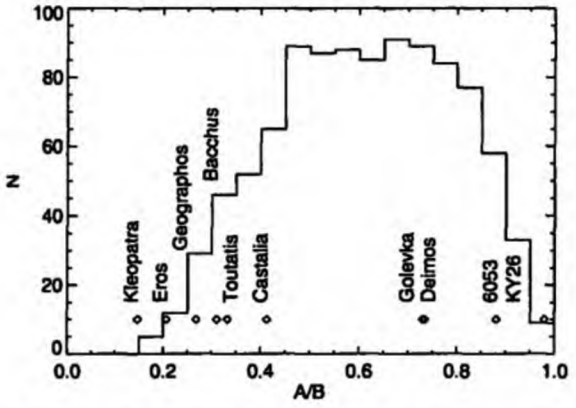

FIG. 3. Distribution of the triaxiality parameter A/B for a set of 1000 generated artificial objects by the technique described in the text. The peak value is at about 0.7; symbols denote values of this parameter for the nine asteroids and Deimos, for which we have determined precise shape models from the inversion of the radar data or satellite observations.

After classifying these individual results, essentially according to the dependence of $\bar{T}_\epsilon$ on the obliquity (with circular orbits assumed), we perform a statistical study to understand which of the different cases is the most typical. To that purpose we use a sample of 500 Gaussian random spheres generated as described in Section 2.2.

Though we use shapes of real (mostly near-Earth) asteroids we relegate the results to a single value of distance from the Sun, notably 2.5 AU. It is easy to understand from Eq. (2) that the results for the averaged torques scale as $\propto 1/d^2$, with d being the mean distance from the Sun. Similarly, though in all cases of real asteroids we keep their true dimensions, it is easy to see that $\bar{T}_s$ and $\bar{T}_\epsilon$ scale as $\propto 1/L^2$, where L is the linear scale of the object. In the case of a statistical sample of Gaussian spheres (Section 3.1.5), we set $a = 1$ km for the scale parameter in Eq. (5). If qualitative results are reported, we always assume homogeneous bodies with a density of $\rho = 2.5$ g/cm^3. If another density is more appropriate, such as for the C-type asteroids, the magnitude of the YORP torques scales as $\propto 1/\rho$.

3.1. Examples of the YORP Results

3.1.1. Type I: Eros, 1998KY26, 6053, and Toutatis

Figure 4 shows the averaged YORP torques $\bar{T}_s/C$ and $\bar{T}_\epsilon/C$ from the right-hand sides of Eqs. (3) for an Eros-shaped object at 2.5 AU. Obviously, we adopt the real orientation of the spin vector in the Eros' body-fixed frame as it corresponds to the real asteroid; only the obliquity (today's value for Eros is ≈82° is allowed to span the entire (0, 180) degree interval. As already discussed, the averaged YORP torques then satisfy the following properties of (anti)symmetry: $\bar{T}_s(\epsilon) = \bar{T}_s(180-\epsilon)$ and $\bar{T}_\epsilon(\epsilon) = -\bar{T}_\epsilon(180-\epsilon)$. The result from Fig. 4 corresponds to that of Rubincam (2000) qualitatively, but as far as the quantitative value is concerned Rubincam indicates YORP torques ≈3 times larger. We have checked our result several times and believe that it is correct. Nonetheless, this minor difference

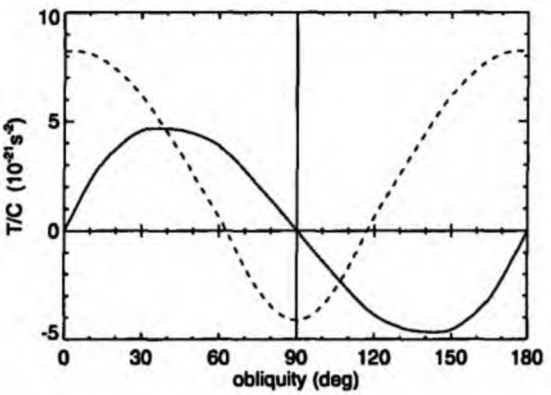

FIG. 4. Obliquity dependence of the averaged YORP torques $\bar{T}_s$ (dashed line) and $\bar{T}_\epsilon$ (solid line) for an Eros-shaped object at a circular orbit with radius of 2.5 AU. The torques are divided by the principal moment of inertia C.

cannot change any of the conclusions from either our or Rubincam's work. Notice, in particular, that the positive value of $\bar{T}_\epsilon$ in the (0°, 90°) obliquity range means that the YORP evolution always asymptotically reaches $\epsilon_f = 90°$ obliquity. Since $\bar{T}_z$ is negative at this value of obliquity, the final state of the YORP evolution corresponds to a permanent deceleration of the rotation. Note, however, that $\bar{T}_z$ is positive up to obliquity of 62°, which means that in the course of the YORP evolution the body may undergo a phase of spinning up of its rotation. This evolution characterizes type I cases in our classification. A similar result was found for asteroids 1998KY26 and 6053 (1993BW3), and Rubincam (2000) reports the same result for Gaspra and Ida.

The strength of the YORP effect may be illustrated in the case of the small asteroid 1998KY26. Rubincam (2000) argued that a characteristic time scale for doubling the rotation period is given by $\approx C\omega/\bar{T}_z$. Applying this estimation to 1998KY26 with a mean value of $\bar{T}_z \approx 10^{-15}$ s^{-2}, we obtain a doubling of its rotation period in only $\approx 10^4$ years. This is a surprisingly short time. We anticipate that a more complete YORP model, which includes the effects of the thermal inertia of the surface (which is neglected here but is likely for such a small object), may prolong this time scale by a factor ≈10–100. Still, a 0.1–1 Myr timespan to significantly alter the rotation state of 1998KY26 (or similar objects) is smaller than the dynamical lifetime of its orbit. It is also interesting to note that the rotation period of 1998KY26 has been measured with $\simeq 4 \times 10^{-5}$ fractional uncertainty during the 1998 observational campaign. Considering our result, its fractional change due to the YORP effect in 26 years, at the next close approach to the Earth in May 2024, is expected to be $\simeq 5 \times 10^{-3}$. We thus predict that the YORP effect is likely to be observable for this object. The previous conclusion also confirms that the YORP effect should still be important for obliquity evolution of the meteorite precursors. Implications of this fact in a combined model with their Yarkovsky delivery toward the Earth (e.g., Bottke *et al.* 2000, Vokrouhlický and Farinella 2000) needs to be studied in the future.

Finally, we mention that the YORP effect on a Toutatis-shaped object was found of this type I (Fig. 5). We should, however, recall that here we assumed the principal-axis rotation of a Toutatis-shape object. Rather than indicating the YORP effect on the real Toutatis we are thus reporting a result for a fictitious asteroid of the same shape (Toutatis is presently in a tumbling rotation state; Ostro *et al.* 1999a). An interesting feature of the YORP solution of the principal-axis rotator of the Toutatis-shaped body is a permanent deceleration of the rotation period ($\bar{T}_z$ is always negative).

3.1.2. *Type II: Deimos and Kleopatra*

Deimos presents an inverted case of the Eros results (see Fig. 6); namely, $\bar{T}_\epsilon$ is negative in the (0°, 90°) obliquity range. As a result, the asymptotic obliquity value of the YORP evolution is $\epsilon_f = 0°$ (or 180°, depending on the initial value of ϵ). The asymptotic despinning of the rotation ($\bar{T}_z(0) < 0$ and $\bar{T}_z(180) < 0$) is a common feature with the previously discussed type I cases.

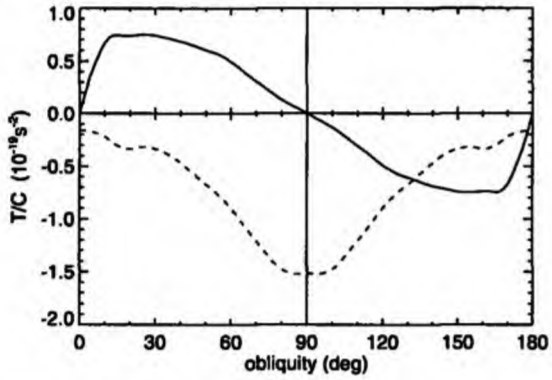

FIG. 5. The same as in Fig. 4, except for a Toutatis-shaped object rotating along its shortest principal axis.

Rubincam (2000) noticed this "anomalous" behavior of YORP on Deimos, but he artificially inverted the rotation axis with respect to the body (or the sense of its rotation). He rightly noted that the inversion causes Deimos to despin rather than to spin up its rotation for the given value of the obliquity, but he missed the point that the asymptotic YORP state is despinning in both cases.

The YORP effect on Kleopatra is qualitatively the same as for Deimos, but its larger size makes the YORP effect on this particular body negligible. The YORP time scale to double Kleopatra's rotation period is of the order of 1000 Gyr, an entirely irrelevant number from the astronomical point of view. However, a kilometer-sized object of Klepatra's shape would double its rotation period in ≈100 Myr only (thanks to the quadratic scaling of the YORP torques in the objects size).

3.1.3. *Type III: Castalia and Geographos*

The third type of our classification is represented by Castalia (see Fig. 7). The value of $\bar{T}_\epsilon$ is positive up to some critical value ϵ_* of the obliquity, while for large values it becomes negative

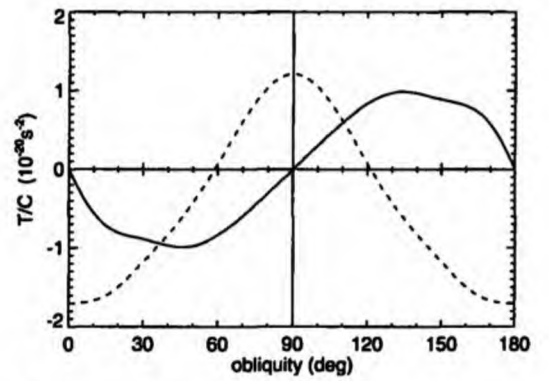

FIG. 6. The same as in Fig. 4, except for a Deimos-shaped object.

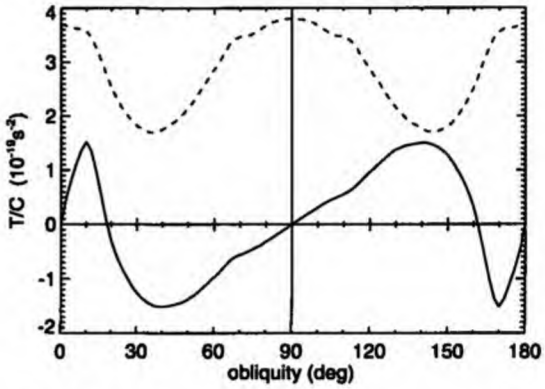

FIG. 7. The same as in Fig. 4, except for a Castalia-shaped object.

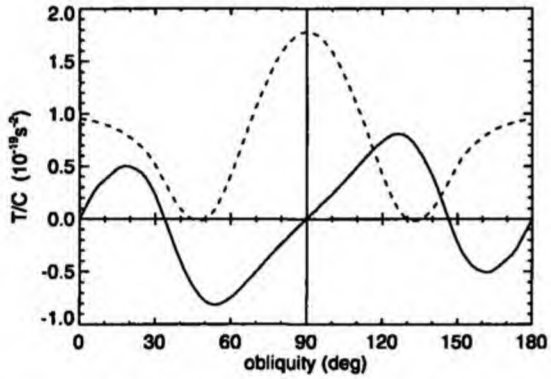

FIG. 8. The same as in Fig. 4, except for a Geographos-shaped object.

($\epsilon_* \simeq 30°$ for Bacchus). This means that ϵ_* (or $180 - \epsilon_*$) is the asymptotic value of obliquity that is reached by the YORP evolution at large time. Castalia's peculiarity is because the $\bar{T}_z$ torque is always positive. This latter fact means that the YORP effect permanently accelerates the body's rotation. This finding is interesting, since there is apparently a single outcome of this evolution, namely, rotational fission. Obviously, in particular cases we should investigate the corresponding time scale needed to reach the fission state. For instance, in Castalia's case we have estimated that its ≈4-h rotation will reach ≈2 h, an approximate disruption limit, in about 10 Myr. Though this estimation of the time scale for doubling Castalia's rotation frequency is not much longer than the estimated dynamical lifetime of its orbit (tens to a hundred million years), and thus it is astronomically relevant, it needs to be validated within a more general model (including eccentricity of Castalia's orbit, possible changes in its shape when approaching the critical rotation limit, deviation from the principal-axis rotation state, etc.). Castalia's rotational fission may also be facilitated by the fact that the cohesion at the junction of the two lobes of this asteroid, believed to be small asteroids that collided in a "subcatastrophic way" (e.g., Ostro *et al.* 1989), may be little lower. In any case, Castalia's result indicates that the YORP-induced bursting of small Solar System objects (see Rubincam 2000) may indeed occur is some special cases. Recall that this was the original motivation for studying the radiation torques (e.g., Radzievskii 1954, Paddack 1969).

The YORP effect on Geographos resembles closely that of Castalia (see Fig. 8). The $\bar{T}_z$ is nearly always positive. Geographos' rotation is thus virtually always accelerated. One easily estimates that the Geographos rotation frequency doubles in about 50 Myr. Again, though interesting, this number needs to be validated by a more precise model as already outlined. Geographos is thought to have undergone a "recent" close approach to the Earth that modified both its shape and its rotation state (e.g., Bottke *et al.* 1999). Such events are rare enough that the YORP effect may secularly change its rotation state before the next deep encounter, but the ≈10- to 100-Myr dynamical lifetime of the Geographos orbit may prevent a significant effect. Anyway, we found it interesting that the sub-kilometer-sized near-Earth asteroids have YORP time scales (to double the rotation frequency) comparable to their dynamical lifetimes.

3.1.4. Type IV: Golevka and Bacchus

The final type of our classification is again characterized by a single node of $\bar{T}_\epsilon$ in the (0°, 90°) obliquity range. An example is given by Golevka, whose averaged YORP torques are shown in Fig. 9. The YORP effect drives the obliquity either to 0° (or 180°) or to 90° depending on the initial state. Assuming a random initial state, there is $(\cos\epsilon_*)$ probability that 0° will be a final state obliquity; as before, ϵ_* is the node of $\bar{T}_\epsilon(\epsilon) = 0$. Interestingly, the rotation rate behaves in a different way for the two possible asymptotic states;namely, it decelerates at 0° (and 180°) and accelerates at 90°. An inverse asymptotic behavior is observed in the Bacchus case (Fig. 10).

In the case of the real asteroidal shapes studied here we did not encounter a situation going beyond our classification, notably with more than one node of $\bar{T}_\epsilon(\epsilon)$ in the (0°, 90°) obliquity range. In principle, this may not be excluded, but it appears less common. Occasionally, two nodes of $\bar{T}_\epsilon$ were observed

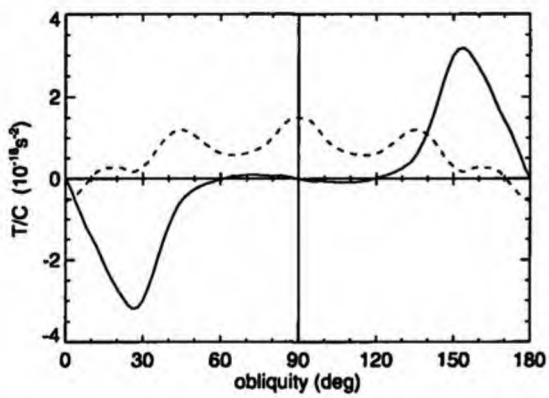

FIG. 9. The same as in Fig. 4, except for a Golevka-shaped object.

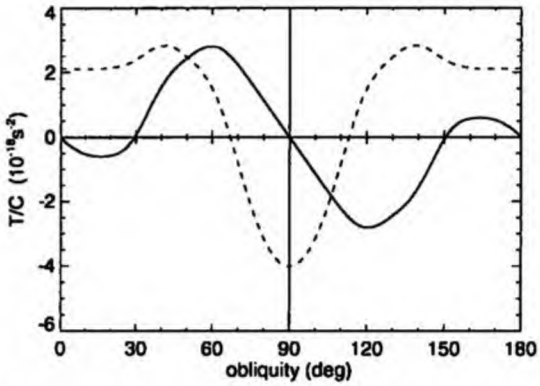

FIG. 10. The same as in Fig. 4, except for a Bacchus-shaped object.

among the randomly generated shapes discussed in the next section.

3.1.5. *Statistical Results for a Sample of Gaussian Spheres*

The quantitative values, though interesting in particular cases, are not the most important conclusion from the previous sections. Rather, we would like to point out the diversity of the YORP results despite the very restricted (and randomly chosen) sample of objects taken into account. This means that there is no "generic" YORP result. We have seen that the obliquity may be driven to any value (with probably a slight preference to 0°, 90°, and 180°) and the asymptotic states may be characterized by either deceleration or acceleration of the rotation rate (with more likely the case of despinning). In several applications, mostly related to the Yarkovsky orbital perturbations on a large sample of "individually undefined" objects, we might be interested in a statistical description of the YORP results. This is the case of understanding the role of the Yarkovsky effect in meteorite or near-Earth asteroid delivery (e.g., Farinella and Vokrouhlický 1999, Bottke *et al.* 2000, 2001a, Vokrouhlický and Farinella 2000) or Yarkovsky-driven diffusion processes in the asteroid families (Nesvorný *et al.* 2002, Bottke *et al.* 2001b). For this purpose we computed the YORP torques on a sample of 500 Gaussian random spheres generated by the Muinonen technique briefly recalled in Section 2.2. All bodies have an equivalent radius of 1 km, have a mean density of 2.5 g/cm^3, and are assumed to move on a circular orbit at 2.5 AU from the Sun.

Figures 11 and 12 show the $\bar{T}_\epsilon$ and $\bar{T}_s$ torques, each for 30 and 10 typical objects (more data would make the figures too busy). To better explore the results we distinguish the different cases according to our previous classification; namely, Fig. 11 shows 30 type I and II results and Fig. 12 shows 10 type III and IV results. We found that the abundance of the type I and II cases is approximately the same, 39.2% and 40.4%, while type III and IV cases occur statistically less frequently (only 10.2 and 6.2% of all cases). As previously, mentioned, we have also occasionally identified peculiar cases with two nodes of $\bar{T}_\epsilon$ in the (0°, 90°) obliquity range that cannot be fit into any of the four classes—there were 20 such cases in the sample of 500 generated objects. In principle, the number of these nodes is not limited and the likelihood of the complicated cases decreases quickly with number of nodes. Since the classification is not a substantial result of our paper (rather it is a mean to more easily distinguish different possible results), we do not extend the classification given here for these more complicated cases.

Separating the results according to the classes introduced here fixes the behavior of the $\bar{T}_\epsilon$ torque, but it does not constrain the $\bar{T}_s$ torque. Figures 11 and 12 indicate that the *asymptotic deceleration* of the rotation frequency is statistically much more likely than its acceleration (here "asymptotic" means at the obliquity value toward which YORP drives the spin axis at long term, i.e., 90° for the type I and 0 or 180° for the type II solutions). This result may look peculiar, but we want to warn the reader not to draw hasty conclusions. We have carefully checked that there is an equal likelihood of positive value of T_s moment *at a given point on the orbit* among the sample of the randomly

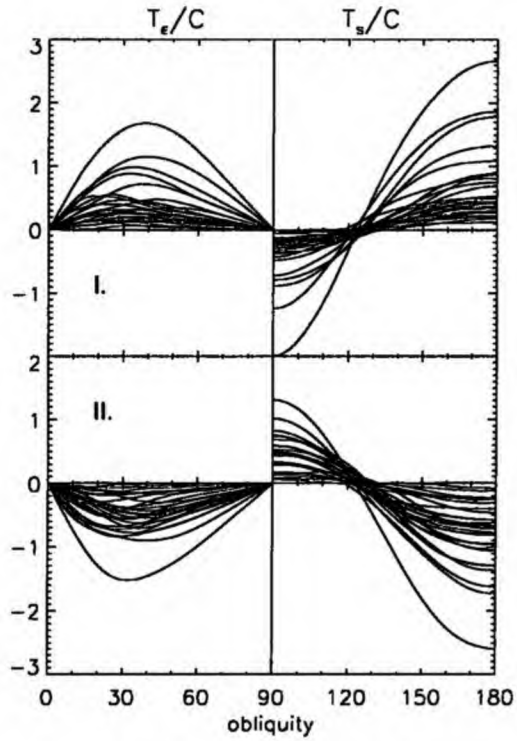

FIG. 11. Behavior of the $\bar{T}_\epsilon(\epsilon)/C$ (left, $\epsilon \leq 90°$) and $\bar{T}_s(\epsilon)/C$ (right, $\epsilon \geq 90°$) for a randomly chosen 30 cases from the sample of Gaussian spheres. The values in the complementary parts of the obliquity interval follow from the obvious symmetries $\bar{T}_\epsilon(180 - \epsilon) = -\bar{T}_\epsilon(\epsilon)$ and $\bar{T}_s(180 - \epsilon) = \bar{T}_s(\epsilon)$. The upper part of the figure corresponds to the type I solutions, while the lower part of the figure corresponds to the type II solutions. The ordinate units are 10^{-18} s^{-2}. Note that in both cases there is an asymmetry in the asymptotic deceleration/acceleration of the rotation frequency toward deceleration.

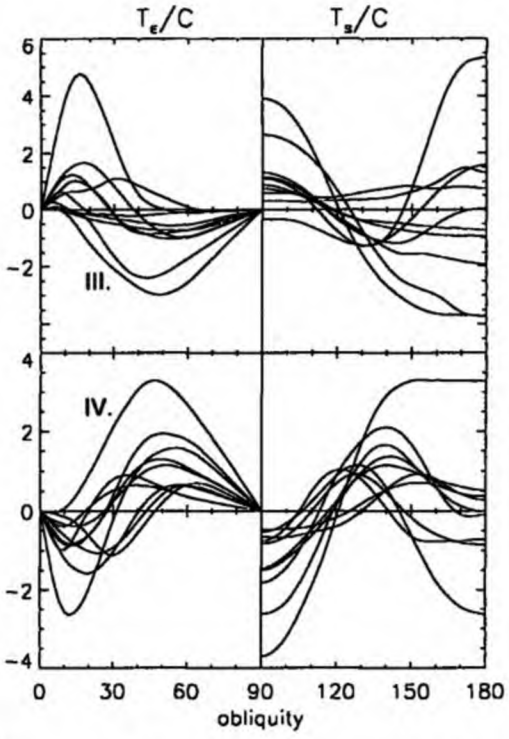

FIG. 12. The same as in the Fig. 11, except for for 10 randomly chosen ype III and IV results (more examples would make the figure too busy). The rdinate units are 10^{-19} s^{-2}.

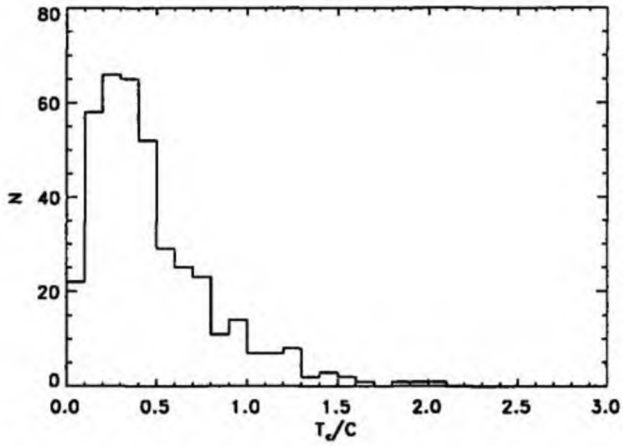

FIG. 13. Distribution of maximum values of $\bar{T}_\epsilon/C$ for type I and II cases among the sample of 500 Gaussian random spheres. Abscissa units are 10^{-18} s^{-2}.

generated asteroids (even when we average over the rotation cycle). This finding fits the intuitive idea that might be gained, for instance, from Fig. 1 in Rubincam (2000): YORP may equally well accelerate or decelerate the rotation (imagine two senses of rotation of the windmill-shaped asteroid). But here we refer on the asymmetry of the YORP effect at the asymptotic value of its long-term evolution (and, moreover, averaged over both the rotation and revolution cycles). This is by no means an intuitive quantity, and we in fact did not find such an easy argument in favor of our result (except a careful check of our code). A part of this problem may also be that our representation is actually not entirely complete; as mentioned in Section 2 the YORP naturally drives the rotation from the principal-axis state. The statistics of the asymptotic rotation at the final state therefore need to be substantiated within a more complete model in the future.

Note that within one type there is a significant scatter of the magnitude of the YORP effect between the minimum and maximum strengths. Obviously, more "regular" objects are subject to a smaller effect while YORP is larger for more irregular-shaped objects. In Section 2 we recalled a trivial result, that the YORP effect is nil for spherical bodies. It can however, be easily shown that the averaged torques $\bar{T}_s(\epsilon)$ and $\bar{T}_\epsilon(\epsilon)$ vanish for triaxial ellipsoids (see Rubincam 2000). Figure 13 shows the distribution of the maximum values of $\bar{T}_\epsilon(\epsilon)$ for obliquities within the (0°, 90°) range for the population of 196 identified type I cases from the entire sample of 500 Gaussian spheres. Although the spherical bodies are statistically absent in our sample (Fig. 2), a relative "excess" of small values in Fig. 13 is caused by objects with shapes that are rather well approximated by an ellipsoid.

Figure 14, showing the distribution $p(\epsilon)$ of the asymptotic obliquity values from the whole sample of objects, confirms that the values 0° (and 180°) and 90° are dominant. The intermediate values, corresponding to the type III class, represent a minority of cases (in total only 6.3%). When constructing $p(\epsilon)$ we assume a random initial orientation of the spin axis. This means, for instance, that in the case of the type IV solution we assign $(\cos\epsilon_*)$ probability of the 90° asymptotic solution of the obliquity and $(\sin^2(\epsilon_*/2))$ probabilities to 0° and 180° asymptotic values of the obliquity. The results indicate that the likelihood of the 90° ("in-plane") asymptotic obliquity is about the same as the sum of the

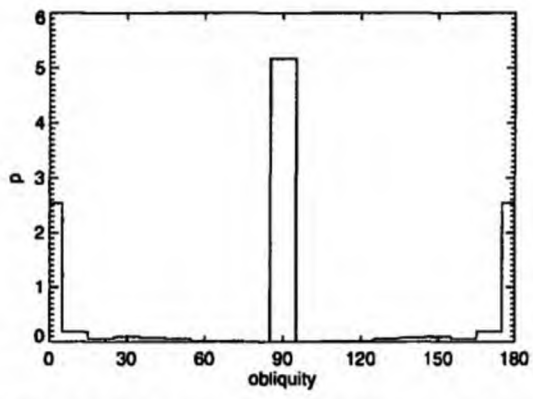

FIG. 14. Distribution $p(\epsilon)$ of the asymptotic obliquities of the YORP evolution for the sample of 500 Gaussian random spheres. The maximum of the distribution is normalized such that the integral $\int_0^\pi d\epsilon p(\epsilon)\sin\epsilon$ is unity.

0° and 180° ("perpendicular") asymptotic states. The majority of these cases are produced by the type I and type II cases.

As mentioned in Section 1, the Yarkovsky effect, together with a slow chaotic diffusion, may significantly influence dispersion of (small) members of the asteroid families and thus help to reconcile inconsistency between the velocity fields inferred from the families and those from the hydrocode simulations (see Nesvorný *et al.* 2002, Bottke *et al.* 2001b). Together with the problem of leaking of small asteroids from the main belt (e.g., Farinella and Vokrouhlický 1999, Bottke *et al.* 2001a), the histories of asteroid families strongly motivate understanding of the spin axis evolution of the kilometer-sized asteroids.

Given this motivation, and using the YORP data on the sample of 500 Gaussian random spheres, we may investigate several interesting problems. For instance, we sought the characteristic YORP time scale to reach the slow-rotation state for the small members of the asteroid families in the main belt. Starting with a generic orientation of the spin axis, assumed isotropic in space, and a 5-h rotation period, we found that a small member of the Themis family with a characteristic radius of 1 km reaches the rotation period of 100 h in ≈35 Myr (in the same time the initial obliquity is tilted to its asymptotic value). This is a median time computed over a large number of simulations where we considered 319 objects of YORP type I and type II from our sample of Gaussian random spheres. For each body we performed 500 simulations of the long-term time evolution of the rotation state. We assumed a bulk density of 1.3 g/cm^3 and recalibrated the mean distance to the Sun to 3.13 AU. Obviously, the rotation of larger bodies would evolve more slowly, approximately with the square of the characteristic size. A similar result was found also for small members of the Flora family; here the closer proximity to the Sun is compensated by the assumed higher bulk density of the asteroids (≈2.5 g/cm^3). Such results indicate that the reinitialization of the rotation state of small family members across the whole asteroid belt might be very frequent since the family formed (≈Gyr or longer in some cases). The influence of the YORP cycles thus needs to be taken into account, or at least estimated, in modeling the long-term dynamical fate of the asteroid families and leakage of kilometer-sized asteroids from the main belt.

3.2. The Role of the Solar Torque and Precession of the Orbit

Apart from the YORP effect and collisions, the gravitational torque due to the Sun represents an additional phenomenon that affects the asteroid spin axis orientation over the long term. (Planetary torques may be relevant for the Earth-crossing population of asteroids, but they are negligible for the main belt asteroids.) Were the orbit fixed in space, the resulting effect of the solar torque would not be important for Yarkovsky applications. Namely, it would consist of a regular precession with frequency ($\approx \alpha \cos\epsilon$, where α is the precession constant "at zero obliquity") around the normal to the orbital plane, thereby leaving the obliquity ϵ constant. Assuming the principal-axis rotation we have

$$\alpha = \frac{3}{2}\frac{C-(A+B)/2}{C}\frac{n^2}{\omega}\frac{1}{(1-e^2)^{3/2}}, \tag{8}$$

where (A, B, C) are principal moments of inertia, n is the mean orbital motion, and ω is the proper rotation frequency. The estimated minimum periods of such forced precession range between ≈0.3 Myr and several million years, depending on the object's oblateness, distance from the Sun, and rotation period. Notably, by taking the average value of the dynamical ellipticity $[C-(A+B)/2]/C \approx 0.3$ for small asteroids (Fig. 2) and a 5-h average rotation period we obtain the maximum precession rates α in different parts of the asteroid belt as indicated in the Table I.

TABLE I

Estimated Values of the Precession Constant α at Zero Obliquity for Asteroids at Different Location in the Main Belt Compared to the Proper Frequency s of the Nodal Precession Rate

Family	α ("/year)	s ("/year)
Flora	27	35
Eunomia	16	52
Themis	10	103

The situation is, however, complicated by the fact that the orbital plane is not fixed in space, but it is instead perturbed by the gravitational influence of the planets. The fundamental point here is that some of the frequencies by which the orbit precesses (or oscillates) may be close to the estimated frequency ($\approx\alpha\cos\epsilon$) at which the asteroid spin axis precesses around the orbit due to the solar torque (see Table I). This proximity may cause complex resonant effects and significantly influence the long-term evolution of the spin axis orientation (and thus its obliquity). Even in the cases when the initial forced precession is outside of resonance with the planetary perturbations of the orbit, the underlying slow obliquity and rotation frequency evolution due to the YORP effect may drive the rotation state toward some of the resonances. Bottke *et al.* (2000) noticed the potential importance of the spin axis precession due to the solar torque, though they did not mention explicitly the possibility of the resonance phenomena [see also a previous work by Vokrouhlický and Farinella (1998)]. Here we want to develop the problem in more detail and show the potential complexity of individual rotation histories of asteroids in different parts of the main belt. Our particular aim is to see whether the YORP evolution itself may represent in average the typical rotation history of a small asteroid in the main belt (including the quantitative aspects such as the time scale to drive the rotation to a slow rotation limit).

We should not neglect to mention that the resonant spin axis dynamics has been extensively studied within the context of the long-term evolution of planetary rotation. Following these works, Skoglöv *et al.* (1996) and Skoglöv (1997, 1999) then

applied the same approach to investigation of the rotation state of asteroids. To our mind, the powerful global approach of Laskar and his collaborators (e.g., Laskar and Robutel 1993, Laskar *et al.* 1993, Néron de Surgy and Laskar 1997) is also the most suitable for our application. We thus refer the reader for more details to Laskar and Robutel (1993) and Néron de Surgy and Laskar (1997), while here we just summarize the principal steps and assumptions.

The power of Laskar's approach is mainly that the irrelevant degrees of freedom are eliminated by averaging, while the fundamental degrees of freedom are retained. In the absence of spin–orbital resonances, appropriate for our application, we can thus average over fast proper rotation and revolution around the Sun (as was done for the YORP effect). Considering the effect of the solar gravitational torque only, the fundamental degree of freedom is described by canonically conjugated variables $X = L\cos\epsilon$ and ψ; here L is the conserved angular momentum of rotation, ϵ is the obliquity, and ψ is the precession in longitude. Note that here we implicitly assume rotation about the principal axis of the inertia tensor, which seems justified for at least multikilometer-sized asteroids (see Section 3.3). It turns out to be suitable to introduce a complex variable $\chi = \sin\epsilon\exp(i\psi)$ (with $i = \sqrt{-1}$), so that $\cos\epsilon = \sqrt{1-\chi\chi^*}$ (where the star denotes a complex-conjugated quantity). The resulting equations describing the long-term evolution of the spin axis orientation then read (e.g., Laskar and Robutel 1993, Néron de Surgy and Laskar 1997)

$$\frac{d\chi}{dt} = i\chi(\alpha\cos\epsilon - 2\Phi) + \Psi^*\cos\epsilon, \tag{9}$$

with the auxiliary functions

$$\Phi = \frac{1}{2i}\left(\zeta\frac{d\zeta^*}{dt} - \zeta^*\frac{d\zeta}{dt}\right), \tag{10}$$

$$\Psi = \frac{2}{\sqrt{1-\zeta\zeta^*}}\left(\frac{d\zeta}{dt} - i\zeta\Phi\right). \tag{11}$$

The complex variable $\zeta = \sin(I/2)\exp(i\Omega)$ describes orientation of the orbital plane in space; I is the inclination and Ω is the longitude of the ascending node. If ζ were constant, we easily verify that the solution of (9) is the regular precession of ψ with frequency $\alpha\cos\epsilon$ (and ϵ = constant). However, the complexity of the problem stems from the fact that ζ is time dependent, describing orbital motion due to planetary perturbations. It may be given by a Fourier series approximation from the analytic theory, or—as in our case—as a purely numerical output from integration of the orbital motion of an asteroid. As a part of another research project we have integrated orbits of hundreds of asteroids in main belt families over hundreds of Millions of years (e.g., Nesvorný *et al.* 2002), and we "borrow" these results for our study of the long-term evolution of their spin axes.

We mention that in our simulations we actually used a slightly modified variable $\chi' = (1-\cos\epsilon)\exp(i\psi)$ that suitably relegates the coordinate singularity to $\epsilon = 180°$. The corresponding dynamical equations then look a little less compact but they are easily obtained from (9).

Equation (9) can be generalized to include the YORP effect by extending the right-hand side by a term

$$\left(\frac{d\chi}{dt}\right)_{\rm YORP} = \chi\frac{\bar{T}_\epsilon}{C\omega}\tan\epsilon. \tag{12}$$

The equation $d\omega/dt = \bar{T}_s/C$ [see (3)] should be considered along with this generalized form of (9). Note that the precession constant α from (8) depends on the rotation rate ω, which presents an additional coupling of the resulting system of three differential equations for variables (χ, ω). Equation (8) apparently suggests $\alpha \propto 1/\omega$; hence increasing the precession constant as the YORP effect asymptotically decelerates the rotation rate, but the exact dependence $\alpha(\omega)$ may be more complicated because the dynamical ellipticity $[C-(A+B)/2]/C$ may also depend on ω. As an example we mention that for planets, with fluid or viscoelastic layers, the rotational deformation leads approximately to $[C-(A+B)/2]/C \propto \omega^2$. For smaller asteroids that are likely to be rubble piles we do not have an exact estimate of the rotational deformation, so that at the zero approximation we shall assume $[C-(A+B)/2]/C \approx$ constant. This should not hold for rotation periods approaching the zero-strength disruption limit by the centrifugal force, which appears to be about 2 h (consistent with the upper limit of the observed rotation periods for asteroids larger than ≈200 m in size; Pravec and Harris 2001).

Following the motivation from the end of Section 3.1.5, we next illustrate the complexity of the long-term evolution due to the aforementioned effects for small members of Themis and Flora families. Interested readers may found additional results for small asteroids in the Eunomia family on our Web site http://sirrah.troja.mff.cuni.cz/~davok/.

3.2.1. *Example: Themis Asteroids*

We intentionally start our discussion with Themis, since the effects of the mutual interaction between the gravitational solar torque and the orbital excitations is weak and restricted to isolated events. There are several reasons for this conclusion, the most important of which are (i) small orbital inclination of the Themis asteroids and (ii) a good separation of the proper and forced frequencies by which the orbital plane is perturbed from the estimated precession rate of the spin axis (see Table I). Fourier analysis of the orbital data, namely, the $\zeta = \sin I/2\exp(i\Omega)$ variable and the Ψ quantity from (11), indicates that in the relevant range of frequencies their spectrum is composed of well-isolated lines (dominant frequencies are the proper frequency $s \approx 103''$/year and the forced frequencies $s_6 \approx 25.7''$/year, $s_7 \approx 2.9''$/year, and $s_8 \approx 0.7''$/year and the relevant sidebands). This suggests a near regularity of the spin axis evolution, except from singular resonant cases. The YORP effect may obviously drive the rotation evolution toward these

resonances, but none of them is expected to trigger a large-scale chaotic motion of the spin axis.

As far as the YORP effect is concerned, we shall use a typical ("average") result from the Gaussian-sphere sample of kilometer-sized objects discussed in Section 3.1.5 and scale them to the appropriate distance from the Sun. In the Themis case, we also renormalize the assumed mean density of the asteroid to 1.3 g/cm^3, which better fits the C-type asteroids. The orbital data are taken from a 150-Myr direct numerical integration of a test particle at 3.13 AU (the eccentricity and inclination fits the mean of the Themis family). Gravitational perturbations of the outer planets were included. Our intention is not to investigate all possible results spanning the whole initial data parameter space, such as the initial period, obliquity, precession constant, and so on, but rather to show several examples. A more systematic search is beyond the scope of this paper.

Figure 15 shows one of the possible histories of the rotation state of a 2-km-sized Themis asteroid (with initial data given in the caption of the figure). As in all the examples that follow, we always compare two simulations: (i) a restricted one with only the YORP effect included, and (ii) a more complete simulation including both the YORP effect and the gravitational solar torque. Notice that both models yield very similar results. In the complete model, the obliquity gets only very slightly perturbed as a consequence of the passage through the s_7 resonance (when $d\psi/dt - s_7 \simeq 0$); apart from this small effect the restricted model, containing the YORP effect only, follows the results of the complete model closely. In both cases, we notice the outstanding characteristics of the YORP evolution (see Rubincam 2000). Notably, the obliquity is secularly driven to an asymptotic value of 90° (type I case); given the small initial obliquity, the rotation period is first decreased to about 4 h, while at later epochs of the YORP evolution it rapidly increases. We terminate the simulation when the rotation period reaches 100 h, since our model is inappropriate and incomplete for longer periods for two reasons. First, nondisruptive collisions may easily modify the rotation state at this slow-rotation phase, and second, the averaging method used for modeling the YORP effect may not be applicable when the rotation period becomes a fair fraction of the revolution period. It may also be noticed that about 90 Myr is enough time to reach the near-asymptotic state and tilt the axis by 70° in obliquity. Regarding the size-scaling of the YORP torques, we may conjecture that this time will scale with the square of the characteristic length of the object. For a 10-km-sized asteroid the evolution from Fig. 15 may thus take ≈2.25 Gyr.

Figure 16 shows another possible history of the Themis kilometer-sized asteroid rotation. The main difference from the previous example concerns the YORP type; here, the asteroid is assumed to belong to the type II class. The obliquity is then driven to the 0° state. Nevertheless, this expected evolution is temporarily inverted in the complete model due to a capture in s_6 and s resonances; the s_7 resonance is too weak for a capture. Figure 16c clearly illustrates that the precession rate $d\psi/dt$ is

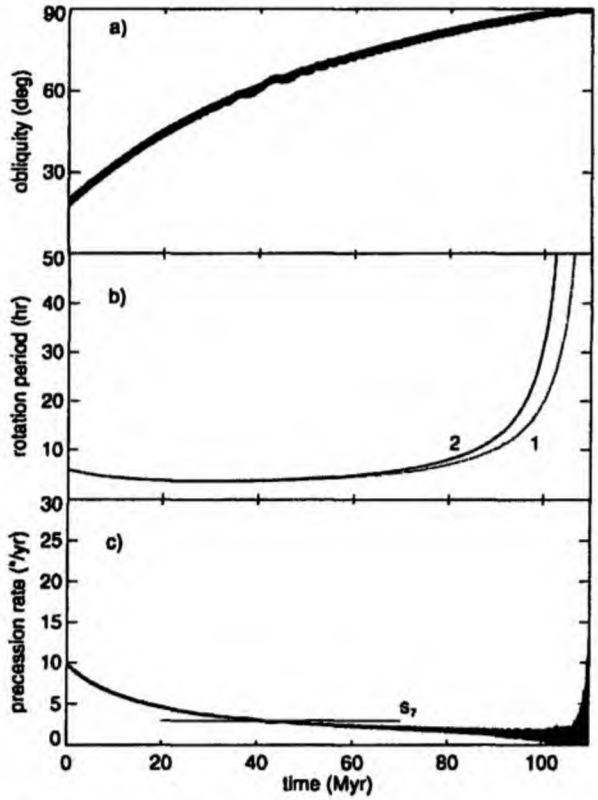

FIG. 15. Long-term evolution of (a) the obliquity ϵ, (b) the rotation period P, and (c) the forced precession frequency $d\psi/dt$ for a typical, kilometer-sized Themis asteroid. The simulation includes the gravitational torque due to the Sun and the YORP effect; initial data are $\epsilon(0) = 20°$, $P(0) = 6$ h, and the precession constant $\alpha = 10''$/year. The black curve (labeled 2) shows evolution with only the YORP effect included, the gray curve (labeled 1) corresponds to evolution with both the YORP effect and the solar gravitational torque. The asteroid orbit evolves due to planetary perturbations. The YORP solution corresponds to type I according to our classification (i.e., driving the spin axis to the orbital plane).

trapped to the resonance value. Since the rotation rate is permanently decayed, the obliquity is forced to decrease, as can be seen between 47 and 56 Myr (Fig. 16a). The situation is similar to a temporary capture of dust particles in the exterior orbital resonances with planets, where eccentricity is forced to increase when the orbit is trapped in the resonance as a result of continuous draining of the angular momentum with "stopped evolution" of the semimajor axis. However, even disregarding such fine details of the evolution, it can still be rather well approximated by the restricted model with the YORP effect. This is true, in particular, with regard to the time scale needed to reach the near-asymptotic state of a very slow rotation.

We have seen in Section 3.1 that the YORP obliquity evolution may asymptotically reach any value in the admissible range. This is the type III case, which is illustrated in Fig. 17. The evolution is fairly similar to that from Fig. 16, with the

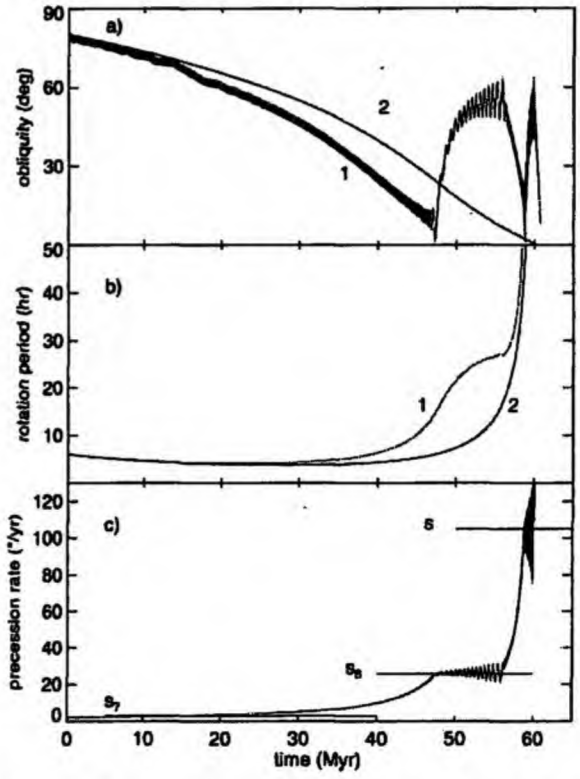

FIG. 16. The same as in the Fig. 15, except for for the initial obliquity $\epsilon(0) = 80°$ and the YORP effect of type II (i.e., the spin axis tends to align with the normal to the orbital plane). Notice that the precession rate $d\psi/dt$ (c) is temporarily captured in the s_6 and s resonances; since the rotation period is constantly increased, the obliquity is forced to resonantly increase (a).

...ly difference being in the asymptotic value of the obliquity. The s_6 and s resonances temporarily capture the slow increase of the precession rate, but the permanent decrease of the rotation energy eventually releases the evolution from these resonances. The unavoidable slow-rotation late phase will then be interrupted by a collision with a sufficiently large projectile. Resonance captures may not necessarily result in prolonging the spin axis evolution; this is actually seen in Fig. 17, since the complete model evolution to the 100-h rotation period takes some 8 Myr less than in the YORP case only. Compared to the entire ≈110-Myr evolution, this is only a minor effect. However, there are also cases where the resonances may halt the rotation evolution for a more considerable period. Figure 18 shows an example with the underlying YORP effect of type IV. We may notice long-lasting captures in the s_6 and s resonances. As a result, the rotation evolutions to the long-period state takes longer (140 Myr compared to 90 Myr) when only the YORP effect is taken into account.

Despite of the limited number of cases discussed here, we may preliminarily conclude that the YORP evolution itself is a very good approximation of the complete model. The rare and separated resonances between the forced precession of the spin axis due to the solar torque and the orbital excitations may temporarily affect the smooth YORP evolution, but they do not generally result in a large-scale wandering of the spin axis.

3.2.2. *Example: Flora Asteroids*

We have repeated the previous examples for the small (kilometer-sized) members of the Flora family. In practice this means that we rescaled the magnitude of the YORP-averaged torques to the 2.2 AU distance from the Sun and we used a numerically integrated orbit of the asteroid Flora over a 140-Myr timespan. We assumed a mean density of 2.5 g/cm^3, conformal to the S-type asteroids. The closer proximity to the Sun results in two important differences if compared to the Themis case: (i) since the orbit is further from Jupiter, the proper nodal frequency s is smaller (see Table I) and gets close to the forced frequencies (especially $s_6 \simeq 25.7''$/year), and (ii) since the revolution period is shorter, the precession constant α increases for a typical Flora asteroid to approximately the s_6 value. The first item means that the Fourier spectrum of the ζ and Ψ variables

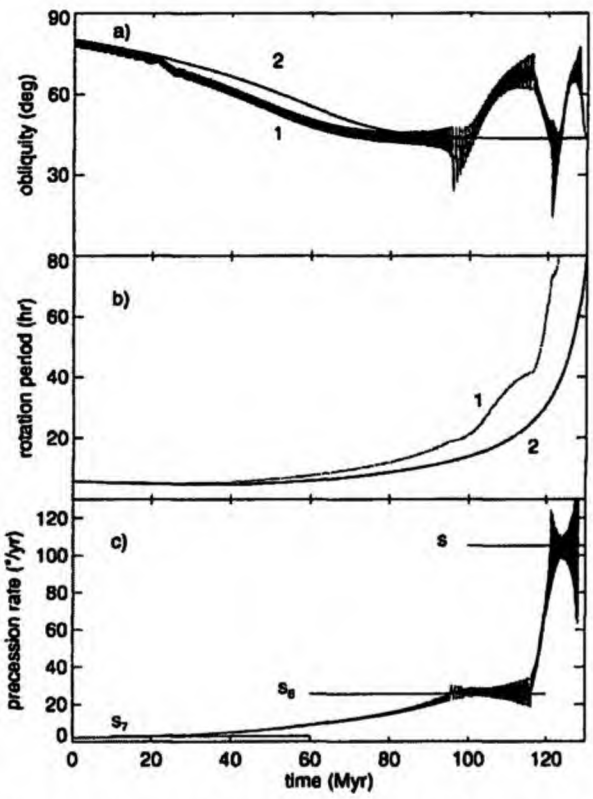

FIG. 17. The same as in the Fig. 15, except for the initial obliquity $\epsilon(0) = 80°$ and the YORP effect of type III (i.e., the obliquity is asymptotically driven to an intermediate value of ≈44°).

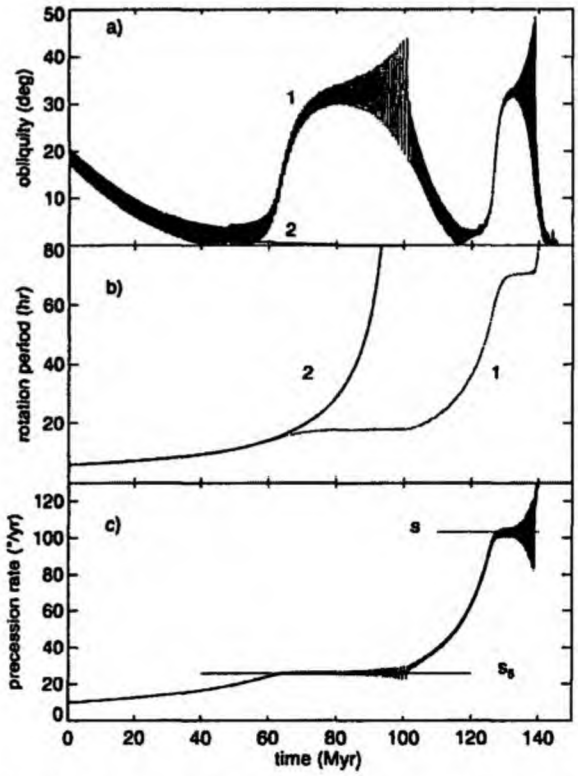

FIG. 18. The same as in the Fig. 15, except for the YORP effect of type IV i.e., the spin axis asymptotically driven either to the orbital plane or into alignment with its normal depending on the initial value of the obliquity; in this case it approaches the 0-obliquity state).

is no longer composed of well-isolated lines, but the bulk of the signal is poorly periodic and the spectrum contains clusters of lines [compare, e.g., with the spectrum of A and B variables for Mars from Laskar and Robutel (1993)]. The resonances may "communicate" with each other and drive the precession rate $d\psi/dt$ over a larger range. Such a chaotic wandering of ψ may trigger a similar effect in the obliquity, as has been found by Laskar and his collaborators for most of the inner planets and Skoglöv for some asteroids. The second item mentioned here means that the typical precession rates for the Flora asteroids should be located close to these resonance clusters. As a result of this qualitative insight, we may expect a less regular evolution of the obliquity than in the Themis case. Additionally, higher inclination of the Flora orbits may cause larger oscillations of the obliquity.

Figure 19 formally corresponds to the same initial data as in Fig. 15, except with the Flora orbit and YORP parameters. Apart from larger amplitude oscillations of the obliquity (and the precession rate), the results are comparable. The YORP evolution itself corresponds rather well to the complete model result. Interestingly, the time scale needed to reach the asymptotic, slow-rotation state is approximately the same as in the Themis case (see also results in Sections 3.1.5); the larger radiation flux in the Flora zone is roughly compensated for by a higher mean density of the Flora S-type asteroids.

Figure 20 shows a more perturbed case of the possible Flora-asteroid rotation history, notably corresponding formally to the same initial data as in Fig. 16. A type II YORP effect drives the alignment with the orbital angular momentum at late epochs of the evolution, which—together with the secularly decelerated rotation rate—means that the precession rate encounters the large resonance zone. When this occurs (at ≈22 Myr), the obliquity undergoes large oscillations. Figure 16c indicates that the evolution alternates in a random way between the nearby s_6 and s resonances. Eventually, the resonance lock is interrupted and the evolution quickly heads the slow-rotation phase. The entire timespan is shortened about 25% compared with the YORP-only evolution.

Significant obliquity perturbations may be also seen in Fig. 21, the Flora counterpart of the Themis simulation shown in Fig. 17. Here, the obliquity approaches an intermediate asymptotic value of about 44° and the resonance phenomena in the complete model largely mask the smooth YORP-only evolution. In

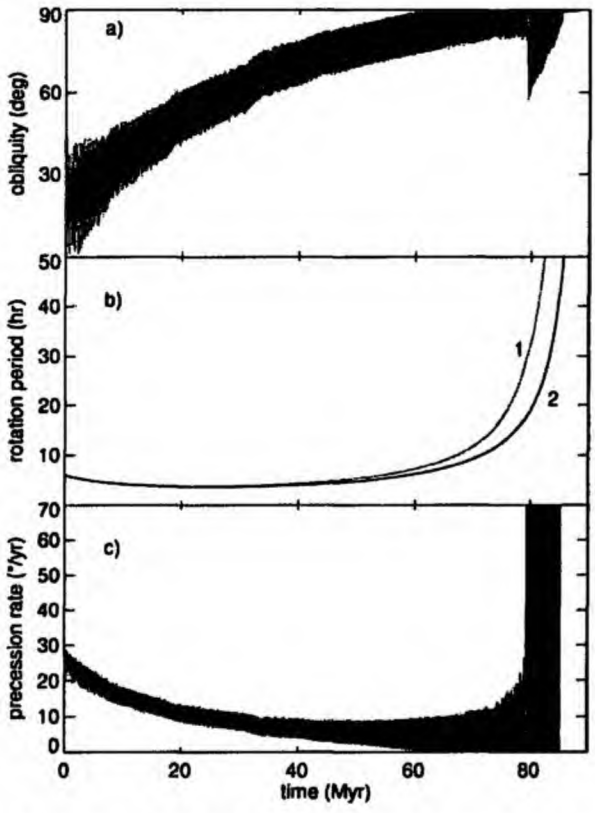

FIG. 19. The same as in the Fig. 15, except for a kilometer-sized Flora asteroid.

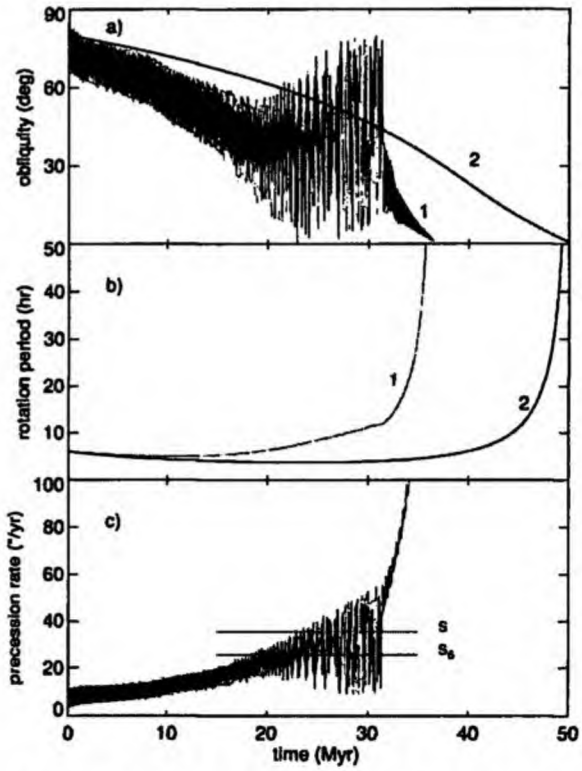

FIG. 20. The same as in the Fig. 16, except for a kilometer-sized Flora teroid.

contrast to the previous example, the resonance effects delay the rotation evolution toward the long-period phase by some 20%. It is, however, very important to notice that despite the difference in the obliquity evolution, the accumulated Yarkovsky change in the semimajor axis would differ by only ≈10%. This actually applies also to the example shown in Fig. 20, since the shorter evolution is partially compensated for by a smaller obliquity (in average), which increases the semimajor axis drift for the diurnal variant of the Yarkovsky effect.

Our final example, Fig. 22, demonstrates a less frequent case when the rotation histories as given by the complete and YORP-only models are significantly different. This is the case of the type IV YORP effect, which may be asymptotically driven either to 0° or 90° obliquity depending on its initial value. The chosen initial data (namely, 20° for the obliquity) are nominally attracted by the 0°-obliquity asymptotic state if only the YORP effect is assumed. However, the large oscillations of the obliquity caused by the s_6 resonance may invert this evolution and drag the obliquity toward the complementary asymptotic value of 90°. This case is actually seen in the evolution presented in the Fig. 22 (we stopped the simulation at 140 Myr since this is the time interval over which we have the orbital data). We should, however, comment that this last example is statistically less frequent (see Section 3.1.5 where we found that the type IV YORP objects comprise only ≈6% of all bodies).

3.3. Comments on Inelastic Relaxation of the Tumbling State of Rotation

The assumption of rotation around the principal axis of the inertia tensor is one of many approximations we adopted in this paper. A single periodicity of lightcurves of most asteroids does suggest that this is a commonly satisfied situation, but in some cases we have evidence for non-principal-axis (tumbling) rotation (e.g., Toutatis and Comet Halley). We have seen the YORP effect implies at least two reasons for analyzing whether the principal-axis rotation is appropriate for small asteroids: (i) the YORP effect naturally produces torque components, which drive the rotation out of the fundamental-energy state, and (ii) even if (i) is weak the predicted long-term evolution of the asteroidal rotation due to the YORP effect may include a final slow-rotation phase, interrupted eventually by a larger collisional event that may increase the rotation rate. After undergoing such an event, the asteroid rotation should be generically placed in an excited (tumbling) state. On the other hand, inelastic processes tend to dissipate the energy of the wobble. A comparison of a characteristic time scale for such dissipative processes with that

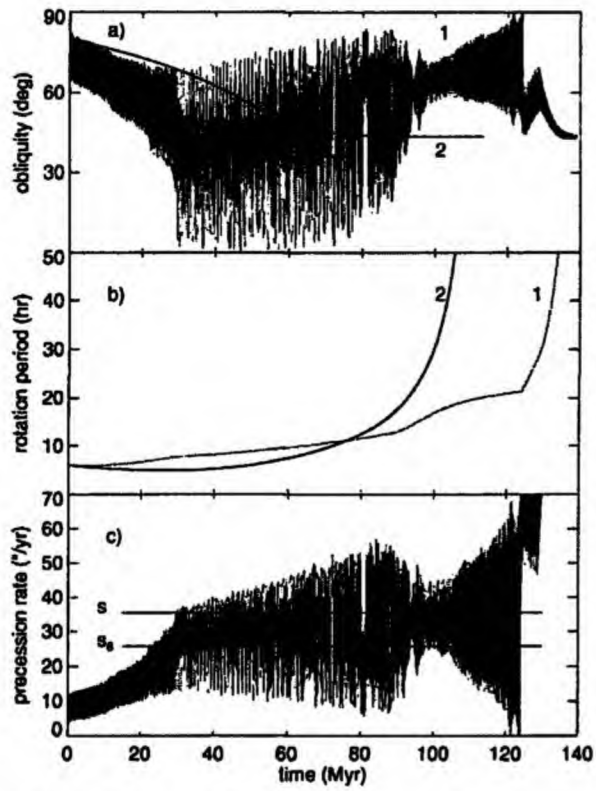

FIG. 21. The same as in the Fig. 17, except for a kilometer-sized Flora asteroid.

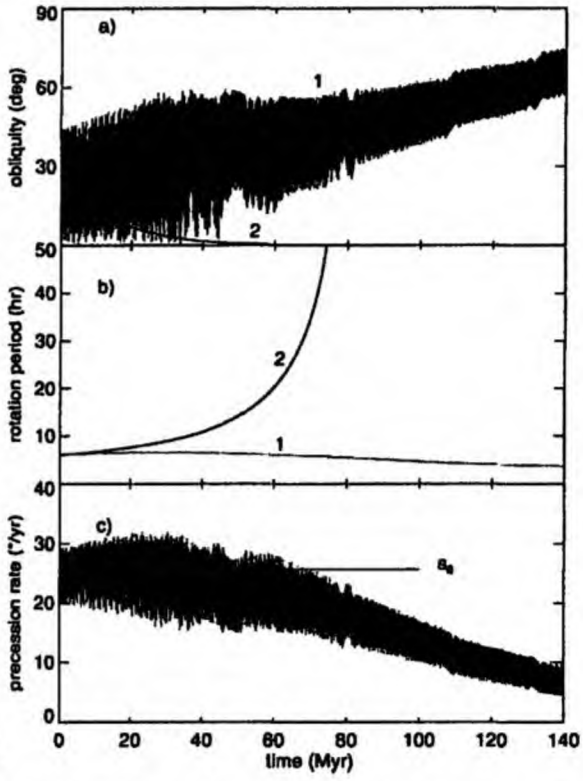

FIG. 22. The same as in the Fig. 18, except for a kilometer-sized Flora asteroid.

of the YORP evolution is then of fundamental importance for understanding whether the principal-axis rotation assumption is justified (over at least a major part of the YORP evolution). Rubincam (2000) noted these facts and here we are try to elaborate the corresponding estimations in somewhat more detail.

Free precession of a rotating body causes alternating stresses in its interior. A variety of processes, such as unpinning of dislocations, sliding at grain boundaries, or interaction of internal faults, then result in irreversible dissipation of the rotation energy, which is thus damped toward the minimum state of rotation around the principal axis of inertia tensor. Since a detailed modeling of such molecular-level microscopic processes is very complicated, if not impossible, one usually characterizes the energy dissipated over one alternating cycle of internal forces by an empirical quality factor Q. Its value has been determined from a number of astronomical observations and laboratory measurements for a variety of materials and frequencies of their excitations. It has been indeed found that the Q values are compositional and frequency dependent. Relevant periods at which asteroidal interiors are strained range from about half a day to several days (excluding the slowly rotating population of asteroids). Not only do we luck any direct observational calibration of the quality factor for asteroids, but also the values obtained by different techniques typically occur at different frequencies and for different composition than the presumed rubble piles for small asteroids. The quality factor Q is thus largely uncertain in our application; admissible values range from about 100 (or even less) to about 300. The upper value is consistent with the high-frequency determinations for lithospheric rocks (both in the laboratory and from the free modes of Earth oscillations). At lower frequencies, Q typically decreases, satisfying roughly a power law, down to about 30 for Earth tides (monthly and semimonthly periods). A value of $Q \approx 100$–150 thus seems to be likely for small, rubble-pile asteroids with strain periods of a few days; this value is also commonly adopted for the small planetary satellites (e.g., Peale 1999). The low-rigidity C types may have even a slightly smaller Q, conformal to the assumed value for Comet Halley.

Burns and Safronov (1973) determined, from general principles and qualitative reasoning, that the characteristic time scale to dissipate the free-precession energy is

$$T \approx \kappa \frac{\mu Q}{\rho R^2 \omega^3}, \tag{13}$$

where R is the radius, ω is the rotation frequency, and μ is the rigidity (or shear elastic modulus) of the asteroid. The major uncertainty here follows from inaccurate knowledge of (i) the quality factor Q (as already mentioned), (ii) the numerical coefficient κ, and to some extent (iii) the rigidity μ. This numerical coefficient κ depends on the geometry of the body and the frequency spectrum of the internal strain. There has recently been some discussion about the appropriate value of κ (e.g., Lazarian and Efroimsky 1999, Efroimsky and Lazarian 2000, Efroimsky 2000), with a tendency for smaller values being favored. Burns and Safronov (1973) determined $\kappa \approx 10$–100 (cgs units), depending on the sphericity of the asteroid (upper value for near spherical objects), while Efroimsky and Lazarian (2000) advocate a value $\kappa \approx 4$–5. Though the latter authors seem to rightly point out the importance of the second harmonic of the wobble frequency, the difference in κ is ultimately not that fundamental given the degree of other simplifications. Moreover (J. A. Burns, private communication), the very low κ results still need to be confirmed by a direct numerical model of a strained, rotating, inelastic body (with currently controversial conclusions). We shall thus assume $\kappa \approx 20$ in the following estimations. As for the rigidity, we shall assume $\approx 5 \times 10^{11}$ dyne/cm^2 for the silicate asteroids (S types), which is consistent with laboratory measurements of elastic moduli of the ordinary chondrites (e.g., Yomogida and Matsui 1983). Actually, this value fits the data of H-chondrites, while L-chondrites have μ typically somewhat smaller. For asteroids located in the outer belt (C types) we assume a smaller value $\approx 5 \times 10^{10}$ dyne/cm^2, fitting approximately the cometary data (with $Q \approx 100$ this is about what other authors suggest; e.g., Jewitt 1997). We thus obtain the following characteristic time scales for relaxation of the free wobble due to the inelastic internal processes: $T \approx 0.36 \times (P_{\rm hr}^3 / R_{\rm km}^2)$ for S types

and $T \approx 0.04 \times (P_{\rm hr}^3/R_{\rm km}^2)$ for C types (here $P_{\rm hr}$ is the rotation period in hours, $R_{\rm km}$ is the radius in kilometers, and T is then given in millions of years). Harris (1994) also considered the problem of the tumbling asteroids and obtains $T \approx 0.05 \times (P_{\rm hr}^3/R_{\rm km}^2)$ in average. This is slightly less than our value for S types, because this author assumed a smaller value of μQ. Taking our estimates and 5 h for the typical rotation period of kilometer-sized asteroids (excluding slow rotators like Mathilde or Toutatis; see, e.g., Pravec and Harris 2001), we have a damping time scale of ≈45 Myr for the S-type and ≈5 Myr for the C-type asteroid of $R_{\rm km} \approx 1$. Since the average rotation rate is approximately constant in the 1–10 range of $R_{\rm km}$, the estimated damping time scales diminish as $\propto 1/R_{\rm km}^2$ in this range of interest.

A comparison with the estimated YORP time scales (e.g., from the statistical result in Section 3.1.5 or the examples in Section 3.2) indicates that the C-type kilometer-sized asteroids might relax toward the fundamental state of rotation around the principal axis of rotation on a time scale shorter than that of YORP evolution. So, as an example, assuming a YORP model with principal axis rotation might be rather well justified for Themis kilometer-sized members. On the other hand, the smallest Flora members may have a damping time scale comparable to (or even longer than) their YORP evolution time scale and we should consider modeling of YORP with some precaution. However, if we would consider Harris's (1994) estimate for the tumbling relaxation, the principal-axis rotation would be well justified even for the small Flora asteroids. We thus tentatively conclude that the simplifying assumption of the principal-axis rotation is rather well justified, being obviously violated only for the unusual, slow-rotation population of asteroids.

4. CONCLUSIONS

The main results of this paper can be summarized as follows:

- We have investigated the role of the thermal radiation torque on the long-term rotation history of small asteroids (up to ≈10 km in size). Except for the unrealistic cases of spherical bodies and perfect ellipsoids, this torque always secularly affects the rotation; in particular the obliquity is slowly driven to some asymptotic value while the rotation period typically secularly increases (a permanent decrease of the rotation period is also possible, but this is statistically less frequent). Four principal approximations were assumed in this text: (i) applicability of the averaging principle, (ii) zero thermal relaxation of the asteroidal surface, (iii) circular orbits (this assumption, however, just conveniently constrains the parameter space of the solutions and does not present a theoretical limitation of our approach), and (iv) the principal-axis rotation state.
- By analysing the functional dependence of the obliquity-affecting torque $\bar{T}_\epsilon$ on the obliquity value, we have classified possible cases of the YORP-induced evolution of the obliquity.
- The YORP torques were computed for 10 shapes of real objects (nine asteroids and Deimos) and also for a large sample of synthetic objects generated by the Gaussian random sphere technique. Since the Gaussian model parameters were fitted to the known shapes of small asteroids, the sample is assumed to well represent the shape characteristics of small Solar System bodies. As a result we were able to estimate a statistically averaged YORP influence on small members of Themis and Flora asteroid families for such properties as the characteristic time scale to reach the asymptotic, slow-rotation regime. This finding is important for improving models of slow semimajor axis dispersion in asteroid families.
- As a particular result, we predict that the YORP effect may be directly observable through change of the rotation frequency of the small near-Earth asteroid 1998KY26 during its next close approach in May 2024.
- If YORP were the only cause of the long-term evolution of the asteroid rotation state, it would drive the obliquity to some particular value (depending on the type). When this value of the obliquity is reached, and the averaging approach is still applicable, the rotation frequency is preferentially decreased. This is a result from the sample of 500 Gaussian random spheres. The less likely case of a permanent spinning up of the body may occur, and we found it, as an example, for an object of Castalia's shape.
- In addition to the slow YORP-induced evolution of the rotation state, we include in our model the influence of the gravitational torque due to the Sun. Since the orbital elements evolve in time due to planetary perturbations, the forced precession of the spin axis may resonantly beat with the orbital excitations. This is indeed the case of small asteroids, with sizes larger than several hundred meters across and with slow enough rotation (≈hours). We illustrate the obliquity effects triggered by such resonant phenomena. The YORP effect may drive the nonresonant states toward the resonances. Meteoroid precursors, with sizes up to tens of meters, presumably rotate fast enough so that the precession rate due to the solar torque is significantly different (smaller) than the orbital excitation. The resonant effects studied in this text are thus likely to be unimportant for these very small objects in the Solar System.
- The assumption of principal-axis rotation seems well justified in average for multikilometer-sized asteroids; however, the kilometer-sized objects may relax toward the principal-axis rotation state slowly. The YORP torque may also continuously drive the rotation state away from the fundamental state of rotation. These effects need to be studied in the future.

A major issue omitted in this paper concerns the role of collisions within the model we investigated. Yet, collisions are necessarily an inherent part of the model, since they must tune the limit to which the asteroids decelerate their rotation rate by the YORP effect. Inclusion of the collisional processes, however, represents an entirely new and vast dimension to the studied problem and we feel that this would already go beyond this introductory paper of the series. We certainly need to return to this issue in the future.

ACKNOWLEDGMENTS

We are grateful to J. Ďurech for indicating to us the importance of the Gaussian random sphere approach by Muinonen; D. Nesvorný is thanked for letting us use available data of his 140-Myr orbital integration of the asteroid Flora. J. Spitale, as a referee, helped to improve the final form of this paper.

REFERENCES

Bottke, W. F., D. C. Richardson, P. Michel, and S. G. Love 1999. 1620 Geographos and 433 Eros: Shaped by planetary tides? *Astron. J.* **117**, 1921–1928.

Bottke, W. F., D. P. Rubincam, and J. A. Burns 2000. Dynamical evolution of main belt meteoroids: Numerical simulations incorporating planetary perturbations and Yarkovsky thermal forces. *Icarus* **145**, 301–330.

Bottke, W. F., D. Vokrouhlický, M. Brož, and A. Morbidelli 2001a. *Yarkovsky-Assisted Escape of Kilometer-Sized Asteroids from the Main Belt.* Presented at *Asteroids 2001*, Palermo, Italy.

Bottke, W. F., D. Vokrouhlický, M. Brož, D. Nesvorný, and A. Morbidelli 2001b. Dynamical spreading of asteroid families via the Yarkovsky effect: The Koronis family and beyond. *Science* **294**, 1693–1696.

Burns, J. A., and V. S. Safronov 1973. Asteroid nutation angles. *Mon. Not. R. Astron. Soc.* **165**, 403–411.

Dobrovolskis, A. R. 1996. Inertia of any polyhedron. *Icarus* **124**, 698–704.

Ďurech, J. 2002. Shape determination of the Asteroid (6053) 1993 BW_3. *Icarus*, in press.

Efroimsky, M. 2000. Precession of a freely rotating rigid body. Inelastic relaxation in the vicinity of poles. *J. Math. Phys.* **41**, 1854–1888.

Efroimsky, M., and A. Lazarian 2000. Inelastic dissipation in wobbling asteroids and comets. *Mon. Not. R. Astron. Soc.* **311**, 269–278.

Farinella, P., and D. Vokrouhlický 1999. Semimajor axis mobility of asteroidal fragments. *Science* **283**, 1507–1511.

Farinella, P., D. R. Davis, P. Paolicchi, A. Cellino, and V. Zappalà 1992. Asteroid collisional evolution: An integrated model for the evolution of asteroid rotation rates. *Astron. Astrophys.* **253**, 604–614.

Farinella, P., D. Vokrouhlický, and W. K. Hartmann 1998. Meteorite delivery via Yarkovsky orbital drift. *Icarus* **132**, 378–387.

Giblin, I., and P. Farinella 1997. Tumbling fragments from experiments simulating asteroidal catastrophic disruption. *Icarus* **127**, 424–430.

Harris, A. W. 1979. Asteroid rotation rates. II. A theory for the collisional evolution of rotation rates. *Icarus* **40**, 145–153.

Harris, A. W. 1994. Tumbling asteroids. *Icarus* **107**, 209–211.

Hartmann, W. K., P. Farinella, D. Vokrouhlický, S. J. Weidenschilling, A. Morbidelli, F. Marzari, D. Davis, and E. Ryan 1999. Reviewing the Yarkovsky effect: New light on the delivery of stone and iron meteorites from the asteroid belt. *Meteorit. Planet. Sci.* **34**, A161–A168.

Jewitt, D. 1997. Cometary rotation: An overview. *Earth, Moon, Planets* **79**, 35–53.

Klinkrad, H., Ch. Koeck, and P. Renard 1990. Precise satellite skin-force modelling by means of Monte-Carlo ray tracing. *ESA J.* **14**, 409–430.

Laskar, J., and P. Robutel 1993. The chaotic obliquity of the planets. *Nature* **361**, 608–612.

Laskar, J., F. Joutel, and F. Boudin 1993. Orbital, precessional, and insolation quantities for the Earth from −20 Myr to +10 Myr. *Astron. Astrophys.* **270**, 522–533.

Lazarian, A., and M. Efroimsky 1999. Inelastic dissipation in a freely rotating body: Application to cosmic dust alignment. *Mon. Not. R. Astron. Soc.* **303**, 673–684.

Love, S. G., and T. J. Ahrens 1997. Origin of asteroid rotation rates in catastrophic impacts. *Nature* **386**, 154–156.

Muinonen, K. 1996. Light scattering by Gaussian random particles. *Earth, Moon, Planets* **72**, 339–342.

Muinonen, K. 1998. Introducing the Gaussian shape hypothesis for asteroids and comets. *Astron. Astrophys.* **332**, 1087–1098.

Muinonen, K., and J. S.V. Lagerros 1998. Inversion of shape statistics for small Solar System bodies. *Astron. Astrophys.* **333**, 753–761.

Néron de Surgy, O., and J. Laskar 1997. On the long term evolution of the spin of the Earth. *Astron. Astrophys.* **318**, 975–989.

Nesvorný, D., A. Morbidelli, D. Vokrouhlický, W. F. Bottke, and M. Brož 2002. The Flora family: A case of the dynamically dispersed collisional swarm? *Icarus* **157**, 155–172.

Ostro, S. J., J. F. Chandler, A. A. Hine, K. D. Rosema, I. I. Shapiro, and D. K. Yeomans 1990. Radar images of asteroid 1989 PB. *Science* **248**, 1523–1528.

Ostro, S. J., and 15 colleagues 1999a. Asteroid 4179 Toutatis: 1996 radar observations. *Icarus* **137**, 122–139.

Ostro, S. J., and 19 colleagues 1999b. Radar and optical observations of Asteroid 1998 KY26. *Science* **285**, 557–559.

Paddack, S. J. 1969. Rotational bursting of small celestial bodies: Effects of radiation pressure. *J. Geophys. Res.* **74**, 4379–4381.

Peale, S. J. 1999. Origin and evolution of the natural satellites. *Annu. Rev. Astron. Astrophys.* **37**, 533–602.

Pravec, P., and A. W. Harris 2001. Fast and slow rotation of asteroids. *Icarus* **148**, 12–20.

Radzievskii, V. V. 1954. A mechanism for the disintegration of asteroids and meteorites. *Dokl. Acad. Nauk SSSR* **97**, 49–52.

Rubincam, D. P. 1995. Asteroid orbit evolution due to thermal drag. *J. Geophys. Res.* **100**, 1585–1594.

Rubincam, D. P. 1998. Yarkovsky thermal drag on small asteroids and Mars–Earth delivery. *J. Geophys. Res.* **103**, 1725–1732.

Rubincam, D. P. 2000. Radiative spin-up and spin-down of small asteroids. *Icarus* **148**, 2–11.

Rubincam, D. P., B. F. Chao, and P. C. Thomas 1995. The gravitational field of Deimos. *Icarus* **114**, 63–67.

Simonelli, D. P., P. C. Thomas, B. T. Carcich, and J. Veverka 1993. The generation and use of numerical shape models for irregular Solar System objects. *Icarus* **103**, 49–61.

Skoglöv, E. 1997. Evolution of the obliquities for nine near-Earth asteroids. *Planet. Space Sci.* **45**, 439–447.

Skoglöv, E. 1999. Spin vector evolution for inner Solar System asteroids. *Planet. Space Sci.* **47**, 11–22.

Skoglöv, E., P. Magnusson, and M. Dahlgren 1996. Evolution of the obliquities for 10 asteroids. *Planet. Space Sci.* **44**, 1177–1183.

Vokrouhlický, D. 1998. Diurnal Yarkovsky effect as a source of mobility of meter-sized asteroidal fragments. I. Linear theory. *Astron. Astrophys.* **335**, 1093–1100.

Vokrouhlický, D. 1999. A complete linear model for the Yarkovsky thermal force on spherical asteroid fragments. *Astron. Astrophys.* **344**, 362–366.

Vokrouhlický, D., and W. F. Bottke 2001. The Yarkovsky thermal force on small asteroids and their fragments. Choosing the right albedo. *Astron. Astrophys.* **371**, 350–353.

Vokrouhlický, D., and P. Farinella 1998. The Yarkovsky seasonal effect on asteroidal fragments: A nonlinearized theory for the plane-parallel case. *Astron. J.* **116**, 2032–2041.

Vokrouhlický, D., and P. Farinella 2000. Efficient delivery of meteorites to the Earth from a wide range of asteroid parent bodies. *Nature* **407**, 606–608.

Vokrouhlický, D., A. Milani, and S. R. Chesley 2000. Yarkovsky effect on small near-Earth asteroids: Mathematical formulation and examples. *Icarus* **148**, 117–146.

Vokrouhlický, D., M. Brož, P. Farinella, and Z. Knežević 2001. Yarkovsky-driven leakage of Koronis family members, I. The case of 2953 Vysheslavia. *Icarus* **150**, 78–93.

Yeomans, D. K., and 15 colleagues 2000. Radio science result during the NEAR–Shoemaker spacecraft rendezvous with Eros. *Science* **289**, 2085–2088.

Yomogida, K., and T. Matsui 1983. Physical properties of ordinary chondrites. *J. Geophys. Res.* **88**, 9513–9533.

cence. At the CIS level, the energy needed to dissociate one NH_3 molecule from the cluster is calculated to be about the same as that available from the exoergicity of the H transfer reaction.

The configuration contributing dominantly to the excited wave function involves promotion of an electron from the highest occupied π orbital of 7HQ to the antibonding orbitals shown in Fig. 4 at different steps of the reaction. For the enol, this is the antibonding π^* orbital of 7HQ shown in Fig. 4A, whereas for HT1 it is an antibonding σ^* orbital on the newly generated NH_4 moiety (Fig. 4B). Accompanying this change of excited-state character is a transfer of about 0.9 electron from the 7HQ moiety to $NH_3(1)$; i.e., the incipient proton transfer becomes a H atom transfer in the vicinity of $TS_{E/1}$. After passing the $TS_{E/1}$ barrier, the lowest excited state retains the $\pi\sigma^*$ character along the translocation coordinate up to $TS_{3/K}$. As seen in Fig. 4, B to D, the σ^* orbital accompanies the H atom as it moves along the ammonia wire via HT1, HT2, and HT3. A reverse $\sigma^* \rightarrow \pi^*$ state switching occurs near $TS_{3/K}$; the 7KQ orbital shown in Fig. 4E is a π^* orbital similar to that of the enol.

The $\pi^* \rightarrow \sigma^* \rightarrow \pi^*$ crossovers correlate with large changes of oscillator strength for the $S_1 \rightarrow S_0$ transition: In C_s symmetry, fluorescence is allowed from the $\pi\pi^*$ but forbidden from the $\pi\sigma^*$ state. Even without symmetry, this selection rule holds approximately: The calculated $S_1 \rightarrow S_0$ oscillator strength from the 7KQ $\pi\pi^*$ state is f = 0.294, whereas from the $\pi\sigma^*$-type states of HT1 to HT3 the f values vary from 0.001 to 0.004. This difference explains why the HT1, HT2, and HT3 forms have much longer radiative lifetimes and why no fluorescence is observed from these intermediates.

We show that single-file H atom transfer can be induced along the ammonia wire of the 7-hydroxyquinoline-$(NH_3)_3$ cluster. The reaction is initiated by $S_1 \leftarrow S_0$ excitation of 7-hydroxyquinoline but does not proceed from the vibrationless S_1 state. Additional excitation of S_1 state ammonia-wire solvent vibrations is necessary to activate the reaction. The measured reaction threshold is only 2.5 kJ mol^{-1}, increasing to 9 kJ mol^{-1} when fully deuterating the ammonia wire. Ab initio calculations of the S_1 and S_2 states predict a crossing of $\pi\pi^*$ and $\pi\sigma^*$ potential energy curves along the H atom transfer coordinate (*21*–*25*) that creates an initial barrier of ~44 kJ mol^{-1}. The first reaction step involves quantum tunneling from the ground state of the O-H mode. It is exothermic by about 30 kJ mol^{-1}, which provides the driving force for the subsequent reaction steps. The ammonia-wire modes that characterize the entrance channel region of the reaction are amenable to detailed spectroscopic investigations both below and above the reaction threshold and will allow state-specific kinetic investigations. The vibrational energy and deuteration dependences underline the crucial role of the solvent coordinates on the tunneling rate (*1*, *9*–*13*).

References and Notes

1. D. Borgis, J. Hynes, *Chem. Phys.* **170**, 315 (1993).
2. N. Agmon, *Chem. Phys. Lett.* **244**, 456 (1995).
3. D. Marx, M. E. Tuckerman, J. Hutter, M. Parrinello, *Nature* **397**, 601 (1999).
4. P. L. Geissler, C. Dellago, D. Chandler, J. Hutter, M. Parrinello, *Science* **291**, 2121 (2001).
5. D. Lu, G. A. Voth, *J. Am. Chem. Soc.* **120**, 4006 (1998).
6. R. Vuilleumier, D. Borgis, *J. Phys. Chem. B* **102**, 4261 (1998).
7. H. S. Mei, M. E. Tuckerman, D. E. Sagnella, M. L. Klein, *J. Phys. Chem. B* **102**, 10446 (1998).
8. R. Pomès, B. Roux, *Biophys. J.* **82**, 2304 (2002).
9. R. I. Cukier, D. G. Nocera, *Annu. Rev. Phys. Chem.* **49**, 337 (1998).
10. R. I. Cukier, J. Zhu, *J. Chem. Phys.* **110**, 9587 (1999).
11. P. K. Agarwal, S. P. Webb, S. Hammes-Schiffer, *J. Am. Chem. Soc.* **122**, 4803 (2000).
12. J. T. Hynes, T.-H. Tran-Thi, G. Granucci, *J. Photochem. Photobiol. A* **154**, 3 (2002).
13. Q. Cui, M. Karplus, *J. Phys. Chem. B* **106**, 7927 (2002).
14. Materials and methods are available as supporting material on *Science* Online.
15. S. F. Mason, J. Philip, B. E. Smith, *J. Chem. Soc. A* **1968** 3051 (1968).
16. S. Schulman, Q. Fernando, *Tetrahedron* **24**, 1777 (1968).
17. A. Bach, S. Leutwyler, *J. Chem. Phys.* **112**, 560 (2000).
18. M. Meuwly, A. Bach, S. Leutwyler, *J. Am. Chem. Soc.* **123**, 11446 (2001).
19. K. Tokumura, M. Itoh, *J. Phys. Chem.* **88**, 3921 (1984).
20. E. Bardez, *Isr. J. Chem.* **39**, 319 (1999).
21. A. L. Sobolewski, W. Domcke, *J. Phys. Chem. A* **103**, 4494 (1999).
22. A. L. Sobolewski, W. Domcke, *Phys. Chem. Chem. Phys.* **1**, 3065 (1999).
23. A. L. Sobolewski, W. Domcke, *J. Phys. Chem. A* **105**, 9275 (2001).
24. A. L. Sobolewski, W. Domcke, C. Dedonder-Lardeux, C. Jouvet, *Phys. Chem. Chem. Phys.* **4**, 1093 (2002).
25. O. David, C. Dedonder-Lardeux, C. Jouvet, *Int. Rev. Phys. Chem.* **21**, 499 (2002).
26. K. Daigoku, S. Ishiuchi, M. Sakai, M. Fujii, K. Hashimoto, *J. Chem. Phys.* **119**, 5149 (2003).

27. This work was supported by the Schweizerische Nationalfonds (project number 2000-68081.02) and by the Centro Svizzero di Calcolo Scientifico in Manno, Switzerland.

Supporting Online Material

www.sciencemag.org/cgi/content/full/302/5651/1736/DC1

Materials and Methods

22 September 2003; accepted 28 October 2003

Direct Detection of the Yarkovsky Effect by Radar Ranging to Asteroid 6489 Golevka

Steven R. Chesley,[1]* Steven J. Ostro,[1] David Vokrouhlický,[2] David Čapek,[2] Jon D. Giorgini,[1] Michael C. Nolan,[3] Jean-Luc Margot,[4] Alice A. Hine,[3] Lance A. M. Benner,[1] Alan B. Chamberlin[1]

Radar ranging from Arecibo, Puerto Rico, to the 0.5-kilometer near-Earth asteroid 6489 Golevka unambiguously reveals a small nongravitational acceleration caused by the anisotropic thermal emission of absorbed sunlight. The magnitude of this perturbation, known as the Yarkovsky effect, is a function of the asteroid's mass and surface thermal characteristics. Direct detection of the Yarkovsky effect on asteroids will help constrain their physical properties, such as bulk density, and refine their orbital paths. Based on the strength of the detected perturbation, we estimate the bulk density of Golevka to be $2.7^{+0.4}_{-0.6}$ grams per cubic centimeter.

The Yarkovsky effect is a weak nongravitational acceleration believed to act on asteroids and meteoroids. According to theory (*1*–*6*), absorbed solar radiation is re-emitted in the infrared with some delay, which is related to the thermal inertia of the surface. This delay, in concert with the object's orbital and rotational motion, offsets the direction of the thermal emission and its associated recoil force from the Sun's direction, resulting in a slow but steady drift in the semimajor axis of the object's orbit. Over millions of years, this drift can move main-belt asteroids and meteoroids until they reach a resonance, at which point gravitational perturbations take over and reroute them into the inner solar system (*3*, *7*–*9*). The Yarkovsky effect also explains meteorite cosmic-ray exposure ages that are too long for the classical delivery scenarios (*3*, *10*) and the large dispersion of asteroid family members that would otherwise have required unrealistically large collisional ejection velocities (*6*, *11*). It can also limit the long-term predictability of possibly hazardous close-Earth approaches (*12*). The Yarkovsky effect has been detected in the motion

[1]Jet Propulsion Laboratory, California Institute of Technology, Pasadena, CA 91109, USA. [2]Institute of Astronomy, Charles University, CZ-18000 Prague 8, Czech Republic. [3]Arecibo Observatory, National Astronomy and Ionosphere Center, Arecibo, PR 00612, USA. [4]Department of Earth and Space Sciences, University of California, Los Angeles, CA 90095, USA.

*To whom correspondence should be addressed. E-mail: steven.chesley@jpl.nasa.gov

of artificial Earth satellites (*13*) but not for any natural bodies. Vokrouhlický *et al.* (*14*, *15*) explored the possibility of direct detection by means of the precise determination of near-Earth asteroid (NEA) orbits and concluded that such a detection would be feasible for NEAs up to a few kilometers in size, given precise radar astrometry spanning a decade or more. In particular, they predicted that radar ranging in May 2003 to the asteroid 6489 Golevka (which has a 530-m diameter) would reveal direct evidence for Yarkovsky accelerations. Here, we report the outcome of that radar experiment, which confirms Yarkovsky-induced modification of asteroid orbits.

Measurements of the distribution of radar echo power in time delay (range) and Doppler frequency (radial velocity) constitute two-dimensional images that can spatially resolve asteroids. The fine fractional precision of radar time-delay measurements and their orthogonality to optical plane-of-sky angular astrometry make them powerful for refining orbits (*16*). Radar observations of Golevka were conducted during its close-Earth approaches in 1991, 1995, and 1999. Delay-Doppler measurements were made at Arecibo, PR, and Goldstone, CA, in 1991 (*17*) and extensively at Goldstone in 1995 (*18*). The asteroid's shape and spin state were determined from the 1995 radar results (*18*). We imaged Golevka from Arecibo on 24, 26, and 27 May 2003 (Fig. 1), during the asteroid's closest Earth approach until 2046. With the shape model (*18*), we used least squares to estimate the location in each image of Golevka's center of mass (COM) (table S1). The radar time delays from 1991 were originally referenced to the peak power of the delay-Doppler distribution (*17*). Delay measurements from the 1995 observations (*18*) were referenced to the COM under the assumption that the COM was 390 m beyond the echo's leading edge in each image, whereas the shape model indicates that the range from the leading edge to the COM for those observations varied from about 225 m to about 320 m. Using images synthesized from the shape model, we reanalyzed the 1991 and 1995 images to estimate revised time delays, which are uniformly referenced to the COM (table S1).

We used a nonlinear numerical Yarkovsky model incorporating Golevka's radar-derived shape and spin state (*18*) to compute the Yarkovsky effect (*19*). The Yarkovsky acceleration depends on a number of physical parameters, including the spin state, which is known for Golevka, the surface conductivity K and the surface density ρ_s, which affect the strength of the recoil force, and the bulk density ρ_b, which only affects the acceleration through the asteroid's mass (*20*). Although our prediction is uncertain, we can place constraints on these parameters if the Yarkovsky effect can be measured. However, the principal measurable feature of the Yarkovsky effect is a drift in the asteroid's mean anomaly that is quadratic with time and is caused by a linear semimajor axis drift da/dt (fig. S1). Because the perturbation is manifested only through the anomaly variation, the signatures of the individual parameters are not separable. The dependence on the bulk density is trivial ($da/dt \propto \rho_b^{-1}$), whereas the parameters K and ρ_s affect da/dt in a complicated way but only through their product $K\rho_s$ (*4*).

Asteroid surface thermal conductivities range from as low as 10^{-4} to 10^{-3} W m^{-1} K^{-1} for highly particulate surfaces [from both laboratory experiments (*21*) and observations (*22*, *23*)] to as high as 0.1 to 1 W m^{-1} K^{-1} for bare-rock surfaces of ordinary chondrite meteorites (*24*). The latter value drops by an order of magnitude when surface porosity increases from 0 to 10% (*24*). The steep surface gravitational slopes of Golevka (*18*) suggest a surface comprising both porous rock and thin regolith, which leads us to conclude that, for Golevka, K should be in the range 10^{-3} to 10^{-1} W m^{-1} K^{-1}. Golevka is classified as a Q-class asteroid (*25*). Whereas there are as of yet no measured Q-class densities, there are several known for the mineralogically related S-class asteroids (*19*). Consistent with these results, we have assumed an a priori bulk density of $\rho_b = 2.5$ g cm^{-3} and a surface density of $\rho_s = 1.7$ g cm^{-3}, because of presumed porosi-

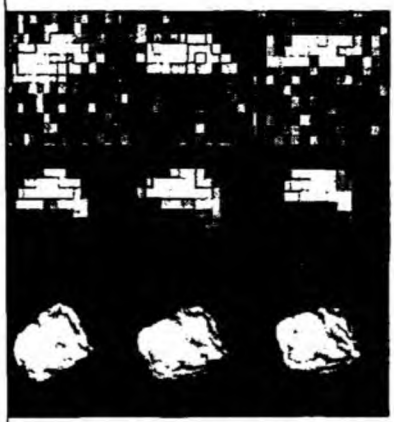

Fig. 1. Arecibo delay–Doppler images of Golevka (top row) along with corresponding synthesized images based on the shape model (*18*) (middle row) and plane-of-sky views of that model (bottom row). The 24, 26, and 27 May results are shown in the left, middle, and right columns, respectively. Each of the nine frames spans a 1.0-km square centered on Golevka's COM. In the radar images, time delay increases from top to bottom and Doppler frequency increases from left to right. The delay resolution is 0.5 μs (75 m in range) and the Doppler resolution is 0.238 Hz, or about 60 m, depending on the observing geometry. North is up in the plane-of-sky views. The images are sums of data from an average of six transmit-receive cycles and span an average of 18° of rotation phase.

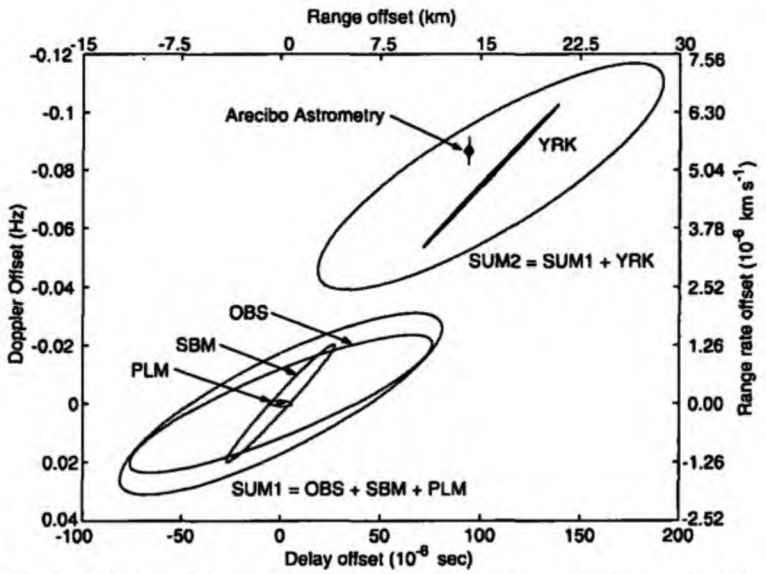

Fig. 2. Predicted Yarkovsky-induced offset with 90% confidence ellipses in the space of radar delay (range) and Doppler (range rate) measurements on 26 May 2003 09:38 UTC. (The depiction is similar for the other radar observation dates in May 2003.) The predictions are based on astrometric data from April 1991 through October 1999, which marked the end of the previous apparition, and do not include observations made during the April to May 2003 observing apparition. The Yarkovsky prediction assumes the nominal values $\rho_b = 2.5$ g cm^{-3} and $K = 0.01$ W m^{-1} K^{-1}. Ellipses labeled OBS, SBM, PLM, and YRK represent the dispersions caused by uncertainties in astrometric measurements, small body masses, planetary masses, and Yarkovsky modeling, respectively. The SUM1 ellipse, which is the combination of the OBS, SBM, and PLM uncertainties, depicts the 90% confidence region for a non-Yarkovsky prediction. Similarly, the SUM2 ellipse, which includes the added uncertainty of the Yarkovsky modeling (*19*), represents the 90% confidence region for the prediction with Yarkovsky accelerations. The actual Arecibo radar delay and derived Doppler (*19*) measurement at this epoch is shown by a diamond with error bar.

ly and particulate matter on the asteroid surface.

The prediction of the orbit of Golevka is uncertain because of noise in the measured astrometric positions and uncertainties in the forces acting on the asteroid. The most significant force-modeling errors arise from solar radiation pressure, gravitational perturbations from the planets and other asteroids, and the Yarkovsky effect (*12*). For Golevka, we considered the prediction errors at the time of the 26 May 2003 radar observation, 12 years after discovery (Fig. 2). We found that direct and reflected radiation pressure causes a minor shift of only 2 to 3 μs in the predicted delay (*19*). Similarly, planetary masses are well determined and associated uncertainties can affect the prediction for Golevka by just 2 to 3 μs (*19*). The masses of perturbing asteroids, however, are very poorly constrained, and this represents a larger source of prediction uncertainty, ~13 μs at 1σ for Golevka (*19*). The modeled Yarkovsky acceleration uncertainty is dominated by uncertainty in the bulk density and surface thermal conductivity of Golevka. Sensitivity tests indicated 1σ dispersions on the order of 16 μs because of realistic uncertainties on these parameters (*19*).

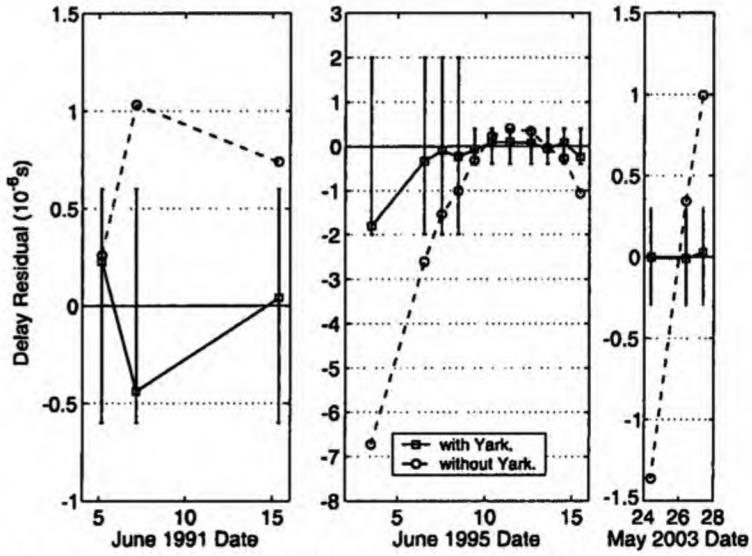

Fig. 3. Radar delay residuals for all Golevka range measurements (table S1). The residuals are the differences between the measured position and the computed postfit prediction. They are expected to be generally smaller than the measurement standard errors, which are indicated by error bars. Residuals that are systematically inconsistent with the measurement errors are indicative of mismodeling, in this case because of the absence of Yarkovsky accelerations in the asteroid force model. In addition to the depicted delay measurements, the fits included 748 right ascension/declination measurements from 15 April 1991 to 22 May 2003. Residuals from fits without the Yarkovsky effect are markedly worse than those from fits with the Yarkovsky effect. For solutions with and without the Yarkovsky acceleration, the root mean square values of the 20 delay residuals, normalized by the assigned measurement uncertainties, are 0.42 and 1.82, respectively.

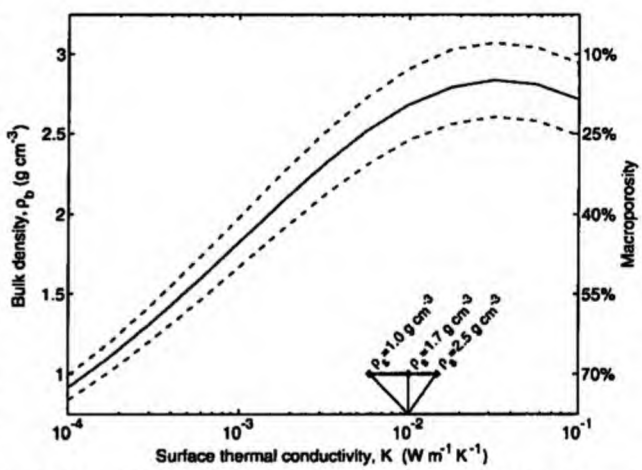

Fig. 4. Estimated bulk density ρ_b of Golevka as a function of the assumed thermal conductivity K. Dashed curves indicate the extent of the formal error estimate. The ρ_b and K constraints assume a surface density of ρ_s = 1.7 g cm^{-3}; varying ρ_s over a reasonable range causes a shift in the abscissa as depicted at the bottom of the plot. The maximum in the curve is positioned fortuitously, allowing us to place an independent upper bound ρ_b < 3.1 g cm^{-3}. Values from the lower left of the plot are inconsistent with probable values for both density and thermal conductivity; however, strictly independent lower limits cannot be determined. The descending branch of the curve for K > 10^{-1} W m^{-1} K^{-1} (*29*) allows reasonable densities, but with unrealistically high conductivities. The macroporosity ordinate is based on the mean bulk density of type L ordinary chondrite meteorites, which is 3.34 g cm^{-3} (*26*).

As radar tracking of NEAs continues, Golevka is likely to be only the first of many objects with detectable Yarkovsky accelerations (*14*). This suggests that the effect will eventually become a crucial component of precision orbit determination for small asteroids, in much the same way that nongravitational accelerations on comets are routinely computed.

The analyses described here can be used to estimate the physical properties of any small NEA for which a sufficient set of radar astrometry can be acquired. If additional observations that would allow decorrelation of ρ_b and K were available (such as infrared or radar backscatter observations) this technique

The separation between the Yarkovsky and non-Yarkovsky orbital predictions (Fig. 2) is about 15 km of range or 100 μs in radar delay, a 6σ discrepancy with respect to the non-Yarkovsky prediction. Thus, none of the estimated uncertainties are large enough to obscure the Yarkovsky effect. The actual Arecibo astrometry falls at 7.5σ from the non-Yarkovsky prediction and 1.3σ from the Yarkovsky prediction (Fig. 2). The formal probabilities of a measurement falling at or beyond these significance levels are ~10^{-12} and 0.43, respectively.

An alternative approach to testing for Yarkovsky acceleration is to use all of the available optical and radar observations and consider how well they fit a particular force model. For Golevka, such fits are unacceptably poor when Yarkovsky accelerations are not used, whereas excellent fits are obtained with Yarkovsky accelerations (Fig. 3). In the latter case, one can fix the Yarkovsky acceleration by fixing ρ_b and K, or one can estimate one or the other of the two parameters. Varying either of these parameters only affects the mean anomaly of the orbit, so they are fully correlated and cannot be simultaneously estimated. Even so, we can form a constraint in (ρ_b, K)-space by estimating ρ_b for a variety of assumed values of K (Fig. 4), or vice versa. For bulk densities in the expected range (2.5 ± 0.5 g cm^{-3}) we find K > 10^{-3} W m^{-1} K^{-1} (Fig. 4). Alternatively, if we assume that K falls in the interval from $10^{-2.5}$ to $10^{-1.5}$ W m^{-1} K^{-1}, then we infer a bulk density of 2.1 to 3.1 g cm^{-3}. Fixing K = 10^{-2} W m^{-1} K^{-1} yields ρ_b = 2.7 ± 0.2 g cm^{-3}, which we take to be the best fitting value and which implies a mass of 2.1 × 10^{11} kg (*20*). Based on the mean bulk density of ordinary chondrite meteorites, 3.34 g cm^{-3} (*26*), the macroporosity p of Golevka is 19% with a range of 7 to 37%, placing it within the "fractured" group of asteroids (*27*). These values of ρ_b and p are comparable to values estimated for much larger S-class asteroids (*27*).

would be strengthened. Still, apart from the roughly one-sixth of the NEA population thought to be binary systems (*28*), measuring the strength of the Yarkovsky acceleration offers the only means of estimating the masses of sub-kilometer NEAs from Earth-based observations.

References and Notes

1. D. P. Rubincam, *J. Geophys. Res.* **100**, 1585 (1995).
2. D. P. Rubincam, *J. Geophys. Res.* **103**, 1725 (1998).
3. P. Farinella, D. Vokrouhlický, W. K. Hartmann, *Icarus* **132**, 378 (1998).
4. D. Vokrouhlický, *Astron. Astrophys.* **335**, 1093 (1998).
5. D. Vokrouhlický, *Astron. Astrophys.* **344**, 362 (1999).
6. W. F. Bottke, D. Vokrouhlický, D. P. Rubincam, M. Brož, in *Asteroids III*, W. F. Bottke Jr., A. Cellino, P. Paolicchi, R. P. Binzel, Eds. (Univ. Arizona Press, Tucson, AZ, 2003), pp. 395–408.
7. W. F. Bottke, D. P. Rubincam, J. A. Burns, *Icarus* **145**, 301 (2000).
8. P. Farinella, D. Vokrouhlický, *Science* **283**, 1507 (1999).
9. A. Morbidelli, D. Vokrouhlický, *Icarus* **163**, 120 (2003).
10. D. Vokrouhlický, P. Farinella, *Nature* **407**, 606 (2000).
11. W. F. Bottke, D. Vokrouhlický, M. Brož, D. Nesvorný, A. Morbidelli, *Science* **294**, 1693 (2001).
12. J. D. Giorgini *et al.*, *Science* **296**, 132 (2002).
13. D. P. Rubincam, *J. Geophys. Res.* **92**, 1287 (1987).
14. D. Vokrouhlický, A. Milani, S. R. Chesley, *Icarus* **148**, 118 (2000).
15. D. Vokrouhlický, S. R. Chesley, A. Milani, *Celest. Mech. Dyn. Astron.* **81**, 149 (2001).
16. D. K. Yeomans, S. J. Ostro, P. W. Chodas, *Astron. J.* **94**, 189 (1987).
17. S. J. Ostro *et al.*, *Bull. Am. Astron. Soc.* **23**, 1144 (1991).
18. R. S. Hudson *et al.*, *Icarus* **148**, 37 (2000).
19. Materials and methods are available as supporting material on *Science* Online.
20. The asteroid's mass and bulk density are related through the volume of the shape model, which is 7.79465×10^7 m³ (*18*).
21. A. E. Wechsler, P. E. Glaser, A. D. Little, J. A. Fountain, in *Thermal Characteristics of the Moon*, J. W. Lucas, Ed. (MIT Press, Cambridge, MA, 1972), pp. 215–242.
22. A. W. Harris, J. S. V. Lagerros, in *Asteroids III*, W. F. Bottke Jr., A. Cellino, P. Paolicchi, R. P. Binzel, Eds. (Univ. Arizona Press, Tucson, AZ, 2003), pp. 205–218.
23. M. G. Langseth, E. M. Drake, D. Nathanson, J. A. Fountain, in *Thermal Characteristics of the Moon*, J. W. Lucas, Ed. (MIT Press, Cambridge, MA, 1972), pp. 169–204.
24. K. Yomogida, T. Matsui, *J. Geophys. Res.* **88**, 9513 (1983).
25. S. J. Bus, R. P. Binzel, *Icarus* **158**, 146 (2002).
26. G. J. Consolmagno, D. T. Britt, C. P. Stoll, *Meteorit. Planet. Sci.* **33**, 1221 (1998).
27. D. T. Britt, D. Yeomans, K. Housen, G. Consolmagno, in *Asteroids III*, W. F. Bottke Jr., A. Cellino, P. Paolicchi, R. P. Binzel, Eds. (Univ. Arizona Press, Tucson, AZ, 2003), pp. 485–500.
28. J. L. Margot *et al.*, *Science* **296**, 1445 (2002).
29. S. R. Chesley *et al.*, data not shown.

30. We thank V. Negrón and the technical staff of the Arecibo Observatory for help with the radar observations; G. Garrad, W. Owen Jr., and T. Spahr for providing precise optical astrometry of Golevka; and S. Hudson for providing his shape reconstruction software. This research was conducted in part at the Jet Propulsion Laboratory, California Institute of Technology under a contract with NASA. Additional support was provided by the Grant Agency of the Czech Republic. The Arecibo Observatory is part of the National Astronomy and Ionosphere Center, which is operated by Cornell University under a cooperative agreement with NSF and with support from NASA.

Supporting Online Material

www.sciencemag.org/cgi/content/full/302/5651/1739/DC1

Materials and Methods
Fig. S1
Table S1
References

12 September 2003; accepted 30 October 2003

Water Isotope Ratios D/H, $^{18}O/^{16}O$, $^{17}O/^{16}O$ in and out of Clouds Map Dehydration Pathways

Christopher R. Webster[1]* and Andrew J. Heymsfield[2]

Water isotope ratios have been measured by laser absorption spectroscopy in and out of cirrus clouds formed in situ and convectively generated in anvils over subtropical regions. Water vapor in the tropical and subtropical upper troposphere shows a wide range of isotopic depletion not observed previously. The range suggests that dehydration of upper tropospheric air occurs both by convective dehydration and by gradual dehydration mechanisms. Twenty-five percent of upper tropospheric water sampled is in ice particles whose isotopic signatures are used to identify those grown in situ from those lofted from below.

Tropospheric water vapor is the most important greenhouse gas and a key component of the climate system (*1*). In the upper troposphere (UT) and lower stratosphere (LS), water vapor, liquid clouds, and ice particles substantially affect the radiation balance, atmospheric circulation, and chemistry (*2*). Cirrus clouds in particular affect UT water ice and vapor content, which global climate models indicate have large effects on Earth's radiative balance (*3–5*), especially in the dry subtropical UT (*6*).

Understanding the sources and sinks of water in the UT and LS and the mechanism of stratospheric dehydration is one of the important remaining challenges in Earth science, because water vapor feedback mechanisms can increase ozone depletion (*7*) and lead to stratospheric cooling (*8*). A doubling in stratospheric humidity over the last half century has been reported (*9*), despite decreasing tropical tropopause temperatures (*10*).

The extent to which the humidity of air transported from the troposphere into the stratosphere is controlled by tropopause minimum temperatures, cloud microphysics and convection, and mixing of air between high and low latitudes is not fully understood. The water vapor content of air entering the LS [3 to 4.1 parts per million volume (ppmv) (*11*)] is lower than the ice saturation mixing ratio (~4.5 ppmv) that would be determined by freeze-drying at the global mean tropopause temperature. Although there is consensus that dehydration occurs principally in the tropical tropopause layer (TTL) [covering the altitude range from ~13 to 19 km (*12*, *13*)], two competing mechanisms have been proposed: "convective dehydration" and "gradual dehydration" (*13*). Convective dehydration results from rising air masses overshooting their level of neutral buoyancy (LNB) to become severely dehydrated (≤1 ppmv by condensation and fallout) before mixing (*14–18*) with moister air. In gradual dehydration (*13*, *19–21*), air detrains from convection near its LNB at the bottom of the TTL and becomes dehydrated during slow ascent through regions that have temperatures below the tropopause global average temperature. This "cold trap" region need not be the local tropopause for a sampled air parcel, because time scales for horizontal versus vertical transport allow air parcels to "visit" far away cold pools such as that of the tropical Western Pacific (*13*).

Water vapor has a long lifetime (*22*), has an observed seasonal cycle (*19*, *23*), and is a good tracer of atmospheric transport. Its stable isotopes, especially HDO and $H_2{}^{18}O$ compared with $H_2{}^{16}O$, suffer large fractionations in an air parcel [expressed as delta-D (δD) and delta-^{18}O ($\delta^{18}O$) (*24*), respectively] as a result of condensation and sedimentation (*25*). Since the first tropospheric (*26*) and stratospheric (*27*) HDO measurements, subsequent studies (*28–33*) have recognized that water isotope fractionation is, in principle, a sensitive tracer for diagnosing transport and dehydration mechanisms.

Gradual dehydration is expected to follow Rayleigh distillation (*34*) in which all condensate is removed during adiabatic cooling. In this case, the vertical profile of δD for atmospheric water vapor is expected to begin at ~−86 per mil (‰) above the ocean [standard mean ocean water (SMOW) is 0‰ (*35*)] and reduce monotonically to ~−950‰ at the coldest tropopause. Few in situ measurements exist, particularly in tropical regions. Before the work presented here, such low values were usually not observed [except −837 ± 100‰ (*36*) in the polar vortex, and −810 ± 213‰ in the UT over Texas (*37*)]. At mid- and low-latitudes, UT values down to −670‰ have been reported (*38*).

[1]Earth and Space Sciences Division, Jet Propulsion Laboratory (JPL), California Institute of Technology, Pasadena, CA 91109, USA. [2]National Center for Atmospheric Research (NCAR), Boulder, CO 80301, USA.

*To whom correspondence should be addressed. E-mail: chris.r.webster@jpl.nasa.gov

A&A 414, L21–L24 (2004)
DOI: 10.1051/0004-6361:20031739

Astronomy & Astrophysics

Detectability of YORP rotational slowing of asteroid 25143 Itokawa

D. Vokrouhlický[1], D. Čapek[1], M. Kaasalainen[2], and S. J. Ostro[3]

[1] Institute of Astronomy, Charles University, V Holešovičkách 2, 180 00 Prague 8, Czech Republic
e-mail: vokrouhl@mbox.cesnet.cz, capek@sirrah.troja.mff.cuni.cz
[2] Rolf Nevanlinna Institute, University of Helsinki, PO Box 4, 00014 Helsinki, Finland,
and Sodankyla Geophysical Observatory, University of Oulu, Tahtelantie 62, 99600 Sodankyla, Finland
e-mail: mjk@rni.helsinki.fi
[3] Jet Propulsion Laboratory, California Institute of Technology, Pasadena, CA 91109-8099, USA
e-mail: ostro@reason.jpl.nasa.gov

Received 14 November 2003 / Accepted 11 December 2003

Abstract. We predict that the YORP thermal-emission effect can be directly detected through a measurable increase in the rotation period of the several-hundred-meter near-Earth asteroid 25143 Itokawa. The fractional change of Itokawa's rotation rate in between 2001 and 2004 should be $(1-2)\times 10^{-4}$, significantly larger than its currently estimated uncertainty $\simeq 5\times 10^{-5}$. The corresponding change of sidereal rotation phase, normalized to unity in a cycle, is $\simeq(0.09-0.25)$ in January 2004, producing $\simeq(1-3)$ h delay of lightcurve maximum.

Key words. solar system: minor planets, asteroids – radiations mechanisms: thermal

1. Introduction

Torques produced by the reflection and thermal re-emission of sunlight from an asteroid's surface can alter its spin state. This Yarkovsky-O'Keefe-Radzievskii-Paddack or YORP effect (Rubincam 2000; Vokrouhlický & Čapek 2002; Vokrouhlický et al. 2003) is related to the Yarkovsky effect, by which the anisotropic re-radiation of absorbed sunlight causes object's orbital semimajor axis to drift at a rate that depends on the object's physical properties, especially its mass, its spin state and its surface's thermal characteristics (Bottke et al. 2002). YORP torques depend on these factors and especially on the shape; energy re-radiated from an irregularly shaped body allows the YORP effect to change the spin period and the obliquity, while there would be no net YORP torques on a homogeneous sphere or ellipsoid.

Whereas the obliquity effect is unlikely to be measureable with ground-based astronomical techniques, rotation rate variations could in principle accumulate rapidly enough to be detectable over time scales as short as several years. Here we argue that precise measurements of the rotation period of the small near-Earth asteroid 25143 Itokawa (1998 SF36) may yield, for the first time, a direct detection of the YORP effect.

Send offprint requests to: D. Vokrouhlický,
e-mail: vokrouhl@mbox.cesnet.cz

2. YORP effect

Solar energy absorbed by an asteroid and re-radiated at thermal wavelengths causes an infinitesimal pressure on each surface element. If conditions for a nonuniform distribution of surface temperature are satisfied, the resulting net force $\boldsymbol{F}$ and torque $\boldsymbol{T}$ from the thermal re-radiation are nonzero. This torque alters the asteroid's angular velocity ω at a rate (see Rubincam 2000; Vokrouhlický & Čapek 2002)

$$\tau = T_s/C = \boldsymbol{T}\cdot\boldsymbol{s}/C, \tag{1}$$

where $\boldsymbol{s}$ is the unit vector along the spin axis and C is the largest proper value of the moment of inertia. This simplified model assumes a body rotating along its shortest axis (a condition well satisfied for Itokawa; Kaasalainen et al. 2003; Ostro et al. 2003). As a result, the rotation rate changes as

$$\omega = \omega_0 + \delta\omega, \tag{2}$$

with

$$\delta\omega(f) = \frac{\eta^3}{n}\int_{f_0}^{f}\frac{\tau(f')\,\mathrm{d}f'}{(1+e\cos f')^2}. \tag{3}$$

Here f is the orbit's true anomaly, ω_0 is a reference value of the rotation rate at f_0, e is the orbit's eccentricity, n its mean orbital motion and $\eta = \sqrt{1-e^2}$. Variation $\delta\omega$ of the rotation rate produces a variation $\delta\Phi$ of the sidereal rotation phase Φ defined as

$$\Phi = \frac{1}{2\pi}\int_{t_0}^{t}\omega\,\mathrm{d}t = \Phi_0 + \delta\Phi, \tag{4}$$

where Φ_0 is a linearly increasing nominal value of the phase corresponding to the constant rotation rate ω_0 (note in this paper the rotation phase is always normalized to unity in a rotation cycle). With Eq. (3) we thus have

$$\delta\Phi(f) = \frac{\eta^3}{2\pi n}\int_{f_0}^{f}\frac{\delta\omega(f')\,\mathrm{d}f'}{(1+e\cos f')^2}. \qquad (5)$$

Note that any (linear) secular change in the rotation rate translates into a quadratic change in the rotation phase, hence propagating faster than observation uncertainty (see also Fig. 3).

3. Results for 25143 Itokawa

Itokawa's orbit, not far from the 3/2 exterior resonance with the Earth, is favorable for detection of YORP modification of the asteroid's spin period. During Itokawa's 2004 close approach, its photometric observability mimics that during its 2001 apparition even though the approach occurs near the descending node. Itokawa will be observable with small and medium size telescopes during two periods: January through March 2004 and June through September 2004; Fig. 1 shows Itokawa's path on the sky during the apparition. It starts January 1 in the upper right corner, turns back around March 15, swoops very fast through the southern latitudes in June/July during the closest approach, and approaches the plane of the ecliptic again in late September. Itokawa's elongation is smaller than 60° between May 20 and June 25 (about when its solar phase angle exceeds 110°). After this, Itokawa is a bright target from late June (when it reaches very high phase angles) until early August. The visual magnitudes in Fig. 1 are estimated from Itokawa's solar phase curve in Kaasalainen et al. (2003); those in May–June at high phases are wide extrapolations and thus uncertain. A similar situation then occurs also in 2007, after it is visited by the Japanese spacecraft Hayabusa during June–November 2005 (Fujiwara et al. 1999; Farquhar et al. 2003). Below we show that this sequence of observation opportunities, their expected precision of rotation period determination, and the estimated strength of the YORP effect imply detectability of the effect.

We have carried out a numerical simulation using the model by Vokrouhlický & Čapek (2002) generalized to include effects of finite surface thermal inertia. The assumed surface parameters are as follows: thermal conductivity $K = 0.05$ W/m/K, heat capacity $C = 800$ J/kg/K and surface density $\rho_{\mathrm{surf}} = 2$ g/cm^3, consistent with Itokawa's value of thermal inertia derived from infrared observations (Ishiguro et al. 2003) and with radar observations reported by Ostro et al. (2003). The assumed thermal conductivity and surface density correspond to appropriate for L chondrites with about (10–20)% surface porosity (Yomogida & Matsui 1983) and the assumed heat capacity, which is very dependent on temperature, corresponds to the mean temperature along the orbit. However, we note that, unlike for the Yarkovsky effect, results of this paper do not depend critically of the value of the surface thermal inertia so that uncertainty in this parameter contributes very little to the error budget of our YORP effect prediction. We assume the value for Itokawa's geometric albedo of ≃(0.23–0.35) from infrared observations reported by Sekiguchi et al. (2003) and Ishiguro et al. (2003). We include the effect of both the torque due to the thermally radiated energy (the "proper" YORP effect) as well as the torque due to radiation reflected in optical. For that component we assume diffuse reflection on the surface and mean geometric albedo of 0.3. The bulk density is taken to be 2.5 g/cm^3 consistent with Itokawa's spectral type S; see e.g. Yeomans et al. (2000) and Ostro et al. (2003). We use the radar-derived shape model from Ostro et al. (2003), which assumes the pole and rotation period of Kaasalainen et al. (2003). (Itokawa's high obliquity (≃172°) contributes to the strength of the YORP effect.) As a check, we also used the shape model derived by Kaasalainen et al. (2003) from analysis of 2001 optical photometry, rescaling its dimensions to make it 18% larger in order to give it the same volume and mass as the radar shape model. The YORP torque from the photometrically derived shape model is about 15% larger than that from the radar shape model.

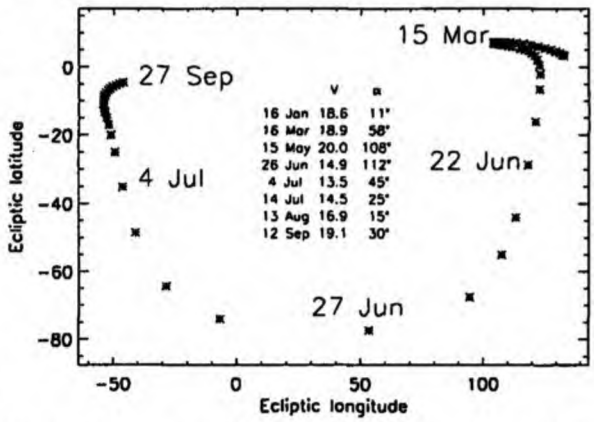

Fig. 1. Itokawa's motion in the sky during most of 2004 (ecliptic longitude and latitude in degrees on axes); legend gives visual magnitude (V) and phase angle (α) on selected dates.

Figure 2 shows time evolution of the relative change $(P - P_0)/P_0$ of Itokawa's rotation period P due to the YORP effect relative to the value $P_0 = 12.132$ h determined during its 2001 apparition. We estimate an uncertainty of 30% in the nominal model prediction, with the following principal components: (i) uncertainty in the shape model (we created 10 "clone" Itokawa models by slight shape variations and verified that the resulting YORP torque does not change by more than 15%); (ii) uncertainty in linear size of Itokawa of ≃10% (Ostro et al. 2003; note that such linear rescaling implies a quadratic rescaling of the YORP torques); (iii) uncertainty in Itokawa's bulk density of ≃10%; (iv) uncertainty in the pole position; and (v) uncertainty in the surface optical and thermal parameters. Even in the worst case, the difference between the YORP modified rotation period in 2004 and that determined in 2001 amounts to about ≃2 standard deviations (expressed in the 2001 uncertainty). Assuming Gaussian statistics, there is about 0.04 probability that such fluctuation would happen in the constant rotation rate model; the probability drops to 0.003 for the result of the nominal YORP model that differs by as much as ≃3 standard deviations from the constant rotation model. Therefore we

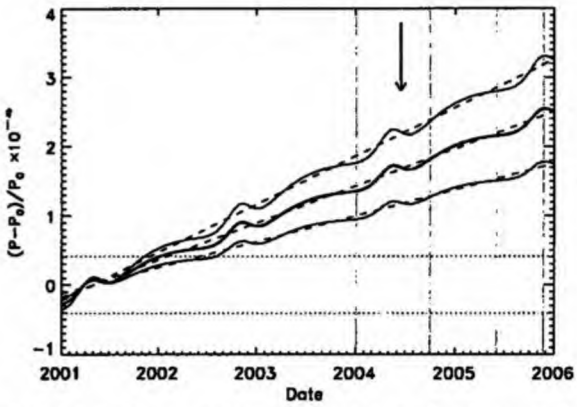

Fig. 2. Relative change of the rotation period P, referred to a nominal value $P_0 = 12.132$ h in MJD = 52 000 (Kaasalainen et al. 2003), as a function of time due to the YORP effect. The thick solid curve corresponds to a nominal model described in the text, and the thin solid curves are results for YORP torques varied by ±30% from the nominal model. Solid curves show the complete expected variation of Itokawa's rotation period, and dashed lines show the mean linear rate of rotational slowing. The dotted lines indicate the formal uncertainty of the rotation period determination from the 2001 campaign. The shaded intervals correspond to future optical observing opportunities, notably in 2004 from Earth and in 2005 from Hayabusa. The arrow shows the asteroid's close encounter with the Earth, during which the rotation period may fractionally change by 3.1×10^{-5} at maximum due to the effect of Earth's gravitational torque (see the text).

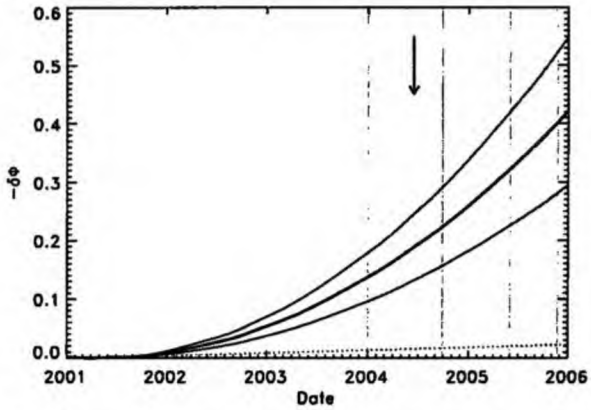

Fig. 3. Change of the rotation phase $\delta\Phi$, with an arbitrary zero value at MJD = 52 000 (Kaasalainen et al. 2003), as a function of time due to the YORP effect; notation as in Fig. 2. The formal uncertainty of the previous determination of asteroid's rotation rate causes a linear increase of the uncertainty in phase (dotted line), while the YORP effect signature in $\delta\Phi$ is quadratic and hence easily observable in the future.

argue that the 2004 observations should be able to detect YORP rotational slowing of Itokawa.

The Hayabusa observations, if comparable in accuracy to those of the NEAR/Shoemaker spacecraft (Yeomans et al. 2000; Konopliv et al. 2003), should be able to contribute importantly to the YORP effect measurement. First, the shape model and thermal properties of the asteroid will be determined more accurately than by the Earth-based observations (though significant refinements of Itokawa's shape model will be also obtained from radar imaging in June 2004 and optical observations throughout 2004). Additionally, Hayabusa measurements should in principle be accurate enough to themselves reveal the YORP-induced deceleration of the asteroid rotation. A link to the previous (and possible future) observations should then give a superb probe of the thermal effects on this body (independently, Ostro et al. 2003, also demonstrate that Hayabusa radio ranging should be also able to detect the Yarkovsky effect affecting Itokawa's orbit around the Sun).

Figure 3 shows the accumulated change $\delta\Phi$ of Itokawa's sidereal rotation phase due to the YORP effect. As expected, $\delta\Phi$ propagates quadratically with time, much faster than the growth in its uncertainty, and by January 2004 the YORP-induced $\delta\Phi$ dominates. The expected value of at least $\simeq 0.09$ translates into a delay of lightcurve maximum by $\simeq 1$ h, which should be easily detectable.

An asteroid's spin state can also be modified by gravitational torques during close approaches (CA) to planets. Scheeres et al. (2000) investigated the effect of a planetary flyby along a hyperbolic orbit on rotation of a quasi-rigid body. With their results we estimate maximum relative change of Itokawa's rotation rate during a flyby as

$$\left(\frac{\delta\omega}{\omega}\right)_{\rm CA} \simeq \frac{1}{2}\frac{B-A}{C}\frac{GM}{q^2 v_\infty}, \qquad (6)$$

where $A \le B \le C$ are proper values of the inertia tensor, G the gravitational constant, M planetary mass, q is minimum distance to the planet during the approach and v_∞ is relative velocity at large distance. For Itokawa we estimate $(B-A)/C \simeq 0.6$. With $v_\infty \simeq 7$ km s^{-1} and $q \simeq 0.013$ AU appropriate for the 2004 encounter (Ostro et al. 2003 and Fig. 2), we thus obtain a maximum impulsive change of Itokawa's rotation rate of about $(\delta\omega/\omega)_{\rm CA} \simeq 3.1 \times 10^{-5}$. The exact value, and its sign, depends on rotation phase at pericenter of the Earth flyby. Though not negligible, the effect of gravitational torques is small compared to YORP.

We noted above that measurement of the YORP-induced slowing of Itokawa's rotation is uncertain due several unknown parameters, principally the asteroid's precise shape, size and mass, but once detected these parameters may be in turn determined. Since the scheduled radar and optical observations during 2004 should reduce uncertainty in shape and size of Itokawa, YORP detection would result mainly in constraining its mass (as it is the case of the Yarkovsky effect detection; Chesley et al. 2003).

Acknowledgements. We thank anonymous referee and L. A. M. Benner who helped to improve the final form of this paper. This research was supported in part by grant 205/02/703 awarded by the Grant Agency of the Czech Republic. Part of this research was conducted at the Jet Propulsion Laboratory, California Institute of Technology, under contract with the National Aeronautics and Space Administration (NASA).

References

Bottke, W. F., Vokrouhlický, D., Rubincam, D. P., & Brož, M. 2002, in Asteroids III, ed. W. F. Bottke, et al. (Tucson: The University of Arizona Press), 395

Chesley, S. R., Ostro, S. J. Vokrouhlický, D., et al. 2003, Science, 302, 1739

Dermawan, B., Nakamura, T., Fukushima, H., et al. 2002, PASJ, 54, 635

Farquhar, R., Kawaguchi, J., Russell, C. T., et al. 2002, in Asteroids III, ed. W. F. Bottke, et al. (Tucson: The University of Arizona Press), 367

Fujiwara, A., Mukai, T., Kawaguchi, J., & Uesugi, K. T. 1999, Adv. Space Res., 25, 231

Ishiguro, M., Abe, M., Ohba, Y., et al. 2003, PASJ, 55, 691

Kaasalainen, M., Kwiatkowski, T., Abe, M., et al. 2003, A&A, 405, L29

Konopliv, A. S., Miller, J. K., Owen, W. M., et al. 2002, Icarus, 160, 289

Ostro, S. J., Benner, L. A. M., Nolan, M. C., et al. 2003, Meteor. Planet. Sci., submitted

Rubincam, D. P. 2000, Icarus, 148, 2

Scheeres, D., Ostro, S. J., Werner, R. A., Asphaug, E., & Hudson, R. S. 2000, Icarus, 147, 106

Sekiguchi, T., Abe, M., Boehnhardt, et al. 2003, A&A, 397, 325

Vokrouhlický, D., & Čapek, D. 2002, Icarus, 159, 449

Vokrouhlický, D., Nesvorný, D., & Bottke, W. F. 2003, Nature, 425, 147

Yeomans, D. K., Antreasian, P. G., Barriot, J.-P., et al. 2000, Science, 289, 2085

Yomogida, K., & Matsui, T. 1983, J. Geophys. Res., 88, 9513

Available online at www.sciencedirect.com
SCIENCE DIRECT
ELSEVIER
Icarus 172 (2004) 526–536
ICARUS
www.elsevier.com/locate/icarus

The YORP effect with finite thermal conductivity

D. Čapek, D. Vokrouhlický *

Institute of Astronomy, Charles University, Prague, V Holešovičkách 2, CZ-18000 Prague 8, Czech Republic

Received 5 May 2004; revised 4 July 2004
Available online 25 September 2004

Abstract

The Yarkovsky–O'Keefe–Radzievskii–Paddack (YORP) effect has been recently suggested to significantly change, on a long-term, rotation state of small asteroids and meteoroids. Though YORP is closely related to the Yarkovsky (orbital) effect, it differs from the latter in two aspects: (i) YORP needs bodies of irregular shape to be effective, and (ii) YORP acts on bodies of zero surface thermal conductivity. To simplify computations, YORP has been so far investigated in the zero surface thermal conductivity limit only. Here we analyze the role of the surface conductivity and we find it substantially changes previous conclusions. Most importantly, unlike in the zero-conductivity limit, (i) YORP preferentially tilts obliquity toward two asymptotic states perpendicular to the orbital plane, and (ii) YORP asymptotically decelerates and accelerates rotation rate in about equal number of cases. Our work also indicates that direct detection of the YORP effect for a small asteroid may significantly constrain its mass.

Keywords: Asteroids, rotation; Meteoroids; YORP effect

1. Introduction

The Yarkovsky–O'Keefe–Radzievskii–Paddack (YORP) effect is a radiation torque due to thermally re-emitted sunlight by cosmic bodies (Rubincam, 2000; Vokrouhlický and Čapek, 2002). On a long-term, YORP can significantly change rotation rate and obliquity of small bodies in the Solar System, driving them toward some asymptotic values. Together, and sometimes in concert, with the related Yarkovsky effect, YORP may represent a key element to explain several puzzling facts about rotational, orbital and physical parameters of small asteroids and meteoroids (Rubincam, 2000; Rubincam et al., 2002; Vokrouhlický and Čapek, 2002; Bottke et al., 2003; Morbidelli and Vokrouhlický, 2003; Vokrouhlický et al., 2003). YORP can be also directly detected through a measurable change in phase of the sidereal rotation of small asteroids (Vokrouhlický et al., 2004a).

These applications require an accurate determination of the YORP effect strength for a given object or a class of objects, a task which is often uneasy because of the intrinsic YORP dependence on its/their detailed shape. The only simplification, as regards to the Yarkovsky effect, is that YORP does not need finite surface thermal conductivity to operate and can be estimated in the (unrealistic) limit of zero conductivity. To our knowledge, previous literature (Rubincam, 2000; Vokrouhlický and Čapek, 2002) adopted this simplifying assumption, mainly to allow faster computation, and at best arbitrary fudge factors have been introduced to account for finite surface conductivity.

In this paper, a follow-up of Vokrouhlický and Čapek (2002), we compute the YORP effect for various individual bodies, and also a large, statistical sample of synthetic bodies, and we account for a finite value of the surface thermal conductivity using a full-fledged thermal model. We find the conclusions of the simplified, zero-conductivity model change both quantitatively and qualitatively. An important specific result concerns ability of YORP to accelerate or decelerate asteroid's rotation rate. By proving that the relevant YORP component depends weakly on surface conductivity

* Corresponding author. Fax: +420-2-2191-2567.
E-mail address: vokrouhl@mbox.cesnet.cz (D. Vokrouhlický).

0019-1035/$ – see front matter
doi:10.1016/j.icarus.2004.07.003

value, we show here that the YORP detection constrains asteroid's mass more tightly than analogous detection of the Yarkovsky effect (Chesley et al., 2003).

2. Theory

We start with a brief comment on the YORP theory. A common basis of the Yarkovsky and the YORP effects is a recoil force $d\mathbf{f}$, applied to an oriented surface element $d\mathbf{S}$, due to thermal re-emission of the absorbed sunlight. With the simplifying assumption of Lambert (isotropic) surface emission we have (Spitale and Greenberg, 2001; Bottke et al., 2003)

$$d\mathbf{f} = -\frac{2}{3}\frac{\varepsilon\sigma T^4}{c}\,d\mathbf{S}, \tag{1}$$

where ε is the thermal emissivity, σ the Stefan–Boltzmann constant, T the surface temperature and c the light velocity. Integrating over the whole surface, one obtains the resulting thermal torque

$$\mathbf{T} = \int \mathbf{r} \times d\mathbf{f}. \tag{2}$$

In practice, we describe irregular shapes using the polyhedral model (see, e.g., Simonelli et al., 1993; Dobrovolskis, 1996; Vokrouhlický and Čapek, 2002), with surface composed of a finite number of triangular facets; fine-resolution models, e.g., Asteroids 1998 KY26, Golevka, Ida or Eros in Section 3, have a couple thousands to tens of thousands elements, while Gaussian spheres in Section 4 are transformed into 1004-facet polyhedrons.[1] The integration (2) is performed as a sum over the triangular surface elements.

Assuming the body rotates around the shortest axis of the inertia tensor (with the moment of inertia C), the main simplification adopted in this paper, we have $\mathbf{L} = C\omega\mathbf{e}$ for the angular momentum of the body; ω is the angular velocity of rotation and $\mathbf{e}$ is the unit vector of the spin axis. The rate of change of $\mathbf{L}$ in the inertial frame is equal to the applied torque $\mathbf{T}$: $d\mathbf{L}/dt = \mathbf{T}$. For C = const. this equation splits into

$$\frac{d\omega}{dt} = \frac{\mathbf{T}\cdot\mathbf{e}}{C} \equiv \frac{T_s}{C}, \tag{3}$$

$$\frac{d\mathbf{e}}{dt} = \frac{\mathbf{T} - (\mathbf{T}\cdot\mathbf{e})\,\mathbf{e}}{C\omega}. \tag{4}$$

It is useful to parametrize the spin vector $\mathbf{e}$ with the obliquity ϵ, the angle between $\mathbf{e}$ and normal vector $\mathbf{N}$ to the orbital plane, and the precession in longitude ψ, such that $\mathbf{e}$ decomposition into orbital plane unit vectors (x-coordinate along the nodal line) reads: $(\sin\epsilon\sin(\psi+\Omega), \sin\epsilon\cos(\psi+\Omega), \cos\epsilon)$, where Ω is the longitude of ascending node (see Fig. 1 for various vectorial and angular variables defined). Then (4) yields

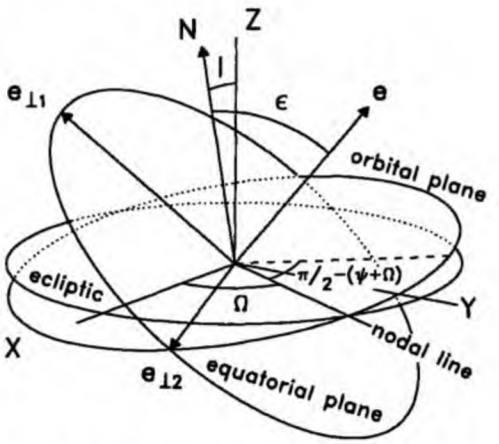

Fig. 1. Vectors and angular parameters introduced in the text; the XYZ reference frame is that of ecliptic of a fixed date, to which the moving orbital plane of date is inclined by I (and the nodal line offset by Ω from the X direction). Spin axis of the asteroid is along the unitary vector $\mathbf{e}$, and the asteroid equatorial plane of date defines auxiliary vectors $\mathbf{e}_{\perp 1}$ and $\mathbf{e}_{\perp 2}$. Obliquity ϵ is the angle between normal vector $\mathbf{N}$ to the orbital plane and the spin vector $\mathbf{e}$. The angular distance of $\mathbf{e}$'s projection onto the orbital plane and nodal line is equal $\pi/2 - (\psi + \Omega)$.

$$\frac{d\epsilon}{dt} = \frac{\mathbf{T}\cdot\mathbf{e}_{\perp 1}}{C\omega} \equiv \frac{T_\epsilon}{C\omega}, \tag{5}$$

$$\frac{d\psi}{dt} = \frac{\mathbf{T}\cdot\mathbf{e}_{\perp 2}}{C\omega} \equiv \frac{T_\psi}{C\omega}, \tag{6}$$

with the unit vectors

$$\mathbf{e}_{\perp 1} = \frac{(\mathbf{N}\cdot\mathbf{e})\,\mathbf{e} - \mathbf{N}}{\sin\epsilon}, \tag{7}$$

$$\mathbf{e}_{\perp 2} = \frac{\mathbf{e}\times\mathbf{N}}{\sin\epsilon}. \tag{8}$$

In reality $\mathbf{T}$ includes, aside to the YORP torque (2), additional contributions such as the gravitational torque due to the primary and/or inertial terms due to the motion of the orbital frame to which the angles ϵ and ψ are referred (e.g., Vokrouhlický and Čapek, 2002). The gravitational and inertial terms generally prevail in the precession component T_ψ, so that the corresponding YORP contribution is negligible and will not be discussed below. On the other hand, their long-term value in T_s and T_ϵ is nil, while YORP produces non-zero secular effects in the rotation speed and obliquity. We thus focus here on these two components of the thermal torque. Since the major effects of the YORP torque act on long time scales, we always assume T_s and T_ϵ averaged over rotation and revolution cycles. We assume no commensurability between rotation and orbital motion. As a simplification, we also assume circular orbit of the body around the primary which implies that T_s and T_ϵ depend on the obliquity only. Our method can be easily used for eccentric orbits too, but for discussion in this paper it would mean further extension of the parameter space. Focusing on the

[1] Our experience shows this number of surface facets makes the YORP strength computation accurate to several up to ten percents in the worst cases; this does not corrupt out statistical conclusions.

role of the surface conductivity, we thus stay with circular orbits.

The major unknown quantity in (1) is the surface temperature T that depends on external sources of energy (such as the incident solar radiation and body's reflectivity in the optical band expressed by the albedo coefficient A), and the way how the absorbed energy is conducted into deeper layers in the body. The latter is the heat diffusion problem (HDP) with appropriate boundary conditions and depends on various thermal constants, primarily thermal conductivity. To avoid necessity of solving HDP, one can, in the crudest approximation, assume a limit of zero thermal conductivity in which thermal radiation is emitted with no time lag; then $\varepsilon\sigma T^4 \approx (1-A)\Phi(\mathbf{n}\cdot\mathbf{n}_0)$, where Φ is the solar radiation flux impinging on the surface element with exterior normal vector $\mathbf{n}$ along direction $\mathbf{n}_0$ (Rubincam, 2000; Vokrouhlický and Čapek, 2002). Rubincam (2000) proposed to account for the effects of the finite thermal conductivity by using a scaling ("fudge") factor 2/3, but we shall see below that this is far too simplified approach.

The main purpose of this paper is to remove the approximation of zero-thermal conductivity and compute YORP for its realistic values. To that end we need to solve HDP, a sufficiently difficult task for a body of irregular shape. The problem may be however reasonably simplified, and still stay fully appropriate for most Solar System applications, when penetration depth of the thermal phenomena is much smaller than the geometric size of the body.[2] In this case, the fully three-dimensional HDP solution is not necessary and one-dimensional model accounting only for depth under a surface element is sufficient. We adopt this approach and solve HDP for each of the surface elements independently calculating temperature T depending on depth z and time t. The heat diffusion equation thus reads

$$\rho C\frac{\partial T}{\partial t} = K\frac{\partial^2 T}{\partial z^2}, \tag{9}$$

where ρ is the density, C is the specific heat capacity and K is the thermal conductivity.[3] Appropriate boundary conditions, notably (i) energy input on the surface, (ii) constancy of the temperature at large depth, and (iii) periodicity of the solution over the rotation and revolution cycles are taken into account. The first two read

$$\varepsilon\sigma T^4(t,0) = K\frac{\partial T}{\partial z}(t,0) + E(t), \tag{10}$$

$$\frac{\partial T}{\partial z}(t,\infty) = 0, \tag{11}$$

where we explicitly made clear the boundary position in depth z. Here $E = (1-A)\Phi(\mathbf{n}\cdot\mathbf{n}_0)$ is the radiative energy flux. The "no-boundary" condition in time is best expressed using the orbital mean anomaly ℓ instead of[4] t, so that $T(\ell, z)$ is constructed 2π-periodic in ℓ. Standard discretization method is used to represent the heat diffusion equation (9) (e.g., Press et al., 1994) and Spencer et al. (1989) scheme is used for the non-linear surface boundary condition (10). The surface energy input function $E(t)$ is computed from the known position of the Sun with respect to the surface element which is a function of the chosen orbit and the rotation pole of the asteroid. We also take into account a possibility of mutual shadowing on the surface. The "isothermal-core" condition (11) is applied at typically 10–15 penetration depths of the seasonal thermal wave. Practice shows that an isothermal initial seed in the whole mesh converges to the desired solution fast enough, so that we stop iterations of the numerical solution when a fractional change in temperature of all surface elements between two successive iterations is smaller than 0.001.

With the procedure outlined above, we obtain temperature T for each of the surface facets at any time along the orbit around the Sun. This value is used in Eq. (1) to compete the corresponding radiative recoil force differential.

3. YORP dependence on surface conductivity: individual cases

In this section we illustrate the role of thermal conductivity for YORP determination in the case of four asteroids whose shape in accurately known from either spacecraft reconnaissance or radar ranging analysis. Though their shapes will be accounted for, the orbits are all assumed circular and at $a = 2.5$ AU distance from the Sun (we note that the YORP torques scale as $\propto 1/a^2$ for circular orbits). In general, elliptic orbits are not considered here in order to demonstrate YORP dependence on the surface thermal conductivity without unnecessarily extending the free-parameter space. However, our method is straightforwardly applicable to specific bodies on elliptic orbits too (e.g., Vokrouhlický et al., 2004a). In what follows we provide accurate results for Golevka and Eros, in order to estimate a possibility of the YORP detection for these targets.

A general feature of the YORP-driven evolution is to tilt the axis toward a specific value of the obliquity. In accord with Rubincam (2000), Vokrouhlický and Čapek (2002) or Bottke et al. (2003), we call this obliquity value asymptotic. While reaching this obliquity state, the YORP model adopted above predicts a permanent increase or decrease of the rotation period (see, however, comments in Section 5).

[2] Note the penetration depth of the seasonal thermal wave in solid rocks is a few meters for typical asteroidal distances from the Sun; the diurnal thermal wave penetrates to a depth smaller by at least an order of magnitude. Our results are thus safely applicable for asteroids larger than tens of meters across.

[3] These physical constants should be understood as effective values in the surface slab with thickness of several penetration depths of the seasonal thermal wave.

[4] It also appears useful to scale depth z with the penetration depth h_T of the diurnal thermal wave, thus introduce $z' = z/h_T$; see Vokrouhlický and Farinella (1998).

3.1. Golevka

Shape models of both Golevka and 1998 KY26, available at http://www.eecs.wsu.edu/~hudson/ as 4092-facet polyhedral figures, were obtained by analysis of radar ranging echoes in 1995 and 1998 (Hudson et al., 2000; Ostro et al., 1999). Both are small near-Earth asteroids on Apollo-type orbits; Golevka resides in the 3/1 mean motion resonance with Jupiter and close to the 4/1 exterior mean motion resonance with the Earth (that makes it now observable in close approaches with the Earth every 4 years during a couple decades). Both Golevka and 1998 KY26 were predicted to be good candidates for detection of the Yarkovsky effect (Vokrouhlický et al., 2000), and in the Golevka's case that detection has been already achieved (Chesley et al., 2003). Assuming a plausible bulk density of 2.5 g/cm^3, Chesley et al. (2003) estimate surface thermal conductivity of $K \simeq 0.01$ W/(m K), also a likely value for the surface characterized as a mixture of dusty areas and exposed porous rocks (Hudson et al., 2000). Below we investigate dependence of the YORP effect strength on Golevka's surface conductivity for the simplest orbital configuration (circular orbit), and then provide accurate computation of the YORP effect for the real Golevka's orbital and spin parameters and the value of the surface conductivity inferred from the Yarkovsky effect detection.

Figure 2 shows mean rate of change of the angular velocity (left) and obliquity (right) due to YORP for a number of values of the surface conductivity K in the range 10^{-9} to 10 W/(m K). Other surface thermal and physical parameters were: surface density 1.7 g/cm^3, mean bulk density 2.5 g/cm^3, specific heat capacity $C = 680$ J/(kg K) and albedo set to zero for simplicity. A striking conclusion from Fig. 2 is a near independence of the angular velocity YORP torque (T_s/C) on K, while in the same time a strong dependence of the obliquity YORP torque (T_ϵ/C) on K. Zero, or very low conductivity YORP model would predict three possible asymptotic obliquity states 0°, 90°, and 180° (Type IV in Vokrouhlický and Čapek, 2002), while only a single asymptotic state—90°—occurs for $K \geqslant 5 \times 10^{-5}$ W/(m K).

The near independence of the rotation rate effect on K is important, see also other results below and discussion in Section 5, and warrants a comment. Equation (3) indicates that the rotation rate change is determined by the torque **T** projection onto the rotation axis **e**. As such, it basically depends on the amount of energy thermally reprocessed at a given latitude on the body. Thermal inertia (conductivity) affects delay with which the absorbed energy is re-emitted, but not the total amount of this energy; rotation cycle averaging, assumed in our procedure, then effaces differences between solutions corresponding to different values of surface thermal conductivity and explains our result. Note that the obliquity variation—Eq. (5)—depends on projection of **T** onto $\mathbf{e}_{\perp 1}$ and thus breaks the symmetry. We only note that as the surface conductivity increases to large values the amplitude of the effect decreases as a response to more latitudinally uniform temperature distribution.

Next we determined YORP-induced evolution of the rotation period and sidereal rotation phase for Golevka using formulation by Vokrouhlický et al. (2004a). Thermal parameters as above, thermal conductivity $K = 0.01$ W/(m K) in accordance with Chesley et al. (2003), but here we consider the true orbital and spin parameters of the asteroid (e.g., Hudson et al., 2000). With that model we estimate the mean value of the fractional change of the rotation period P, $(dP/dt)/P \simeq -2.2 \times 10^{-7}$ yr^{-1}. This translates into a sidereal rotation phase change of $\simeq 70°$ by 2010 and $\simeq 95°$ by 2015, assuming origin in 1995 when a large international campaign was organized to determine Golevka's rotation state (Mottola et al., 1997). Unfortunately no photometry was recorded during the last decent close approach to the Earth in May 2003 and this means that the uncertainty interval of the sidereal phase, as follows from the 1995 data, is

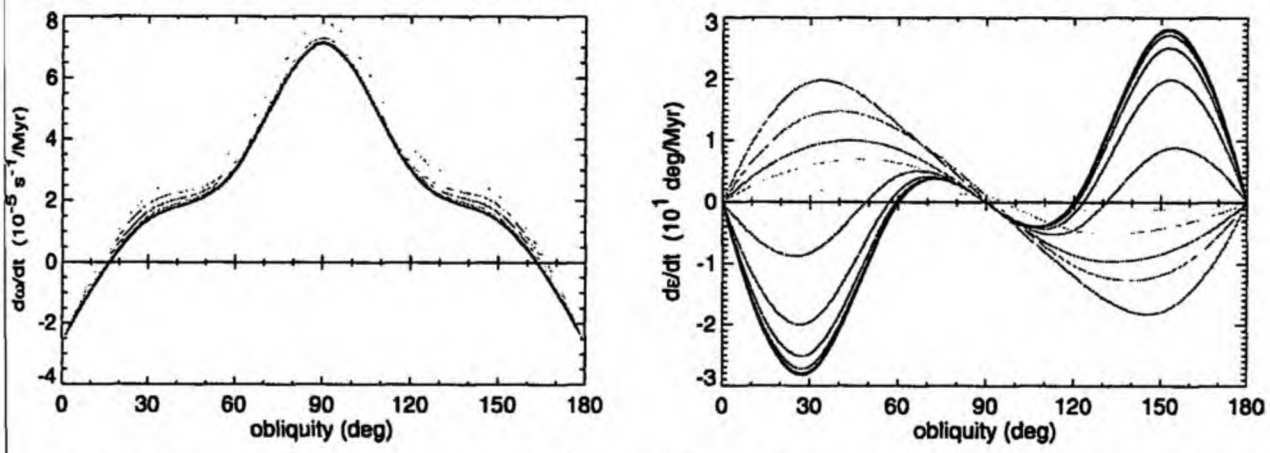

Fig. 2. YORP-induced mean rate of change of the rotation rate ω and obliquity ϵ as a function of the obliquity for Asteroid 6489 Golevka (a circular orbit at 1.5 AU assumed). Eleven values of the surface thermal conductivity $\log K = -9, -8, \ldots, -1, 0, 1$ are shown in the decreasing scale of grey (the result for the lowest value—black—is identical to the zero-conductivity case analyzed by Vokrouhlický and Čapek, 2002). The rotation effect shows small dependence on K, while the obliquity effect depends on K significantly.

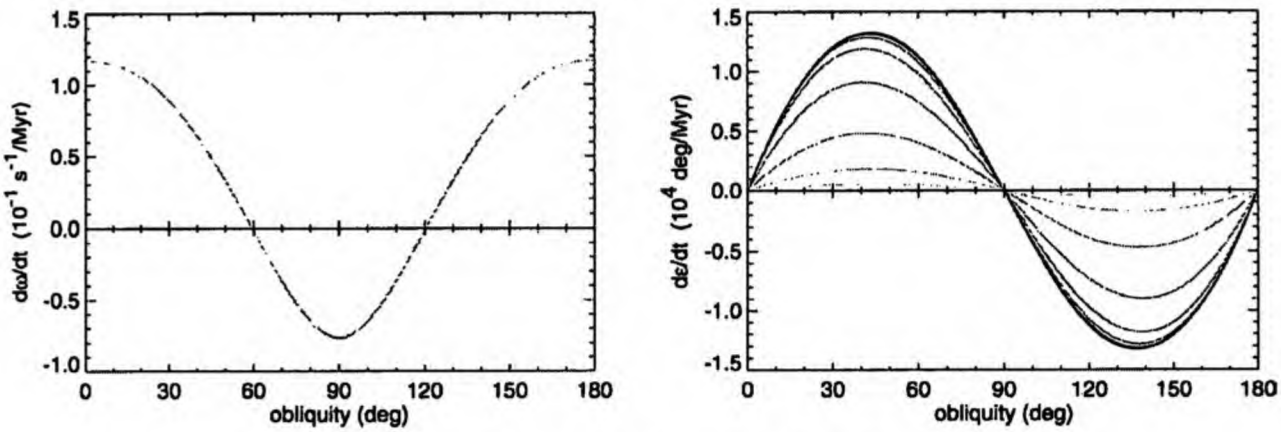

Fig. 3. The same as in Fig. 2 but for Asteroid 1998 KY26.

larger than the YORP signal up until $\simeq$ 2020. We did not investigate in detail whether analysis of the radar echoes from May 2003 (and those from June 1991) could help to significantly reduce the phase uncertainty. The next observation possibilities occur in October/November 2007, 2011, 2015, and 2019, but the object fades from $\simeq$ 20.4 to $\simeq$ 22.3 mean visible magnitude. Given the rather large effect, and reliably well known shape of Golevka, we deem to think that a combined analysis of the available data and from those future apparitions might have a power to reveal existence of the YORP effect on this target. This appears interesting since in combination with the Yarkovsky measurement (Chesley et al., 2003) the bulk and surface parameters of this asteroid might be better constrained.

3.2. *1998 KY26*

This is an unusual case of a very small asteroid whose fortuitously close encounter with the Earth in June 1998 allowed a detailed radar and photometric observations (Ostro et al., 1999). Analysis of the radar data allowed shape reconstruction, but rotation pole remains uncertain (though probably far from the ecliptic plane; P. Pravec, private communication). Little is also known about the physical properties (narrow-band photometry color indexes and radar polarization data slightly preferring C-type classification), but the small size and the fast rotation suggest a dust-free surface with likely a higher conductivity value.

1998 KY26's small size gives fewer chances to observe the target than it is usual; luckily the orbit has been secured by optical astrometry taken in February 2002 (Tholen, 2003) and fairly good prospects are to observe in September 2013, when the asteroid becomes a $\simeq$ 23.4 magnitude object, and especially in June 2024 during the next decent[5] close approach to the Earth. Vokrouhlický et al. (2000) predicted that by that time the Yarkovsky effect should be easily detected for this asteroid, and Vokrouhlický and Čapek (2002) noticed that the YORP effect should be revealed too (using the zero-conductivity model). Here we substantiate the second of these predictions by using a thermal model and YORP computation that takes into account a finite value of the surface conductivity.

Figure 3 shows mean rate of change of the angular velocity (left) and obliquity (right) due to YORP for the surface conductivity K values in the same range as above for Golevka. We again note near-independence of the rotation rate effect on K, and a strong dependence of the obliquity effect on K. In this case, the increasing value of K decreases strength of the obliquity effect without modifying its asymptotic values.

If our result is scaled to the pericenter distance of $\simeq$ 1 AU we confirm that YORP should fractionally change sidereal rotation period of this asteroid in June 2024 by $\simeq (1-2) \times 10^{-3}$, a comfortably large value to be detected.[6] However, already the 2013 apparition of 1998 KY26 may represent a first possibility to directly detect the YORP effect for this target. The September observations, with a large ($\simeq$ 3-m) telescope, might by themselves reveal the effect since the affordable synodic rotation period uncertainty in a two-week period observation run could be $\leqslant 10^{-4}$ (fractionally). By that time, the expected fractional change of the sidereal rotation period due to the YORP effect should be $\simeq (5-10) \times 10^{-4}$. Moreover observation during the April 2013 opposition could yield data at entirely different phase than in 1998, helping thus to constrain pole orientation (and thus determining transformation between the synodic and sidereal rotation periods). We note the 2024 encounter is closer to the Earth, but does not yield a possibility of such a larger phase coverage as the 2013 apparition.

[5] On June 1, 2024 the asteroid distance from the Earth becomes $\simeq$ 0.03 AU, smaller than any other value till 2099.

[6] The same result might be also obtained for a very small target 2004 FH, for which P. Pravec and his group measured the synodic rotation period of $\simeq$ 3.02 min with a fractional error of $\simeq 1.6 \times 10^{-4}$ in March 2004. This asteroid gets in a close approach in January 2018, and with even a smaller size than 1998 KY26, notably $D \simeq 20$ m, we may expect the YORP change of the rotation period is safely larger that the uncertainty level in 2004.

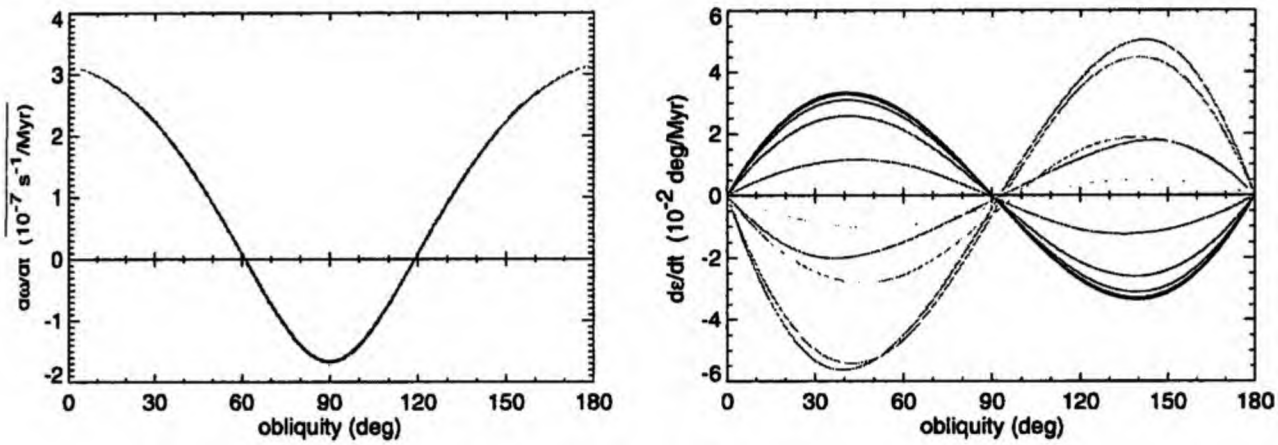

Fig. 4. The same as in Fig. 2 but for Asteroid 433 Eros.

3.3. Eros

From the multitude of the Eros shape models in the post-NEAR era (e.g., Miller et al., 2002; Konopliv et al., 2002), we use the 7790 facet representation downloaded from the PDS node http://pdssbn.astro.umd.edu. This is a convenient compromise between satisfactory accuracy and yet reasonable computer time expenses to solve HDP for each of the surface elements along one revolution about the Sun.

The mean YORP-induced variations of the Eros-shaped object on a circular orbit at 2.5 AU distance from the Sun are shown at Fig. 4. We again conclude near-independence of the rotation rate effect on the value of surface conductivity K, while significant dependence of the obliquity effect on that parameter. In particular, for $K \simeq 5 \times 10^{-4}$ W/(m K) the asymptotic obliquity values become 0° and 180°, while for lower conductivities was 90° (in Section 4 we find this behavior typical for high-conductivity situation). Interestingly, this 5×10^{-4} W/(m K) threshold value is near the plausible one that Eros might have had when it was residing in the main asteroid belt. This might suggest that the characteristic YORP timespan to modify initial obliquity was perhaps long, comparable or longer than the Solar System age. On the other hand, the characteristic YORP timespan to modify rotation rate is of the order of $\simeq 750$ Myr. This information is interesting after Vokrouhlický et al. (2004, work in preparation) have found Eros rotation state unusual and speculate about its implication about past orbital (and rotational) evolution of this asteroid.

To check a possibility of the YORP detection we computed the corresponding orbit-averaged torque components for the actual Eros' orbit and its spin state (e.g., Miller et al., 2002). We used surface conductivity $K \simeq 0.005$ W/(m K), specific heat capacity $C = 680$ J/(kg K), surface and bulk densities of 2 and 2.67 g/cm^3, respectively corresponding to predominantly powdered regolith (e.g., Morrison, 1976; Harris and Davies, 1999; Sullivan et al., 2003). With those parameters we obtained the mean fractional change of Eros' rotation period $(dP/dt)/P \simeq 1.4 \times 10^{-9}$ yr^{-1}.

Eros is the largest near-Earth asteroid so it is not surprising that detection of the YORP effect, despite of very accurate NEAR/Shoemaker data, is unlikely. With results above, we estimate that the sidereal rotation phase change due to YORP at around 1900 was $\simeq 4°$, more than an order of magnitude smaller than would be necessary.[7] Eros is obviously easily observable target, but we estimate that YORP would be discernible only after decades. Yet, it might have sense to record Eros lightcurve in the future (enough once every decade) as a low priority, long-term project for detection of the YORP effect at this target; amateur astronomers might perhaps be interested in this effort.

3.4. Ida

The shape of Ida, 2° × 2° latitude–longitude grid model constructed from Galileo images (Thomas et al., 1996), has been obtained from the PDS node http://pdssbn.astro.umd.edu and transformed to the appropriately dense polyhedral model. Figure 5 shows mean rate of change of the angular velocity and obliquity due to YORP for different values of the surface conductivity for this body. As expected from the work of Vokrouhlický et al. (2003), YORP drives obliquity toward its extreme values (0° or 180°) while decelerating its rotation rate. The characteristic YORP timescale, such as to double its rotation rate, is $\simeq 2$ Gy in a very good agreement with Vokrouhlický et al.'s model. The only surprising element is the asymptotic deceleration of Ida's rotation rate, since its rotation period of $\simeq 4.63$ hr is comparatively fast. Formation event of the small moon Dactyl might have recently perturbed Ida's rotation, but without more constraints we cannot resolve this problem.

[7] We thank J. Ďurech for having shown us his careful analysis of early Eros photometric data from the beginning of 20th century prior publication.

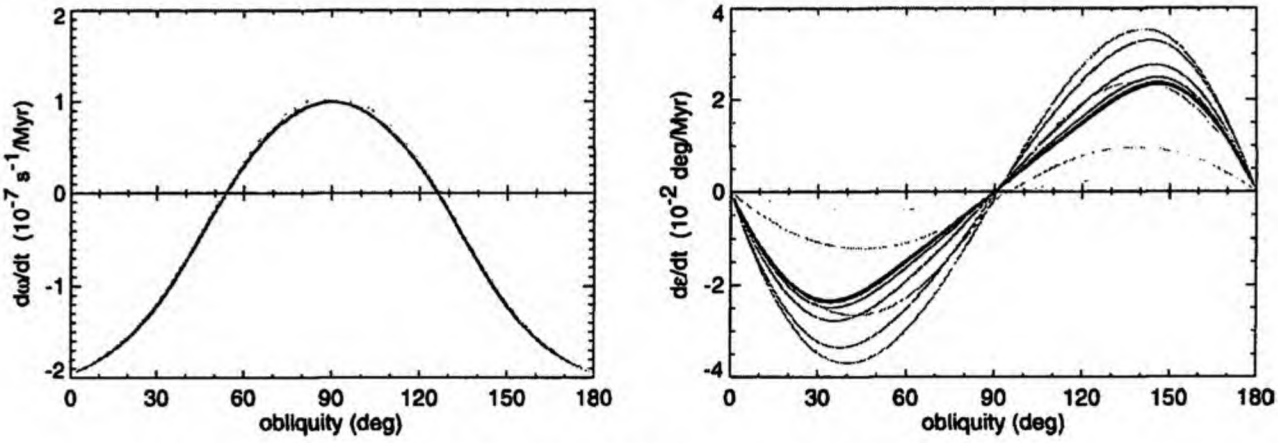

Fig. 5. The same as in Fig. 2 but for Asteroid 243 Ida.

4. YORP dependence on surface conductivity: statistical analysis

Above we dealt with individual bodies, for which spacecraft or radar observations allowed detailed shape reconstruction. There is, however, only a limited number of such cases and we need additional sample of plausible asteroid-shape objects that could serve to derive statistical characterization of YORP. To date, the best suited technique introduced by Muinonen (1998), and Muinonen and Lagerros (1998), uses Gaussian random spheres to construct a large set of shapes in an automated way. Parameters of the Gaussian random spheres used in this paper are those of Muinonen and Lagerros (1998) fitted to a limited sample of small main-belt asteroids. Similar bodies have been already used by Vokrouhlický and Čapek (2002) to characterize statistical properties of YORP in the zero conductivity limit.

In what follows we considered a sample of 200 Gaussian random spheres normalized to have the same volume, equal to a sphere with a radius of 1 km. All bodies were assumed to revolve about the Sun on a circular orbit with semimajor axis of 2.5 AU. Mean bulk and surface densities were 2.5 g/cm^3, surface heat capacity 680 J/(kg K) and albedo set to zero for simplicity. Surface thermal conductivity varied from 0.001 W/(m K), appropriate for highly particulate, regolith-type surface, to 0.01 W/(m K), appropriate to a mixture of particulate and stony surface. For comparison we also performed simulations with zero surface conductivity using the technique of Vokrouhlický and Čapek (2002). Higher values of conductivity were not investigated in this study, partly because of large CPU expenses and partly because high-conductivity surfaces are less likely for small, kilometer-size inner-main-belt asteroids (compatible with S spectral classes; e.g., Harris and Lagerros, 2003). For sake of definiteness we assumed 6 hr rotation period when reporting mean values of the obliquity change, but these results may be easily re-scaled to an arbitrary value of rotation period using Eq. (5).

Figure 6 shows orbit-averaged rate of change of the rotation rate (right part) and obliquity (left part) due to YORP effect in the zero-conductivity limit. We note about the same likelihood of asymptotically approaching 0° (or 180°) and 90° obliquity. Comparison of bottom and top panels, where we separated the solutions with different asymptotic obliquity values, indicate that in majority of the cases rotation becomes asymptotically decelerated (see also Fig. 11 in Vokrouhlický and Čapek, 2002). A typical timescale to evolve the rotation state, e.g., double the rotation period or significantly change the obliquity, is about 15 Myr for our test objects (see also Fig. 9).

Figures 7 and 8 show the same quantities as in the Fig. 6, but here the surface conductivity K was 0.001 and 0.01 W/(m K), respectively. As expected from results in Section 3, the rotation rate variation $d\omega/dt$ is little modified by the finite value of the surface conductivity, while the rate $d\epsilon/dt$ by which obliquity changes due to YORP depends significantly on the K value. Most importantly, as the conductivity increases, majority of bodies are asymptotically driven to 0° (or 180°) obliquity; for instance this happens in 95% of the cases for $K = 0.01$ W/(m K). Because the rotation rate torque did not change much, this result also implies that YORP with finite surface conductivity nearly equally accelerates and decelerates bodies rotation. These conclusions are in sharp contradiction with those from the zero-conductivity model, indicating that the value of the surface conductivity significantly influences statistical properties of the way how YORP modifies rotation of small bodies.

Another perspective to see these results is given in Fig. 9 to 11 where characteristic strength of both YORP torques—T_s/C and T_ϵ/C—is compared for the three surface conductivity cases: $K = 0$ W/(m K) (Fig. 9), $K = 0.001$ W/(m K) (Fig. 10), and $K = 0.01$ W/(m K) (Fig. 11). The left panels of these figures show characteristic timescale to double nominal rotation period of 6 hr by YORP at the asymptotic obliquity value binned in 5 Myr cells, while the right panels show maximum value of the obliquity rate $d\epsilon/dt$ due to YORP binned in 2.5 deg/Myr cells. Median values, roughly

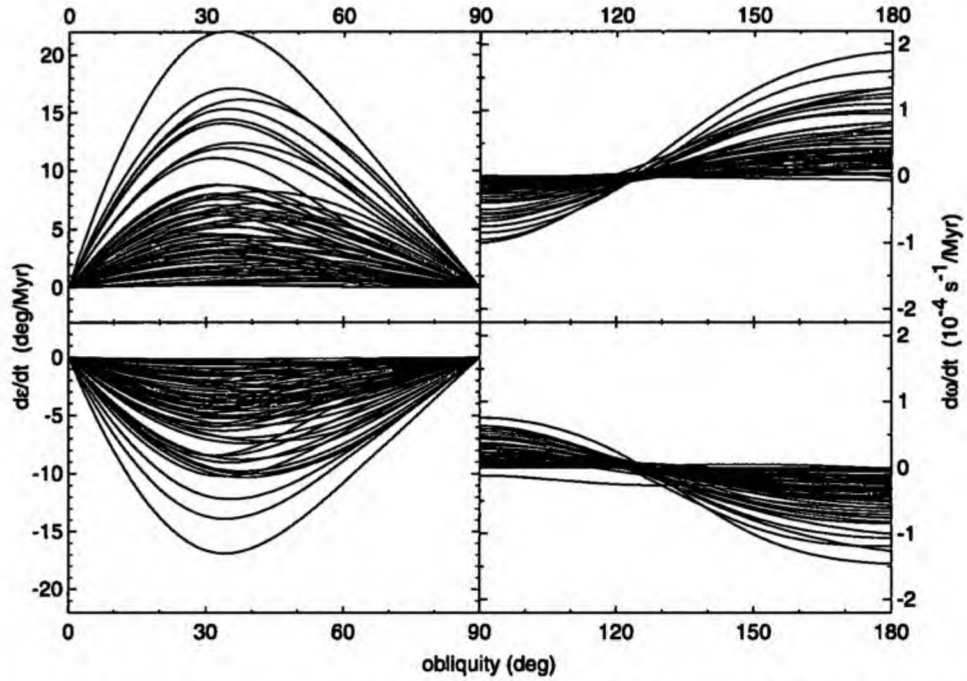

Fig. 6. Estimated mean rate of change of the rotation frequency (right parts) and the obliquity (left parts) due to the YORP effect as a function of obliquity. A sample of 200 Gaussian random spheres used, all normalized to have a volume of a sphere with a radius of 1 km and rotation period of 6 hr; the obliquity rate is proportional to the assumed rotation period. Results here assume zero surface thermal conductivity. We note $d\omega/dt$ is symmetric in the complementary obliquity interval, while $d\epsilon/dt$ is antisymmetric under this transformation (see discussion in Vokrouhlický and Čapek, 2002). For clarity, we separate solutions whose asymptotic obliquity value is 90° (upper panels), from those whose asymptotic obliquity value is 0° (180°; bottom panels). In this way we note that here is approximately equal number of cases for each of the asymptotic obliquity values, while most of the cases—95%—asymptotically decelerate rotation rate.

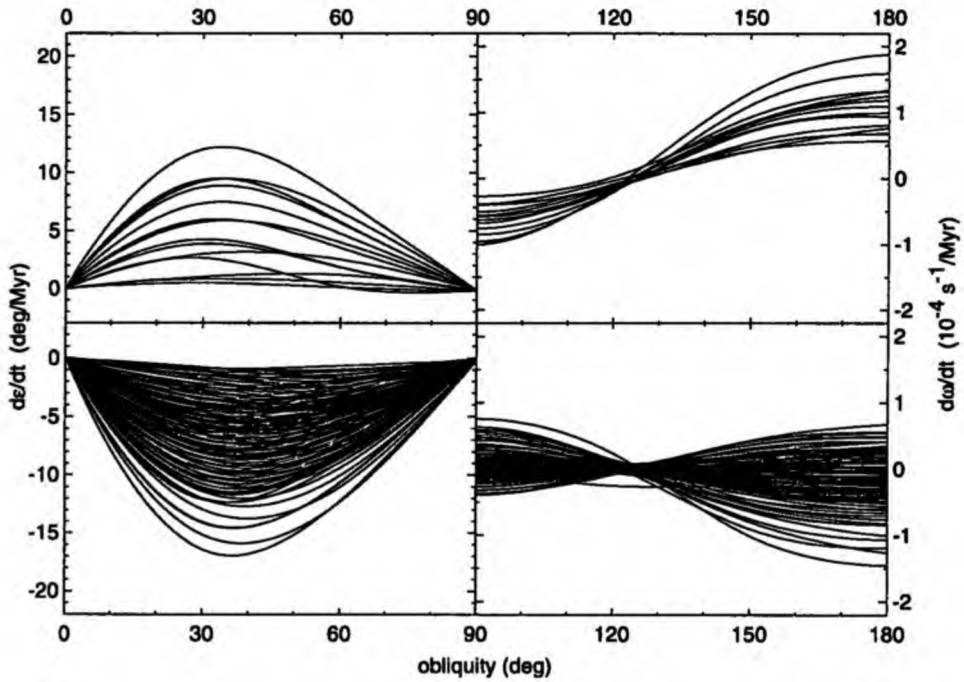

Fig. 7. The same as in Fig. 6 but now a surface thermal conductivity of 10^{-3} W/(m K) assumed. Here about 80% of cases is driven toward the asymptotic obliquity values of 0° or 180°, and about 40% of objects asymptotically accelerate rotation rate.

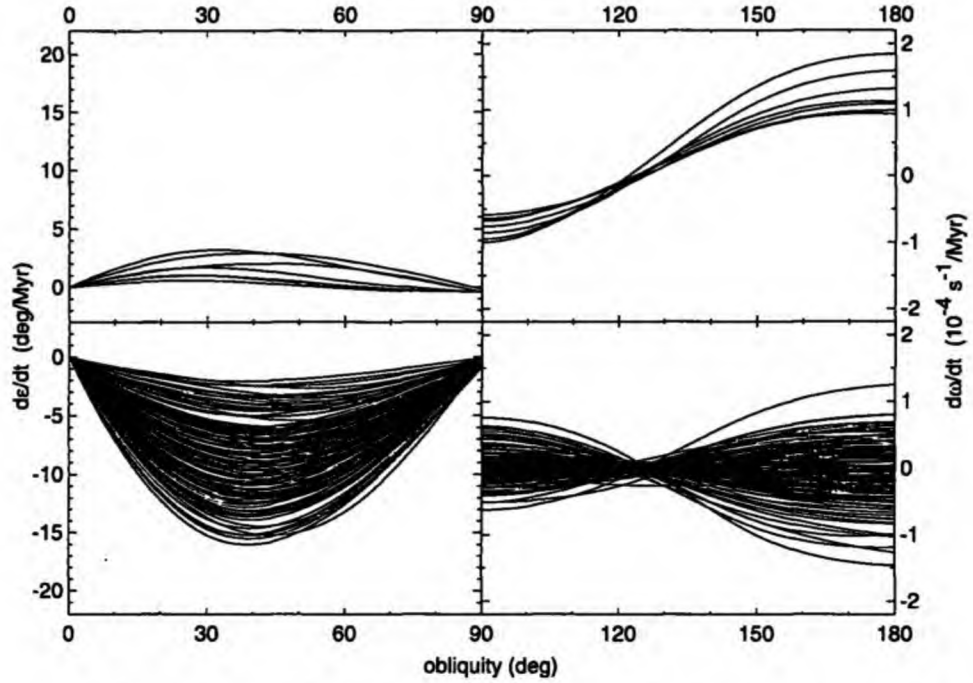

Fig. 8. The same as in Fig. 6 but now a surface thermal conductivity of 10^{-2} W/(m K) assumed. Here about 95% of cases is driven toward the asymptotic obliquity values of 0° or 180°, and about equal number of bodies asymptotically accelerate and decelerate rotation rate.

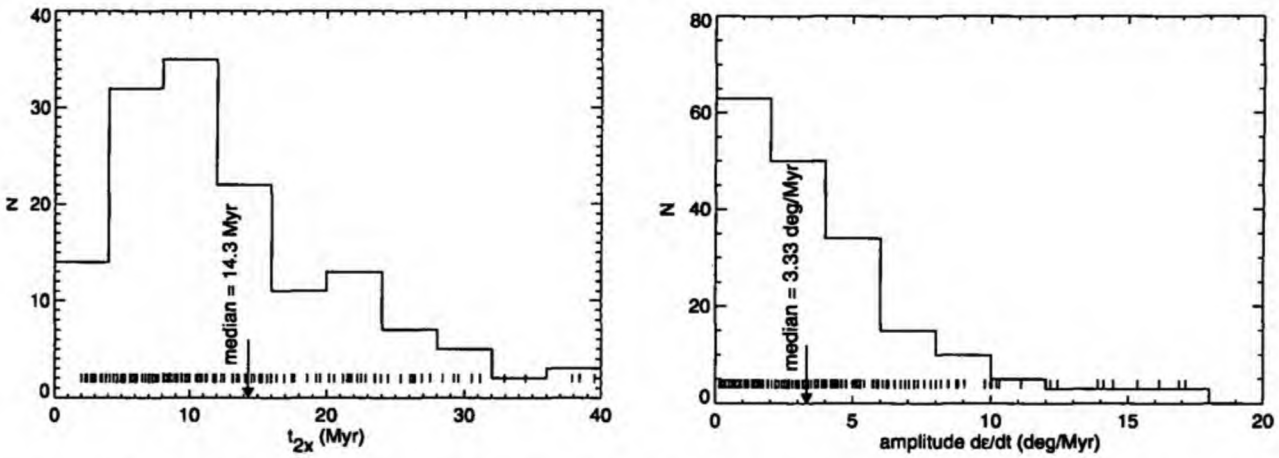

Fig. 9. Statistical occurrence of the characteristic timescale to double rotation period at the asymptotic obliquity value (left) and maximum obliquity rate (right) over a sample of Gaussian random spheres. Small bars at bottom indicate the actual values and the arrow shows median values. These results assume bodies with volume equivalent to a sphere of 1 km radius and rotation period of 6 hr; the doubling-timespan scales inversely proportionally, while the obliquity rate proportionally to the assumed rotation period. Zero surface thermal conductivity for all bodies.

10–15 Myr and a couple deg/Myr, are also indicated. While the rotation rate characteristics are similar for all values of the surface conductivity K, the obliquity variation strength increases as K increases.

5. Discussion and conclusions

Finite (non-zero) value of the surface conductivity is not necessary for YORP to operate, but here we proved that it significantly affects YORP component tilting spin axis with respect the orbital plane, while leaving unaffected the component accelerating or decelerating rotation rate. Using a large sample of Gaussian random spheres, believed to represent shape of small main-belt asteroids, we determined that for vast majority of bodies YORP drives spin axis to become perpendicular to the orbital plane. In the same time, rotation rate may appear accelerated or decelerated with about equal probability. Both these results are novel and in contradiction with conclusions from zero surface conductivity model.

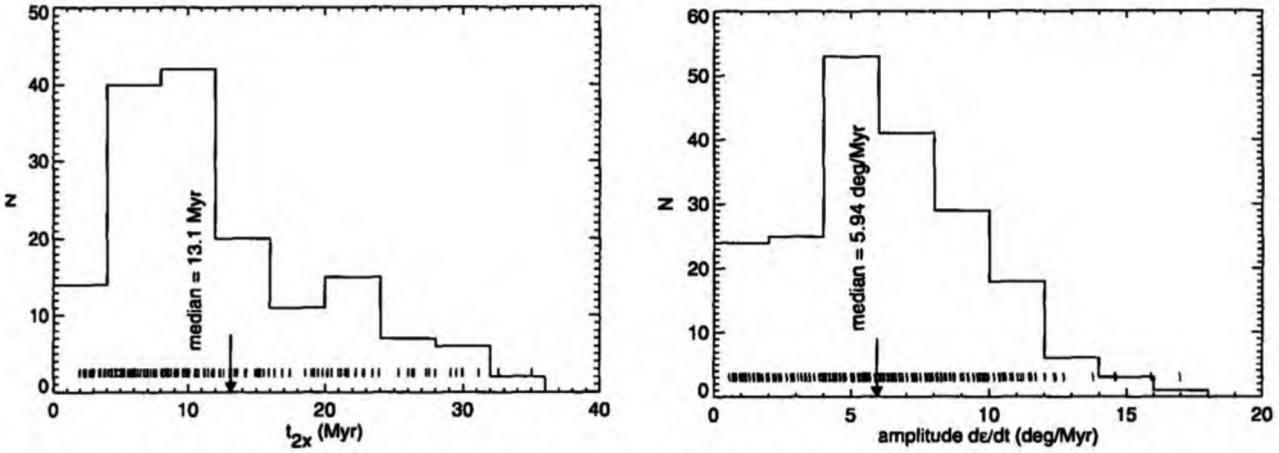

Fig. 10. The same as in Fig. 9 but here for a surface thermal conductivity of 10^{-3} W/(m K). While the median doubling timespan shortens, the median obliquity rate increases.

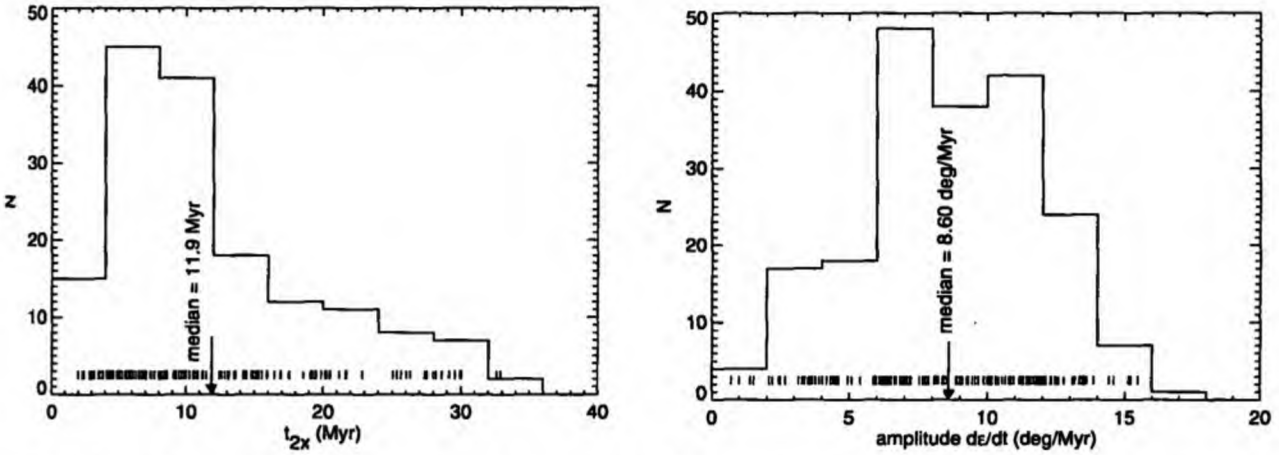

Fig. 11. The same as in Fig. 9 but here for a surface thermal conductivity of 10^{-2} W/(m K). While the median doubling timespan shortens, the median obliquity rate increases.

Results of Vokrouhlický et al. (2003) are in accordance with these conclusions, because their model explaining anomalous distribution of spin axis orientation and rotation rates of Koronis asteroids requires preferential evolution of the obliquity toward its extreme values. Another hint may come from a slightly preferential overall orientations of asteroid rotation axes toward poles of the ecliptic (e.g., Pravec et al., 2003; La Spina et al., 2004). However, before drawing more detailed conclusions we need to account, aside to YORP, for additional important effects such as secular spin–orbit resonances or mutual asteroid collisions.

Vokrouhlický et al. (2004b) have recently suggested that several detections of the Yarkovsky effect every year are likely during the next decade. The YORP detection possibilities (e.g., Vokrouhlický et al., 2004a) will be also searched, and certainly rapidly increase in number in the next years. Here we investigated YORP discovery possibilities for Golevka, 1998 KY26 and Eros, and found (or confirmed) very good prospect for 1998 KY26 and perhaps Golevka. Moreover, a discovery of a very weak dependence of the relevant YORP torque on the surface conductivity is important in general because it suggests the YORP detections might constrain asteroid's mass independently from its surface thermal conductivity. Obviously a caveat of such a YORP determination of asteroid's mass is the necessity to know its shape very precisely; so far only radar ranging or direct spacecraft reconnaissance meet the required level of accuracy. However, it also seems likely that good YORP detection candidates would also allow detection of the Yarkovsky effect (e.g., Ostro et al., 2004), and conjunction of both detections would fairly well constrain asteroid's mass and surface thermal properties in an uncorrelated way.

All previous studies of the YORP effect (Rubincam, 2000; Vokrouhlický and Čapek, 2002), including this paper, assumed principal axis rotation and rigid shape of the body. These assumptions are well satisfied for "normal rotators" (rotation periods of several hours, say) but fail for slow rotators (Pravec et al., 2004) or very fast rotators (Pravec et al., 2003). Not only the current YORP models cannot be applied to these extreme cases, but more importantly, by making the

bodies to evolve toward fast and slow rotators, YORP makes a generic link between normal and extreme rotators. What exactly happens along this evolutionary path cannot be determined with the limited YORP models today. For instance, YORP may despin rotation enough to trigger non-principal-axis rotation mode and become thus a natural mechanism to explain a class of tumbling asteroids (Pravec et al., 2004). In the opposite limit, YORP may steadily accelerate rotation rate of an asteroid until structural changes, and possibly even fission, occur; this would make YORP an interesting candidate mechanism for creating binary systems. Further YORP-work needs to be directed along these generalizations of the current models.

Acknowledgments

This work has been supported by the Grant Agency of the Czech Republic, under the grant No. 205/02/0703. We also thank Observatory and Planetarium at Hradec Králové whose computer facility has been partly used. Suggestions from D. Nesvorný and D.P. Rubincam, as referees, helped to improve the original form of this paper.

References

Bottke, W.F., Vokrouhlický, D., Rubincam, D.P., Brož, M., 2003. Dynamical evolution of asteroids and meteoroids using the Yarkovsky effect. In: Bottke, W.F., Cellino, A., Paolicchi, P., Binzel, R.P. (Eds.), Asteroids III. Univ. of Arizona Press, Tucson, pp. 395–408.

Chesley, S.R., Ostro, S.J., Vokrouhlický, D., Čapek, D., Giorgini, J.D., Nolan, M.C., Margot, J.-L., Hine, A.A., Benner, L.A.M., Chamberlin, A.B., 2003. Direct detection of the Yarkovsky effect via radar ranging to near-Earth Asteroid 6489 Golevka. Science 302, 1739–1742.

Dobrovolskis, A.R., 1996. Inertia of any polyhedron. Icarus 124, 698–704.

Harris, A.W., Davies, J.K., 1999. Physical characteristics of near-Earth asteroids from thermal infrared spectrophotometry. Icarus 142, 464–475.

Harris, A.W., Lagerros, J.S.V., 2003. Asteroids in the thermal infrared. In: Bottke, W.F., Cellino, A., Paolicchi, P., Binzel, R.P. (Eds.), Asteroids III. Univ. of Arizona Press, Tucson, pp. 205–218.

Hudson, R.S., 26 colleagues, 2000. Radar observations and physical modeling of Asteroid 6489 Golevka. Icarus 148, 37–51.

Konopliv, A.S., Miller, J.S., Owen, W.M., Yeomans, D.K., Giorgini, J.D., Garmier, R., Barriot, J.-P., 2002. A global solution for the gravity field, rotation, landmarks, and ephemeris of Eros. Icarus 160, 289–299.

La Spina, A., Paolicchi, P., Kryszczińska, A., Pravec, P., 2004. Retrograde spins of near-Earth asteroids from the Yarkovsky effect. Nature 428, 400–401.

Miller, J.K., 10 colleagues, 2002. Determination of shape, gravity, and rotational state of Asteroid 433 Eros. Icarus 155, 3–17.

Morbidelli, A., Vokrouhlický, D., 2003. The Yarkovsky-driven origin of near Earth asteroids. Icarus 163, 120–134.

Morrison, D., 1976. The diameter and thermal inertia of 433 Eros. Icarus 28, 125–132.

Mottola, S., 28 colleagues, 1997. Physical model of near-Earth Asteroid 6489 Golevka (1991 JX) from optical and infrared observations. Astron. J. 114, 1234–1245.

Muinonen, K., 1998. Introducing the Gaussian shape hypothesis for asteroids and comets. Astron. Astrophys. 332, 1087–1098.

Muinonen, K., Lagerros, J.S.V., 1998. Inversion of shape statistics for small Solar System bodies. Astron. Astrophys. 333, 753–761.

Ostro, S.J., 19 colleagues, 1999. Radar and optical observations of Asteroid 1998 KY26. Science 285, 557–559.

Ostro, S.J., 15 colleagues, 2004. Radar observations of Asteroid 25143 Itokawa (1998 SF36). Meteorit. Planet. Sci. 39, 407–424.

Pravec, P., Harris, A.W., Michałowski, T., 2003. Asteroid rotation. In: Bottke, W.F., Cellino, A., Paolicchi, P., Binzel, R.P. (Eds.), Asteroids III. Univ. of Arizona Press, Tucson, pp. 113–122.

Pravec, P., 18 colleagues, 2004. Tumbling asteroids. Icarus. In press.

Press, W.H., Flannery, B.P., Teukolsky, S.A., Vetterling, W.T., 1994. Numerical Recipes. Cambridge Univ. Press, Cambridge.

Rubincam, D.P., 2000. Radiative spin-up and spin-down of small asteroids. Icarus 148, 2–11.

Rubincam, D.P., Rowlands, D.D., Ray, R.D., 2002. Is Asteroid 951 Gaspra in a resonant obliquity state with its spin increasing due to YORP? J. Geophys. Res. 107 (E9), 5065.

Simonelli, D.P., Thomas, P.C., Carcich, B.T., Veverka, J., 1993. The generation and use of numerical shape models for irregular Solar System objects. Icarus 103, 49–61.

Spencer, J.R., Lebofsky, L.A., Sykes, M.V., 1989. Systematic biases in radiometric diameter determinations. Icarus 78, 337–354.

Spitale, J., Greenberg, R., 2001. Numerical evaluation of the general Yarkovsky effect: effects on semimajor axis. Icarus 149, 222–234.

Sullivan, R.J., Thomas, P.C., Murchie, S.L., Robinson, M.S., 2003. Asteroid geology from Galileo and NEAR Shoemaker data. In: Bottke, W.F., Cellino, A., Paolicchi, P., Binzel, R.P. (Eds.), Asteroids III. Univ. of Arizona Press, Tucson, pp. 331–350.

Tholen, D.J., 2003. Recovery of 1998 KY26: implications for detecting the Yarkovsky effect. Bull. Am. Astron. Soc. 35, 972.

Thomas, P.C., Belton, M.J.S., Carcich, B.T., Chapman, C.R., Davies, M.E., Sullivan, R., Veverka, J., 1996. The shape of Ida. Icarus 120, 20–32.

Vokrouhlický, D., Čapek, D., 2002. YORP-induced long-term evolution of the spin state of small asteroids and meteoroids. Rubincam's approximation. Icarus 159, 449–467.

Vokrouhlický, D., Farinella, P., 1998. The Yarkovsky seasonal effect on asteroidal fragments: a non-linearized theory for the plane-parallel case. Astron. J. 116, 2032–2041.

Vokrouhlický, D., Milani, A., Chesley, S.R., 2000. Yarkovsky effect on small near-Earth asteroids: mathematical formulation and examples. Icarus 148, 118–138.

Vokrouhlický, D., Nesvorný, D., Bottke, W.F., 2003. Thermal torques produce spin vector alignments among Koronis family asteroids. Nature 425, 147–152.

Vokrouhlický, D., Čapek, D., Kaasalainen, M., Ostro, S.J., 2004a. Detectability of YORP rotational slowing of Asteroid 25143 Itokawa. Astron. Astrophys. 414, L21–L24.

Vokrouhlický, D., Čapek, D., Chesley, S.R., Ostro, S.J., 2004b. Yarkovsky-detection opportunities. I. Solitary asteroids. Icarus. In press.

Available online at www.sciencedirect.com
SCIENCE DIRECT
ELSEVIER
Icarus 173 (2005) 166–184
ICARUS
www.elsevier.com/locate/icarus

Yarkovsky detection opportunities. I. Solitary asteroids

D. Vokrouhlický [a,*], D. Čapek [a], S.R. Chesley [b], S.J. Ostro [b]

[a] *Institute of Astronomy, Charles University, V Holešovičkách 2, CZ–18000 Prague 8, Czech Republic*
[b] *Jet Propulsion Laboratory, California Institute of Technology, Pasadena, CA 91109-8099, USA*

Received 28 May 2004; revised 22 July 2004

Available online 25 September 2004

Abstract

We show that, over the next two decades, the current radar and optical astrometric technology is adequate to allow detection of the Yarkovsky effect acting on at least two dozen NEAs from a variety of orbital regimes and with effective diameters ranging from about ten meters up to several kilometers. The Yarkovsky effect will likely be detected for objects of rarer spectral types X, C, and E, as well as the more common S and Q. The next predicted detection of the Yarkovsky effect is for 4179 Toutatis in October 2004, which would be also the first multi-kilometer case. The Asteroid 25143 Itokawa, with a likely detection at the end of 2005, could offer an important test due to the independent "ground-truth" measurements of the asteroid mass and surface thermal inertia expected from the Hayabusa spacecraft. Earth co-orbital asteroids (e.g., 2000 PH5 or 2003 YN107) are the best placed for rapid determination of the Yarkovsky effect, and the timespan between discovery of the object and detection of the Yarkovsky effect may be as short as 3 years. By 2012, the motion of potential Earth impactor (29075) 1950 DA will likely reveal the magnitude of the Yarkovsky effect, which in turn will identify which of two possible pole orientations is correct. Vis-a-vis the 2880 impact, this new information will allow a substantial improvement in the quality of long term predictions.

Keywords: Asteroids; Yarkovsky effect; Orbit determination

1. Introduction

The Yarkovsky effect is a tiny non-gravitational self-acceleration of asteroids and meteoroids due to radiative recoil of the anisotropic thermal emission (Bottke et al., 2003). There is an inevitable time delay between the absorption of solar radiation on the Sun-facing side and its subsequent re-emission as thermal radiation, thus the resulting recoil force on the body is offset from the solar direction because of the asteroid's rotational and orbital motion. This produces an along-track perturbation of the orbital motion, specifically a secular variation of the osculating semimajor axis and an associated variation of the osculating orbital longitude that increases quadratically with time. This quadratic runoff allows the Yarkovsky acceleration to be detected much more rapidly, despite its very small magnitude, which distinguishes it from the majority of other perturbing effects, such as planetary perturbations.

The ability to steadily change the orbital semimajor axis means the Yarkovsky effect is a fundamental transport mechanism for small bodies in the Solar System. In particular, the majority of Earth-crossing meteoritic and asteroidal material has presumably been supplied by certain mean motion and secular resonances in or near the main belt, which are in turn fed by the Yarkovsky-driven transport of material (Vokrouhlický and Farinella, 2000; Morbidelli and Vokrouhlický, 2003). As the bodies continue their motion in the planet-crossing region, the brief but intense gravitational tugs during planetary encounters, rather than the continuous Yarkovsky-force perturbations, determine their lifetime. However, the Yarkovsky effect may also be important for precise orbit determination on a short timespan, as noted by Vokrouhlický et al. (2000, 2001), who predicted the Yarkovsky perturbation may surpass the orbital uncertainty for a few near-Earth asteroids (NEAs) in the first decade

* Corresponding author. Fax: +420-2-2191-2567.
E-mail address: vokrouhl@mbox.ccsnet.cz (D. Vokrouhlický).

0019-1035/$ – see front matter
doi:10.1016/j.icarus.2004.08.002

of the 21st century. Following their prediction, Chesley et al. (2003) conducted radar observations of 6489 Golevka in May 2003 and confirmed Yarkovsky perturbation in its orbit. This result immediately implies that the Yarkovsky effect should be detected in the orbits of many more NEAs in the near future.[1,2] Moreover, the strength of the Yarkovsky perturbation depends on a number of notoriously inaccessible physical parameters that can actually be constrained by measuring the Yarkovsky orbital displacement. The asteroid's mass (and hence bulk density unless the volume is poorly known) is the most important of these parameters.

Here we continue the work of Vokrouhlický et al. (2000) and discuss a sample of NEAs that may permit detection of the Yarkovsky effect within the next decade or so. In some cases we correct errors or substantiate conclusions from that early work. We also note several objects overlooked by Vokrouhlický et al. (2000), and we find new bodies discovered after 2000 that are suitable for the Yarkovsky detection. A recent discovery does not necessarily mean that we need to wait "generations" for detection of the Yarkovsky effect. In Golevka's case it took 12 years between the asteroid discovery (Helin et al., 1991) and the Yarkovsky detection. In what follows we show, that for a small body on a suitable orbit the period between discovery and the Yarkovsky detection may be as short as 3–6 years.

1.1. Selection criteria

It appears difficult, and perhaps even unnecessary, to perform our analysis for all known NEAs and we thus adopted the following selection criteria. The first, and the most straightforward, is that the Yarkovsky effect strength increases for small objects. Second, the Yarkovsky effect becomes discernible as a perturbation of the orbital longitude that increases with time. Third, astrometry as accurate as possible is needed. With those rules, we note several categories of candidate objects: (i) bodies with suitably long optical astrometry, past radar astrometry (even if modest in quality) and having an opportunity to be radar ranged once or twice soon (e.g., Apollo, Aten, Icarus; Section 2), (ii) very small bodies (e.g., 2000 UK11, 1998 KY26, 2002 JR100; Section 4) and (iii) bodies on unusual orbits allowing extensive radar astrometry in the near future (e.g., 2000 PH5, 1999 MN; Section 3) or bodies with unusual observation circumstances (e.g., Itokawa to be visited by Hayabusa spacecraft). Each of these groups has its own difficulties, especially because a "productive" Yarkovsky detection requires additional information like the rotation pole position and rotation period, the shape model, etc. Surprisingly, in spite of the large strength of the Yarkovsky effect for the smallest bodies, these are generally not the most attractive candidates since it is difficult to acquire this additional information for them. The currently most interesting candidate group are bodies a few hundreds of meters across that make frequent close encounters with the Earth during the next decade or so. We discuss the special case of binary asteroids in a separate paper.

The selection rules described so far should isolate the most promising candidates for a successful Yarkovsky detection. But since a main purpose is to acquire physical information, as well as orbit refinement, we may also adopt additional criteria. For instance, we may wish to select a sample of asteroids whose spectral classes are as heterogeneous as possible. Although NEAs are known for their spectral diversity, S- and Q-types dominate (e.g., Binzel et al., 2003, 2004), so our selection criteria may be "biased" towards bodies of spectral classes other than S and Q. Similarly, despite the difficulties mentioned above, we may seek the Yarkovsky signal in orbits of asteroids of diverse sizes, from tens of meters to kilometers. This is an important goal, recalling that the Yarkovsky detection analysis constrains bulk density of the target and thus its interior structure. Experimental and theoretical work dating to the 1960s has converged to a consensus that a fundamental change, from the strength-dominated regime to the gravity-dominated regime, occurs in the structure of Solar System bodies as sizes increase beyond about 100–200 m (e.g., Asphaug et al., 2003). The Yarkovsky effect detections may offer a unique possibility to probe the two regimes by constraining the bulk density of bodies ranging from as small as ten meters up to a few kilometers in diameter.

1.2. Methodology

For any given asteroid the methodology of our work is the same as in Vokrouhlický et al. (2000). We use all available past optical and radar astrometry data to fit orbits using two different force models, one with only gravitational interactions and the other with the addition of Yarkovsky accelerations. For both models, the best-fitting orbit and its uncertainty[3] are propagated to the nearest close encounter

[1] We also note the work of Nesvorný and Bottke (2004) who showed that semimajor axes of the young Asteroid Karin cluster members have changed during the past 5.8 Myr in a way compatible with prediction of the Yarkovsky effect, obtaining thus the first direct evidence of Yarkovsky effect acting on the main-belt asteroids.

[2] We find it symbolic that the Yarkovsky effect might be detected in the orbits of 1862 Apollo and 2062 Aten, "the namesakes of their dynamical groups," within the next decade (Section 2).

[3] In this work, we consider the uncertainty due to the observation errors only. As in Chesley et al. (2003), an extended analysis taking into account uncertainty in the gravitational influence of asteroids, planets and parameters of the Yarkovsky effect may be necessary when real data are processed. Experience with Golevka shows that predictions made in this paper are reliable and that the influence of the uncertain mass of asteroids does not overwhelm the observation-based uncertainty intervals (and becomes actually negligible for orbits sufficiently decoupled from the main asteroid belt). Uncertainty in Mercury's mass may be a concern for some deep Atens (e.g., Section 3.3), but in the post-Messenger era this effect should be negligible. In the cases of long-lasting encounters with unusually small relative velocity (e.g., Section 3.2), the role of the Earth-mass uncertainty should be also checked.

with the Earth that allows good-quality radar data to be taken. In practice we require the single day signal-to-noise ratio (SNR) of the radar echoes (e.g., Ostro, 1993; Ostro et al., 2003) to be larger than 10.[4] We assume ranging from the Arecibo or Goldstone facilities, as appropriate, using the current system parameters (see http://echo.jpl.nasa.gov/). At the next radar observation opportunity we check for overlap or separation of the two prediction uncertainty ellipses (one with and one without Yarkovsky) in the delay/Doppler (range/range-rate) plane. If the separation of the two confidence ellipses is statistically significant then observations at that epoch can reveal Yarkovsky acceleration.

Unfortunately for our purposes, however, the uncertainty regions often overlap. In that situation, the radar astrometry serves to further constrain orbital uncertainty and a *subsequent* radar opportunity allows the actual detection of the Yarkovsky effect. To consider this scenario, we *simulate* radar observations during the next close encounter and check overlap/separation of the no-Yarkovsky and the Yarkovsky solutions during the subsequent approach. In some cases we also simulate optical astrometry. It should be pointed out that the purpose of these simulations is to see how *they confine future orbital uncertainty* and not to "guide the orbit along some direction" and thus they are constructed in accord with the current observations. We assume current technology for the simulation of optical and radar astrometry, typically taking the estimated size of the object as a formal uncertainty of the radar observations, and one arcsecond as a formal uncertainty of the optical observations. It is likely that future astrometry technology, such as the GAIA project (e.g., Mignard, 2002, and http://astro.estec.esa.nl/GAIA), will enhance Yarkovsky detection possibilities; also if radar systems are upgraded, or a dedicated NEA radar network is eventually built (e.g., Ostro, 1997), Yarkovsky detections could become more frequent.

Our analyses used two different software sets: The `OrbFit` package (http://newton.dm.unipi.it/) and the JPL orbit determination program. Both programs implement a linearized formulation of the diurnal and seasonal variants of the Yarkovsky effect (e.g., Vokrouhlický et al., 2000) that assumes spherical bodies with constant thermal and rotational parameters. Our Golevka experience has shown that predictions made with this simplified approach can be considered reliable, so in most of the simulations reported below we used the linearized models and `OrbFit`. But in two cases the linear method was judged unreliable so we used the JPL software, which has a special high-accuracy mode that allows the lookup of externally computed Yarkovsky force components. This approach, which was also used for Golevka (Chesley et al., 2003), applies force components that are pre-computed and tabulated as a function of asteroid true anomaly. These high accuracy forces are obtained with dedicated software that accommodates such details as (i) the precise shape of the body, (ii) a complete, non-linear heat diffusion numerical solver and (iii) temperature and depth dependence of the thermal parameters. A particular novelty in the present paper is a full-fledged nonlinear computation of the Yarkovsky force components for Toutatis, characterized with a non-principal-axis rotation (such that the spin vector undergoes free wobble about the long body axis; Hudson and Ostro, 1995; Ostro et al., 1995a, 1999). We also use this formulation to refine our earlier prediction for Geographos, taking into account its extremely elongated shape (Ostro et al., 1995b, 1996).

In what follows, we investigate the possibility of Yarkovsky detection for a number of objects in the three different classes noted above. These objects are tabulated in Table 1. For each case, we summarize the basic information relevant for estimation of the strength of the Yarkovsky effect, and, when needed, we comment on the simulated future observations, outlining an optimum schedule for an early detection.

2. Targets with long observation records

In this section we discuss Yarkovsky detectability for objects having a long record of optical astrometry. Yeomans (1991, 1992) analyzed several NEAs with long observational histories (most also having some radar astrometry) for empirical accelerations common to the motion of active short-period comets, eventually reaching the conclusion that there was at the time no evidence for nongravitational accelerations on any NEAs. However, the passage of time and the corresponding increase of optical and radar astrometry for these objects will soon enable the detection of much smaller forces than was possible in 1991. Conveniently, except the cases with pre-discovery identifications, these are typically large asteroids with enough photometric observations to reveal the pole direction. Sometimes we also make use of infrared observations that help to constrain the surface thermal inertia. Of course, a detrimental factor for these bodies is their large size and the correspondingly small strength for the Yarkovsky effect. An extreme case is the large (32 km long) Asteroid 433 Eros, with the longest known observational history among NEAs. Surprisingly, the possibility of detecting the Yarkovsky effect for Eros is not out of the question in light of the fact that the NEAR Shoemaker mission enabled a series of high-accuracy range measurements to be derived from the spacecraft tracking data. A major hindrance in this case, however, is a very unlucky orientation of the spin axis, with obliquity of $\simeq 90°$ (e.g., Konopliv et al., 2002; Souchay et al., 2003), which diminishes the otherwise dominant diurnal variant of the Yarkovsky effect.

[4] Whenever we report a SNR value we mean the matched-filtered SNR in one day of observation.

Table 1
Selected candidate asteroids for Yarkovsky detection within the next two decades

Note	Asteroid		Spectral class	Size [m]	Year of Yarkovsky detectability	Required pre-detection observations	
	No.	Ident.				Radar	Optical
a,b	4179	Toutatis	S	2450[c]	2004?–2008	(2004)	
a	25143	Itokawa	S	360[c]	2005	2004	
a	54509	2000 PH5	?	100	2006	2004, 2005	
a		2003 YN107	?	20	2006	2005	2004[d]
a	1862	Apollo	Q	1400	2007	2005	
a,b	1620	Geographos	S	2560[c]	2008?–2019	(2008)	
a		1999 MN	?	250	2010	2005, 2009	
a		2000 UK11	?	32	2010?	2005	2005[d]
a	3103	Eger	E	1750	2011	2006	
a	29075	1950 DA	?	1100	2012?–2023		2004–2012[d]
a	2062	Aten	Sr	900	2014	2012, 2013	2011
a	1566	Icarus	SU, Q	1270	2015	2006	
		2000 WN10	?	350	2015?	pre-2015 possibilities	
	33342	1998 WT24	E	500	2015?	2012	
a	2100	Ra–Shalom	Xc	2780	2016?–2019	2006 (2016)	
		2001 YE4	?	250	2016?–2017	2007, 2012	2006[d]
		1989 VA	Sq	800	2017	2007, 2012	
a		2002 JR100	?	50	2018	2010, 2011	2010[d]
a		1991 VG	?	10	2018		2017[d]
		1998 SD9	?	50	2018?–2021	2008, 2011	2008[d]
		2002 BF25	?	115	2020	2010, 2012	2010[d]
b		1998 KY26	C?	30[c]	2020?–2024		2009, 2013
	2340	Hathor	Sq	530	2021	2007, 2014	
	3361	Orpheus	Sq	500	2021	2017	
		2004 FH	?	25	2021	2018	2018[d]
		1995 CR	?	80	2022	2014, 2017	2005[d]
	7341	1991 VK	Sr	1400	2022?	2007, 2012, 2017	
	6037	1988 EG	?	600	2023	2008, 2013	

Note. Objects are sorted according to the estimated year of Yarkovsky detection. Only solitary asteroids are considered here; binary asteroid systems are to be reported in a follow-on paper. Additional candidate objects will be posted on http://sirrah.troja.mff.cuni.cz/~davok/.

[a] A full simulation and discussion is included in this paper.

[b] Previously analyzed by Vokrouhlický et al. (2000). Here we report refined results for Geographos and Toutatis for which we compute the Yarkovsky acceleration using a complete nonlinear model accounting for their specific shape and rotation state.

[c] A precise shape is known. We indicate the diameter of a sphere with equivalent volume.

[d] Accurate optical astrometry is required for a successful detection.

2.1. *1862 Apollo*

Like Golevka, Apollo is a Q-type candidate for the detection of the Yarkovsky effect.[5] Apollo has a long, though not exceedingly extensive, optical astrometry data series since December 1930. Radar astrometry comprises a single campaign in November 1980 with modest accuracy (see Ostro et al., 2002), but still providing a valuable constraint on the orbit.

Assuming data from Binzel et al. (2003), namely the absolute magnitude $H = 16.23$ and the geometric albedo $p_V = 0.26$ (implying, with the slope parameter 0.23, a Bond albedo[6] $A \simeq 0.12$), one obtains for Apollo an effective size $D \simeq 1.4$ km. These results are in accord with Harris (1998), who used a thermo-physical model to remove drawbacks of the standard thermal analysis by Lebofsky et al. (1981), yielding a size in the range 1.2–1.5 km with slightly higher value of the albedo. Ostro et al. (2002) place an upper limit of 1.6 km on the effective diameter from the analysis of 1980 radar data. Hereafter we use the Binzel et al. values.

The rotation period ($P = 3.065$ hr) and pole information (ecliptic longitude $\ell = 56°$ and latitude $b = -26°$ both with formal uncertainty less than 10°) are due to Harris et al. (1987). We note a similar rotation period but slightly different value of pole position ($\ell = 38° \pm 12°$ and $b = -36° \pm 10°$) by De Angelis (1995), who also indicates polar flattening of about 1.87. From shape inversion, J. Ďurech (2003, private communication) obtained a solution with a still larger obliquity (relevant for the Yarkovsky effect strength) and an asteroid silhouette compatible with Ostro et al. (2002), but the statistical significance of this solution does not exceed those mentioned above. Good photometry and radar data during Apollo's 2005 apparition should significantly improve pole and shape solutions. At present we use Harris et al.'s solution which is, in a sense, conservative, since

[5] Apollo was inadvertently omitted from the analysis of Vokrouhlický et al. (2000).

[6] We note that Bond's albedo is used in the expression for the Yarkovsky force within the linearized theory; Vokrouhlický and Bottke (2001).

it has the lowest obliquity and thus the minimum strength of the Yarkovsky force.

Lebofsky et al. (1981) recorded radiometric observations of Apollo in the range 4.8–20 μm; these data were also analyzed by Harris (1998) who used his empirical thermophysical model to conclude that this target should have a non-zero, but small, surface thermal inertia. (The beaming factor $\eta \simeq 1.15$ suggests a slightly larger thermal inertia than that of Eros.) Without more detailed information, we adopted the following tentative set of surface thermal parameters: thermal conductivity $K = 0.01$ W/(m K), specific heat capacity $C = 680$ J/(kg K), and surface and bulk densities $\rho_s = 2.0$ g/cm^3 and $\rho_b = 2.6$ g/cm^3, all corresponding to a mixture of particulate layer and rocks. The Yarkovsky acceleration scales inversely with ρ_b, but a less trivial scaling relates the other parameters (except for a correlated dependence on $\rho_s K$; see, e.g., Chesley et al., 2003). With the other parameters fixed, the maximum Yarkovsky signal occurs for $K \simeq 0.05$ W/(m K).

There are two good opportunities to observe Apollo, in November 2005 from Goldstone and Arecibo and in May 2007 only from Goldstone. The Arecibo 2005 signal should reach SNR of nearly 5000, while Goldstone in 2007 peaks at SNR $\simeq 80$. A single ranging in either 2005 or 2007 will not unambiguously reveal the Yarkovsky effect, hence it will be necessary to acquire radar data in both 2005 and 2007. The importance of the 2005 run is twofold: (i) it should yield an accurate shape model and pole position for Apollo, and (ii) it should reduce orbital uncertainty. We simulated two Arecibo range/range-rate measurements separated by two days in early November 2005.[7] Assumed uncertainties are 0.5 km in range and 0.75 km/day in range-rate.

With these simulated observations, plus all previous optical and radar observations, we determined the separation of the no-Yarkovsky and Yarkovsky orbits, together with their uncertainty regions, in mid-May 2007, when the asteroid is within range of the Goldstone radar. Figure 1 promises a good separation of the two solutions with no statistically significant overlap of the uncertainty regions,[8] permitting an unambiguous Yarkovsky detection.

The next deep close approach to the Earth is not until 2046, but we note that Apollo will be within reach of Arecibo radar during shallow approaches in December 2021 (peak SNR $\simeq 40$) and June 2023 (peak SNR $\simeq 70$). We also note an interesting close approach of Apollo to 4 Vesta in 2017; post-2017 radar and optical astrometry data may produce an independent estimate of Vesta's mass, provided Apollo's orbit is well modeled, including good characterization of the Yarkovsky perturbation.

[7] Apollo has been also scheduled for Goldstone observations in November 2005 (http://echo.jpl.nasa.gov/), but these are not considered here.

[8] Should the surface conductivity be an order of magnitude smaller, say $K = 0.001$ W/(m K), which is unlikely (Harris, 1998), the Yarkovsky displacement in Fig. 1 would be reduced by half.

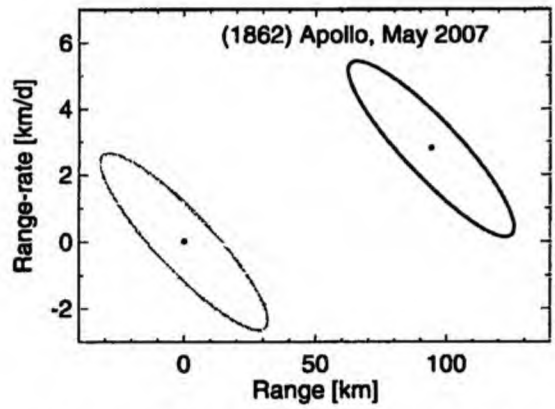

Fig. 1. Predicted Yarkovsky-induced offset with 3σ (99%) confidence ellipses in the space of radar range and range-rate for 1862 Apollo on May 11.6, 2007. The statistical significance of the potential Yarkovsky detection opportunity is indicated by the degree of separation between the no-Yarkovsky prediction (gray ellipse, centered on origin) and Yarkovsky prediction (black ellipse). The predictions assume simulated Arecibo radar astrometry in November 2005 as described in the text.

2.2. 1566 Icarus

The case of Icarus has already been considered by Vokrouhlický et al. (2000), but we update their prediction for two reasons: (i) There are ambiguities in size of this object, and Vokrouhlický et al. (2000) selected what now appears to be an unlikely diameter, and (ii) a low-SNR possibility to radar range Icarus in 2006 was overlooked. Specifically, system upgrades at Arecibo should allow ranging to Icarus in late June 2006, when the SNR peaks at around 14 as the asteroid approaches the Earth at $\simeq 0.3$ AU. There is also some likelihood, not considered here, that optical astrometry in 2006, 2009, and 2010 will reduce the orbit uncertainty (Vokrouhlický et al., 2001).

Vokrouhlický et al. (2000) assumed an effective diameter $D = 0.9$ km based on a value of the geometric albedo $p_V = 0.6$, which was rather high, but consistent with the IRAS standard thermal model. However, like other similar cases (Harris, 1998), this was almost certainly wrong. Harris (1998), using an empirical thermo-physical model, obtained a more reasonable interpretation of Icarus' radiometric data with $D = 1.27$ km and $p_V = 0.33$, which, with a slope parameter 0.09 implies a Bond albedo of $A = 0.12$. The approach of Harris (1998) does not let us solve for surface thermo-physical parameters, like thermal inertia $\Gamma = \sqrt{K\rho_s C}$, directly, yet the high value of the beaming factor $\eta = 1.15$ suggests a substantial value for Γ. Moreover, the low perihelion orbit of this asteroid also suggests a high thermal inertia, since all factors in Γ increase with effective temperature[9] (e.g., Wechsler et al., 1972). As a result, we assume the following set of parameters in our simulations: thermal conductivity $K = 0.05$ W/(m K), spe-

[9] Moreover, fast rotation of Icarus may suggest fewer regolith deposits on its surface.

cific heat capacity $C = 800$ J/(kg K), surface and bulk densities $\rho_s = 2.0$ g/cm^3 and $\rho_b = 2.6$ g/cm^3. Rotation period ($P = 2.274$ hr) and pole direction (ecliptic longitude $\ell = 214° \pm 5°$ and latitude $b = 5° \pm 12°$) are from De Angelis (1995).

To test different hypotheses, we briefly report the results of several model runs. First, we propagated Icarus' orbit, as defined by the currently available set of astrometric observations, to the nearest future encounters with the Earth, in June 2006 and June 2015. The 2015 approach is close enough to gather detailed information about this target with both the Arecibo system (SNR $\simeq$ 3500) and at Goldstone (SNR $\simeq$ 600). Figure 2 shows the no-Yarkovsky and Yarkovsky predictions and their associated uncertainty regions in the radar-observable plane in both 2006 and 2015. Unfortunately, at both epochs a partial overlap of the uncertainty regions occurs, so that the statistical significance of the Yarkovsky acceleration is modest, perhaps 2–3 sigma.[10] In fact, results by Vokrouhlický et al. (2000, Fig. 11) are somewhat similar. As discussed above, the way to improve the Yarkovsky signal is to further constrain the 2015 prediction using the 2006 ranging opportunity. To this purpose we have simulated Arecibo delay and Doppler astrometric data taken on June 27, 2006 with an equivalent range accuracy of 2 km and range-rate accuracy of 7 km/day. As a result, the orbit uncertainty region in 2015 is considerably diminished (Fig. 2b, interior ellipses), enough to ensure a statistically significant detection of the Yarkovsky effect.[11]

2.3. 2062 Aten

Like Apollo, Aten is another enigmatic "leader in its group," the first asteroid discovered having semimajor axis smaller than 1 AU (Helin et al., 1976). Apart from exceptional cases, Aten-like orbits typically suffer from sparse observational possibilities, especially for large orbital inclination. As a result, past optical astrometry of this target is sporadic, although the observed arc is long, from December 1955 (three pre-discovery observations) until February 1997. Also, a single Doppler measurement has been obtained from Goldstone in January 1995 (Benner et al., 1997).

Early radiometry of Aten (Morrison et al., 1976; Cruikshank and Jones, 1977; Veeder et al., 1989) resulted in an estimation of its diameter $D \simeq 900$ m for $p_V = 0.2$, yielding a Bond albedo $A \simeq 0.1$. Because of the orbital and spectral similarity to Icarus (e.g., Lebofsky et al., 1979; Binzel et al., 2003) we assume the same thermal surface parameters listed above for Icarus.

[10] Higher values of the surface thermal inertia increase the significance, but still not enough to remove ambiguity, even in 2015.

[11] Figure 2a suggests the range measurement in 2006 places the most significant constraint to reduce orbital uncertainty (required for the 2015 detection of the Yarkovsky effects). It can be replaced with a single Doppler measurement equivalent to a range-rate datum with an uncertainty better than $\simeq 0.5$ km/day.

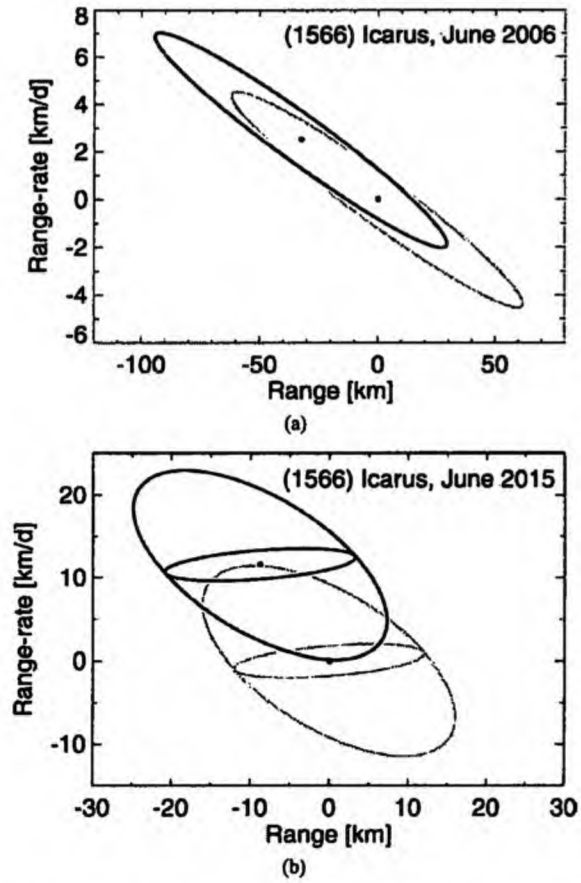

Fig. 2. Yarkovsky offsets for 1566 Icarus on (a) June 27, 2006 and (b) June 19.6, 2015, depicted as in Fig. 1. Only currently available astrometry is used, except for the interior ellipses in (b), which include simulated Arecibo radar astrometry from June 2006 when the target is barely observable with the Arecibo radar (SNR $\simeq$ 14).

Reliable photometry of Aten has been recorded during the 1995 apparition by Mottola et al. (1995), who report a synodic rotation period of $P = 40.77$ hr. So far, no constraint on the rotation pole orientation has been obtained, undermining an accurate prediction of the Yarkovsky perturbation. We assume an arbitrary pole orientation, $\ell = 0°$ and $b = +30°$, with corresponding obliquity $\simeq 43°$, which gives an "average" strength to the Yarkovsky effect.

Low solar elongation makes Aten barely observable till 2009, but a series of yearly encounters with the Earth from 2012 to 2015 gives a good prospect for accurate orbit determination, including the possibility to detect the Yarkovsky effect. Arecibo can range this target during its shallow encounters in July 2012 and June 2013 with a maximum SNR of $\simeq$ 18 and $\simeq$ 20, respectively. Deeper encounters with the Earth occur in January 2014 (SNR $\simeq$ 135) and 2015 (SNR $\simeq$ 45). Our analysis indicates that the 2012 and 2013 radar opportunities are important to constrain the orbit uncertainty of this target. Assuming delay-Doppler measurements with effective noise levels of $\simeq$ 1 km range and $\simeq$ 2 km/day range-rate are acquired at both of these radar

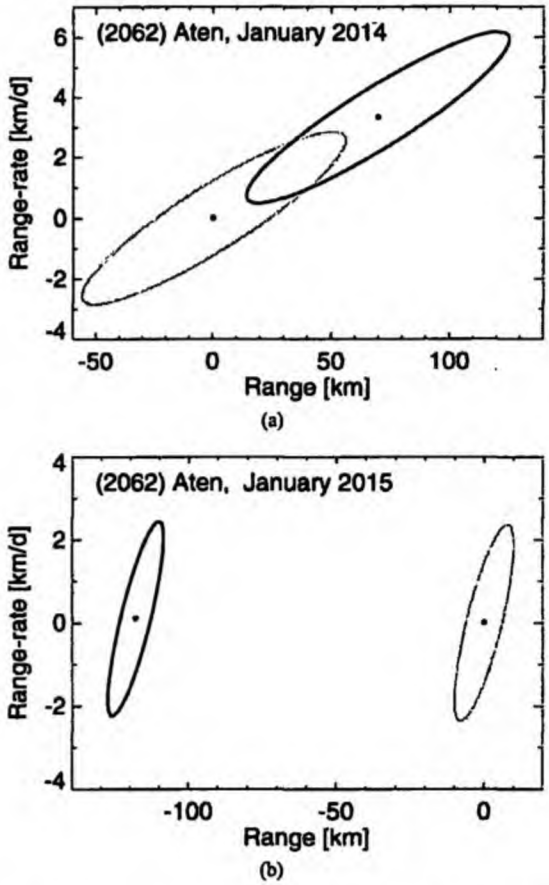

Fig. 3. Yarkovsky offsets for 2062 Aten on (a) January 8.4, 2014 and (b) January 17.8, 2015, depicted as in Fig. 1. In (a) we have simulated Arecibo radar astrometry in 2012 and 2013; in (b) we extend the data set to include the 2014 radar astrometry.

opportunities, the January 2014 ranging can marginally reveal the Yarkovsky perturbation for this object (Fig. 3a). A year later (January 2015), a more statistically substantial detection can be reached with radar astrometry acquired during previous possibilities[12] (Fig. 3b).

2.4. 2100 Ra–Shalom

This asteroid has a good record of optical astrometry since October 1975) and four radar runs with increasing levels of accuracy (from August 1981 to August 2003). With nearly 3 km diameter, Ra–Shalom is the largest asteroid for which we expect the Yarkovsky effect may be detected within the next decade or so.

This is a first chance to detect the Yarkovsky effect for an Xc-type body. Prior to accurate radiometry, there was a fair amount of fluctuation in estimates of this object's size. The latest work of Delbó et al. (2003) confirms earlier estimates (e.g., Lebofsky et al., 1979; Veeder et al., 1989; Harris et al., 1998) of a large size $D \simeq 2.78$ km and small albedo $p_V = 0.083$, which is consistent with the spectral type and with the analysis of the radar data (Shepard et al., 2000, 2004). These authors conclude Ra–Shalom should have an unusually high value of the surface thermal inertia, "comparable to, or exceeding, that of solid rock." Thus we adopt thermal conductivity $K = 1$ W/(m K) and specific heat capacity $C = 800$ J/(kg K). We use low surface and bulk densities $\rho_s = \rho_b = 2.0$ g/cm^3, as appropriate for the spectral type Xc. This choice of parameters yields approximately the same value of surface thermal inertia ($\Gamma \simeq 1100$ J/(m^2 K s$^{1/2}$)) as that reported by Harris et al. (1998).

Kaasalainen et al. (2004) recently re-analyzed the available photometry on this asteroid and obtained a sidereal rotation period of $\simeq 19.8$ hr with pole direction $\ell = 73°$ and $b = 13°$. A preliminary, convex shape model was also derived, consistent with Shepard et al.'s (2000) conclusion that this object is not elongated.

Ra–Shalom has an exceptionally good record of close encounters with the Earth,[13] though none of them is particularly deep within the next century or so. Nevertheless, Arecibo is able of observe this target several times in the near future, with the best opportunities occurring in August 2006 (SNR $\simeq 130$), September 2016 (SNR $\simeq 70$) and September 2019 (SNR $\simeq 170$) and still better possibilities in the early 2020s. There is also a more challenging radar window in September 2013 with the peak SNR $\simeq 25$. An "optimistic" scenario is to constrain Ra–Shalom's orbit by the 2006 radar observations (in our simulation we assumed one range observation of 0.3 km accuracy and one range-rate observation of 0.75 km/day accuracy) and achieve the Yarkovsky effect detection with the 2016 radar observations. However, Fig. 4a (envelope ellipses) suggests that the orbital uncertainty remains large, leaving some overlap for the no-Yarkovsky and Yarkovsky predictions.

There are two ways to improve the situation. First, we simulated low-quality radar astrometry from September 2013,[14] specifically a range measurement with 2 km uncertainty and a range-rate measurement with 7.5 km/day uncertainty. These reduced the uncertainty regions in 2016 enough to allow a statistically significant detection of the Yarkovsky effect in 2016 (Fig. 4a, interior ellipses).

Another option is to record radar astrometry in 2006 and 2016 (for the latter we simulated data as in 2006) and attempt to detect the Yarkovsky effect by September 2019. Figure 4b confirms that the Yarkovsky effect should be easily revealed in this scenario.

[12] We checked that this result can be obtained with ranging in 2013 and 2014 only.

[13] This is because Ra–Shalom belongs to what Milani et al. (1989) classify as a "Toro orbital class"; in particular, this asteroid presently resides in the 21/16 mean motion resonance with the Earth. Note this is close to the 4/3 resonance and thus Ra–Shalom appears to encounter the Earth every 3 years in separated periods of time.

[14] We did not investigate the possibility of numerous and accurate optical astrometry in 2013.

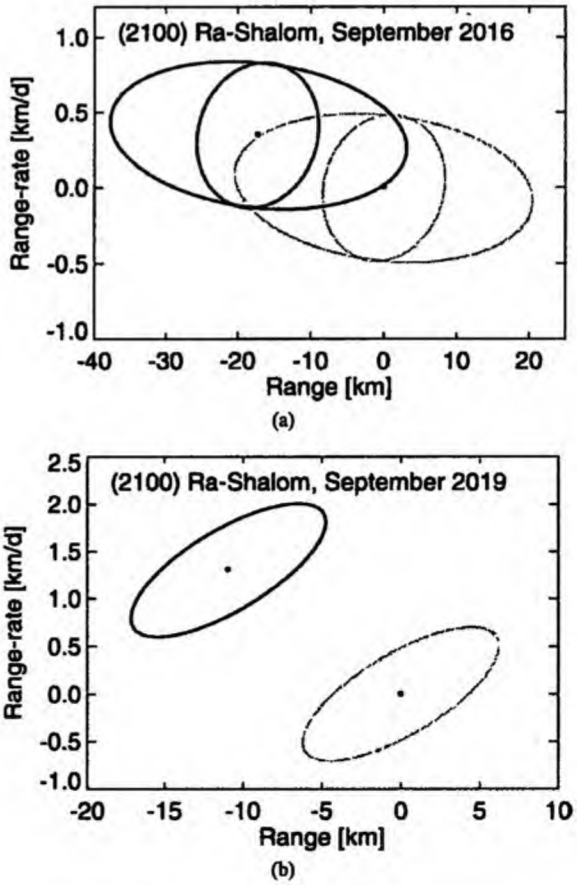

Fig. 4. Yarkovsky offsets for 2100 Ra–Shalom on (a) September 12.6, 2016 and (b) September 9.8, 2019, depicted as in Fig. 1. The larger pair of ellipses in (a) assume a simulated Arecibo radar observation in August 2006, while the smaller ellipses include simulated radar measurements from both 2006 and September 2013. In (b) we assume simulated radar apparitions in August 2006 and September 2016.

2.5. 3103 Eger

After being recognized as the first E-type NEA (Veeder et al., 1989), this target has attracted attention as a putative parent body of the enstatite achondrite meteorites (Gaffey et al., 1992). Since this result, additional spectrally-similar bodies have been identified among the NEA population (e.g., Binzel et al., 2003), but Eger remains somewhat enigmatic as a large body residing on what may be an unusually long-lived planet-crossing orbit.[15] This suggests a possible link to the spectrally similar group of Hungaria asteroids, which have similarly large values for inclination and which tend to heliocentric distances similar to Eger's aphelion distance. So far, we do not have density information about any of the rare

[15] Milani et al. (1989) recognized the orbit being presently locked in the exterior 3/5 mean motion resonance with the Earth, providing thus a protection mechanism against close encounters with the planet; moreover, the collisional probability to encounter/interact with other planets is decreased by the high orbital inclination.

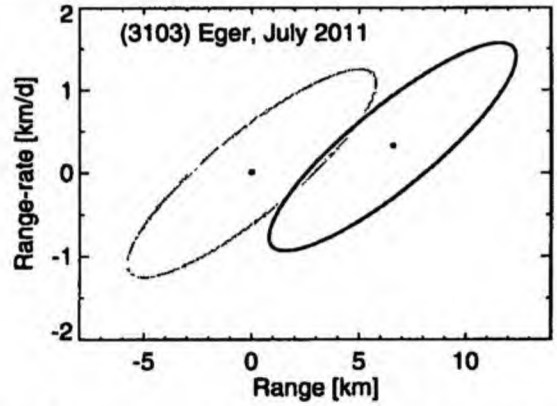

Fig. 5. Yarkovsky offsets for 3103 Eger on July 24.0, 2011, depicted as in Fig. 1. These solutions assume simulated Arecibo astrometry from 2006.

E-type asteroids (Britt et al., 2003), so the Yarkovsky effect measurement might provide an interesting clue.

The orbit of 3103 Eger has not been heavily observed, although its available optical astrometry, dating to 1982, and two moderately accurate radar apparitions (July 1986 and July 1996) form a solid basis for detecting the Yarkovsky effect. However, some uncertainty does arise from poor knowledge of the size of this asteroid. We adopt the radar-suggested effective value $D \simeq 1.75$ km (Benner et al., 1997). Biaxiality of the asteroid shape was found by Kaasalainen et al. (2002) from lightcurve inversion. The same analysis gave reliable information about Eger's pole direction ($\ell = 10°$, $b = -50°$) and sidereal rotation period ($P = 5.707$ hr). The retrograde sense of rotation (obliquity $\simeq 121°$) makes the orbit drift inward to the Sun due to the (diurnal and seasonal) Yarkovsky effect.

Little is known about the surface properties of this asteroid, except for a high radar circular polarization (Benner et al., 1997), which may be interpreted as a signature of extreme near-surface roughness at centimeter to meter scales. This would suggest a higher value of the surface thermal inertia, but a thin dusty cover of a few penetration depths of the diurnal thermal wave is certainly not excluded. We thus assume moderate values of thermal conductivity $K = 0.01$ W/(m K), specific heat capacity $C = 800$ J/(kg K), and surface and bulk densities $\rho_s = 2.0$ g/cm^3 and $\rho_b = 2.6$ g/cm^3.

The same resonant orbit that protects Eger from collision with the Earth is responsible for shallow close approaches once every 5 years. This pattern allows Arecibo observations in July 2006 (SNR $\simeq 120$), July 2011 (at SNR $\simeq 85$), July 2016 (SNR $\simeq 52$), as well as a 2021 approach with a still lower value of SNR. We find that the 2006 observations, while helpful for refining the shape and spin state, are definitely needed to constrain the orbital uncertainty so that radar observations in 2011 observation will reveal the Yarkovsky effect. To that end we simulated 2006 radar astrometry with a 0.2 km range measurement and a 0.5 km/day range-rate measurement at the time of the peak SNR. Fig-

ure 5 confirms that the no-Yarkovsky and the Yarkovsky predictions are distinct at the 6σ level, with minimal overlap of the 3σ confidence regions. Obviously, the 2016 radar measurements would further refine the solution reducing its uncertainties.

2.6. 1620 Geographos

Geographos has been considered as a Yarkovsky-detection candidate already by Vokrouhlický et al. (2000). Here we refine that solution by (i) taking into account Geographos' extreme elongation as derived by previous radar and optical observations (e.g., Ostro et al., 1995b, 1996; Magnusson et al., 1996; Hudson and Ostro, 1999), and (ii) by removing a mistakenly considered possibility to radar-sense the asteroid in March 2015 (should have been in August 2019).

Geographos underwent its closest post-discovery approach to the Earth in August 1994 and during that apparition detailed radar data were acquired (Ostro et al., 1995b, 1996). Based on those observations, Hudson and Ostro (1999) constructed a shape model of this asteroid. Since Geographos appears to be one of the most elongated objects known, we wondered how reliable was the prediction of Vokrouhlický et al. (2000), who assumed a spherical asteroid. In our present simulation, we use the 4092 surface-facet polyhedral model available at http://www.psi.edu/pds/archive/rshape.html. Heat diffusion is numerically solved in a one-dimensional approximation (e.g., Vokrouhlický and Farinella, 1998) for each of the surface facets, taking into account daily and seasonal cycles of illumination, and any mutual shadowing between different parts of the asteroid surface. After the recoil force is computed for each of the surface elements as a function of time and true anomaly, their effects are combined to obtain the resulting total Yarkovsky force along one revolution and exported as a look-up table used by the orbit determination program.[16] Our model assumes the effective thermal parameters of the surface are constant; we fixed the value of the specific heat capacity to $C = 680$ J/(kg K), surface and bulk densities $\rho_s = 1.7$ g/cm^3 and $\rho_b = 2.5$ g/cm^3, while leaving the value of the surface conductivity to span a wide range of values between 10^{-4} and 1 W/(m K). As noted by Chesley et al. (2003) these results may be scaled to obtain solutions with other values of the fixed parameters; namely the Yarkovsky acceleration (i) scales inversely proportionally with ρ_b, and (ii) is invariant for $\rho_s K$ constant.

The radar shape model uses a pole position at ecliptic longitude $\ell = 55° \pm 6°$ and ecliptic latitude $b = -46° \pm 4°$ and a sidereal rotation period of 5.2233 hr. These are identical to the values derived by Magnusson et al. (1996) from the photometric lightcurve data.

We first note that the orbit-averaged value of the semimajor axis drift due to the Yarkovsky effect determined with a fully numerical model in this paper and the much simplified solution used in Vokrouhlický et al. (2000) yield surprisingly similar results (Fig. 6), with a maximum difference of $\simeq 10\%$ when $K \simeq 0.03$ W/(m K).

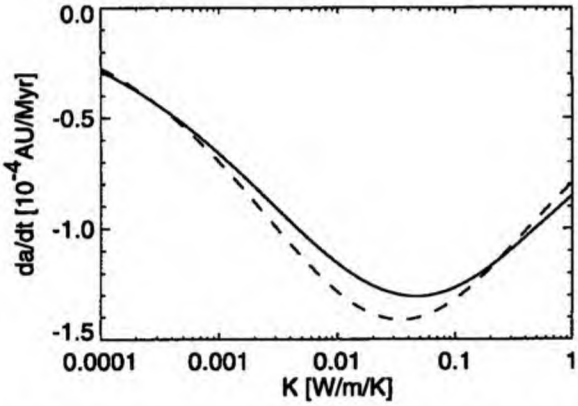

Fig. 6. The Yarkovsky-induced average semimajor axis drift rate $\langle da/dt \rangle$ for Geographos, as a function of surface conductivity K. The solid line is the result from the complete numerical model accounting for details of Geographos' irregular shape. The dashed line shows the result from a linearized approximation of heat conduction and a fictitious spherical body having the same volume as Geographos, which is equivalent to the approximation used by Vokrouhlický et al. (2000).

Geographos approaches Earth in March 2008 (offering SNR $\simeq 625$ from Arecibo) and in September 2019 (offering SNR $\simeq 15$ from Arecibo). Figure 7a indicates that the detectability of the Yarkovsky effect in 2008 is somewhat dubious, with the Yarkovsky signal at about the 2σ level. Constraining the current uncertainty seems difficult, although in December 2004 Geographos' sky-plane uncertainty in right ascension will increase up to $\simeq 0.036$ arcsec. High accuracy optical astrometry—if successful and prolific—may slightly improve the situation. For the sake of an illustration we simulated 0.01 arcsec astrometry on December 15, 2004, and we verified that it can shrink the 2008 uncertainty ellipse to about 2/3 of its current extent. This would shift the estimated Yarkovsky displacement to about 3σ value in the uncertainty region.

Ultimately, even though the 2008 radar astrometry may be only suggestive of the Yarkovsky displacement, it would confine the orbital uncertainty enough to make the Yarkovsky effect detectable in 2019 (Fig. 7b).

2.7. (29075) 1950 DA

1950 DA has been the object of considerable attention due to a small possibility of Earth impact in the year 2880 (Giorgini et al., 2002). Although they did not compute an impact probability, Giorgini et al. did place an upper bound at 3.3×10^{-3}. Interestingly enough for the present paper, the chief obstacle to computing the impact probability relates to uncertainty surrounding the Yarkovsky effect. In particular, the pole orientation was not uniquely determined by the 2001 radar imaging, so there are two equally probable spin

[16] Data available at http://sirrah.troja.mff.cuni.cz/~davok/.

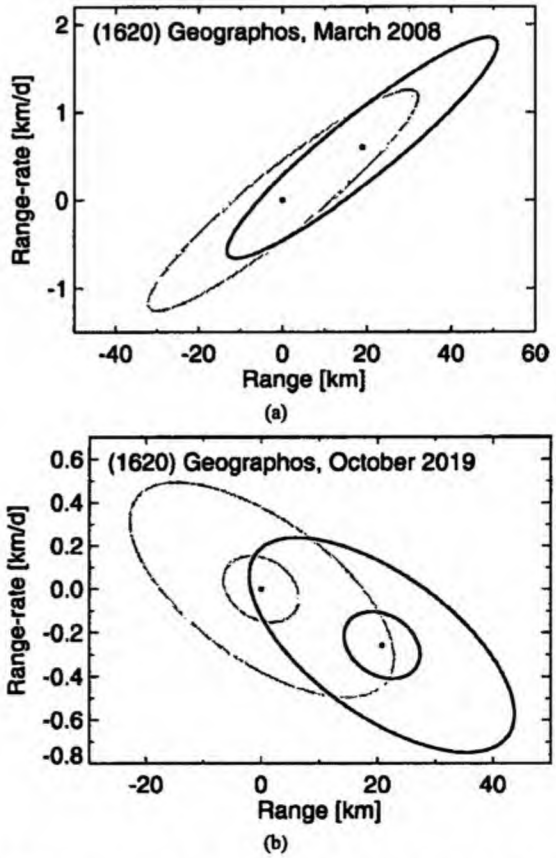

Fig. 7. Yarkovsky offsets for 1620 Geographos on (a) March 3.1, 2008 and (b) October 5.0, 2019, depicted as in Fig. 1. Only currently available astrometry is used, except for the interior ellipses in (b), which include simulated Arecibo radar astrometry from 2008, despite the poor observability at that time (SNR $\simeq$ 15).

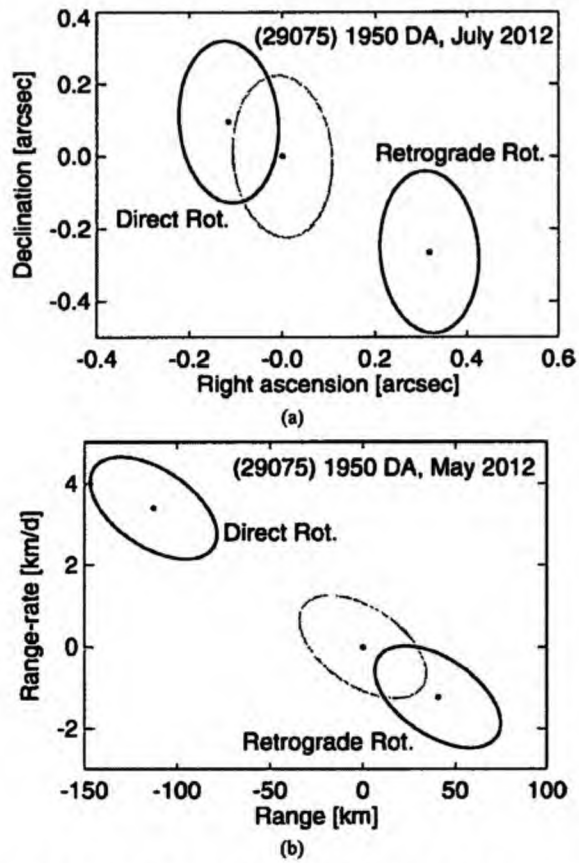

Fig. 8. Yarkovsky offsets for (29075) 1950 DA for (a) optical astrometry on July 1, 2012 and (b) radar astrometry on May 29, 2012, depicted as in Fig. 1. The offsets are presented for the two possible pole solutions described in the text. The solutions include 32 simulated optical observations over the period from November 2004 to March 2012.

axes, a direct solution ($\ell = 97°$, $b = 79°$) and a retrograde solution ($\ell = 18°$, $b = -40°$). Giorgini et al. showed that the impact is effectively ruled out by the retrograde rotation pole, but the impact remains possible for the direct rotation pole.

The observation set for 1950 DA is robust. It was discovered in February 1950 and observed for a period of 17 days at that time. It was rediscovered in the last hours of 2000 and observed heavily during 2001, including radar ranging from Goldstone and Arecibo in March 2001. Additionally, observations from 1981 have been measured on archival plates. The combination of long optical baseline and precise radar measurements provide an excellent constraint on the orbit, but not enough to reveal the Yarkovsky effect directly.

The next Earth close approach—and Yarkovsky detection opportunity—for 1950 DA occurs in May 2012. To account for ongoing observations between now and then, we have simulated precise optical astrometry on 16 nights (two observations per night with accuracy of $0''.2$) from late 2004 to mid-2012. Radar ranging from Arecibo in 2012 will be challenging, with peak SNR $\sim$ 15, but precise optical astrometry will be straightforward, with magnitudes brighter than $V = 17$. Figure 8 indicates the observability of the Yarkovsky signal in 2012, for both radar and optical measurements and for both putative pole solutions. From the figure it is clear that the correct pole solution should be easily discerned from either optical or radar observations in 2012. In the case of direct rotation, the Yarkovsky signal will be readily apparent in 2012, but the 2880 impact possibility would likely persist at some level. If, on the other hand, the retrograde pole solution is favored then the actual Yarkovsky detection will be less clear (although the *combined* power of radar and optical measurements should strengthen the Yarkovsky signal beyond the level indicated by Fig. 8), but the possibility of impact would presumably be eliminated. We note that it is very likely that the pole will have been independently determined through lightcurve inversion by late 2012. In any event, even if the detection in 2012 is somehow marginal, a conclusive detection during the subsequent approach in 2023 is all but guaranteed from optical measurements alone.

The simulations in Fig. 8 assume diameter $D = 1.1$ km, albedo $A = 0.1$, thermal conductivity $K = 0.01$ W/(m K), specific heat capacity $C = 680$ J/(kg K), and surface and

bulk densities $\rho_s = 1.7\,\mathrm{g/cm^3}$ and $\rho_b = 3.0\,\mathrm{g/cm^3}$. The high value of bulk density is suggested to strengthen gravitational binding in order to prevent rotational fusion; note 1950 DA has one of the shortest rotational periods $P \simeq 2.11$ hr for bodies of its size.

3. Targets on unusual orbits

This is currently the most promising class of objects for Yarkovsky detection. Except for 25143 Itokawa, for which results have already been reported by Ostro et al. (2004) and which is only briefly mentioned here, a key characteristic of bodies in this group is a series of frequent close encounters with the Earth. As we have seen, the Yarkovsky acceleration is generally evident at the third suitably accurate radar apparition, and so objects that support frequent radar observing opportunities are particularly favored for an early detection.

Asteroids visited and orbited by a spacecraft form an interesting (and "expensive") exception. After 433 Eros, 25143 Itokawa is expected to be the second such near-Earth asteroid (Farquhar et al., 2003). The Japanese spacecraft Hayabusa will hover near this target in the May–September 2005 time frame, performing observations in several spectral bands and collecting a small sample of the asteroid surface to be returned back to the Earth. The telecommunication link to the satellite can be used to generate pseudo-range observations to the asteroid with about 100 m accuracy. Since Itokawa has been successfully radar-ranged in June 2004 both by Goldstone and Arecibo, the Hayabusa data should be enough to convincingly reveal the Yarkovsky signal in this asteroid's motion[17] (Ostro et al., 2004).

The Yarkovsky detection for Itokawa would be fundamental for two reasons. First, measurement of the Hayabusa motion near Itokawa itself will allow an independent determination of the target's mass (from its gravitational effect on the spacecraft) and the on-board infrared observations should allow detailed understanding of the temperature variations on the surface. Both parameters are those that are, in a correlated way, determined through the measurement of the Yarkovsky perturbation. Independent measurements of these properties will help us to test the reliability of estimates derived from measuring the Yarkovsky effect. Secondly, Vokrouhlický et al. (2004) suggested the YORP effect, a rotational variant of the Yarkovsky effect, might also be detected for Itokawa by 2004 (and nearly certainly in 2005 using Hayabusa observations). Hence 25143 Itokawa would be the first target for which both Yarkovsky and YORP effects will be simultaneously determined. Also, Vokrouhlický et al. (2004) report that the YORP effect depends only little on the surface thermal inertia value while still depending on the asteroid's mass or bulk density (see also Čapek and Vokrouhlický, 2004), thus the YORP detection itself would also help to decorrelate the Yarkovsky-detected parameters (mass and the surface thermal inertia).

3.1. 4179 Toutatis

This asteroid is exceptional in several respects. Toutatis, like Golevka, currently resides in the 3/1 mean motion resonance with Jupiter, but it also temporarily interacts with much weaker exterior 1/4 mean motion resonance with the Earth (e.g., Marsden, 1970; Whipple and Shelus, 1993). As a result, Toutatis undergoes close encounters with the Earth every 4 years for some period of time around 2000. This fact gives a splendid opportunity to acquire good orbital data, including radar astrometry.[18] Secondly, early after Toutatis' discovery, Bardwell (1989) established a connection between its orbit and that of lost object 1934 CT. Pre-discovery identifications are now frequent,[19] but linking observations nearly 60 years apart is still unusual. It has been also claimed for some time (e.g., Sitarski, 1998), that these early Toutatis observations are not exactly aligned with modern data, and actually lie several arc-seconds from the prediction. Speculations have been made about comet-like propulsion effects on this orbit. Prompted by these puzzles, Vokrouhlický et al. (2000) asked whether the Yarkovsky effect might be the missing element in the long-term Toutatis dynamics, but concluded negatively. Here we confirm this finding.

As in the case of Geographos, we have several reasons to revisit the Vokrouhlický et al. (2000) analysis of this object. First, Toutatis is highly elongated with an accurate shape model (Hudson and Ostro, 1995, 1998; Ostro et al., 1999; Hudson et al., 2003), and we want to know whether the simple spherical model used by Vokrouhlický et al. (2000) gives reasonable results. Second, and more important, Vokrouhlický et al. (2000) included two errors in their analysis that likely affect their conclusions: (i) they assumed a spherical Toutatis-equivalent body of 5.5 km size, more than twice the real value (2.45 km; Hudson and Ostro, 1995, 1998), and (ii) they assumed a 7 hr rotation period instead of much longer proper periods of the non-principal-axis rotation of the real body (see below).

[17] Here we specify parameters of the Yarkovsky model used in Ostro et al. (2004): (i) rotation period $P = 12.132$ hr and rotation pole ecliptic longitude $\ell = 355°$ and latitude $b = -84°$ by Kaasalainen et al. (2003), (ii) radar shape model by Ostro et al. (2004), and (iii) thermal and bulk physical parameters, the surface thermal conductivity $K = 0.05\,\mathrm{W/(m\,K)}$, the specific heat capacity $C = 800\,\mathrm{J/(kg\,K)}$, the surface and bulk densities $\rho_s = 2.0\,\mathrm{g/cm^3}$ and $\rho_b = 2.5\,\mathrm{g/cm^3}$. These latter parameters are consistent with Ishiguro et al.'s (2003) radiometric observations indicating the surface thermal inertia $\Gamma = 290\,\mathrm{J/(kg\,m^2\,s^{1/2})}$, thus the thermal parameter $\Theta = 1.3$ at about 1 AU. These infrared observations also suggest a geometric albedo $p_V = 0.35$, that, with the slope parameter $G = 0.29$, implies a Bond albedo of $A = 0.17$.

[18] Radar data were obtained at all of these possibilities, with particularly accurate measurements in 1992 and 1996.

[19] In fact, Toutatis has been recovered on five more pre-discovery plates taken in July 1988.

Hudson et al. (2003) recently derived the highest resolution model of Toutatis' shape, a model with 39996 triangular facets of roughly equal area. However, the purpose of this work does not need such fine resolution, which would require unrealistically large computational costs. We instead use a 12796 facet model derived by Hudson and Ostro (1995); the corresponding source files can be found at http://www.psi.edu/pds/archive/rshape.html. We assume the following thermal and physical parameters: geometric albedo $p_V = 0.08$ (Ostro et al., 1999; see also Lupishko et al., 1995), specific heat capacity $C = 800$ J/(kg K), surface and bulk densities of $\rho_s = 2.0$ g/cm^3 and $\rho_b = 2.6$ g/cm^3 (compatible with results of Ostro et al., 1999). The value $K = 0.01$ W/(m K) is most compatible with the thermal inertia reported by Howell et al. (1994), so we use that value in our 2004 Yarkovsky displacement prediction (Fig. 10).

Modeling of the Yarkovsky effect for Toutatis is particularly difficult because of its curious rotation state. Indeed, this is the first case for which a computation of the Yarkovsky effect has been performed for an asteroid in a non-principal-axis mode of rotation. We use the spin state derived by Hudson and Ostro (1995) (see also Hudson and Ostro, 1998, and Ostro et al., 1999), namely (i) Euler angles characterizing transformation of the ecliptic (inertial) frame and the body-fixed frame of principal axes of the inertia tensor, and (ii) projection of the angular velocity vector onto the principal axes (in the body-fixed frame) for given epoch. These initial conditions are propagated numerically (e.g., Landau and Lifschitz, 1976; Kryszczyńska et al., 1999), giving at any time the transformation matrix between the body-fixed frame and the inertial (ecliptic) frame. We note the period of free motion of the angular velocity vector about the longest axis of the inertia tensor in the body fixed frame—$\simeq 5.37$ days—and the period of precession of the body-fixed frame about the nearly-constant angular momentum vector in the inertial frame—$\simeq 7.42$ days (Hudson and Ostro, 1995; Ostro et al., 1999; see also Scheeres et al., 1998). A particular problem, relevant to the heat diffusion modeling, is that there is no exact periodicity in Toutatis' rotation state (e.g., Landau and Lifschitz, 1976). Though in principle Toutatis never returns to the same configuration in inertial space, there is a near-exact periodicity of $\simeq 1454.4$ days, curiously close to Toutatis orbital period. This near periodicity of Toutatis' orientation in space after one revolution is important, because it facilitates formulation of the boundary conditions for the heat diffusion problem, which are otherwise trivial for principal axis rotation.

With the asteroid shape and rotation specified, we use the same numerical method as in the Geographos case to solve the heat diffusion problem, namely we use a one-dimensional reduction to depth and time variables for each of the surface facets. The surface boundary condition is a nonlinear energy conservation law. As described above, the solution is forced to be periodic with a period of the asteroid's revolution about the Sun. A look-up table of numerically computed Yarkovsky acceleration components along the asteroid's orbit is exported[20] and later used in the orbit determination program.

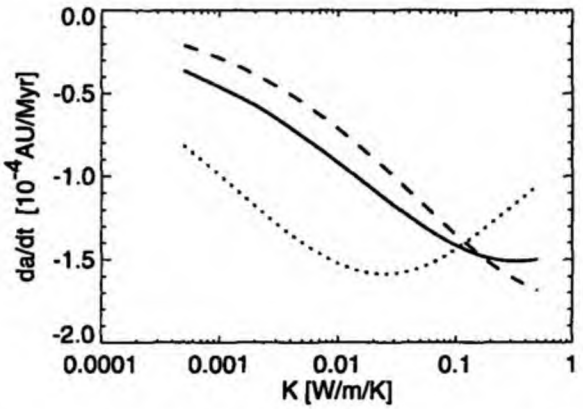

Fig. 9. The Yarkovsky-induced average semimajor axis drift rate (da/dt) for Toutatis, as a function of surface conductivity K. The solid line is the result from complete numerical model described in the text. The other two lines show the result from a linearized approximation of heat conduction and a fictitious spherical body having the same volume as Toutatis rotating about an axis directed along Toutatis' angular momentum with periods of 7.42 days (dashed) and 5.39 days (dotted), respectively.

Figure 9 shows the orbit-averaged value of semimajor axis drift due to the Yarkovsky effect as a function of surface thermal conductivity. We noted above that our result supersedes that of Vokrouhlický et al. (2000, Fig. 5); the Yarkovsky effect is stronger than previously reported mainly due to correction in size, and, due to slow rotation, the maximum effect now occurs for high conductivity. Interestingly, the much simplified linearized approach of the Yarkovsky force computation using a spherical body and a fictitious spin axis in the direction of Toutatis angular momentum (dashed curve) gives a fairly satisfactory result. Future analyses of the Yarkovsky effect on tumbling objects may thus use this simplified formulation as a reliable zero-order approximation.

Ahead of us are four radar-observable close approaches of Toutatis to the Earth, and it is virtually certain that the Yarkovsky perturbation will be detected; the question is when. The close encounters in October 2004 and December 2012 are particularly deep so that Arecibo's SNR for such a large object will reach 50,000. In November 2008 the encounter is more distant, yet the SNR for the Arecibo system is still $\simeq 4000$, and the latest radar-astrometry possibility until 2069 occurs in January 2017 (with SNR $\simeq 70$). In what follows we argue that already the first chance, October 2004, will likely reveal existence and strength of the Yarkovsky effect for this target; further observations will only sharpen this information. Toutatis will thus be the first multi-kilometer asteroid for which the Yarkovsky effect would be measured, and it will be also the first target for which the Yarkovsky perturbation may be repeatedly measured and refined.

[20] Data available at http://sirrah.troja.mff.cuni.cz/~davok/.

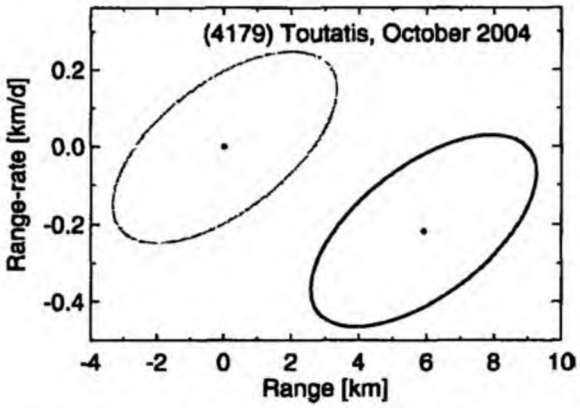

Fig. 10. Yarkovsky offsets for 4179 Toutatis on October 8.5, 2004, depicted as described in Fig. 1.

Figure 10 shows the predicted orbital displacement due to the Yarkovsky effect in October 2004, assuming the surface and bulk parameters as described above. We note the Yarkovsky signal, subject to our assumptions, surpasses the 6σ significance level for all dates, ensuring a Yarkovsky detection. The Goldstone radar is unavailable due to scheduled maintenance, but the relevant observations have been proposed at Arecibo.

3.2. (54509) 2000 PH5

This body belongs to an interesting subgroup of NEAs, namely the Earth co-orbital asteroids (see, e.g., Christou, 2000; Wiegert et al., 2000; Morais and Morbidelli, 2002) that temporarily librate about the unitary circle in the Solar System. Occasionally, this motion causes the asteroid to experience a sequence of yearly close approaches whenever the heliocentric longitudes of the Earth and the co-orbital are similar.[21] In the case of 2000 PH5 such radar-observable close encounters will last until 2006 (for distances less than $\simeq 0.08$ AU).

In spite of its small size ($D \simeq 100$ m assuming a mid-range geometric albedo of 0.15) and recent discovery (Hergenrother, 2000), the unusual orbit has allowed observers to obtain some useful information about this target. So far we know accurately the rotation period $P = 12.173$ min (e.g., http://www.asu.cas.cz/~ppravec/), although no good constraint is available on the rotation pole except for P. Pravec's (2004, personal communication) claim that $|b| > 30°$, based on an extensive photometric campaign during 2003. Hereafter we presume a pole position of $\ell = 0°$ and $b = +30°$. (Any position closer to the ecliptic poles makes the Yarkovsky perturbation stronger, up to a factor of 2.) We also, somewhat conservatively, use $D = 120$ m because the

[21] Similarly, bodies inside or near the 1/2 exterior resonance with the Earth may happen to closely approach the Earth every second year; a good example, and also a good Yarkovsky-detection candidate, is the Asteroid 2003 YT70.

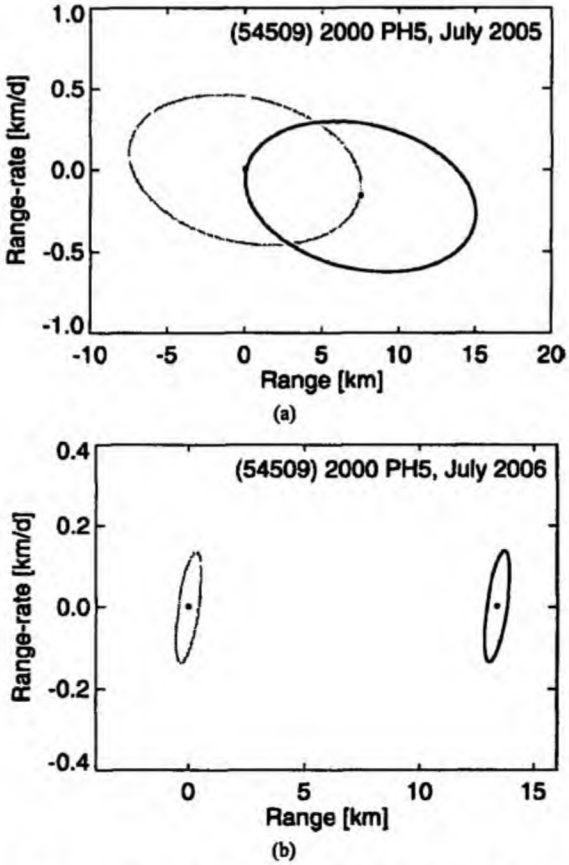

Fig. 11. Yarkovsky offsets for (54509) 2000 PH5 on (a) July 26.7, 2005 and (b) July 22.6, 2006, depicted as in Fig. 1. In (a) we assume Arecibo radar astrometry in July 2004. In (b) we assume radar astrometry from 2004 and 2005.

size is currently derived from the absolute magnitude only and no constraint on albedo is available, although in 2004 the situation should much improve if radar ranging from Arecibo is successful. Similarly, we have little information about this target's surface properties. We adopt the following plausible values: thermal conductivity $K = 0.05$ W/(m K), specific heat capacity $C = 800$ J/(kg K), surface and bulk densities $\rho_s = 2.0$ g/cm^3 and $\rho_b = 2.6$ g/cm^3.

2000 PH5 will be observable annually from Arecibo during the next three years with a fading SNR: $\simeq 20000$ in July 2004, $\simeq 1200$ in July 2005 and $\simeq 37$ in July 2006. With radar astrometry in July 2000 and optical astrometry since then, the Yarkovsky effect should be easily detectable. In 2004, however, the observations cannot serve for that purpose, yet they will be very important. First, the very large SNR value should provide an excellent opportunity for physical characterization, including shape, size, rotation state and surface properties. Moreover, the orbit uncertainty will be dramatically reduced, so that radar astrometry in July 2005 or 2006 should reveal the Yarkovsky perturbation (Fig. 11). In our simulation we assumed radar astrometry of 50-m accuracy taken in July 2004 and 2005. The 2005 data may still be ambiguous judging from the partial overlap of the confidence

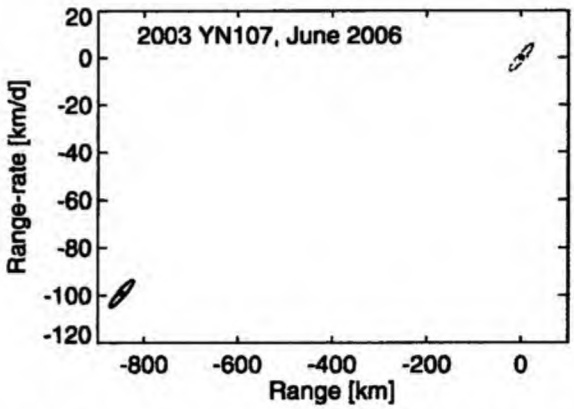

Fig. 12. Yarkovsky offsets for 2003 YN107 on June 13.4, 2006, depicted as in Fig. 1. These solutions assume current optical astrometry together with a simulated optical recovery in December 2004 and Arecibo ranging in 2005 as described in the text.

regions (Fig. 11a), and this motivates the 2006 observations (Fig. 11b).

3.2.1. Other remarkable co-orbitals

For the same reason discussed for 2000 PH5, several other Earth co-orbitals are promising candidates for Yarkovsky effect detection: Yearly repetition of close encounters with the Earth allows us to gather very detailed orbital and physical information. Below we briefly outline several other interesting objects in this class, although we do not present a detailed simulation for all of them.

- *1998 UP1.* This $\simeq$ 250 m object unfortunately fades from radar detectability by 2007, but yearly data may have the power to reveal the Yarkovsky effect before that point. The two pre-discovery observations from October 1990 are both offset in right ascension (on average by $\simeq$ 2 arcsec); this might already be an effect of the Yarkovsky force acting on this body.
- *2003 YN107.* This $\simeq$ 20 m object was discovered during its close encounter in December 2003 after being missed during a series of close approaches since 1997; any recovery from archival data would be important (but may be contingent on estimation of the Yarkovsky perturbation). 2003 YN107 resides on an exceptional quasi-satellite orbit around the Earth (Brasser et al., 2004), with numerous close encounters at distance $\leqslant$ 0.07 AU till May 2007. The radar ranging possibilities are in December 2004, June 2005 and June 2006 (the latter two at SNR $\geqslant$ 200 and $\simeq$ 600 from Arecibo). According to our estimate (Fig. 12), the 2006 radar astrometry should reveal existence of the Yarkovsky perturbation at a very significant statistical level. This solution assumes recovery of the target in mid-December 2004, which is necessary for further steps in our scenario, and Arecibo ranging in June 2005 (with $\simeq$ 200 m and $\simeq$ 500 m/day uncertainties in range and range rate). Obviously, none of the physical parameters needed for accurate estimation of the Yarkovsky effect strength are known today so we have adopted the following values: rotation period $P \simeq 10$ min, pole orientation $\ell = 0°$ and $b = +30°$, thermal conductivity $K = 0.1$ W/(m K), specific heat capacity $C = 800$ J/(kg K), surface and bulk densities $\rho_s = 2.0$ g/cm^3 and $\rho_b = 2.6$ g/cm^3.
- *2003 WP25.* This $\simeq$ 50 m body has been observed since October 2002. It may be radar detected from Arecibo in February 2008 and in March 2009, while optical astrometry may be obtained yearly till 2010. The nearly 10-year timebase should allow Yarkovsky detection.
- *2000 WN10.* This $\simeq$ 350 m object will be undergoing shallow close approaches to the Earth (within $\simeq$ 0.2 AU distance) up until November 2027. On several occasions between November 2005 and November 2014, Arecibo SNR surpasses 20, allowing $\simeq$ 1 km accurate radar astrometry. If at least some of these ranging possibilities are used, the Yarkovsky effect should be readily detected.
- *1999 JV6.* This 350–400 m size body is drifting toward close approaches with the Earth in between January 2014 and January 2018. At each of these occasions the target is observable either from Arecibo or Goldstone with comfortably large SNR values, the best in January 2016 from Arecibo when SNR surpasses 1000. Apart from that, this asteroid is optically observable every year.

3.3. 1999 MN

This is an example of another interesting class of NEAs: A deep Aten-type object with aphelion distance (1.12 AU) just outside the Earth's orbit and perihelion distance (0.22 AU) well inside Mercury's orbit. Its proximity to the Sun indicates that the Yarkovsky effect should be particularly strong on this orbit. Moreover, this body is also among the 25 NEAs whose relativistic perihelion drift exceeds 10 arcsec/cy (it is 18.8 arcsec/cy for 1999 MN), and which may serve to test relativity theory (Margot, 2003). Here we do not study a possible correlation of the Yarkovsky and relativity parameters, and we focus on the Yarkovsky signal only.

Little is known about the body right now, except for the likely value of the rotation period of $\simeq$ 5.5 hr, kindly communicated to us by C. Hergenrother. 1999 MN was recovered by Spacewatch in late May 2004, and subsequently scheduled for both Goldstone and Arecibo observations in June and July 2004. The orbit is unusual in its frequent close encounters with the Earth (and both Venus and Mercury) during the next decade or so. Favorable approaches to the Earth occur in July 2004, June 2005, July 2009 and June 2010 (to mention the nearest only). At all these occasions Arecibo can range this target with SNR larger than 35 (a minimum peak value for the 2009 encounter). Results presented below are to be considered more as a feasibility

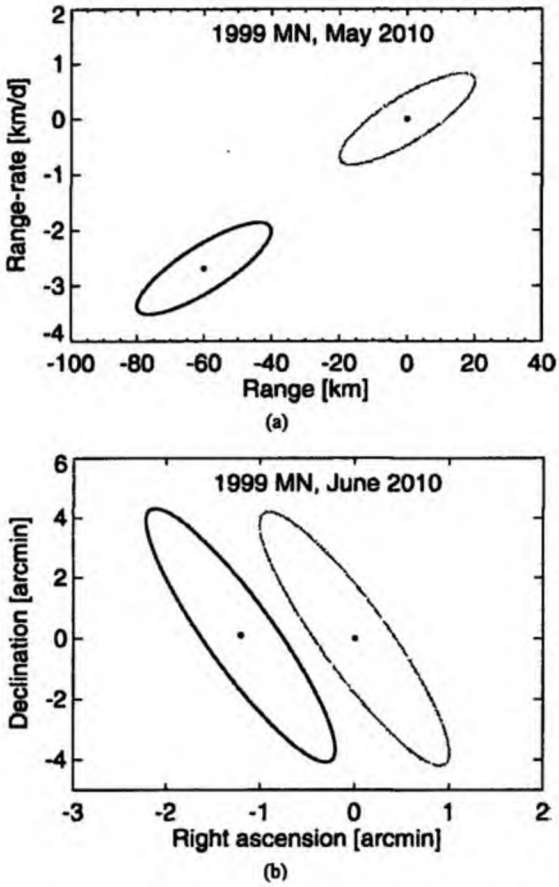

Fig. 13. Yarkovsky offsets for 1999 MN on May 30, 2010 (a) and June 3, 2010 (b), depicted as in Fig. 1. Part (a) shows the range and range-rate plane, appropriate for radar astrometry, while part (b) shows the sky-plane, appropriate for optical astrometry. These solutions assume the current optical astrometry together with simulated Goldstone radar observation in 2004 and Arecibo radar observations in 2005 and 2009 as described in the text.

analysis than a real prediction, since they make use of the four nearest radar apparitions mentioned above.

In the absence of other information, we use a fictitious pole position ($\ell = 0°$, $b = +30°$) in our simulations, which yields about an average strength of the Yarkovsky effect. We further assume a size of $D \simeq 170$ m. Also, we expect the surface thermal parameters are affected by the proximity to the Sun along most of the orbit, hence the following values seem appropriate: thermal conductivity $K = 0.05$ W/(m K), specific heat capacity $C = 800$ J/(kg K), surface and bulk densities $\rho_s = 2.0$ g/cm^3 and $\rho_b = 2.6$ g/cm^3.

As expected, the orbit uncertainty must be well constrained before attempting to detect a perturbation as fine as the Yarkovsky effect; we find that any astrometry from 2004, 2005, and most likely also 2009, will serve only that purpose. However, Fig. 13 indicates that in May 2010 we may expect a fairly strong Yarkovsky signal revealed both in radar and optical astrometry (we assumed 300-m range, and 800-m/day range-rate, astrometry during the pre-2010 ranging possibilities).

We also note 1999 MN undergoes further close encounters with the Earth in June 2015 and June 2020 when additional orbital information may improve the Yarkovsky solution for this object.

4. Very small targets

Here we discuss examples of very small NEAs for which the strength of the Yarkovsky effect is generally large and thus the possibility to detect it is good, at least a priori. However, it is often difficult to acquire necessary information about the physical properties of the object (rotation state, constraints on the surface thermal parameters, etc.). In most of the cases discussed below we do not yet know these characteristics, so our analyses should be considered only as feasibility studies rather than accurate predictions.

The case of 1998 KY26 was discussed by Vokrouhlický et al. (2000) and we do not have new results for that object, although we note that challenging recovery observations were obtained from Mauna Kea in early 2002 (Tholen, 2003). Also, we have already discussed the small co-orbital Asteroids 2003 WP25 and 2003 YN107 that would naturally fall into this category. Another interesting case is the recently spotted small Asteroid 2004 FH ($D \simeq 25$ m) that on March 18, 2004 passed at a geocentric distance of only 49100 km. In spite of observations spanning just $\simeq 3$ days, the body may be recovered in January 2018, when it undergoes a more distant Earth encounter. If radar astrometry is recorded during that flyby (marginally possible from Arecibo), the Yarkovsky effect should be easily detected in February 2021.

4.1. 2000 UK11

Virtually nothing is known about this body, except its small size;[22] the absolute magnitude $H \simeq 25$ implies a size in the interval 20–50 m (in our simulations we consider $D = 32$ m). Optical astrometry includes observations during October and November 2000, when radar data were also acquired. No additional information that would hint about the rotation or physical properties of this object exist. Given the small size of this body and its Aten orbit we consider it reasonable to assume a higher value of the surface thermal inertia, hence the thermal conductivity $K = 0.05$ W/(m K), the specific heat capacity $C = 800$ J/(kg K), surface and bulk densities $\rho_s = 2.0$ g/cm^3 and $\rho_b = 2.6$ g/cm^3. Consistent with results for other small asteroids (e.g., Pravec et al., 2004), we assume a short rotation period, $P = 10$ min, and an arbitrary pole position, $\ell = 0°$ and $b = +30°$.

A common feature to many of the "small-target scenarios" is the necessity of their recovery. In the 2000 UK11 case

[22] At the revision of this manuscript, M. Nolan communicated to us that the 2000 Arecibo radar data indicate a very fast rotator at the limit of $\simeq 3$ min period. Re-analysis of those data might also provide a more tight radar astrometry that would shrink uncertainty intervals in Fig. 14.

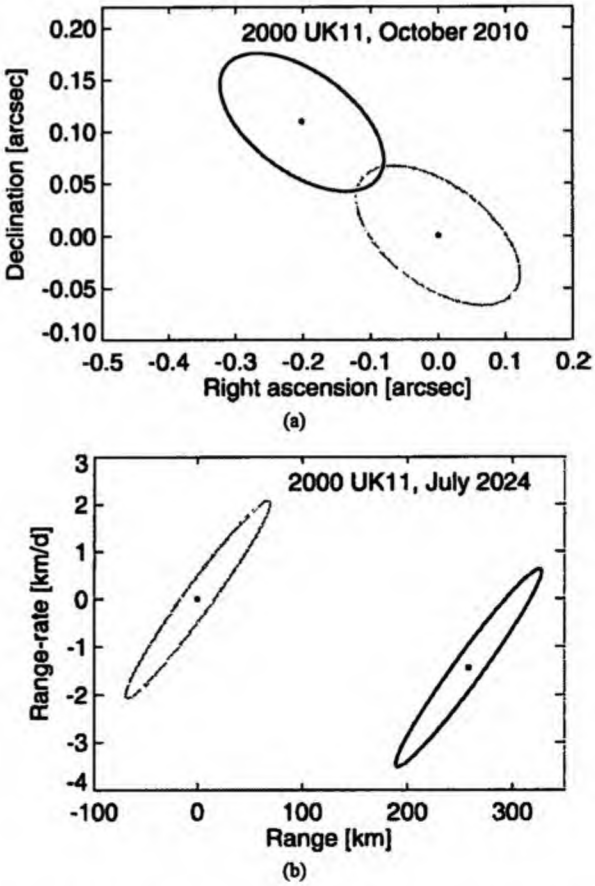

Fig. 14. Yarkovsky offsets, depicted as in Fig. 1, for 2000 UK11 in (a) the plane-of-sky on October 10, 2010 and (b) in the range vs. range-rate projection on July 7, 2024. These solutions assume the current optical astrometry plus Arecibo radar observations in 2005.

the task is reasonably simple: In late October 2005 the object will be at visual magnitude[23] $\simeq 20.8$ and the sky-plane uncertainty will be $\simeq 1$ arcmin along the line of variation. The recovery would be timely because in early November 2005 the target is observable from Arecibo with an estimated SNR of $\simeq 350$. New radar astrometry would be crucial to constrain the orbital uncertainty and to acquire additional information about the body itself. Here we assume radar ranging in 2005 with 300 m uncertainty. The Yarkovsky effect detection itself should, however, wait for later close encounters with the Earth.

Should the technology allow, the Yarkovsky effect could be detected optically by October 2010 when the asteroid approaches the Earth at 0.159 AU. Figure 14a shows the difficulty: The target is at magnitude $\simeq 24.1$, and the sought sky-plane displacement, though surpassing the 3σ-uncertainty, is less than half an arcsecond. Should the rotation pole be closer to the pole of the ecliptic, the effect may be a little larger, perhaps by a factor of 2, but, on the other hand, a higher surface conductivity might hamper detection, making the orbital displacement smaller, by as much as a factor of 5. We conclude that the Yarkovsky detection in 2010 may be difficult, but is indeed possible, even with current technology, as long as the magnitude of the Yarkovsky acceleration is not much less than we have modeled.

Further close approaches to the Earth occur in July 2024 and August 2029. During the first, shallower encounter this target is barely observable by the Arecibo radar (estimated SNR $\simeq 10$), though Fig. 14b suggests the Yarkovsky displacement might be readily detected. Hopefully, future radar systems devoted to asteroid observation will have the capability to reach this target at significantly higher SNR value.

4.2. 2002 JR100

In many respects this body resembles 2000 UK11, though the estimated size, $D \simeq 50$ m, is a little larger. We assume the same thermal and bulk properties as for 2000 UK11, the same pole orientation, and a rotation period of 15 min. Current observations of this object cover only about two weeks in May 2002, but future possibilities to observe this object are considerably better than in the case of 2000 UK11. Promising radar-observability windows occur during April/May 2010, September 2011 and April/May 2018.

In the ideal scenario, the target will be recovered in April 2010, when it becomes reasonably bright ($\simeq 20$ magnitude) and the sky-plane uncertainty stretches over about 2° along the line of variations. After recovery the orbit may be secured within a few days, in time for the optimum Arecibo (SNR $\simeq 1200$) or Goldstone (SNR $\simeq 180$) observing windows. If this scheme succeeds and some 200-m radar ranging is obtained in 2010, plus some less precise ranging in September 2011,[24] we may expect later observations would reveal the Yarkovsky perturbation. Figure 15a shows the estimated range vs. range-rate Yarkovsky displacement relative to the no-Yarkovsky solution in April 2018 (the estimated SNR of the Arecibo system is $\simeq 1450$). Note the comfortably large separation of the 3σ-uncertainty intervals of the two orbits. In fact, even the sky-plane position is significantly displaced by the Yarkovsky effect and by itself may reveal the sought signal (Fig. 15b).

4.3. 1991 VG

With an estimated absolute magnitude $H \simeq 28.4$, 1991 VG is among the smallest objects ever observed. Assuming a diameter $D \simeq 10$ m, it is comparable to or smaller than the estimated size of the precursors of several meteorites. 1991 VG was discovered during its deep close encounter with the Earth in November 1991 (Scotti and Marsden, 1991), and it was briefly observed again in April 1992.

[23] As an optimistic scenario we may hope to obtain lightcurve data in the same epoch.

[24] In our simulation we assumed 500 m accurate range measurement and 1 km/day accurate range-rate measurement from Arecibo.

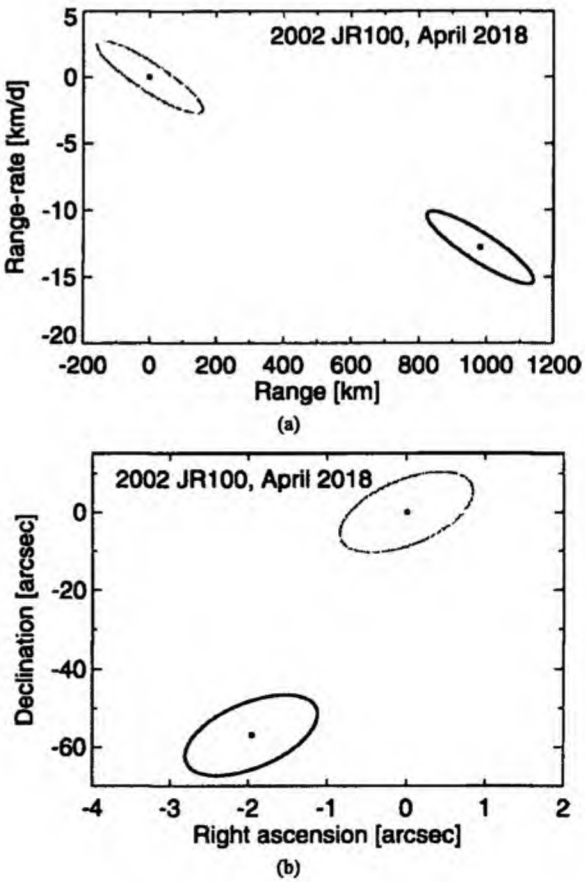

Fig. 15. Yarkovsky offsets, depicted as in Fig. 1, for 2002 JR100 on April 29.9, 2018. Both radar (a) and optical (b) offsets are plotted. These solutions assume the current optical astrometry plus Goldstone and Arecibo radar observations in 2010 and 2011.

This secured the orbit remarkably well: The sky-plane uncertainty is only a few arcmin during its next close encounter with the Earth in August 2017. And, at a visual magnitude of $\simeq 23.4$, we expect it to be recovered and the orbit dramatically improved (Fig. 16), enabling a possible measurement of the Yarkovsky perturbation in February 2018.

To demonstrate feasibility of this scenario, we first simulated the effect of recovery in 2017 on the orbit uncertainty—dashed lines 1 and 2 on Fig. 16. We simulated three optical measurements with 1 arcsec uncertainty in both right ascension and declination, which reduces the sky-plane uncertainty below $\simeq 0.3$ arcsec. As a result, the orbit uncertainty remains sub-arcsecond during the 2018 approach to the Earth. The estimated sky-plane displacement due to the Yarkovsky effect (up to $\simeq 9$ arcsec; Fig. 16) during that apparition might be measurable, but a large telescope is needed for this task since the visual magnitude peaks at only $\simeq 24.5$. This solution assumes the following surface and bulk parameters: thermal conductivity $K = 0.1$ W/(m K), specific heat capacity $C = 800$ J/(kg K), surface and bulk densities $\rho_s = 2$ g/cm^3 and $\rho_b = 3$ g/cm^3, and rotation period

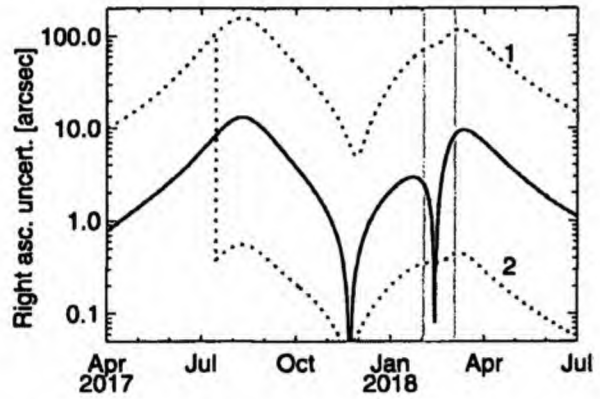

Fig. 16. Right-ascension uncertainty (formal 1σ-value) of 1991 VG during the 2017–2018 period; the upper dashed curve (1) is a solution with the current observational data, the lower dashed curve (2) accounts for simulated optical observations in August 2017 when the object closely approaches to the Earth. The 2017 observations cause a sharp "collapse" of the orbital uncertainty. The thick solid curve shows the estimated maximum right-ascension displacement due to the Yarkovsky effect (see the text). This signal could be observable during the February 2018 apparition (shaded period, during which the estimated visual magnitude drops below 25).

$\simeq 5$ min. Should the asteroid rotate more slowly, or should the surface conductivity be smaller, the effect would be still larger, up to a factor of 5. On the other hand, our adopted pole maximizes the Yarkovsky effect.

With this simulation, we tentatively conclude that the peculiar object 1991 VG might be the first case for which the Yarkovsky perturbation would be determined without any radar astrometry data at all. This certainly remains exceptional, but future high-accuracy optical astrometry projects (including space missions like GAIA;[25] e.g., Mignard, 2002, and http://astro.estec.esa.nl/GAIA/) might boost power of "non-radar means" to detect the Yarkovsky effect.

5. Conclusions

In this paper we point out a number of asteroids for which the Yarkovsky effect might be detected within a decade or two. Additional candidate objects will certainly be discovered after publication, as the automatic programs will continue their search for smaller objects (e.g., Stokes et al., 2003). For that reason we plan to maintain a web site (http://sirrah.troja.mff.cuni.cz/~davok/) where the list of candidate bodies will be updated. We have intentionally postponed to a follow-on paper the discussion of possible Yarkovsky detection for binary asteroid systems, for which the orbital analysis is much more complicated than for single asteroids.

[25] Note, however, that limiting magnitudes might prevent efficient observations of very small targets by these cosmic astrometric missions and the radar astrometry during their close encounters with the Earth may remain to be the principal tool for decades.

The wide variety of asteroids and circumstances for which the Yarkovsky effect could be detected suggests that this technique could become an important tool in asteroid science. The capability of measuring the mass of a candidate asteroid is the most important finding.[26] However, to complement the radar astronomy, an interdisciplinary collaboration—including light curve observations to constrain shape and spin states, optical astrometry to refine the orbits and infrared observations to constrain the thermal properties—is needed to fully exploit this information.

Acknowledgments

The work of D.V. and D.Č. has been supported by the Grant Agency of the Czech Republic, under the grant No. 205/02/0703. The research of S.R.C. and S.J.O. was conducted at the Jet Propulsion Laboratory, California Institute of Technology under a contract with NASA.

References

Asphaug, E., Ryan, E.V., Zuber, M.T., 2003. Asteroid interiors. In: Bottke, W.F., Cellino, A., Paolicchi, P., Binzel, R.P. (Eds.), Asteroids III. Univ. of Arizona Press, Tucson, pp. 463–484.

Bardwell, C.M., 1989. 1989 AC = 1934 CT. MPC 14356-14357. http://cfa-www.harvard.edu/iauc/RecentIAUCs.html.

Benner, L.A.M., 12 colleagues, 1997. Radar detection of near-Earth Asteroids 2062 Aten, 2102 Adonis, 3103 Eger, 4544 Xanthus, and 1992 QN. Icarus 130, 296–312.

Binzel, R.P., Lupishko, D.F., Di Martino, M., Whiteley, R.J., Hahn, G.J., 2003. Physical properties of the near-Earth objects. In: Bottke, W.F., Cellino, A., Paolicchi, P., Binzel, R.P. (Eds.), Asteroids III. Univ. of Arizona Press, Tucson, pp. 255–271.

Binzel, R.P., Rivkin, A.S., Stuart, J.S., Harris, A.W., Bus, S.J., Burbine, T.H., 2004. Observed spectral properties of near-Earth objects: results for population distribution, source regions, and space weathering processes. Icarus 170, 259–294.

Bottke, W.F., Vokrouhlický, D., Rubincam, D.P., Brož, M., 2003. Dynamical evolution of asteroids and meteoroids using the Yarkovsky effect. In: Bottke, W.F., Cellino, A., Paolicchi, P., Binzel, R.P. (Eds.), Asteroids III. Univ. of Arizona Press, Tucson, pp. 395–408.

Brasser, R., Innanen, K.A., Connors, M., Veillet, C., Wiegert, P., Mikkola, S., Chodas, P.W., 2004. Transient co-orbital asteroids. Icarus 171, 102–109.

Britt, D.T., Yeomans, D.K., Housen, K., Consolmagno, G., 2003. Asteroid density, porosity, and structure. In: Bottke, W.F., Cellino, A., Paolicchi, P., Binzel, R.P. (Eds.), Asteroids III. Univ. of Arizona Press, Tucson, pp. 485–500.

Čapek, D., Vokrouhlický, D., 2004. The YORP effect with finite thermal inertia. Icarus. In press.

Chesley, S.R., Ostro, S.J., Vokrouhlický, D., Čapek, D., Giorgini, J.D., Nolan, M.C., Margot, J.L., Hine, A.A., Benner, L.A.M., Chamberlin, A.B., 2003. Direct detection of the Yarkovsky effect by radar ranging to Asteroid 6489 Golevka. Science 302, 1739–1742.

Christou, A.A., 2000. A numerical survey of transient coorbitals of the terrestrial planets. Icarus 144, 1–20.

Cruikshank, D.P., Jones, T.J., 1977. The diameter and albedo of Asteroid 1976 AA. Icarus 31, 427–429.

De Angelis, G., 1995. Asteroid spin, pole and shape determinations. Planet. Space Sci. 43, 649–682.

Delbó, M., Harris, A.W., Binzel, R.P., Pravec, P., Davies, J.K., 2003. Keck observations of near-Earth asteroids in the thermal infrared. Icarus 166, 116–130.

Farquhar, R., Kawaguchi, J., Russell, C.T., Schwehm, G., Veverka, J., Yeomans, D.K., 2003. Spacecraft exploration of asteroids: the 2001 perspective. In: Bottke, W.F., Cellino, A., Paolicchi, P., Binzel, R.P. (Eds.), Asteroids III. Univ. of Arizona Press, Tucson, pp. 367–376.

Gaffey, M.J., Reed, K.L., Kelley, M.S., 1992. Relationship of E-type Apollo Asteroid 3103 (1982 BB) to the enstatite achondrite meteorites and the Hungaria asteroids. Icarus 100, 95–109.

Giorgini, J.D., 13 colleagues, 2002. Asteroid 1950 DA's encounter with Earth: physical limits of collision probability prediction. Science 296, 132–136.

Harris, A.W., 1998. A thermal model for near-Earth asteroids. Icarus 131, 291–301.

Harris, A.W., Young, J.W., Goguen, J., Hammel, H.B., Hahn, G., Tedesco, E.F., Tholen, D.J., 1987. Photoelectric lightcurves of the Asteroid 1862 Apollo. Icarus 70, 246–256.

Harris, A.W., Davies, J.K., Green, S.F., 1998. Thermal infrared spectrophotometry of the near-Earth Asteroids 2100 Ra–Shalom and 1991 EE. Icarus 135, 441–450.

Helin, E., Bus, S.J., Pryor, C.P., 1976. Discovery of 1976 AA. Bull. Am. Astron. Soc. 8, 458.

Helin, E., Lawrence, K., Rose, P., Williams, G., 1991. 1991 JX. IAU Circ. 5268, 1.

Hergenrother, C.W., 2000. MPEC 2000-P32. http://cfa-www.harvard.edu/iauc/RecentIAUCs.html.

Howell, E.S., Britt, D.T., Bell, J.F., Binzel, R.P., Lebofsky, L.A., 1994. Visible and near-infrared spectral observations of 4179 Toutatis. Icarus 111, 468–474.

Hudson, R.S., Ostro, S.J., 1995. Shape and non-principal axis spin state of Asteroid 4179 Toutatis. Science 270, 84–86.

Hudson, R.S., Ostro, S.J., 1998. Photometric properties of Asteroid 4179 Toutatis from lightcurves and a radar-derived physical model. Icarus 135, 451–457.

Hudson, R.S., Ostro, S.J., 1999. Physical model of Asteroid 1620 Geographos from radar and optical data. Icarus 140, 369–378.

Hudson, R.S., Ostro, S.J., Scheeres, D.J., 2003. High-resolution model of Asteroid 4179 Toutatis. Icarus 161, 346–355.

Ishiguro, M., Abe, M., Ohba, Y., Fujiwara, A., Fuse, T., Terada, H., Goto, M., Kobayashi, N., Tokunaga, A.T., Hasegawa, S., 2003. Near-infrared observations of MUSES-C mission target. Publ. Astron. Soc. Japan 55, 691–699.

Kaasalainen, M., Torppa, J., Piironen, J., 2002. Models of twenty asteroids from photometric data. Icarus 159, 369–395.

Kaasalainen, M., 15 colleagues, 2003. CCD photometry and model of MUSES-C target (25143) 1998 SF36. Astron. Astrophys. 405, L29–L32.

Kaasalainen, M., 21 colleagues, 2004. Photometry and models of eight near-Earth asteroids. Icarus 167, 178–196.

Konopliv, A.S., Miller, J.K., Owen, W.M., Yeomans, D.K., Giorgini, J.D., Garmier, R., Barriot, J.-P., 2002. A global solution for the gravity field, rotation, landmarks and ephemeris of Eros. Icarus 160, 289–299.

Kryszczyńska, A., Kwiatkowski, T., Breiter, S., Michałowski, T., 1999. Relation between rotation and lightcurve of 4179 Toutatis. Astron. Astrophys. 345, 643–645.

Landau, L.D., Lifschitz, E.M., 1976. Mechanics, third ed. Pergamon, Oxford.

Lebofsky, L.A., Lebofsky, M.J., Rieke, G.H., 1979. Radiometry and surface properties of Apollo, Amor and Aten asteroids. Astron. J. 84, 885–888.

Lebofsky, L.A., Veeder, G.J., Rieke, G.H., Lebofsky, M.T., Matson, D.L., Kowal, C., Wynn-Williams, C.G., Becklin, E.E., 1981. The albedo and diameter of 1862 Apollo. Icarus 48, 335–338.

[26] Little mentioned, but also important, is the Yarkovsky effect role as an impact-hazard tuning parameter (e.g., Giorgini et al., 2002, and Section 2.7).

Lupishko, D.F., Vasilyev, S.V., Efimov, Yu.S., Shakhovskoj, N.M., 1995. UBVRI-polarimetry of Asteroid 4179 Toutatis. Icarus 113, 200–205.

Magnusson, P., 45 colleagues, 1996. Photometric observations and modeling of Asteroid 1620 Geographos. Icarus 123, 227–244.

Margot, J.L., 2003. Candidate asteroids for discerning GR and solar oblateness. Bull. Am. Astron. Soc. 35, 1039.

Marsden, B.G., 1970. On the relationship between comets and minor planets. Astron. J. 75, 206–217.

Mignard, F., 2002. Observation of Solar System objects with GAIA. I. Detection of NEOs. Astron. Astrophys. 393, 727–731.

Milani, A., Carpino, M., Hahn, G., Nobili, A.M., 1989. Dynamis of planet-crossing asteroids: classes of orbital behaviour. Icarus 78, 212–269.

Morais, H., Morbidelli, A., 2002. The population of near-Earth asteroids in coorbital motion with the Earth. Icarus 160, 1–9.

Morbidelli, A., Vokrouhlický, D., 2003. The Yarkovsky-driven origin of near-Earth asteroids. Icarus 163, 120–134.

Morrison, D., Gradie, J.C., Rieke, G.H., 1976. Radiometric diameter and albedo of the remarkable Asteroid 1976 AA. Nature 260, 691.

Mottola, S., De Angelis, G., Di Martino, M., Erikson, A., Hahn, G., Neukum, G., 1995. The near-Earth objects follow-up program: first results. Icarus 117, 62–70.

Nesvorný, D., Bottke, W.F., 2004. Detection of the Yarkovsky effect for main-belt asteroids. Icarus 170, 324–342.

Ostro, S.J., 1993. Planetary radar astronomy. Rev. Mod. Phys. 65, 1235–1279.

Ostro, S.J., 1997. Radar reconnaissance of near-Earth objects at the dawn of the next millennium. Ann. New York Acad. Sci. 882, 118–139.

Ostro, S.J., 13 colleagues, 1995a. Radar images of Asteroid 4179 Toutatis. Science 270, 80–83.

Ostro, S.J., 11 colleagues, 1995b. Extreme elongation of Asteroid 1620 Geographos from radar images. Nature 375, 474–477.

Ostro, S.J., 12 colleagues, 1996. Radar observations of Asteroid 1620 Geographos. Icarus 121, 46–66.

Ostro, S.J., 15 colleagues, 1999. Asteroid 4179 Toutatis: 1996 radar observations. Icarus 137, 122–139.

Ostro, S.J., Rosema, K.D., Campbell, D.B., Shapiro, I.I., 2002. Radar observations of Asteroid 1862 Apollo. Icarus 156, 580–583.

Ostro, S.J., Hudson, R.S., Benner, L.A.M., Giorgini, J.D., Magri, C., Margot, J.-L., Nolan, M.C., 2003. Asteroid radar astronomy. In: Bottke, W.F., Cellino, A., Paolicchi, P., Binzel, P. (Eds.), Asteroids III. Univ. of Arizona Press, Tucson, pp. 151–168.

Ostro, S.J., 15 colleagues, 2004. Radar Observations of Asteroid 25143 Itokawa (1998 SF36). Meteorit. Space Sci. 39, 407–424.

Pravec, P., 19 colleagues, 2004. Tumbling asteroids. Icarus. In press.

Scheeres, D.J., Ostro, S.J., Hudson, R.S., Suzuki, S., de Jong, E., 1998. Dynamics of orbits close to Asteroid 4179 Toutatis. Icarus 132, 53–79.

Scotti, J.V., Marsden, B.G., 1991. 1991 VG. IAU Circ. 5387, 1.

Shepard, M.K., Benner, L.A.M., Ostro, S.J., Harris, A.W., Rosema, K.D., Shapiro, I.I., Chandler, J.F., Cambell, D.B., 2000. Radar observations of Asteroid 2100 Ra–Shalom. Icarus 147, 520–529.

Shepard, M.K., 10 colleagues, 2004. Multi-wavelength observations of 2100 Ra–Shalom: radar and lightcurves. In: Proc. Lunar Planet. Sci. Conf. 35th. Abstracts book.

Sitarski, G., 1998. Motion of the minor planet 4179 Toutatis: can we predict its collision with the Earth? Acta Astron. 48, 547–561.

Souchay, J., Kinoshita, H., Nakai, H., Roux, S., 2003. A precise modeling of Eros 433 rotation. Icarus 166, 285–296.

Stokes, G.H., Evans, J.B., Larson, S.M., 2003. Near-Earth asteroid search programs. In: Bottke, W.F., Cellino, A., Paolicchi, P., Binzel, E.P. (Eds.), Asteroids III. Univ. of Arizona Press, Tucson, pp. 45–54.

Tholen, D.J., 2003. Recovery of 1998 KY26: implications for detecting the Yarkovsky effect. Bull. Am. Astron. Soc. 35, 972.

Veeder, G.J., Hanner, M.S., Matson, D.L., Tedesco, E.F., Lebofsky, L.A., Tokunaga, A.T., 1989. Radiometry of near-Earth asteroids. Astron. J. 97, 1211–1219.

Vokrouhlický, D., Farinella, P., 1998. The Yarkovsky seasonal effect on asteroidal fragments: a non-linearized theory for the plane-parallel case. Astron. J. 116, 2032–2041.

Vokrouhlický, D., Farinella, P., 2000. Efficient delivery of meteorites to the Earth from a wide range of asteroid parent bodies. Nature 407, 606–608.

Vokrouhlický, D., Bottke, W.F., 2001. The Yarkovsky thermal force on small asteroids and their fragments: choosing the right albedo. Astron. Astrophys. 371, 350–353.

Vokrouhlický, D., Milani, A., Chesley, S.R., 2000. Yarkovsky effect on small near-Earth asteroids: mathematical formulation and examples. Icarus 148, 118–138.

Vokrouhlický, D., Chesley, S.R., Milani, A., 2001. On the observability of radiation forces acting on near-Earth asteroids. Celest. Mech. Dynam. Astron. 81, 149–165.

Vokrouhlický, D., Čapek, D., Kaasalainen, M., Ostro, S.J., 2004. Detectability of YORP rotational slowing of Asteroid 25143 Itokawa. Astron. Astrophys. 414, L21–L24.

Wechsler, A.E., Glaser, P.E., Little, A.D., Fountain, J.A., 1972. Thermal properties of granulated materials. In: Lucas, J.W. (Ed.), Thermal Characteristics of the Moon. MIT Press, Cambridge, pp. 215–241.

Whipple, A.L., Shelus, P.J., 1993. Long-term dynamical evolution of the minor planet (4179) Toutatis. Icarus 105, 408–419.

Wiegert, P., Innanen, K., Mikkola, S., 2000. Earth Trojan asteroids: a study in support of observational searches. Icarus 145, 33–43.

Yeomans, D.K., 1991. A comet among the near-Earth asteroids? Astron. J. 101, 1920–1928.

Yeomans, D.K., 1992. Erratum: a comet among the near-Earth asteroids? Astron. J. 104, 1266.

Available online at www.sciencedirect.com
SCIENCE DIRECT
Icarus 179 (2005) 128–138
ICARUS
www.elsevier.com/locate/icarus

Yarkovsky detection opportunities II. Binary systems

D. Vokrouhlický [a,*], D. Čapek [a], S.R. Chesley [b], S.J. Ostro [b]

[a] *Institute of Astronomy, Charles University, V Holešovičkách 2, CZ-18000 Prague 8, Czech Republic*
[b] *Jet Propulsion Laboratory, California Institute of Technology, Pasadena, CA 91109-8099, USA*

Received 14 December 2004; revised 7 June 2005
Available online 8 August 2005

Abstract

We consider the possibility of detecting the Yarkovsky orbital perturbation acting on binary systems among the near-Earth asteroids. This task is significantly more difficult than for solitary asteroids because the Yarkovsky force affects both the heliocentric orbit of the system's center of mass and the relative orbit of the two components. Nevertheless, we argue these are sufficiently well decoupled so that the major Yarkovsky perturbation is in the simpler heliocentric motion and is observable with the current means of radar astrometry. Over the long term, the Yarkovsky perturbation in the relative motion of the two components is also detectable for the best observed systems. However, here we consider a simplified version of the problem by ignoring mutual non-spherical gravitational perturbations between the two asteroids. With the orbital plane constant in space and the components' rotation poles fixed (and assumed perpendicular to the orbital plane), we do not examine the coupling between Yarkovsky and gravitational effects. While radar observations remain an essential element of Yarkovsky detections, lightcurve observations, with their ability to track occultation and eclipse phenomena, are also very important in the case of binaries. The nearest possible future detection of the Yarkovsky effect for a binary system occurs for (66063) 1998 RO_1 in September 2006. Farther out, even more statistically significant detections are possible for several other systems including 2000 DP_{107}, (66391) 1999 KW_4 and 1996 FG_3. Published by Elsevier Inc.

Keywords: Asteroids; Yarkovsky effect; Orbit determination

1. Introduction

In a recent paper (Vokrouhlický et al., 2005; see also Vokrouhlický et al., 2000, 2001), we demonstrated that future radar and optical astrometric observations of near-Earth asteroids (NEAs) will likely provide many opportunities to detect the Yarkovsky effect (e.g., Bottke et al., 2002) in their orbital motion. We considered candidate asteroids with a variety of sizes, orbital parameters, shapes, rotation states, spectral types, etc., but we intentionally omitted discussion of binary systems in that work. The purpose of this paper is to extend the analysis in Vokrouhlický et al. (2005) to account for these cases.

The possibility of detecting the Yarkovsky effect for binary systems is both appealing and challenging. The attractive quality, as compared to solitary asteroids, is due to an independent constraint on the total mass of the system from analysis of the relative motion. Experience from the first successful detection of the Yarkovsky effect (Chesley et al., 2003) reveals an "unpleasant intrinsic correlation" of the surface thermal inertia and the asteroid's mass. When one of these parameters is independently known the Yarkovsky signal may be used to determine the other, or if both parameters are somehow independently constrained their uncertainties may be reduced. Binary systems naturally offer this possibility. The other face of the same reasoning, however, is the necessity of solving both the motion of the two asteroids relative each other and the motion of their center of mass

* Corresponding author. Fax: +420 2 21 91 25 67.
E-mail addresses: vokrouhl@mbox.cesnet.cz (D. Vokrouhlický), capek@sirrah.troja.mff.cuni.cz (D. Čapek), steve.chesley@jpl.nasa.gov (S.R. Chesley), ostro@reason.jpl.nasa.gov (S.J. Ostro).

0019-1035/$ – see front matter Published by Elsevier Inc.
doi:10.1016/j.icarus.2005.06.003

(COM) about the Sun. This dramatically increases the complexity of the problem.

Although the methodology of our work remains basically the same as described in Vokrouhlický et al. (2005), and already in Vokrouhlický et al. (2000), we need to complement our discussion by an appropriate analysis of the relative motion of the two binary components. This is done in Section 2, and in Appendix A, using the simplest possible approach. In particular, we do not model the coupling between the gravitational perturbations (due to non-sphericity of the components) and the Yarkovsky perturbation, a problem marvelously difficult requiring numerical solution. Rather, we illustrate the principal Yarkovsky effect for the relative binary motion as if the mutual gravitational perturbations did not exist. This allows us to assume the orbital plane of the two components stays fixed in space, as well as their rotation axes (that we additionally assume perpendicular to their orbital plane). For that reason, however, our analysis is not sufficient to study long-term dynamics of the binary system and the role of the Yarkovsky forces for its stability, but we focus solely on a short-term scale. The theory is applied in Section 3, where we consider one binary system—2000 DP_{107}—as an illustration, and some considerations concerning validity of our assumptions are in Section 4. Even though the Yarkovsky detection might be obtained sooner for other systems, we consider it premature to discuss them because their key physical and dynamical parameters have not yet been reported in the peer-reviewed literature. This paper thus sets the concepts, which could be applied to any binary system when enough data are available.

2. Theory

Determination of the Yarkovsky effect for close binary systems, which predominate among the NEA binary population, is difficult because it affects both parts of their motion in space: (i) heliocentric motion of the system's COM ("global motion"), and (ii) relative motion of the two asteroids about the COM ("local motion"). A combined analysis of global and local dynamics certainly relies on numerical simulation whose complexity goes beyond standard orbit determination programs. However, we show that the local and global motions are largely decoupled,[1] and the major Yarkovsky perturbation occurs for the global motion, for which the analysis is much simpler.

Let $\mathbf{R}$ denote the heliocentric position vector of the system COM and $\mathbf{r}$ the relative position of the secondary component with respect to the primary component. Then the global motion is described by

$$\frac{\mathrm{d}^2\mathbf{R}}{\mathrm{d}t^2} = -\frac{GM}{R^3}\mathbf{R} + (\text{tidal quadrupole coupling}) + X_1\mathbf{f}_1 + X_2\mathbf{f}_2, \tag{1}$$

where G is the gravitational constant and M is the solar mass. The term "tidal quadrupole coupling" denotes the leading tidal term due to interaction of the internal motion with the quadrupole part of the external gravity fields, which are, for the solar influence, smaller by a factor[2] of $\simeq(r/R)^2 \simeq 10^{-10}$ than the solar monopole acceleration[3] GM/R^2 and may be safely neglected. There are even smaller terms due to higher multipole interactions and the interaction of the solar monopole with quadrupole fields of both asteroids not shown in Eq. (1). In general, however, *the point-masses model is a very good approximation of the global motion*, except perhaps for very long timescales or deep encounters with planets. The Yarkovsky perturbation is represented by the terms in the second row; $\mathbf{f}_1$ and $\mathbf{f}_2$ are the Yarkovsky accelerations of both components with masses m_1 and m_2, and $X_1 = m_1/m$ and $X_2 = m_2/m$ are the respective fractions with which they contribute to the total mass $m = m_1 + m_2$ of the system. Note the relative magnitude of the Yarkovsky effective acceleration $|X_1\mathbf{f}_1 + X_2\mathbf{f}_2|$ with respect to the solar monopole acceleration is $\simeq 5 \times 10^{-10}$ for the 2000 DP_{107} case studied below. But even more important than the absolute magnitude is a non-zero mean acceleration component transverse to the heliocentric position vector that produces a fast growing perturbation in the orbital longitude.

The local motion is given by

$$\frac{\mathrm{d}^2\mathbf{r}}{\mathrm{d}t^2} = -\frac{Gm}{r^3}\mathbf{r} + (\text{quadrupole coupling}) + \mathbf{f}_2 - \mathbf{f}_1, \tag{2}$$

where "quadrupole coupling" stands for quadrupole (and higher multipole) interactions of the two asteroids and for their monopole interactions with the solar and planetary (quadrupole) tidal fields. The Yarkovsky perturbation is again represented by the second row. Due to a typical proximity of the binary components in NEAs, the local motion solution is very complicated, also because the quadrupole interaction is intimately coupled with evolution of the spin state of both asteroids. *Representation of the relative motion with a point mass model is inadequate on any timescale of interest.*

While the Yarkovsky perturbation of the global motion is a weighted sum of both Yarkovsky forces, its effect on the local motion is given by their difference. Assuming that the rotation periods of both components are comparable (within an order of magnitude) and that their rotation axes collinear, and neglecting mutual shadowing effects, we may approximate $\mathbf{f}_1 \simeq \xi\mathbf{f}_2$, where $\xi = D_2/D_1 \leqslant 1$

[1] General discussion of a coupling between the global and local motions is in Damour (1987).

[2] This interaction is generally very small and it does not result in a significant long-term perturbation of the orbit; a special topic that warrants a deeper analysis are close encounters with planets (Earth) that may temporarily surpass the solar tidal influence.

[3] Note this is only slightly more than the uncertainty in GM or equivalently the astronomical unit (e.g., IERS, 2003).

is the ratio of characteristic sizes of the two components (here we arbitrarily assume $D_1 \geqslant D_2$). With that, one easily shows[4] $X_1\mathbf{f}_1 + X_2\mathbf{f}_2 \simeq (1+\xi^2)\mathbf{f}_1/(1+\xi^3) \simeq \mathbf{f}_1$. The effective Yarkovsky acceleration for global motion in (1) is dominated by the Yarkovsky effect ($D_1 \geqslant D_2$) on the *larger* component. On the contrary, $\mathbf{f}_2 - \mathbf{f}_1 \simeq (1-\xi)\mathbf{f}_2$ is dominated by the Yarkovsky effect on the *smaller* component (except for cases with binary components of comparable size). These rules likely maximize the total result; mutual shadowing, non-collinear rotation axes and other effects perhaps lessen the effective Yarkovsky force and should be investigated numerically.

2.1. Thermal solution for binaries

In the analyses shown below we develop a detailed thermal model for binary systems.[5] Our approach treats both components as irregular bodies whose shape is given by a polyhedral model (e.g., Simonelli et al., 1993). For each of the surface facets, we solve the heat diffusion problem (HDP) in a one-dimensional formulation where the temperature is considered a function of time and depth below the surface (see, e.g., Vokrouhlický and Farinella, 1998). The non-linear boundary condition at the surface, namely the energy balance between the absorbed solar radiation and the heat emitted into space and conducted into the body, is solved by a standard approximation scheme (e.g., Appendix of Spencer et al., 1989). We take into account the mutual shadowing of the surface elements on each of the components and also the effects of eclipses between the two asteroids[6]; both determine the input of solar radiation energy on each of the surface elements and thus affect the HDP. The timestep of the numerical HDP solution is a small fraction of the primary rotation period,[7] typically 10–50 s. The numerical step in depth is a small fraction of the estimated penetration depth of the diurnal thermal wave. At large depths, in practice $\simeq$10 times the penetration depth of the seasonal thermal wave, we impose an isothermal core as a second boundary condition. The last boundary condition of the HDP is a periodicity in time after one revolution of the COM about the Sun. The solution of the HDP is iterated until the surface temperature has a fractional variation smaller than 10^{-4}.

With the surface temperature determined for each of the surface facets at any time instant during one revolution about the Sun, we can compute the recoil force due to the thermally emitted radiation (e.g., Vokrouhlický and Farinella, 1998; Bottke et al., 2002). Summing up over the whole surface of the asteroid, one gets the total Yarkovsky accelerations $\mathbf{f}_1$ and $\mathbf{f}_2$ on each of the two components. These results are stored in a computer file[8] and used for further analysis, such as the prediction of global and local Yarkovsky displacements.

Fig. 1 illustrates several important features of the thermal solution in the case of the system 2000 DP_{107}. Most importantly, we note the effective COM perturbation is indeed close to the effect on the primary component. Moreover, the smaller secondary causes only insignificant eclipse phenomena on the primary, so that a first glimpse of the effect may be obtained by considering the Yarkovsky force on the "solitary" primary component (see Fig. 2). On the contrary, the Yarkovsky perturbation of the local (relative) motion of the two components is fundamentally affected by the mutual eclipsing phenomena (see Appendix A) and only adds to the complexity of the interpretation of their relative motion. The principal Yarkovsky perturbations of the global and local motions are of the same nature, namely a secular change in semimajor axis of the respective orbits. The key difference, however, is due to the relative position of the Sun in the two cases. For the COM motion about the Sun only the COM (and not the Sun) is affected by thermal forces that are internal to the system, whereas for the binary relative motion, where the radiation is external to the system, the thermal effects act on both components of the binary.[9] This circumstance produces two variants of the thermal-force perturbations (both previously studied in satellite geodesy):

- The heliocentric motion is steadily perturbed by the off-radial force component due to the time lag between sunlight absorption and thermal re-emission in exactly the same way as the Yarkovsky effect acts on single asteroids.
- The relative motion of the two asteroids, for which the Sun is an external rather than internal source of radiation, is on a long term affected by the uneven thermal cooling and heating during and after the eclipse phases (see Appendix A and Fig. 1).

From the latter item it follows that eclipses are a necessary condition for Yarkovsky to secularly affect the internal motion. Compactness of the NEA binary systems implies such eclipses are the rule rather than the exception, and thus

[4] Comparable densities of the two components are also assumed.

[5] A zero level estimate of the Yarkovsky strength in the COM's motion may be obtained with a simpler model that contains only the primary's motion (Fig. 2). However, analysis of the Yarkovsky effect for the local motion necessarily requires a detailed thermal description of both the primary and secondary components because the main, long-term Yarkovsky perturbation of local motion stems from a sequence of shadowing effects.

[6] We assume some zero approximation description of the relative motion for the two binary components, usually a circular orbit. This procedure may be, however, iteratively improved as the analysis becomes more constrained.

[7] In fact we make sure the timestep is several times smaller than the time-lag of the diurnal thermal effect (e.g., Vokrouhlický, 1998).

[8] Our results are publicly available through http://sirrah.troja.mff.cuni.cz/~davok/.

[9] At this stage we disregard mutual thermal irradiation of the two binary components.

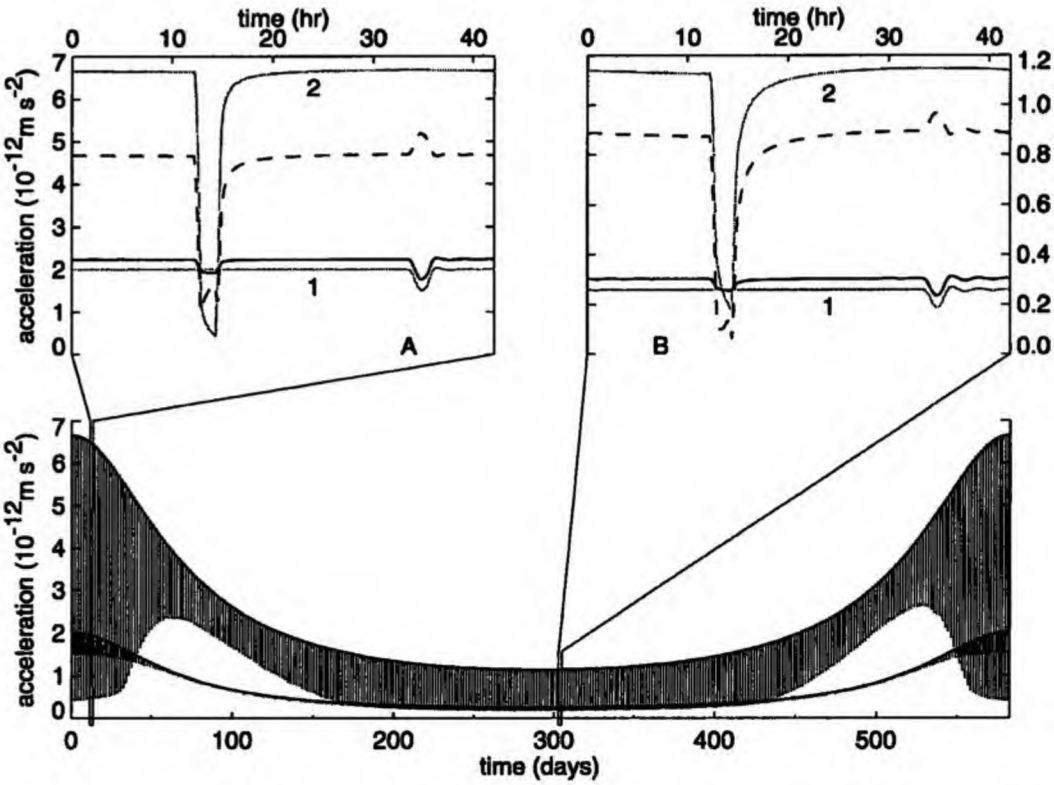

Fig. 1. Time history of the magnitude of the Yarkovsky acceleration for the 2000 DP_{107} system. Bottom: The abscissa covers one revolution of the COM around the Sun with time equal zero at the pericenter. The larger-amplitude curve is the acceleration of the secondary $|\mathbf{f}_2|$, and the smaller-amplitude curve is the acceleration of the primary $|\mathbf{f}_1|$. The large oscillation of the secondary's acceleration is due to eclipse phenomena, mainly near the pericenter and apocenter where the eclipses are total; around quadrature (e.g., time $\simeq$ 80 days) the secondary eclipses are only partial and the relative oscillation is reduced. Top: Details of the Yarkovsky acceleration during one revolution of the binary components about their common COM. The gray solid curves (labeled "1" for the primary and "2" for the secondary) are the individual effects on the two components. The solid black curve is the magnitude of the weighted sum $|X_1\mathbf{f}_1 + X_2\mathbf{f}_2|$ from Eq. (1), which is the effective Yarkovsky acceleration of the system's COM, and the dashed black curve is the magnitude of $|\mathbf{f}_2 - \mathbf{f}_1|$ from Eq. (2), which is the effective Yarkovsky acceleration for the relative motion. The left part (A) is the situation near the pericenter of the heliocentric orbit (at $\simeq$0.85 AU), and the right part (B) is the situation near apocenter (at $\simeq$1.88 AU). In both cases mutual eclipses occur. First the primary component totally eclipses the secondary component and causes a deep drop of the perturbation, and a half-revolution later the secondary component partially eclipses the primary component causing a smaller effect. Since the primary component is larger by a factor $\simeq$8/3 than the secondary component, the Yarkovsky perturbation of the secondary is significantly larger. As discussed in the text, the net perturbation of the heliocentric motion is roughly the effect on the primary, while the effective perturbation of the relative motion is close to the effect on the secondary. The main reason for the larger (smaller) perturbation at the pericenter (apocenter) is the variation of solar radiation flux, which immediately explains a factor $\simeq$5 difference. The additional factor is due to the Yarkovsky force dependence on the thermal parameter Θ (see, e.g., Vokrouhlický, 1998). For the dominating diurnal variant of the Yarkovsky effect, on the secondary component, for example, $\Theta \simeq 0.74$ at the pericenter and $\Theta \simeq 1.33$ at the apocenter. The larger value of Θ near the apocenter means a longer relaxation time after the eclipse seen in part (B), whereas in part (A) the secondary acceleration returns much more quickly to the baseline. This effect is also seen for the primary component, where the partial eclipse is followed with a relaxation phase lasting a few rotation-cycles. Note that the details of the shadowing events are not important for the perturbation of the heliocentric motion, while they are essential for the perturbation of the relative motion.

we should readily expect a strong Yarkovsky influence on the local motion, as well as the global motion.

3. Candidate systems: an example

Currently, as of November 2004, we know of 23 binary systems in the NEA population (e.g., Merline et al., 2002, and updates on http://www.asu.cas.cz/~ppravec/). The amount of information about each of these systems is unequal and depends on their optical observation history and, especially, whether they have been observed by radar (Ostro et al., 2002). However, even for the best known systems today, their full orbital analysis is complicated and depends on many still unknown or poorly known parameters. For that reason we do not discuss all candidate systems,[10] but rather we summarize them in Table 1. We have selected one of them solely to illustrate the basic concepts that should be

[10] A good candidate system is judged by estimating strength of the Yarkovsky effect together with a possibility to acquire high-quality astrometry data.

Table 1
Selected Yarkovsky-detection candidates among the binary asteroid systems within the next two decades or so

Asteroid	Spectral class	ρ^* [g/cm^3]	D_1/D_2** [m]	Year of Yarkovsky detectability	Required pre-detection observations	
					Radar	Optical
1998 RO_1			800/400	2006?	2005	2007
2000 DP_{107}	C	1.7	800/300	2016	2008	2005, 2011, 2013
1999 KW_4	Q	2.6	1200/400	2019	2017, 2018	2016
1996 FG_3	C	1.4	1400/430	2022	2009, 2011	2010
1994 AW_1			900/480	2023	2015, 2022	2008, 2016
2003 YT_1	V		1000/200	2023	2009, 2011, 2016	
1998 ST_{27}	C		800/100	2024	2021	2012, 2015, 2018

Note. Objects sorted according to the estimated year of Yarkovsky detection. None of the listed systems requires future astrometric recovery, and the indicated "optical observations" stand for putative photometry that should constrain solution of the asteroids' relative motion (those are typically also possible during the radar apparitions). Additional candidate objects will be posted on http://sirrah.troja.mff.cuni.cz/~davok/.

* ρ is the bulk density from analysis of the relative motion of the two asteroids (typically with a large error bar).

** Sizes are usually estimated from absolute magnitude and geometric albedo, when known, and from the lightcurve eclipses; in a few cases radar ranging allowed to better estimate the characteristic size of the components (none of these is however known better than to $\simeq$ 10–20%).

kept in mind when analyzing binaries for which a prolific dataset is available.

3.1. 2000 DP_{107}

Most information about 2000 DP_{107} comes from an extensive radar campaign in September/October 2000 (Margot et al., 2002). The system consists of two components, a primary of diameter $D_1 \simeq 800$ m and a secondary of diameter $D_2 \simeq 300$ m, each revolving about the system center of mass with a period of about 1.755 day. The primary rotates at a near critical rate with period of $\simeq$2.775 h (Pravec et al., 2000), while the secondary likely has a synchronous rotation rate. Separation between the two components is $\simeq$2620 m and the relative orbit is near circular. The primary component was found to be a C-type object,[11] and a preliminary solution of the relative motion from the radar imaging suggests a bulk density of 1.7 ± 1.1 g/cm^3, appropriate for that spectral type (Margot et al., 2002). There is not enough information to resolve poles of rotation for the two components. For sake of simplicity we assume here that the synchronized secondary component has rotation pole normal to the plane of mutual motion, which would be compatible with a spin–orbit synchronization history. Without observational constraints, we assume the same pole orientation for the fast rotating primary. The preliminary solution of the mutual motion of asteroids in this system from Margot et al. (2002) would give these poles at ecliptic longitude $\ell = 280°$ and ecliptic latitude $b = 73°$, consistent with lightcurve-detected eclipses (P. Pravec, personal communication).

In our simulation we consider the following surface physical parameters for both components: thermal conductivity $K = 0.01$ W/m/K, specific heat capacity $C = 800$ J/kg/K, surface and bulk densities $\rho_s = \rho_b = 1.7$ g/cm^3. We note that, a priori, there is no strict reason why the components should have exactly the same physical parameters, and here this is only one of many simplifying assumptions. Both components are considered spherical and represented with 1000-facet polyhedra.

With these assumptions, we have determined the orbit-averaged value of the semimajor axis drift due to the Yarkovsky effect (Fig. 2). The effect of non-linearity is a 10–20% reduction of the Yarkovsky acceleration (see also Vokrouhlický and Farinella, 1998, 1999), while the contribution of the secondary component increases the Yarkovsky strength for larger values of the surface thermal inertia (this because of its slow rotation). Generally, though, the linearized theory yields fairly satisfactory results.

The nearest radar observation opportunities for this system are two close encounters in September 2008 and August 2016; there is also good reason to take precise optical astrometry during periods when the sky-plane uncertainty exceeds an arcsecond (e.g., during January–March 2005, November 2005–February 2006, and the early months of 2008). Photometry in December 2005, January 2011, and December 2013 would be also useful to track the relative motion of the components if mutual eclipses are recorded.

3.1.1. Heliocentric motion of the center of mass

We primarily focus on the Yarkovsky perturbation in the heliocentric COM motion for which our force model is adequate and we can produce a reliable estimate. Currently, the available observations constrain the orbit too weakly to allow statistically significant detection of the Yarkovsky displacement during the next close approach in 2008. We thus adopt the same method as in Vokrouhlický et al. (2000, 2005), simulating the 2008 Arecibo astrometry to make the solutions with and without Yarkovsky accelerations statistically distinct during the close approach in 2016. The 2008 apparition is close enough (Arecibo peak SNR $\simeq$ 4000) to allow a high-quality determination of the system's COM; we assume one range measurement with formal accuracy of $\simeq$50 m.

With this simulated data point, and with all past optical and radar astrometry, we propagated the two orbital solu-

[11] Alternately X-type, e.g., Yang et al. (2003).

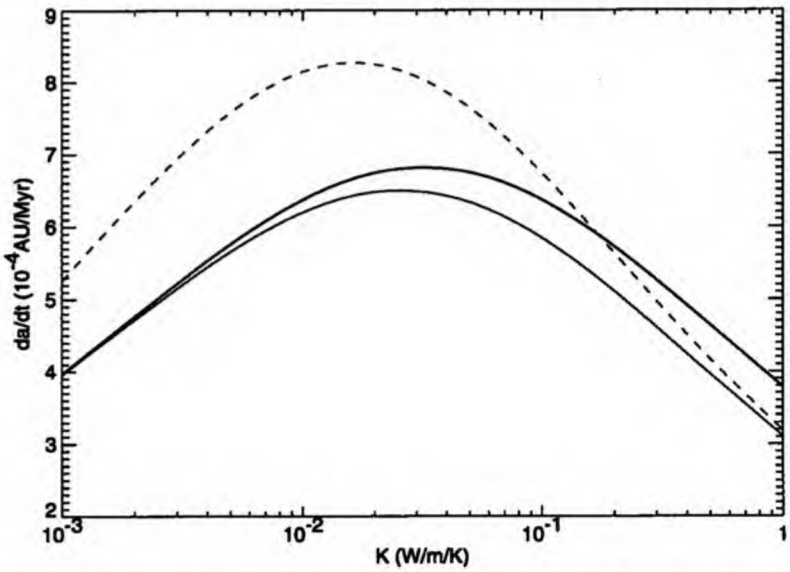

Fig. 2. The orbit-averaged value of the COM heliocentric motion semimajor axis change $\langle da/dt \rangle$ (in 10^{-4} AU/My) due to the Yarkovsky effect for 2000 DP_{107} shown as a function of surface conductivity K (in W/m/K; other surface thermal parameters as described in the text). The thick solid line is the result from complete numerical model accounting for non-linear analysis of HDP on both binary components and their mutual shadowing effects (Fig. 1). The thin solid line is the non-linear HDP numerical model but only the primary asteroid is considered (as if the system did not contain the secondary). The dashed line shows the result from a linearized approximation of heat conduction and a perturbation of the primary component only (note the non-linearity makes the Yarkovsky signal smaller; see, e.g., Vokrouhlický and Farinella, 1998, 1998). Since the secondary component rotates slowly, its own Yarkovsky drift peaks for higher value of the conductivity and thus contributes more importantly to the total signal. This is the reason for the divergence of the solid curves at larger K.

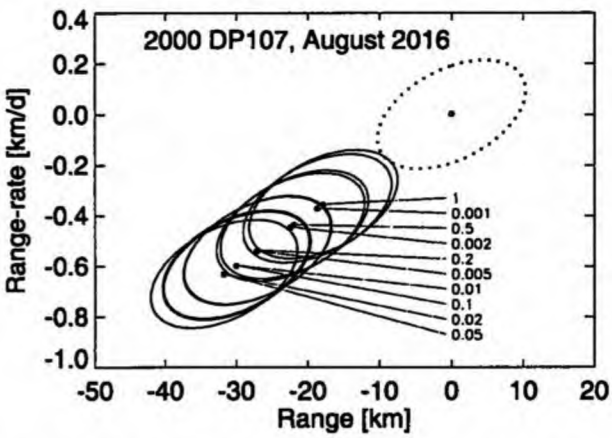

Fig. 3. Range and range-rate projected 3σ-uncertainty ellipses of the no-Yarkovsky (dashed) and Yarkovsky (solid) COM heliocentric orbits of 2000 DP_{107} on August 24.9, 2016. Arecibo radar offers a $\simeq$50 SNR ranging opportunity at that epoch. The origin is the no-Yarkovsky orbital solution. These solutions assume all past optical and radar astrometry and a simulated Arecibo radar astrometry in September 2008 as described in the text. Different displaced ellipses of the Yarkovsky-solution are for different values of the surface thermal conductivity K, whose values (in W/m/K) are indicated in the figure. Note a degeneracy—one ellipse may correspond to two conductivity values—that is due to the fact the same $\langle da/dt \rangle$ value may correspond to two different values of conductivity K (Fig. 2).

tions, with and without Yarkovsky, by numerically integrating (1) with all necessary planetary and other perturbations to 2016. Nominal predictions with their formal 3σ confidence ellipses were projected onto the plane of radar observables, delay and Doppler, or equivalently range and range-rate. Fig. 3 confirms that during the 2016 close approach, when Arecibo can acquire astrometric data at SNR $\simeq$ 50, the Yarkovsky effect could be comfortably detected as a large COM displacement of the two solutions beyond their formal 3σ uncertainty regions.

3.1.2. Relative motion of the components

Our solution may also be used to get a preliminary estimate of the observability of the Yarkovsky perturbation in the relative motion of the two asteroids. However, we emphasize that these results are suggestive rather than predictive since the force model in our simulation is not entirely adequate to describe the details of the internal dynamics of the 2000 DP_{107} system, and at present several key parameters, such rotation poles, are only weakly constrained.

With our solution of the Yarkovsky effect for both binary components we constructed the radial, transverse and normal projections of the effective perturbation $\mathbf{f}_2 - \mathbf{f}_1$, and from those quantities we determined the corresponding displacements about the zero order circular orbit (see (A.6)–(A.8) in Appendix A). The result is shown in Fig. 4.

First, we confirm the principal orbital perturbation of the local motion of the two components is a quadratic advance of the transverse displacement η (related to the linear radial displacement ξ; upper panels) due to a non-zero mean transverse Yarkovsky acceleration (for a broader context see Appendix A). This effect is specific to the dissipative thermal effects and cannot, on a long-term, correlate with gravitational perturbations that are conservative. In spite of in-

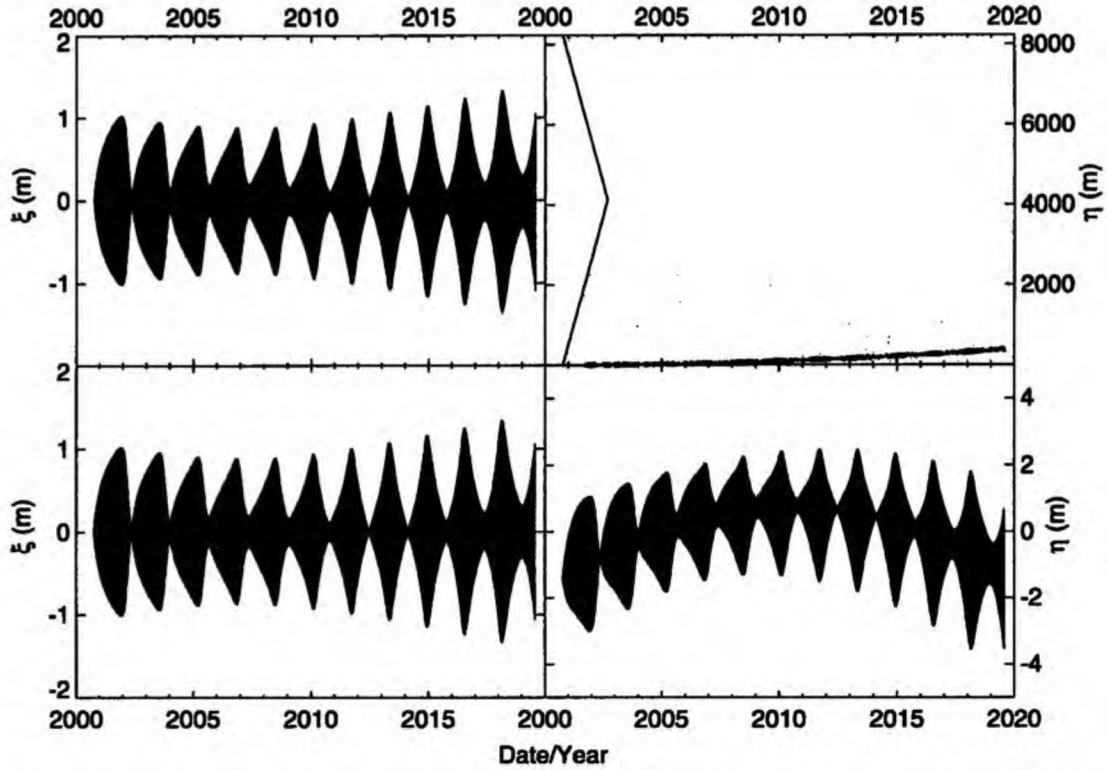

Fig. 4. The Yarkovsky displacement of the relative motion of the two components of 2000 DP_{107}, according to an approximate (linearized) solution described in Appendix A. Top: Time history of radial ξ (left) and transverse η (right) perturbations, relative to the circular orbit approximation, with origin at the midpoint of radar observations in 2000. The transverse displacement is folded into an interval equal to the circumference of the unperturbed circular orbit. The principal secular effect, due to the non-zero average value of the transverse Yarkovsky acceleration (discussed in Appendix A), produces a linear drift in the radial component (masked by periodic terms at this short timespan) and a quadratic drift in the transverse component. The latter effect is very distinct from (neglected) multipole interactions of the gravity fields of the two asteroids and it should be in principle observable. Obstacles are (i) the large observational uncertainty (that from the 2000 observations is shown as a shaded area; note this prevents an unambiguous link of the 2000 and 2008 observations), and (ii) its weakness (the total transverse displacement amounts to only $\simeq$240 m in 19 yr shown in this figure). When sparse observational data are only available, a correlation between this quadratic and a linear terms in η may be high and hinder the Yarkovsky signal. Bottom: Same as top part, but here the average values of the radial and transverse perturbing accelerations have been removed. The remaining sub- to few meter displacements are well below the model uncertainties associated with the absence of multipole interactions of the gravity fields of the two asteroids.

completeness of our force model we may thus conclude that the principal Yarkovsky perturbation could be observable. Mismodeling of the system mass, which would produce a linear advance in the transverse perturbation, could mask the effect when data from only a few apparitions are available. In general, however, more observations constrain the solution better and thus sooner or later should reveal the Yarkovsky signal in the local motion.

However, Fig. 4 also indicates two obstacles of an early detection of the Yarkovsky effect in the relative motion of binaries. First, a large orbital phase uncertainty is currently the primary hindrance to detection of the Yarkovsky perturbation of the relative motion. By the end of 2002 the formal uncertainty of the solution by Margot et al. (2002) had already spread over the entire range of values from 0° to 360°. That situation does not allow proper linking of the 2008 phase observations with those from 2000 and thus prevents determination of the Yarkovsky effect. When more data are obtained from short-enough interval of time, such as possible photometry and radar observations in between March 2008 and January 2011 (Table 1), the uncertainty in phase might be reduced. Then a tie to phases of more distant observations in time, namely those in September/October 2000, and later December 2013, could be possible.

Even if successful, Fig. 4 suggests the Yarkovsky signal in the relative motion is very weak. The linear component in the radial displacement ξ (upper left panel) is not actually seen at this scale and the related quadratic effect in the transverse displacement η (upper right panel) amounts to only ~240 m in 19 years. This stretches to circumference of the unperturbed circular orbit in more then a century. A very long-term data about the system might in principle reveal the Yarkovsky signal, but a more involved study of the relative motion would be needed to see these prospects realistically.

Fig. 5 shows the mean along-track component f_τ of the Yarkovsky acceleration $\mathbf{f}_2 - \mathbf{f}_1$ as a function of the assumed surface conductivity K of both asteroids. Like the mean semimajor axis drift $\langle da/dt \rangle$ for the global motion (Fig. 2), the mean along-track acceleration is the principal "tuning parameter" of the secular Yarkovsky effect for the local mo-

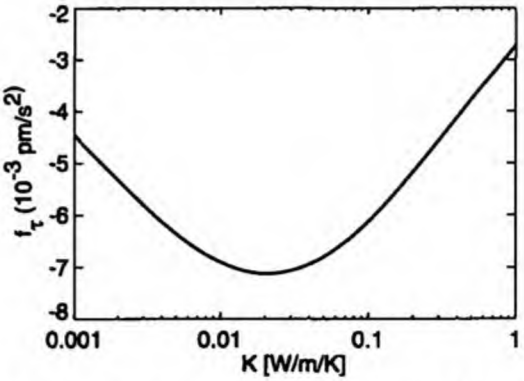

Fig. 5. Mean along-track Yarkovsky acceleration f_τ (in 10^{-3} pm/s^2) as a function of the surface conductivity K (in W/m/K) for 2000 DP_{107} system. Geometry of spin axes, and other surface physical parameters as in the text.

tion, since the rate/speed of the semimajor axis drift (Fig. 4, upper left) directly depends on its value. We find it natural that f_τ depends on K is a similar way as $\langle da/dt \rangle$.

4. Conclusions

The formation and evolution of near-Earth binary systems is becoming a particular focus of planetary science. From the perspective of the present work, a key characteristic of binaries is the fact that one can solve for the total mass of the system from tracking the relative motion of the two asteroids about their COM. With principles of gravitational physics, which set a body's acceleration independent of its mass, this seems to be a singular opportunity. Moreover, non-gravitational perturbations are mass-selective and their detection opens a second possibility of estimating asteroids' mass (e.g., Chesley et al., 2003). This applies both to solitary asteroids (Vokrouhlický et al., 2000, 2005) and also to the binary systems.

In this paper we demonstrated that the prime non-gravitational perturbation in the asteroid's motion—the Yarkovsky effect—can be detected in the global motion of the system's COM about the Sun and, in the best cases, also in the local motion of the two asteroids relative to each other. The double detection of the Yarkovsky effect for binaries—if achieved in remote future or for more suitable systems than known today—would allow a more profound investigation of the systems physical parameters. Ideally one could characterize parameters of each of the two asteroids separately, but the degree of correlation with other perturbations and uncertainties should be studied for each of the binary systems individually.

The most restrictive assumption in this study, to be removed in a detailed analysis of particular systems, is that of fixed rotation poles of the two asteroids, and a related assumption of the fixed orbital plane of the relative motion of the two asteroids. Tidal evolution (whose timescale is uncertain but perhaps fast for close binaries; Margot et al., 2002; Merline et al., 2002) generally leads to spin synchronization of the satellite (lighter component) and tilts its axis toward the Cassini states 1 or 2, locked to the orbital plane motion (e.g., Peale, 1977, 1999; Gladman et al., 1996). The latter generally depends on dynamical flattening of the satellite and precession rate of its orbital plane; as in the lunar case, rapid precession of the orbital plane likely excludes Cassini state 1 and the only terminal occupancy of the satellite spin is perpendicular to the orbital plane. Radar observations of the 2000 DP_{107} are consistent with this situation (Margot et al., 2002).

Long-term evolution of the primary's spin state is more uncertain. In compact systems with fast rotating primary, typical for NEA binaries (e.g., Merline et al., 2002), the total angular momentum of the system is weakly dominated by the rotational angular momentum of the primary.[12] This implies a possibly complicated interplay between the rotational and orbital motion, affecting stability of the system (a problem not considered in detail so far). Since the secondary components of typical NEA systems bear a non-negligible fraction of mass, gravitational torque due to the secondary dominates solar gravitational torque, causing the primary's axis to evolve toward a state similar to that occupied by the secondary, but timescales depend on many uncertain parameters. Nevertheless, dominance of the primary's angular momentum in the system makes us think its pole is the most stable direction. As a result, we think the COM Yarkovsky displacement (see Fig. 3), related to the thermal effects on the primary, is the most justified result above. On the other hand, as the orbit of relative motion precesses, or the secondary's pole moves, the linear drift in the relative distance of the two asteroids (see Fig. 4A) becomes periodic. The results given above are likely an overestimate of the internal Yarkovsky effect, though they are hopefully appropriate within the assumed model and the $\simeq$20 yr timescale.

To verify these conclusions we constructed a toy model describing relative motion and spin evolution of two quadrupole-field axial bodies that retains some, though certainly not all, dynamical elements of NEA binaries. Initial orbital data and various parameters were chosen close to the 2000 DP_{107} system and the initial rotation poles of both components were varied within $\pm 15°$ in the ecliptic longitude and latitude about the normal to the orbital plane of their relative motion. With those initial data we numerically integrated the Euler–Lagrange equations for 20 yr timespan[13] and we found small variations of the primary's pole (generally within 10° from the initial position), but a rather large

[12] For instance, in the 2000 DP_{107} case the ratio between the rotation angular momentum of the primary and orbital angular momentum of the pair is $\simeq$(2–3).

[13] The primary and secondary components were modeled as homogeneous spheroids with ratio of equatorial and polar radii equal to 1.05 and 1.1, respectively, yielding thus only moderate dynamical ellipticity.

variation in the secondary's pole[14] (up to tens of degrees from its initial position). Clearly, more observational constraints are needed to fully address details of the Yarkovsky perturbation of the local motion.

Acknowledgments

The work of D.V. and D.Č. has been supported by the Grant Agency of the Czech Republic, under the grant No. 205/05/2737. The research of S.R.C. and S.J.O. was conducted at the Jet Propulsion Laboratory, California Institute of Technology under a contract with NASA. We are grateful to Matija Ćuk who, as a referee, helped us to correct an error in the earlier version of this paper.

Appendix A. Linearized perturbation of the local motion

In Section 2 we noted that the local motion of the binary system components relative each other is far more complicated than the global (heliocentric) motion of its COM. This is because proximity of the two components implies that couplings of many multipole harmonics in gravity fields of the two asteroids are important and contribute to complexity of their local motion. Moreover, these couplings intimately depend, and in the same time affect, rotation state of both components. Detailed analysis of these effects is well beyond the scope of this paper, both because they should be studied in context of the individual systems [it is hard to imagine that quantitative features, except from general constraints such as in Scheeres (2002a, 2002b), can be derived] and also because our primary focus here is to determine the major signatures of the Yarkovsky effect. For that reason, we relegate the in-depth model of the internal motion when rich enough data are available to study some of the systems.

Our approach here is to examine general properties of the linear perturbation theory of the Keplerian circular motion in Cartesian variables as the simplest possible representation of the Yarkovsky displacement in the relative position of the components in the binary system. We assume an (Yarkovsky) acceleration $\delta\mathbf{f}$ affects a circular orbit $\mathbf{r}_0$ (often a good zero approximation of the binary motion) to produce a small perturbation $\delta\mathbf{r}$ ($|\delta\mathbf{r}| \ll r_0$). With m the total mass of the system we have

$$\frac{\mathrm{d}^2\delta\mathbf{r}}{\mathrm{d}t^2} + \frac{Gm}{r_0^3}\left[\delta\mathbf{r} - 3\mathbf{r}_0\frac{(\mathbf{r}_0\cdot\delta\mathbf{r})}{r_0^2}\right] = \delta\mathbf{f}. \tag{A.1}$$

It is common to split the displacement vector $\delta\mathbf{r}$ into radial $\xi = \delta\mathbf{r}\cdot\boldsymbol{\rho}$, transverse $\eta = \delta\mathbf{r}\cdot\boldsymbol{\tau}$ and normal $\zeta = \delta\mathbf{r}\cdot\mathbf{n}$ components. Here $\boldsymbol{\rho} = \mathbf{r}_0/r_0$ is unit vector in the radial direction, $\mathbf{n}$ unit vector normal to orbital plane along direction of the orbital angular momentum, and $\boldsymbol{\tau} = \mathbf{n}\times\boldsymbol{\rho}$ the unit vector in the transverse direction. We assume $\mathbf{n}$ is fixed, while $\boldsymbol{\rho}$ and $\boldsymbol{\tau}$ uniformly rotate in space with angular velocity equal to the mean motion[15] n_0: $\mathrm{d}\boldsymbol{\rho}/\mathrm{d}t = n_0\boldsymbol{\tau}$ and $\mathrm{d}\boldsymbol{\tau}/\mathrm{d}t = -n_0\boldsymbol{\rho}$. It appears useful to introduce scaled quantities $\delta\mathbf{f} \to (\alpha_\rho, \alpha_\tau, \alpha_\zeta)$ so that $\alpha_\rho = (\delta\mathbf{f}\cdot\boldsymbol{\rho})/n_0^2$, $\alpha_\tau = (\delta\mathbf{f}\cdot\boldsymbol{\tau})/n_0^2$, $\alpha_\zeta = (\delta\mathbf{f}\cdot\mathbf{n})/n_0^2$, and replace time t with a phase angle of the rotating (sidereal) system $t \to \tau = n_0 t$. With these new variables, (A.1) reads[16] (e.g., Nordtvedt, 1991)

$$\frac{\mathrm{d}^2\xi}{\mathrm{d}\tau^2} + \xi = 2\Phi + \alpha_\rho = \Sigma(\tau), \tag{A.2}$$

$$\frac{\mathrm{d}^2\zeta}{\mathrm{d}\tau^2} + \zeta = \alpha_\zeta = \Gamma(\tau), \tag{A.3}$$

$$\frac{\mathrm{d}\eta}{\mathrm{d}\tau} = \Phi - 2\xi, \tag{A.4}$$

where

$$\Phi = \int_0^\tau \mathrm{d}\tau'\,\alpha_\tau(\tau'), \tag{A.5}$$

When $\delta\mathbf{f} = 0$, solutions of the system (A.2)–(A.4) represent change from one elliptic orbit to another due to variation of the initial conditions. This is characterized by periodic terms in all variables (with anomalistic frequency), a constant term in ξ_{free} [a slight change in the semimajor axis due to variation of the orbital angular momentum, a term eliminated from the right had side of (A.2)] and a related linear term in η_{free}. Strictly speaking coefficients of constant and linear terms in ξ_{free} and η_{free} are correlated, but when the total mass of the system is not known they independently couple to this additional parameter.

When $\delta\mathbf{f} \neq 0$, the system (A.2)–(A.4) admits the following particular solution:

$$\xi(\tau) = \int_0^\tau \mathrm{d}\tau'\,\Sigma(\tau')\sin(\tau-\tau'), \tag{A.6}$$

$$\eta(\tau) = \int_0^\tau \mathrm{d}\tau'\,[\Phi(\tau') - 2\xi(\tau')], \tag{A.7}$$

$$\zeta(\tau) = \int_0^\tau \mathrm{d}\tau'\,\Gamma(\tau')\sin(\tau-\tau'). \tag{A.8}$$

Special cases warrant investigation. For ($\alpha_\rho = \alpha$, $\alpha_\tau = 0$, $\alpha_\zeta = 0$) the proper mode of the perturbation is $\eta_{\mathrm{prop}} =$

[14] When the initial pole positions were placed further from the perpendicular orientation to the mutual orbital plane, the system often evolved quickly toward satellite escape or collision.

[15] We note that n_0 here plays the role of sidereal frequency, which is in fact affected by both the solar tidal field and the multipole fields of the two asteroids. Such details are not studied in this paper.

[16] We note the unitary frequency in the left hand sides of (A.2) and (A.3) should be affected, in a more detailed theory, by the solar tidal terms and multipole interactions of the asteroids' gravity fields, and should become anomalistic frequency (i.e., the natural pericenter frequency).

$-\alpha\tau/2$, i.e., a "stronger gravity" requires motion with higher angular speed at the circular orbit of a given radius. Obviously, this perturbation is fully correlated with the solution of a priori unknown total mass of the system. More important is the case of a permanent along-track acceleration ($\alpha_\rho = 0, \alpha_\tau = \alpha, \alpha_\zeta = 0$), which results in the proper perturbation modes $\xi_{\text{prop}} = 2\alpha\tau$ and $\eta_{\text{prop}} = -3\alpha\tau^2/2$, analogous to the heliocentric COM perturbation due to the Yarkovsky effect: a linear drift in semimajor axis produces a quadratic advance in the longitude in orbit. This is by far the most significant effect both in the global and local dynamics. Finally, linearity of the system (A.2)–(A.4) implies any periodic term in $\delta\mathbf{f}$ produces perturbation $\delta\mathbf{r}$ containing the same spectral components. As typical in linear resonant systems, forcing terms with periodicity close to the natural (anomalistic) period of the binary component revolution are amplified due to the presence of small denominators (e.g., Nordtvedt, 1991, 1995).

Out of these fundamental modes, the one due to the non-vanishing along-track acceleration is the most important on a long-term (since the related orbital displacement propagates quadratically in time). Whether we should expect this effect in the internal motion of the binary system or not arises, interestingly, from an analogy with motion of the geodynamics Earth satellites among which the case of LAGEOS has been the most thoroughly studied (e.g., Afonso et al., 1989; Métris et al., 1997; Slabinski, 1997). Thermal effects (the so called photon thrust or Yarkovsky–Schach effect in that context) are well known to produce secular along-track orbital acceleration when the spacecraft enters the Earth shadow. The Earth-spacecraft pair represents "an extreme binary system" where the secondary component (spacecraft) has a vanishing size, and only the primary (Earth) eclipses the secondary. In the case of NEA binaries both components are of the same size and produce a complex series of mutual eclipsing events, but the overall conclusion is the same: thermal relaxation in re-radiation of the absorbed sunlight during eclipses results in a non-vanishing along-track acceleration. The analogy with the spacecraft dynamics makes us also to think that precession of the orbital plane, defined by the relative motion of the two components, approximately averages out this principal effect on a timescale larger than the precession period (roughly a couple of centuries as for the solar gravitational torque). Certainly this compensation is not exact, but the purpose of this paper is not to study the long-term dynamics of the binary asteroids due to the Yarkovsky forces, but to determine its observability on a short-term scale. Our basic model of the fixed zero-approximation relative orbital plane of the two components is thus justified.

In practice we chose a zero approximation relative orbit of the two asteroids and solve the HDP problem (Section 2.1) to obtain the Yarkovsky accelerations $\mathbf{f}_1$ and $\mathbf{f}_2$ for both asteroids. These series are combined to get the effective Yarkovsky accelerations in the global and local dynamics, Eqs. (1) and (2). From the latter, a difference $\mathbf{f}_2 - \mathbf{f}_1$, we compute the radial (α_ρ), transverse (α_τ) and normal (α_ζ) perturbation components and numerically evaluate the quadratures in (A.6)–(A.8). From the resulting displacement vector (ξ, η, ζ) we subtract a part identical to the free mode $(\xi_{\text{free}}, \eta_{\text{free}}, \zeta_{\text{free}})$ which goes in the solution of the initial orbital elements and the total mass of the system. Most importantly, we disregard a linear term in η; however, any non-linearity in η should be observable and possibly interpreted as a proper Yarkovsky perturbation in the local motion of the system.

References

Afonso, G., Barlier, F., Carpino, M., Farinella, P., Mignard, F., Milani, A., Nobili, A.M., 1989. Orbital effects of LAGEOS seasons and eclipses. Ann. Geophys. 7, 501–514.

Bottke, W.F., Vokrouhlický, D., Rubincam, D.P., Brož, M., 2002. Dynamical evolution of asteroids and meteoroids using the Yarkovsky effect. In: Bottke, W.F., Cellino, A., Paolicchi, P., Binzel, R.P. (Eds.), Asteroids III. Univ. of Arizona Press, Tucson, pp. 395–408.

Chesley, S.R., Ostro, S.J., Vokrouhlický, D., Čapek, D., Giorgini, J.D., Nolan, M.C., Margot, J.L., Hine, A.A., Benner, L.A.M., Chamberlin, A.B., 2003. Direct detection of the Yarkovsky effect by radar ranging to Asteroid 6489 Golevka. Science 302, 1739–1742.

Damour, T., 1987. The problem of motion in Newtonian and Einsteinian gravity. In: Hawking, S.W., Israel, W. (Eds.), 300 Years of Gravitation. Cambridge Univ. Press, Cambridge, pp. 128–198.

Gladman, B., Quinn, D.D., Nicholson, P., Rand, R., 1996. Synchronous locking of tidally evolving satellites. Icarus 122, 166–192.

IERS Conventions, 2003. http://maia.usno.navy.mil/conv2003.html.

Margot, J.L., Nolan, M.C., Benner, L.A.M., Ostro, S.J., Jurgens, R.F., Giorgini, J.D., Slade, M.A., Campbell, D.B., 2002. Binary asteroids in the near-Earth object population. Science 296, 1445–1448.

Merline, W.J., Weidenschilling, S.J., Durda, D.D., Margot, J.-L., Pravec, P., Storrs, A.D., 2002. Asteroids do have satellites. In: Bottke, W.F., Cellino, A., Paolicchi, P., Binzel, R.P. (Eds.), Asteroids III. Univ. of Arizona Press, Tucson, pp. 289–312.

Métris, G., Vokrouhlický, D., Ries, J.C., Eanes, R.J., 1997. Nongravitational effects and the LAGEOS eccentricity excitations. J. Geophys. Res. 102, 2711–2729.

Nordtvedt, K., 1991. Lunar laser ranging reexamined: The non-null relativistic contribution. Phys. Rev. D 43, 3131–3135.

Nordtvedt, K., 1995. The relativistic orbit observables in lunar laser ranging. Icarus 114, 51–62.

Ostro, S.J., Hudson, R.S., Benner, L.A.M., Giorgini, J.D., Magri, C., Margot, J.-L., Nolan, M.C., 2002. Asteroid radar astronomy. In: Bottke, W.F., Cellino, A., Paolicchi, P., Binzel, R.P. (Eds.), Asteroids III. Univ. of Arizona Press, Tucson, pp. 151–168.

Peale, S.J., 1977. Rotation histories of the natural satellites. In: Burns, J.A. (Ed.), Planetary Satellites. Univ. of Arizona Press, Tucson, pp. 87–111.

Peale, S.J., 1999. Origin and evolution of the natural satellites. Annu. Rev. Astron. Astrophys. 37, 533–602.

Pravec, P., Kusnirak, P., Hicks, M., Holliday, B., Warner, B., 2000. 2000 DP_{107}. IAU Circ. 7504, 1.

Scheeres, D.J., 2002a. Stability of binary asteroids. Icarus 159, 271–283.

Scheeres, D.J., 2002b. Stability in the full two-body problem. Celest. Mech. Dynam. Astron. 83, 155–169.

Simonelli, D.P., Thomas, P.C., Carcich, B.T., Veverka, J., 1993. The generation and use of numerical shape models for irregular Solar System objects. Icarus 103, 49–61.

Slabinski, V.J., 1997. A numerical solution for LAGEOS thermal thrust: The rapid-spin case. Celest. Mech. Dynam. Astron. 66, 131–179.

Spencer, J.R., Lebofsky, L.A., Sykes, M.V., 1989. Systematic biases in radiometric diameter determinations. Icarus 78, 337–354.

Vokrouhlický, D., 1998. Diurnal Yarkovsky effect for meter-sized asteroidal fragments' mobility. I. Linear theory. Astron. Astrophys. 335, 1093–1100.

Vokrouhlický, D., Farinella, P., 1998. The Yarkovsky seasonal effect on asteroidal fragments: A non-linearized theory for the plane-parallel case. Astron. J. 116, 2032–2041.

Vokrouhlický, D., Farinella, P., 1999. The Yarkovsky seasonal effect on asteroidal fragments: A non-linearized theory for spherical bodies. Astron. J. 118, 3049–3060.

Vokrouhlický, D., Milani, A., Chesley, S.R., 2000. Yarkovsky effect on small near-Earth asteroids: Mathematical formulation and examples. Icarus 148, 118–138.

Vokrouhlický, D., Chesley, S.R., Milani, A., 2001. On the observability of radiation forces acting on near-Earth asteroids. Celest. Mech. Dynam. Astron. 81, 149–165.

Vokrouhlický, D., Čapek, D., Chesley, S.R., Ostro, S.J., 2005. Yarkovsky detection opportunities. I. Solitary asteroids. Icarus 173, 166–184.

Yang, B., Zhu, J., Gao, J., Zhang, H.T., Zheng, X.Z., 2003. Observations of 2000 DP_{107} in NAOC: Rotation period and reflectance spectrum. Planet. Space. Sci. 51, 411–414.

Dynamics of Populations of Planetary Systems
Proceedings IAU Colloquium No. 197, 2005
Z. Knežević and A. Milani, eds.

DOI: 10.1017/S1743921304008622

Accurate model for the Yarkovsky effect

David Čapek and David Vokrouhlický

Institute of Astronomy, Charles University, V Holešovičkách 2, CZ-18000 Prague 8, Czech Republic
email: capek@sirrah.troja.mff.cuni.cz, vokrouhl@mbox.cesnet.cz

Abstract. Yarkovsky effect (YE), a tiny nongravitational force due to radiative recoil of the anisotropic thermal emission, is known to secularly affect the orbital semimajor axis. Therefore, angular phases such as longitude in orbit or proper longitude of node undergo a quadratic perturbation. This is fast enough to allow direct detection of the YE. The first positive case was obtained for (6489) Golevka in 2003 and prospects are very good for many more detections in the near future. To make productive scientific use of the YE detections, we need to accurately compute its strength for a given body. Simple models, available so far, will likely not be adequate in many of the forthcoming YE detection possibilities. We thus developed a complex numerical approach capable of treating most of them. Here we illustrate its power by discussing the cases of: (i) Toutatis, with a tumbling (non-principal-axis) rotation state, and (ii) 2000 DP107, a binary system.

Keywords. Minor planets, asteroids: individual (Toutatis, 2000 DP107).

1. Introduction

The Yarkovsky effect (YE), and its consequences for planetary science, has attracted a considerable attention during the past decade (e.g. Bottke *et al.* 2003; Vokrouhlický *et al.*, this volume). It became a vital part of models for meteorite and asteroid delivery to the planet-crossing region (e.g. Farinella *et al.* 1998; Farinella & Vokrouhlický 1999; Vokrouhlický & Farinella 2000; Morbidelli & Vokrouhlický 2003), dynamical aging of the asteroid families (e.g. Bottke *et al.* 2001; Vokrouhlický *et al.* 2002; Nesvorný & Bottke 2004) or populating metastable asteroidal orbits (e.g. Vokrouhlický *et al.* 2001; Tsiganis *et al.* 2003; Brož *et al.*, this volume). Though important, these applications assume large samples of bodies and do not allow direct detection of the YE (with the unusual exception of the Karin family; Nesvorný & Bottke 2004).

Since the YE continues to perturb accurately known orbits of the planet-crossing asteroids, Vokrouhlický *et al.* (2000) suggested a direct detection can follow from their precise tracking (see also Vokrouhlický & Milani (2000) who discuss effects of other radiative forces on the motion of planet-crossing asteroids). This is because the YE makes a steady perturbation of the orbital semimajor axis, producing a quadratic advance along the orbit; in a number of cases the resulting displacement exceeds ephemerides uncertainty and allows YE detection. With that goal, Chesley *et al.* (2003) conducted a successful experiment by radar ranging to the near-Earth asteroid (6489) Golevka. Their analysis also proved the YE detection contains a significant scientific information, most importantly it has the capability to constrain an asteroid's mass. Vokrouhlický *et al.* (2004a,b) recently reviewed future possibilities for YE detection and noted about a dozen cases might be obtained in the next decade, with more possibly later on. Several of these candidate objects present unforseen difficulties in terms of the YE computation.

This situation motivated us to develop dedicated software for accurate YE computation: the purpose of this paper is to discuss its properties. Our goal is to tackle most of the

"real-world" cases, including bodies of unusual shape, orbit and/or rotation state. Here we discuss two spectacular objects: (i) 4179 Toutatis, a body with the most accurately known tumbling state, and (ii) 2000 DP107, a binary system. If the YE is detected in the Toutatis' motion in October 2004 (see Vokrouhlický *et al.* 2004a), Toutatis might become a landmark case in several respects: (i) this will be the first multi-kilometre asteroid for which YE would be detected, and (ii) with further observation possibilities till 2012 this might be the first case for which the YE will be repeatedly measured. Similarly, if YE signal is too weak for 1998 RO1, the system 2000 DP107 might be the first binary for which YE will be detected (see also Vokrouhlický *et al.* 2004b).

2. Numerical model

Analytical expression of the Yarkovsky force components have been obtained so far for a spherical body residing on a low-eccentricity orbit (e.g. Vokrouhlický 1998, 1999; Vokrouhlický & Farinella 1999); moreover, these results assume linearization of the boundary condition (2.2). Though largely simplified, this formulation was successfully used by Vokrouhlický *et. al.* (2000) for low-accuracy, but reliable, predictions and is available at `http://newton.dm.unipi.it/` as a Fortran source within the `OrbFit` software package.

Apart from a non-linear nature of the heat diffusion problem (HDP), computation of the Yarkovsky force for near-Earth asteroids (NEAs) frequently brings some, or a combination, of the following complexities: (i) large orbital eccentricity, (ii) highly irregular shape (such as a part of the surface may cast shadow on another part), (iii) temperature-dependent thermal constants and/or (iv) unusual rotation state (including free motion of the rotation axis in the body, i.e. the "tumbling state"). Moreover, a fair fraction of NEAs are not solitary but compose binary systems (e.g. Merline *et al.* 2003). All these factors could invalidate the very simplified analytical approach and need to be considered for a high-accuracy YE computation.

Formulation of the heat diffusion problem.– In general, a fully 3D formulation of the HDP is needed to characterize the temperature inside and on the surface of a body. However, since we assume external energy sources only (such as impinging sunlight), in the most relevant situations the body consists of an isothermal core with temperature variations occurring in a thin surface slab. In that case, one can adopt a simplified, 1D approach with temperature $T(t,z)$ dependent on the depth z below the surface and time t (for an early formulation see Wesselink 1948). This is justified when the penetration depth of the most important thermal wave (diurnal or seasonal) is significantly smaller than the size of the body. Bodies larger than $\simeq 20$ m generally meet this condition, unless a very high thermal inertia†. The HDP is thus solved for each of the (infinitesimal) surface elements separately, as if there were no thermal communication between them through latitudinal thermal gradients.

The heat diffusion equation now reads

$$\rho C \frac{\partial T}{\partial t} = \frac{\partial}{\partial z}\left(K \frac{\partial T}{\partial z} \right) , \tag{2.1}$$

where ρ is the density, C is the specific heat capacity and K is the thermal conductivity, all of which might be temperature dependent. If this effect is taken into account, we

† An exceptional group of very small NEAs, such as 1998 KY26 or 2003 YN107, may require a full-fledged 3D analysis as in Spitale & Greenberg (2000).

use empirical fits to laboratory and/or space measurements (e.g. Wechsler *et al.* 1972; Yomogida & Matsui 1983).

The system (2.1) must be supplemented with boundary conditions to make the solution unique. In the space coordinate this means (i) energy input on the surface, and (ii) constancy of the temperature at large depth; put in mathematics we have

$$\varepsilon\sigma T^4(t,0) = K\frac{\partial T}{\partial z}(t,0) + E(t)\ , \tag{2.2}$$

$$\frac{\partial T}{\partial z}(t,\infty) = 0\ , \tag{2.3}$$

where we explicitly made clear depth z of the boundary. Here ε is the surface infrared emissivity, σ the Stephan-Boltzmann constant and $E = (1-A)\Phi(\mathbf{n}\cdot\mathbf{n}_0)$ is the radiative energy flux through the surface element; A is the albedo value in optical, Φ the incident solar radiation flux, $\mathbf{n}$ is the external unitary normal vector to the surface facet and $\mathbf{n}_0$ is the local direction to the Sun. We note E is nil, when $\mathbf{n}\cdot\mathbf{n}_0 < 0$ and also when another part of the body casts a shadow onto the chosen surface element (see below).

In the time coordinate we impose periodicity after interval P, thus $T(t,z) = T(t+P,z)$ for all grid nodes. After the period P the body must be brought into the same conditions, namely experience the same exterior radiation field. In practice this means to be at the same phase of revolution about the Sun and to have the same orientation in space. Though most asteroids of interest are in the principal-axis rotation mode, their rotation and revolution periods are not necessarily commensurate. However, the rotation period $P_{\rm rot}$ is usually much shorter than the revolution period $P_{\rm rev}$ and it is without loss of accuracy in evaluation of the YE to slightly modify $P_{\rm rot}$ in order to become commensurate with $P_{\rm rev}$. Then $P = P_{\rm rev}$. A more tricky situation occurs for a special class of tumbling asteroids (e.g. Pravec *et al.*, 2004), for which their orientation in space might not repeat at any time. Luckily, near-repetitions are usually found and they could be made commensurate with $P_{\rm rev}$; see Sec. 3 for an example.

We note that scaled, rather than physical, variables are best suitable in our problem. Depth z is expressed in terms of the penetration depth $h_T = \sqrt{KP_{\rm rot}/2\pi\rho C}$ of the diurnal thermal wave, thus introducing $z' = z/h_T$. Time t is replaced with the mean anomaly ℓ of the orbital motion. The "isothermal-core" condition (2.3) is applied at typically $10-15$ penetration depths of the seasonal thermal wave ($= \sqrt{P_{\rm rev}/P_{\rm rot}}\,h_T$), and the solution is (multiply) 2π periodic in the ℓ variable. Standard discretization methods are used to represent the heat diffusion equation (2.1) and Spencer *et al.* (1989) scheme is used for the non-linear surface boundary condition (2.2). An isothermal initial seed in the whole mesh quickly converges to the desired solution, though faster convergence is achieved when analytical approximation are used (such as in Wesselink 1948). We stop iterations of the numerical solution when a fractional change in temperature of all surface elements between two successive iterations is smaller than 10^{-4}.

Rotation state.– The surface energy input function $E(t)$ in (2.2) is computed from the known position of the Sun with respect to the surface element and it is a function of the asteroid orbit and its orientation in space. The latter is expressed using a rotation matrix $\mathbf{R}$ that refers body-fixed frame to an inertial frame. In general $\mathbf{R}$ may be parametrized by three Euler angles; for principal-axis rotators those depend on pole position, rotation period and epoch of local meridian,† while for tumbling asteroids the Euler

† In fact the result only weakly depends on the phase of local meridian at a given time, so that this information may be waived and replaced with an arbitrary zero value.

equations are numerically integrated with given initial data (e.g. Landau and Lifschitz 1976; Kryszczyńska *et al.* 1999).

Shape/shadowing.– We use polyhedron representation of the asteroid shape with typically several thousands triangular surface elements. These models are mostly due to radar sensing analysis, to lesser extend due to direct satellite reconnaissance and/or lightcurve inversion (data are generally available at the PDS node `http://www.psi.edu/pds/archive/rshape.html`). Solution of the HDP is preceded with a preliminary analysis, where we store in computer memory all combinations of mutual shadowing effects of different parts of the asteroid. This information is used for evaluation of the energy source function $E(t)$ in (2.2).

Yarkovsky force.– Once the surface temperature is determined by the numerical analysis described above, we compute components of the Yarkovsky force. For an oriented surface facet $d\mathbf{S} = \mathbf{n}\,dS$ their infinitesimal values read (see e.g. Milani *et al.* 1987)

$$d\mathbf{f}(\ell) = -\frac{2}{3}\frac{\varepsilon\sigma T^4(\ell,0)}{c}\,\mathbf{n}\,dS\,, \tag{2.4}$$

where the isotropic (Lambert) thermal emission is used. Total force† components are expressed as a sum of partial results for all surface elements and they are exported in an output file (with an appropriate header describing model parameters). In complex situations, like those discussed below, we export the resulting force components once every fraction of the diurnal cycle (typically $20 - 200$ times per asteroid rotation). In the case of solitary asteroids with principal-axis rotation, we further locally average over a diurnal cycle, making roughly $100 - 500$ normal points of the Yarkovsky force components per asteroid's revolution about the Sun. This procedure makes then the orbit determination faster.

Data and their availability.– Examples of our results are available through the `http://sirrah.troja.mff.cuni.cz/~davok/` web site where we also maintain a page coordinating efforts for the future YE detections.

3. Two examples

In what follows we briefly discuss results for two cases that require a high-accuracy YE computation. More details can be found in Vokrouhlický *et al.* (2004a,b).

Toutatis: a tumbling asteroid.– Toutatis was the first asteroid for which the non-principal-axis (tumbling) rotation state was discovered and accurately determined (Hudson & Ostro 1995). With the orbit residing near the 1/4 exterior mean motion resonance with the Earth, Toutatis undergoes frequent close Earth encounters during a couple of decades and this might permit YE to be detected (Vokrouhlický *et al.* 2004a). Accurate radar astrometry was acquired in 1992 and 1996 (Ostro *et al.* 1999), and a single Doppler measurement from 2000 is less useful but still makes a valuable constraint on the orbit. A spectacularly close encounter which occurs late September 2004 may give the first opportunity to detect YE (Vokrouhlický *et al.* 2004a), with further refinements during 2008 and 2012 encounters (all within the reach of the current radar systems; see `http://echo.jpl.nasa.gov/`).

As noted in Sec. 1, a productive use the YE measurement requires ability of a high

† We also standardly compute total thermal torque $d\mathbf{t} = \mathbf{r} \times d\mathbf{f}$ ($\mathbf{r}$ is the position vector of the surface element) affecting body's rotation, the so called YORP effect; e.g. Bottke *et al.* (2003). As an example, this has been used for prediction of the YORP observability in the case of asteroid (25143) Itokawa (Vokrouhlický *et al.* 2004c).

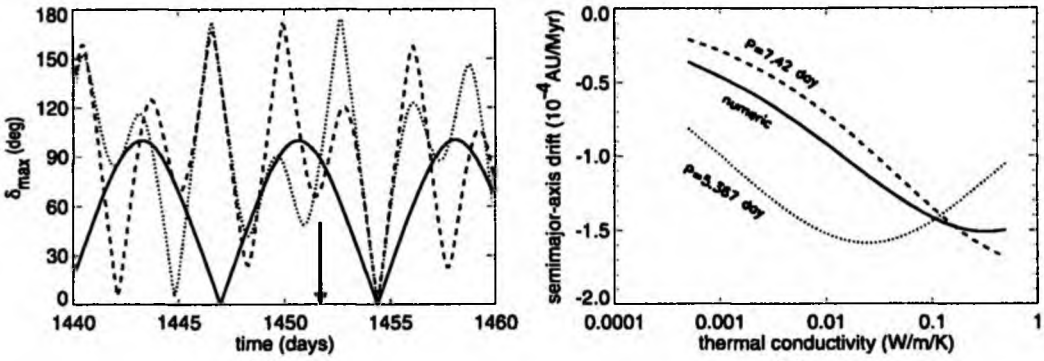

Figure 1. *Part a*: The angle between body principal axes at the initial epoch and time t (abscissa; in days): (i) solid for the longest axis, (ii) dotted for the middle axis, and (iii) dashed for the shortest axis. There is a sharp minimum in all angles at time $\simeq$ 1454.4 d, meaning a near coincidence with the initial-epoch orientation (better than 0.5°; initial epoch from Ostro *et al.* 1999). The arrow indicates orbital period. *Part b*: Estimated mean drift rate of the semimajor axis of Toutatis orbit due to the YE as a function of the surface thermal conductivity. Solid curve from the high-accuracy model, dashed and dotted curves from a simplified analytic approach assuming a spherical body with two characteristic periods: (i) 5.367 d (dotted), and (ii) 7.42 d (dashed); this model assumes spin axis along the total angular momentum of Toutatis.

accuracy Yarkovsky force computation. This appears non-trivial for elongated and tumbling Toutatis. The particular trouble for this body is its non-axial rotation: spin vector wobbles around the longest body axis in 5.367 d (in the body-fixed frame) and the longest body axis precesses around the nearly conserved total angular momentum in 7.42 d (in the inertial frame). Both motions are slow, which means the diurnal thermal lag is small and this strengthens requirements on accurate prediction of the YE magnitude. As for the boundary condition issue we note Toutatis undergoes a near repetition of its space orientation in $\simeq$ 1454.4 d, remarkably close to the orbital period $P_{\rm rev} \simeq 1451.7$ d (Fig. 1a). Except an unlikely case of random coincidence, we do not have explanation for this interesting commensurability that may warrant future theoretical work. It appears important for our work, since we can take $P = P_{\rm rev}$ for the periodicity of the temperature solution.

We use a high-quality polyhedral model with 12 796 triangular facets adopted from `http://www.psi.edu/pds/archive/rshape.html`. Surface parameters are as follows: the mean density $\rho = 2\,{\rm g/cm^3}$, the mean specific thermal capacity $C = 800\,{\rm J/kg/K}$, the surface albedo $A = 0.1$ and the mean thermal conductivity varied in the interval $K = 0.0005 - 0.5$ W/m/K (though we consider $\simeq 0.01$ W/m/K the most likely value, compatible with the estimated thermal inertia reported by Howell *et al.* (1994)). When converting the Yarkovsky force to acceleration components, we adopt a bulk density $\rho_b = 2.6\,{\rm g/cm^3}$, slightly higher than ρ (presumably affected by surface microporosity).

Figure 1b shows the resulting mean rate of change of Toutatis' semimajor axis due to the YE as a function of the poorly constrained surface conductivity K. Because of the slow rotation the YE strength drops for small values of K. For interest, we also show prediction of the linearized analytical theory that would assume an equivalent spherical body uniformly rotating about the direction of Toutatis angular momentum with two characteristic periods. Interestingly, the 7.42 d period does a fairly good job, especially for high conductivity values. Adopting $K = 0.01$ W/m/K we predict the YE displacement should exceed during the early October 2004 a 3σ formal orbit-determination error due to uncertainty in observations, thus being possibly detectable at a statistically significant level (more details in Vokrouhlický *et al.* (2004a)). It is, however, yet to be verified that

Pravec, P., Harris, A.W., Scheirich, P., Kušnirák, P., Šarounová, L., Hergenrother, C.W., Mottola, S., Hicks, M.D., Masi, G., Krugly, Y.N., Shevchenko, V.G., Nolan, M.C., Howell, E.S., Kaasalainen, M., Galád, A., Brown, P., DeGraff, D.R., Lambert, J.V., Cooney, W.R. & Foglia, S. 2004, *Icarus*, in press

Spencer, J.R., Lebofsky, L.A. & Sykes, M.V. 1989 *Icarus* 78, 337

Spitale, J.N. & Greenberg, R. 2000, *Icarus* 149, 222

Tsiganis, K., Varvoglis, H. & Morbidelli, A. 2003, *Icarus* 166, 131

Vokrouhlický, D. 1998, *Astron. Astrophys.* 335, 1093

Vokrouhlický, D. 1999, *Astron. Astrophys.* 344, 362

Vokrouhlický, D. & Farinella, P. 1999, *Astron. J.* 118, 3049

Vokrouhlický, D. & Milani, A. 2000, *Astron. Astrophys.* 362, 746

Vokrouhlický, D., Milani, A. & Chesley, S.R. 2000, *Icarus* 148, 118

Vokrouhlický, D., Brož, M., Farinella, P. & Knežević, Z. 2001, *Icarus* 150, 78

Vokrouhlický, D., Brož, M., Morbidelli, A., Bottke, W.F., Nesvorný, D., Lazzaro, D. & Rivkin, A.S. 2002, Yarkovsky footprints in the Eos family, abstract 12-01, ACM 2002 meeting in Berlin, p. 115

Vokrouhlický, D., Čapek, D., Chesley, S.R. & Ostro, S.J. 2004a, *Icarus*, in press

Vokrouhlický, D., Čapek, D., Chesley, S.R. & Ostro, S.J. 2004b, *Icarus*, submitted

Vokrouhlický, D., Čapek, D., Kaasalainen, M. & Ostro, S.J. 2004c, *Astron. Astrophys.* 414, L21

Wechsler, A.E., Glaser, P.E., Little, A.D. & Fountain, J.A. 1972, in: Lucas, J.W. (ed.), *Thermal Characteristics of the Moon* (The MIT Press), p. 215

Wesselink A.J. 1948, *Bull. Astron. Inst. Nether.* 10, 351

Yomogida, K. & Matsui, T. 1983, *J. Geophys. Res.* 88, 9513

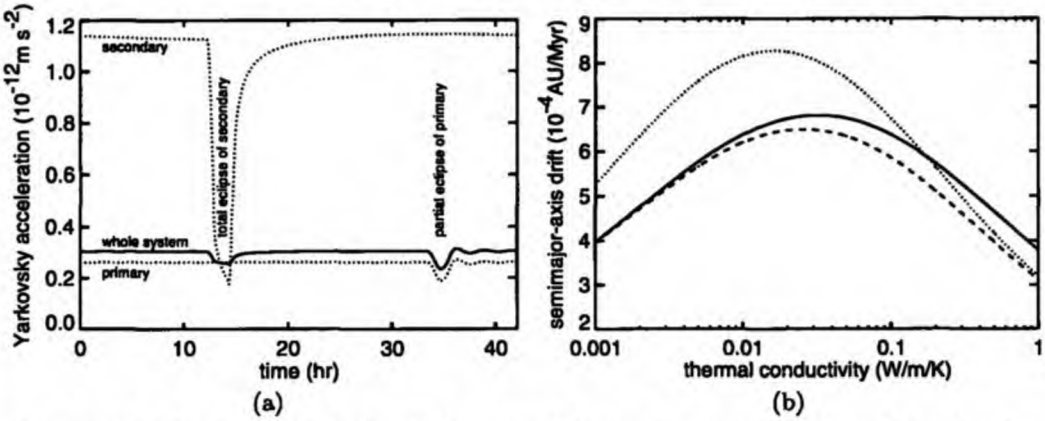

Figure 2. *Part a*: The effect of mutual eclipses between components of 2000 DP107 system: amplitude of the Yarkovsky acceleration during one revolution about their common center of mass. Eclipses produce dips in the signal; smooth variation during the shadow/eclipse entry and exit is due to a finite value of the surface thermal inertia (note the different effects for the fast rotating primary and the slowly rotating secondary asteroid). Solid curve is the effective Yarkovsky acceleration as it appears in the translational motion of the center of mass about the Sun. *Part b*: Drift rate of the orbital semimajor axis of the 2000 DP107 system due to the YE as a function of surface thermal conductivity K: (i) solid curve is for the whole system, (ii) dashed curve is for the primary component only, as if it were a solitary asteroid (no eclipses), and (iii) the dotted curve is for the primary component only and with the analytic formulation of the YE. A fair agreement indicates the effect of the secondary is minor, except for large value of K.

the orbit uncertainty due to gravitational perturbation by asteroids does not prevent the YE detection. This concern is mainly because of a low inclination of Toutatis' orbit (0.44°), thus leading to frequent encounters with many asteroids in the main belt. Assuming the encounter probability scales inversely proportinally with inclination (e.g. Öpik 1951, 1976), we might expect about 5 times larger orbit-uncertainty due to gravitational effects of asteroids than in the case of (6489) Golevka. This latter has been estimated to be about 15 μs in delay measurement (Chesley *et al.* 2003; note the predicted delay displacement due to the YE is in between $15 - 30\,\mu$s in October 2004).

2000 DP107: a binary system.– 2000 DP107 belongs to the $10 - 15\%$ population of binary asteroids among NEAs (e.g. Margot *et al.* 2002; Merline *et al.* 2003). It consists of two components, a primary with estimated size of $\simeq 800$ m and a secondary of $\simeq 300$ m. The primary component exhibits a fast rotation with $P_1 \simeq 2.775$ h, while the secondary component is likely orbit-synchronous with a period of $P_2 \simeq 1.755$ d (in our model we slightly tweaked these values to become commensurable with the orbital period of the system about the Sun, namely P_1 be 1/5034 and P_2 be 1/332 part of that value). The mutual orbit of the two asteroids is quasi-circular with radius of $\simeq 1310$ m. Current data do not allow shape resolution, so that we use spherical models for both components, represented in our model by 1004-facet polyhedra, with spin axes perpendicular to their mutual orbital plane (all data from Margot *et al.* (2002)).

In compact binaries, such as 2000 DP107, mutual eclipses produced by the two asteroids play important role and must be taken into account (Fig. 2a). We accordingly adapted our software to compute simultaneously Yarkovsky force for both asteroids in the system. The C-type classification for the primary component and tracking of mutual motion of the two components suggest lower density of 1.7 g/cm^3 (Margot *et al.* 2002; we assume this value for both surface and bulk density). The specific thermal capacity is taken to be

$\simeq 800\,\mathrm{J/kg/K}$, the surface optical albedo $A = 0.1$, while we again let the surface thermal conductivity to change in a broad range of values $0.001 - 1\ \mathrm{W/m/K}$.

Figure 2b shows the mean drift rate of the semimajor axis of the center of mass orbital motion about the Sun due to the Yarkovsky effect (one easily shows that the effective YE for the center of mass heliocentric motion is given by a mass-weighted mean of the YE on the two asteroids). We note the contribution of the secondary component is small, but not entirely negligible. Not shown here, however, is the role of the YE for motion of the two components about their common center of mass, where the effect on the secondary component plays determining role (see Vokrouhlický *et al.* (2004b) for detailed discussion). With that result, Vokrouhlický *et al.* (2004b) conclude the YE should be comfortably detected for this system during its close encounter in August 2016 provided accurate radar observations are acquired in September 2008.

Acknowledgements

This work was supported by the Grant Agency of the Czech Republic under the contract No. 205/02/0703. We thank Bill Bottke for several useful suggestions that helped to improve the final form of this paper.

References

Bottke, W.F., Vokrouhlický, D., Rubincam, D.P. & Brož, M. 2003, in: Bottke, W.F., Cellino, A., Paolicchi, P. & Binzel, R.P. (eds.), *Asteroids III* (The University of Arizona Press, Tucson), p. 395

Bottke, W.F., Vokrouhlický, D., Brož, M., Nesvorný, D. & Morbidelli, A. 2001, *Science* 294, 1693

Chesley, S.R., Ostro, S.J., Vokrouhlický, D., Čapek, D., Giorgini, J.D., Nolan, M.C., Margot, J-L., Hine, A.A., Benner, L.A.M. & Chamberlin, A.B. 2003, *Science* 302, 1739

Farinella, P. & Vokrouhlický, D. 1999, *Science* 283, 1507

Farinella, P., Vokrouhlický, D. & Hartmann, W.K. 1998, *Icarus* 132, 378

Giorgini, J.D., Ostro, S.J., Benner, L.A.M., Chodas, P.W., Chesley, S.R., Hudson, R.S., Nolan, M.C., Klemola, A.R. Standish, E.M., Jurgens, R.F., Rose, R., Chamberlin, A.B., Yeomans, D.K. & Margot, J.-L. 2002, *Science* 296, 132

Howell, E.S., Britt, D.T., Bell, J.F., Binzel, R.P. & Lebofsky, L.A. 1994, *Icarus* 111, 468

Hudson, R.S. & Ostro, S.J. 1995, *Science* 270, 84

Hudson, R.S., Ostro, S.J. & Scheeres, D.J. 2003, *Icarus* 161, 346

Kryszczyńska, A., Kwiatkowski, T., Breiter, S. & Michałowski, T. 1999, *Astron. Astrophys.* 345, 643

Landau, L.D. & Lifschitz, E.M. 1976, *Mechanics* (3rd Ed.) (Pergamon, Oxford)

Margot, J.-L., Nolan, M.C., Benner, L.A.M., Ostro, S.J., Jurgens, R.F., Giorgini, J.D., Slade, M.A. & Campbell, D.B. 2002, *Science* 296, 1445

Merline, W.J., Weidenschilling, S.J., Durda, D.D., Margot, J.-L., Pravec, P. & Storrs, A.D. 2003, in: Bottke, W.F., Cellino, A., Paolicchi, P. & Binzel, R.P. (eds.), *Asteroids III* (The University of Arizona Press, Tucson), p. 289

Milani, A., Nobili, A.-M. & Farinella, P. 1987, *Non-gravitational Perturbations and Satellite Geodesy* (A. Hilger, Bristol)

Morbidelli, A. & Vokrouhlický, D. 2003, *Icarus* 163, 120

Nesvorný, D. & Bottke, W.F. 2004, *Icarus* 170, 324

Ostro, S.J., Hudson, R.S., Rosema, K.D., Giorgini, J.D., Jurgens, R.F., Yeomans, D.K., Chodas, P.W., Winkler, R., Rose, R., Choate, D., Cormier, R.A., Kelley, D., Littlefair, R., Benner, L.A.M., Thomas, M.L. & Slade, M.A. 1999, *Icarus* 137, 122

Öpik, E.J. 1951, *Proc. Roy. Irish Acad.* 54, 165

Öpik, E.J. 1976, *Interplanetary Encounters* (Amsterdam: Elsevier Press)

Plausible constraint on Golevka's regolith from an accurate Yarkovsky/YORP effect model

David Čapek and David Vokrouhlický

Institute of Astronomy, Charles University,
V Holešovičkách 2, 180000 Prague 8, Czech Republic

Abstract

The Yarkovsky effect, a recoil force due to thermal radiation, is an important perturbation in the dynamics of small Solar System bodies. In an attempt to determine the Yarkovsky force as accurately as possible we develop numerical model capable to remove most of simplifying assumptions of the analytic theories. A novel feature discussed here is a possibility to account for a multi-layer surface structure. Assuming a high-conductivity core we are thus able to constrain thermal and geometric parameters of the surface lower-conductivity slab for the asteroid 6489 Golevka. With that we substantiate conclusions from Chesley et al. (2003) [1] who detected the Yarkovsky effect in its orbit.

Introduction and motivation

The Yarkovsky effect is caused by the pressure of thermal radiation from a surface of an asteroid or meteoroid. A finite value of thermal inertia makes the maximum temperature (thus the thermal recoil force) to be tilted from the direction to the heating source (the Sun). This effect produces a nonzero transverse component of the total radiation force and results in a secular change of the orbital semimajor axis a.

Most of the analytical theories of the Yarkovsky effect require a large number of simplifying assumptions such as the spherical shape, thermal parameters constant, linearization at the heat diffusion problem, circular orbit etc. In spite of all this, their results are useful for problems when statistical behavior of a large sample of bodies is to be determined (e.g. [4]).

Predictions of the analytical theories are, however, questionable when a high-accuracy computation of the Yarkovsky effect is desired (such as with the aim to detect it when applied one particular object). Numerical solution of the heat diffusion problem may relax most of the simplifications mentioned above at the expense of longer computing time. Models with different levels of sophistication are available today (e.g. [5], [6]).

Here we continue this effort by still improving our previous model to account for possible details of the surface composition. In particular, we allow the body to consist of several layers with different thermal properties, such as the high-conductivity core buried under a slab of low-conductivity surface layer (regolith of just fragmented/porous region). Previous models required constant thermal parameters.

We test implications of such an improved Yarkovsky force computation in the case of 6489 Golevka. Chesley et al. [3] succeeded to detect the Yarkovsky effect in the orbit of this small asteroid using precise radar astrometry data. Observationally, the effect amounted to ~ 15 km displacement from the Arecibo dish in May 2003 as compared to the standard (non-Yarkovsky) ephemerides. This effect fully stems from a non-zero secular drift of Golevka's semimajor axis of $\langle da/dt \rangle \sim -5.5 \times 10^{-4}$ AU/My.

The numerical model description

Shape model

The best available model of 6489 Golevka is a triangulated 4092 polyhedron derived from Arecibo radar ranging ([7]; see *http://echo.jpl.nasa.gov/links.html*). To speed the computations we also use an acceptable approximation with a uniform 248-hedron of the same volume as Golevka.

Physical parameters

Our working hypothesis assumes a low-conductivity (and density) particulated surface layer covering a high-conductivity core composed of a fresh basalt. Thus the thermal conductity of the core is set to be 2.5 W/m/K, while the surface layer has $K = A + BT^3$ with tested values A=0.001-0.1 W/m/K and B=2x10^{-11}W/m/K^4 (e.g. [2]). The core and the surface layer have assumed bulk densities of 2.5 g/cm^3 and 1.7 g/cm^3. The specific heat capacity C is also assumed temparature-dependent as given in the literature (e.g. [2]).

One-dimensional approximation for HDE

We use 1-D approximation of the heat diffusion problem. Thus the temperature T is computed separately for each of the surface elements and it depends on time t and depth z only. This is justified when neighboring elements do not thermally communicate enough. The size of the body D must be (much) larger than the penetration depth of the lowest frequency (seasonal) themal wave. For a basaltic body at ~ 2 AU heliocentric distance this turns out to constrain D > 50-100 m.

Crank-Nicholson scheme

used here is a unconditionally stable implicit solver of the diffusion problem. Temperature profile in the next timestep T^{l+N} is determined by solving a set of linear equations (together with boundary conditions):

$$\boldsymbol{D}\ T^{l+N} = R,$$

where $\boldsymbol{D}$ is a tridiagonal matrix and R is a vector. The main problem here is, that $\boldsymbol{D}$, as well as R, depend on an unknown temperature T^{l+N}; this occurs because of temperature-depedence of the thermal parameters (see above). We solve this problem, as well as the non-linear surface boundary condition, iteratively, taking $T^{l+N} = T^l$ in the first step.

Boundary conditions

The first, usually linearized in analytic theories, follows from energy balance between incoming, conducted and re-radiated energy at the surface. The second is constant temperatute in the core (at large depth). Finally we assume that orientation of the body with respect to the Sun is periodic, thus repeats after some interval of time P (usually equal to the revolution period).

The space and time steps

We use constant timestep Δt=300s, and spatial step exponentially increasing according to $\Delta z_k = \Delta z_0 \exp(0.1\ k)$, where Δz_0=0.01mm.

Yarkovsky thermal force

When the temperature T of all surface elements has been computed, a recoil force due to thermal radiation is determined by

$$f = \int df, \quad df = -2\sigma/(3c)T^4 n\ dS,$$

where c is speed of light, n is the unit vector normal to the surface and dS is the area of the surface element.

Results

We studied the influence of depth and thermal conductivity of the surface layer on the Yarkovsky semimajor axis drift da/dt for 6489 Golevka. Our results are summarized in the following two plots:

Figure 1 shows dependance of da/dt on the surface layer depth for three values of its conductivity parameter A (see the label).

Figure 2 describes dependance of da/dt on both the thermal conductivity parameter A and the depth of the surface layer. The thick solid line is a penetration depth of the diurnal temperation variations l_d and the dashed lines correspond to 1/4 l_d and 4 l_d. The value of da/dt=-5.5x10^{-4}AU/My, together with its 10% uncertainty interval, is marked by the thick contour and the dotted area respectively.

Results in Fig. 2 indicate that when the surface layer > 10 l_d, about an meter deep for all A, the value of da/dt is the same as it would correspond to the A conductivity value in a model with constant thermal parameters used previously (in either analytical [3] or numerical [1] approaches). Conversely, when the thickness of the surface layer shrinks to zero, da/dt becomes ~ -3x10^{-4}AU/My corresponding the A=2.5W/m/K uniform model.

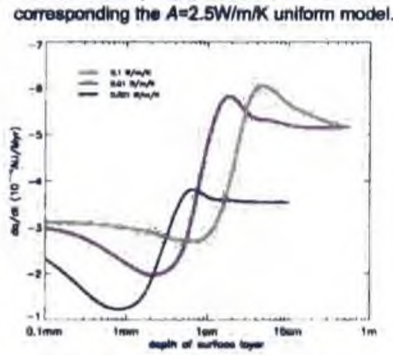

Figure 1: Yarkovsky semimajor axis drift as a function of the surface layer depth. See the text for details.

These two limiting regimes are connected with a transition zone of a non-trivial da/dt behavior. The most steep variations occur when the depth of the surface layer is ~l_d (Fig. 2).

Figure 2 results may be used to a correlated determination of A and the surface layer depth h provided a certain value of da/dt is known. In the case of 6489 Golevka the region of admissible (A,h)-values is highlighted by the dotted area in Fig. 2.

Conclusions

- Our experiments indicate that the radiative term BT^3 in thermal conductivity K is not critical in evaluation of Golevka's semimajor axis drift da/dt. Droping this term from our analysis would significantly speed the computations.
- Low-conductivity surface layer may significantly change the resulting da/dt value if its depth is comparable to the penetration depth of the diurnal thermal wave (1-10 cm).
- If Golevka's interior is consistent with our assumption, high-conductivity basalt rock, our results constrain its surface parameters. In particular, its thermal parameter A>0.004 W/m/K and its depth larger than 1 cm. The infered A-value excludes a possibility of having regolith layer on Golevka, since its thermal conductivity would be still lower than our minimum value. The surface of Golevka is likely a highly porous rock.

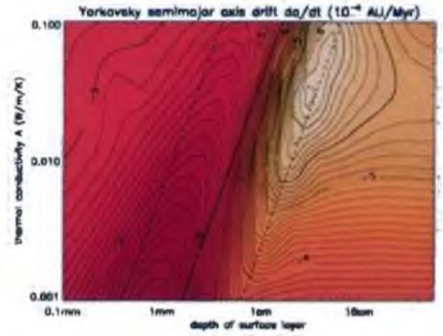

Figure 2: Yarkovsky semimajor axis drift as a function of the surface layer depth and thermal conductivity parameter A. Labels are da/dt values in 10^{-4}AU/My. See the text for details.

References

[1] S.R. Chesley, S.J. Ostro, D. Vokrouhlický et al., *Science* **302**, 1739 (2003)
[2] M.L. Urquhart, S.M. Jakosky, *J. Geophys. Res.*, **102**, 10969 (1997)
[3] D. Vokrouhlický, *Astron. Astrophys.* **344**, 362 (1999)
[4] W.F. Bottke, D.Vokrouhlický, D.P. Rubincam, M. Brož, in *Asteroids III*, University of Arizona Press, p. 395 (2002)
[5] J. Spitale, R. Greenberg, *Icarus*, **149**, 222 (2001)
[6] D. Čapek, D. Vokrouhlický, in *Dynamics of Populations of Planetary Systems*, Cambridge University Press, p. 171 (2005)
[7] R.S. Hudson, S.J. Ostro, R.F. Jurgens, et al., *Icarus*, **148**, 37 (2000)

Bibliography

[Bertotti et al., 2003] Bertotti, B., Farinella, P. and Vokrouhlický, D. (2003). *Physics of the Solar system (Dynamics and evolution, space physics, and spacetime structure)*. Kluwer Academic Press, Dordrecht.

[Bottke et al., 2001] Bottke, W. F., Vokrouhlický, D., Brož, M., Nesvorný, D., and Morbidelli, A. (2001). Dynamical spreading of asteroid families by the Yarkovsky effect. *Science*, 294:1693–1696.

[Bottke et al., 2002] Bottke, W. F., Morbidelli, A., Jedicke, R., Petit, J.-M., Levison, H. F., Michel, P. and Metcalfe, T. S. (2002). Debiased orbital and absolute magnitude distribution of the near-Earth objects. *Icarus*, 156:399–433.

[Breiter et al., 2007] Breiter, S., Michalska, H., Vokrouhlický, D. and Borczyk, W. (2007). Radiation induced torques on spheroids. *Astronomy and Astrophysics*, 471:345–354.

[Brož, 2006] Brož, M. (2006). *Yarkovsky effect and the dynamics of the Solar System. PhD thesis.* Charles University, Prague. (http://sirrah.troja.mff.cuni.cz/~mira/mp/phdth/).

[Burns and Safronov, 1973] Burns, J. A. and Safronov, V. S. (1973). Asteroid nutation angles. *Monthly Notices of the Royal Astronomical Society*, 165:403–411.

[Burns et al., 1979] Burns, J. A., Lamy, P. L. and Soter, S. (1979). Radiation forces on small particles in the solar system. *Icarus*, 40:1–48.

[Čapek and Vokrouhlický, 2002] Čapek, D. and Vokrouhlický, D. (2002). Yarkovsky force and torque on Gaussian random spheres. Poster at *Asteroids, Comets and Meteors*, Berlin, Germany.

[Čapek and Vokrouhlický, 2004] Čapek, D. and Vokrouhlický, D. (2004). The YORP effect with finite thermal conductivity. *Icarus*, 172:526–536.

[Čapek and Vokrouhlický, 2005a] Čapek, D. and Vokrouhlický, D. (2005a). Accurate model for the Yarkovsky effect. In Knežević, Z. and Milani, A., editors, *IAU Colloq. 197: Dynamics of Populations of Planetary Systems*, pages 171–178.

[Čapek and Vokrouhlický, 2005b] Čapek, D. and Vokrouhlický, D. (2005b). Plausible constraint on Golevka's regolith from an accurate Yarkovsky/YORP effect model. Poster at *Asteroids, Comets and Meteors*, Búzios, Rio de Janeiro, Brazil.

[Chesley et al., 2003] Chesley, S. R., Ostro, S. J., Vokrouhlický, D., Čapek, D., Giorgini, J. D., Nolan, M. C., Margot, J.-L., Hine, A. A., Benner, L. A. M. and Chamberlin, A. B. (2003). Direct detection of the Yarkovsky effect by radar ranging to asteroid 6489 Golevka. *Science*, 302:1739–1742.

[Chesley et al., 2006] Chesley, S. R., Vokrouhlický, D. and Matson, R. D. (2006). Direct measurement of the Yarkovsky effect acting on near-Earth asteroid 1992 BF. In *Bull. Am. Astron. Soc.*, volume 38, page 591.

[Cremers, 1972] Cremers, C. J. (1972). Thermal conductivity of Apollo 12 fines at intermediate density. *Moon*, 4:88.

[Davies et al., 1996] Davies, M. E., Colvin, T. R., Belton, M. J. S., Veverka, J. and Thomas, P. C. (1996). The direction of the north pole and the control network of asteroid 243 Ida. *Icarus*, 120:33–37.

[Delbò et al., 2006] Delbò, M., dell'Oro, A., Harris, A. W., Mottola, S. and Mueller, M. (2006). Thermal inertia of near-Earth asteroids and strength of the Yarkovsky effect. In *Bull. Am. Astron. Soc.*, volume 38, pages 581–582.

[Delbò et al., 2007] Delbò, M., dell'Oro, A., Harris, A. W., Mottola, S. and Mueller, M. (2007). Thermal inertia of near-Earth asteroids and implications for the magnitude of the Yarkovsky effect. *Icarus*, in press.

[Demura et al., 2006] Demura, H., Kobayashi, S., Nemoto, E., Matsumoto, N., Furuya, M., Yukishita, A., Muranaka, N., Morita, H., Shirakawa, K., Maruya, M., Ohyama, H., Uo, M., Kubota, T., Hashimoto, T., Kawaguchi, J., Fujiwara, A., Saito, J., Sasaki, S., Miyamoto, H. and Hirata, N. (2006). Pole and global shape of 25143 Itokawa. *Science*, 312:1347–1349.

[Dobrovolskis, 1996] Dobrovolskis, A. R. (1996). Inertia of any polyhedron. *Icarus*, 124:698–704.

[Ďurech, 2005] Ďurech, J. (2005). 433 Eros - comparison of lightcurve extrema from 1901-1931 with the present rotation state. *Astronomy and Astrophysics*, 431:381–383.

[Efroimsky and Lazarian, 2000] Efroimsky, M. and Lazarian, A. (2000). Inelastic dissipation in wobbling asteroids and comets. *Monthly Notices of the Royal Astronomical Society*, 311:269–278.

[Farinella et al., 1998] Farinella, P., Vokrouhlický, D. and Hartmann, W. K. (1998). Meteorite delivery via Yarkovsky orbital drift. *Icarus*, 132:378–387.

[Farinella et al., 1992] Farinella, P., Davis, D. R., Paolicchi, P., Cellino, A. and Zappalà, V. (1992). Asteroid collisional evolution - an integrated model for the evolution of asteroid rotation rates. *Astronomy and Astrophysics*, 253:604–614.

[Gaskell et al., 2006] Gaskell, R., Saito, J., Ishiguro, M., Kubota, T., Hashimoto, T., Hirata, N., Abe, S., Barnouin-Jha, O. S. and Scheeres, D. (2006). Global topography of asteroid 25143 Itokawa. In Mackwell, S. and Stansbery, E., editors, *37th Annual Lunar and Planetary Science Conference*, page 1876.

[Giorgini et al., 2002] Giorgini, J. D., Ostro, S. J., Benner, L. A. M., Chodas, P. W., Chesley, S. R., Hudson, R. S., Nolan, M. C., Klemola, A. R., Standish, E. M., Jurgens, R. F., Rose, R., Chamberlin, A. B., Yeomans, D. K. and Margot, J.-L. (2002). Asteroid 1950 DA's Encounter with Earth in 2880: Physical Limits of Collision Probability Prediction. *Science*, 296:132–136.

[Hamilton and Matson, 1987] Hamilton, R. H. and Matson, D. L. (1987). Thermal effects of insolation propagation into the regoliths of airless bodies. *Icarus*, 72:84–94.

[Helin et al., 1991] Helin, E., Lawrence, K., Rose, P. and Williams, G. (1991). 1991 JX. *IAU Circ.*, 5268:1.

[Hudson and Ostro, 1995] Hudson, R. S. and Ostro, S. J. (1995). Shape and non-principal axis spin state of asteroid 4179 Toutatis. *Science*, 270:84–86.

[Hudson and Ostro, 1999] Hudson, R. S. and Ostro, S. J. (1999). Physical Model of asteroid 1620 Geographos from radar and optical data. *Icarus*, 140:369–378.

[Hudson et al., 2000] Hudson, R. S., Ostro, S. J., Jurgens, R. F., Rosema, K. D., Giorgini, J. D., Winkler, R., Rose, R., Choate, D., Cormier, R. A., Franck, C. R., Frye, R., Howard, D., Kelley, D., Littlefair, R., Slade, M. A., Benner, L. A. M., Thomas, M. L., Mitchell, D. L., Chodas, P. W., Yeomans, D. K., Scheeres, D. J., Palmer, P., Zaitsev, A., Koyama, Y., Nakamura, A., Harris, A. W. and Meshkov, M. N. (2000). Radar observations and physical model of asteroid 6489 Golevka. *Icarus*, 148:37–51.

[Hudson et al., 2003] Hudson, R. S., Ostro, S. J. and Scheeres, D. J. (2003). High-resolution model of asteroid 4179 Toutatis. *Icarus*, 161:346–355.

[Isachenko et al., 1969] Isachenko, V., Osipova, V. and Sukomel, A. (1969). *Heat transfer*. Mir publishers, Moscow.

[Kaasalainen et al., 2003] Kaasalainen, M., Kwiatkowski, T., Abe, M., Piironen, J., Nakamura, T., Ohba, Y., Dermawan, B., Farnham, T., Colas, F., Lowry, S., Weissman, P., Whiteley, R. J., Tholen, D. J., Larson, S. M., Yoshikawa, M., Toth, I. and Velichko, F. P. (2003). CCD photometry and model of MUSES-C target (25143) 1998 SF36. *Astronomy and Astrophysics*, 405:L29–L32.

[Kaasalainen et al., 2007] Kaasalainen, M., Ďurech, J., Warner, B. D., Krugly, Y. N. and Gaftonyuk, N. M. (2007). Acceleration of the rotation of asteroid 1862 Apollo by radiation torques. *Nature*, 446:420–422.

[Kryszczyńska et al., 1999] Kryszczyńska, A., Kwiatkowski, T., Breiter, S. and Michałowski, T. (1999). Relation between rotation and lightcurve of 4179 Toutatis. *Astronomy and Astrophysics*, 345:643–645.

[La Spina et al., 2004] La Spina, A., Paolicchi, P., Kryszczyńska, A. and Pravec, P. (2004). Retrograde spins of near-Earth asteroids from the Yarkovsky effect. *Nature*, 428:400–401.

[Lowry et al., 2007] Lowry, S. C., Fitzsimmons, A., Pravec, P., Vokrouhlický, D., Boehnhardt, H., Taylor, P. A., Margot, J.-L., Galád, A., Irwin, M., Irwin, J. and Kusnirák, P. (2007). Direct Detection of the Asteroidal YORP Effect. *Science*, 316:272–.

[Margot et al., 2002] Margot, J. L., Nolan, M. C., Benner, L. A. M., Ostro, S. J., Jurgens, R. F., Giorgini, J. D., Slade, M. A. and Campbell, D. B. (2002). Binary asteroids in the near-Earth object population. *Science*, 296:1445–1448.

[Miller et al., 2002] Miller, J. K., Konopliv, A. S., Antreasian, P. G., Bordi, J. J., Chesley, S., Helfrich, C. E., Owen, W. M., Wang, T. C., Williams, B. G., Yeomans, D. K. and Scheeres, D. J. (2002). Determination of shape, gravity, and rotational state of asteroid 433 Eros. *Icarus*, 155:3–17.

[Morbidelli and Vokrouhlický, 2003] Morbidelli, A. and Vokrouhlický, D. (2003). The Yarkovsky-driven origin of near-Earth asteroids. *Icarus*, 163:120–134.

[Mottola et al., 1997] Mottola, S., Erikson, A., Harris, A. W., Hahn, G., Neukum, G., Buie, M. W., Sears, W. D., Harris, A. W., Tholen, D. J., Whiteley, R. J., Magnusson, P., Piironen, J., Kwiatkowski, T., Borczyk, W., Howell, E. S., Hicks, M. D., Fevig, R., Krugly, Y. N.,

Velichko, F. P., Chiorny, V. G., Gaftonyuk, N. M., di Martino, M., Pravec, P., Sarounova, L., Wolf, M., Worman, W., Davies, J. K., Schober, H.-J., and Pych, W. (1997). Physical model of near-Earth asteroid 6489 golevka (1991 JX) from optical and infrared observations. *The Astronomical Journal*, 114:1234–1245.

[Muinonen, 1996] Muinonen, K. (1996). Light scattering by gaussian random particles. *Earth, Moon and Planets*, 72:339–342.

[Muinonen, 1998] Muinonen, K. (1998). Introducing the gaussian shape hypothesis for asteroids and comets. *Astronomy and Astrophysics*, 332:1087–1098.

[Muinonen and Lagerros, 1998] Muinonen, K. and Lagerros, J. S. V. (1998). Inversion of shape statistics for small solar system bodies. *Astronomy and Astrophysics*, 333:753–761.

[Nesvorný and Bottke, 2004] Nesvorný, D. and Bottke, W. F. (2004). Detection of the Yarkovsky effect for main-belt asteroids. *Icarus*, 170:324–342.

[Nesvorný and Vokrouhlický, 2007] Nesvorný, D. and Vokrouhlický, D. (2007). Analytic theory of the YORP effect for near-spherical objects. *The Astronomical Journal*, in press.

[Öpik, 1951] Öpik, E. J. (1951). Collision probability with the planets and the distribution of planetary matter. *Proc. R. Irish Acad. Sect. A*, 54:165–199.

[Ostro et al., 1991] Ostro, S. J., Harmon, J. K., Hine, A. A., Perillat, P., Campbell, D. B., Chandler, J. F., Shapiro, I. I., Jurgens, R. F. and Yeomans, D. K. (1991). High-resolution radar ranging to near-Earth asteroids. In *Bulletin of the American Astronomical Society*, volume 23, page 1144.

[Ostro et al., 1999a] Ostro, S. J., Hudson, R. S., Rosema, K. D., Giorgini, J. D., Jurgens, R. F., Yeomans, D. K., Chodas, P. W., Winkler, R., Rose, R., Choate, D., Cormier, R. A., Kelley, D., Littlefair, R., Benner, L. A. M., Thomas, M. L. and Slade, M. A. (1999). Asteroid 4179 Toutatis: 1996 radar observations. *Icarus*, 137:122–139.

[Ostro et al., 1999b] Ostro, S. J., Pravec, P., Benner, L. A. M., Hudson, R. S., Šarounov, L., Hicks, M. D., Rabinowitz, D. L., Scotti, J. V., Tholen, D. J., Wolf, M., Jurgens, R. F., Thomas, M. L., Giorgini, J. D., Chodas, P. W., Yeomans, D. K., Rose, R., Frye, R., Rosema, K. D., Winkler, R. and Slade, M. A. (1999). Radar and optical observations of asteroid 1998 KY26. *Science*, 285(5427):557–559.

[Ostro et al., 2004] Ostro, S. J., Benner, L. A. M., Nolan, M. C., Magri, C., Giorgini, J. D., Scheeres, D. J., Broschart, S. B., Kaasalainen, M., Vokrouhlický, D., Chesley, S. R., Margot, J.-L., Jurgens, R. F., Rose, R., Yeomans, D. K., Suzuku, S. and de Jong, E. M. (2004). Radar observations of asteroid 25143 Itokawa (1998 SF36). *Meteoritics and Planetary Science*, 39:407–424.

[Ostro et al., 2006] Ostro, S. J., Margot, J.-L., Benner, L. A. M., Giorgini, J. D., Scheeres, D. J., Fahnestock, E. G., Broschart, S. B., Bellerose, J., Nolan, M. C., Magri, C., Pravec, P., Scheirich, P., Rose, R., Jurgens, R. F., De Jong, E. M. and Suzuki, S. (2006). Radar imaging of binary near-Earth asteroid (66391) 1999 KW4. *Science*, 314:1276–1280.

[Paddack, 1969] Paddack, S. J. (1969). Rotational bursting of small celestial bodies: Effects of radiation pressure. *Journal of Geophysical Research*, 74:7379–4381.

[Peterson, 1976] Peterson, C. (1976). A source mechanism for meteorites controlled by the Yarkovsky effect. *Icarus*, 29:91–111.

[Press et al., 1992] Press, W. H., Teukolsky, S. A., Vetterling, W. T. and Flannery, B. P. (1992). *Numerical recipes, 2nd edition.* Cambridge University Press, New York.

[Radzievskii, 1952] Radzievskii, V. V. (1952). A mechanism for the disintegration of asteroids and meteorites. *Astron. Zh.*, 29:162–170.

[Radzievskii, 1954] Radzievskii, V. V. (1954). A mechanism for the disintegration of asteroids and meteorites. *Dokl. Akad. Nauk SSSR*, 97:49–52.

[Robie et al., 1970] Robie, R. A., Hemingway, B. S. and Wilson, W. H. (1970). Specific heats of lunar surface materials from 90° to 350°K. *Geochimica et Cosmochimica Acta Supplement*, 1:2361.

[Rubincam, 1987] Rubincam, D. P. (1987). LAGEOS orbit decay due to infrared radiation from Earth. *Journal of Geophysical research*, 92:1287–1294.

[Rubincam, 1990] Rubincam, D. P. (1990). Drag on the Lageos satellite. *Journal of Geophysical research*, 95:4881–4886.

[Rubincam, 2000] Rubincam, D. P. (2000). Radiative spin-up and spin-down of small asteroids. *Icarus*, 148:2–11.

[Saito et al., 2006] Saito, J., Miyamoto, H., Nakamura, R., Ishiguro, M., Michikami, T., Nakamura, A. M., Demura, H., Sasaki, S., Hirata, N., Honda, C., Yamamoto, A., Yokota, Y., Fuse, T., Yoshida, F., Tholen, D. J., Gaskell, R. W., Hashimoto, T., Kubota, T., Higuchi, Y., Nakamura, T., Smith, P., Hiraoka, K., Honda, T., Kobayashi, S., Furuya, M., Matsumoto, N., Nemoto, E., Yukishita, A., Kitazato, K., Dermawan, B., Sogame, A., Terazono, J., Shinohara, C. and Akiyama, H. (2006). Detailed images of asteroid 25143 Itokawa from Hayabusa. *Science*, 312:1341–1344.

[Scheeres, 2007] Scheeres, D. J. (2007). The dynamical evolution of uniformly rotating asteroids subject to YORP. *Icarus*, 188:430–450.

[Scheeres et al., 2007] Scheeres, D. J., Abe, M., Yoshikawa, M., Nakamura, R., Gaskell, R. W. and Abell, P. A. (2007). The effect of YORP on Itokawa. *Icarus*, 188:425–429.

[Sedlák and Štoll, 1993] Sedlák, B. and Štoll, I. (1993). *Elektřina a magnetismus.* Academia and Charles University, Prague.

[Simonelli et al., 1993] Simonelli, D. P., Thomas, P. C., Carcich, B. T. and Veverka, J. (1993). The generation and use of numerical shape models for irregular Solar System objects. *Icarus*, 103:49–61.

[Slivan, 2002] Slivan, S. M. (2002). Spin vector alignment of Koronis family asteroids. *Nature*, 419:49–51.

[Spencer et al., 1989] Spencer, J. R., Lebofsky, L. A. and Sykes, M. V. (1989). Systematic biases in radiometric diameter determinations. *Icarus*, 78:337–354.

[Svoboda and Bakule, 1992] Svoboda, E. and Bakule, R. (1992). *Molekulová fyzika.* Academia, Praha.

[Swihart, 1971] Swihart, T. L. (1971). *Basic physics of stellar atmospheres.* Astronomy and astrophysics series. In: Intermediate short texts in Astrophysics, Tucson: Pachart Publishing House, 1971.

[Taylor et al., 2007] Taylor, P. A., Margot, J. L., Vokrouhlický, D. Scheeres, D. J., Pravec, P., Lowry, S. C., Fitzsimmons, A., C., N. M., Ostro, S. J., Benner, L. A., Giorgini, J. D. and Magri, C. (2007). Increasing spin rate of asteroid 54509 (2000 PH5) a result of the YORP effect. *Science,* in press.

[Thomas et al., 1996] Thomas, P. C., Belton, M. J. S., Carcich, B., Chapman, C. R., Davies, M. E., Sullivan, R. and Veverka, J. (1996). The shape of Ida. *Icarus*, 120:20–32.

[Urquhart and Jakosky, 1997] Urquhart, M. L. and Jakosky, B. M. (1997). Lunar thermal emission and remote determination of surface properties. *Journal of Geophysical Research*, 102:10 959–10 969.

[Vitásek, 1987] Vitásek, E. (1987). *Numerické metody.* Státní nakladatelství technické literatury, Praha.

[Vokrouhlický, 1998a] Vokrouhlický, D. (1998a). Diurnal Yarkovsky effect as a source of mobility of meter-sized asteroidal fragments. I. Linear theory. *Astronomy and Astrophysics*, 335:1093–1100.

[Vokrouhlický, 1998b] Vokrouhlický, D. (1998b). Diurnal Yarkovsky effect as a source of mobility of meter-sized asteroidal fragments. II. Non-sphericity effects. *Astronomy and Astrophysics*, 338:353–363.

[Vokrouhlický and Farinella, 1998] Vokrouhlický, D. and Farinella, P. (1998). Orbital evolution of asteroidal fragments into the ν_6 resonance via Yarkovsky effects. *Astronomy and Astrophysics*, 335:351–362.

[Vokrouhlický, 1999] Vokrouhlický, D. (1999). A complete linear model for the Yarkovsky thermal force on spherical asteroid fragments. *Astronomy and Astrophysics*, 344:362–366.

[Vokrouhlický and Brož, 1999] Vokrouhlický, D. and Brož, M. (1999). An improved model of the seasonal Yarkovsky force for regolith-covered asteroid fragments. *Astronomy and Astrophysics*, 350:1079–1084.

[Vokrouhlický and Farinella, 1999] Vokrouhlický, D. and Farinella, P. (1999). The Yarkovsky seasonal effect on asteroidal fragments: A nonlinearized theory for spherical bodies. *The Astronomical Journal*, 118:3049–3060.

[Vokrouhlický and Farinella, 2000] Vokrouhlický, D. and Farinella, P. (2000). Efficient delivery of meteorites to the Earth from a wide range of asteroid parent bodies. *Nature*, 407:606–608.

[Vokrouhlický and Milani, 2000] Vokrouhlický, D. and Milani, A. (2000). Direct solar radiation pressure on the orbits of small near-Earth asteroids: observable effects? *Astronomy and Astrophysics*, 362:746–755.

[Vokrouhlický et al., 2000] Vokrouhlický, D., Milani, A. and Chesley, S. R. (2000). Yarkovsky effect on small near-Earth asteroids: Mathematical formulation and examples. *Icarus*, 148:118–138.

[Vokrouhlický and Čapek, 2002] Vokrouhlický, D. and Čapek, D. (2002). YORP-induced long-term evolution of the spin state of small asteroids and meteoroids: Rubincam's approximation. *Icarus*, 159:449–467.

[Vokrouhlický et al., 2003] Vokrouhlický, D., Nesvorný, D. and Bottke, W. F. (2003). The vector alignments of asteroid spins by thermal torques. *Nature*, 425:147–151.

[Vokrouhlický et al., 2004] Vokrouhlický, D., Čapek, D., Kaasalainen, M. and Ostro, S. J. (2004). Detectability of YORP rotational slowing of asteroid 25143 Itokawa. *Astronomy and Astrophysics*, 414:L21–L24.

[Vokrouhlický et al., 2005a] Vokrouhlický, D., Čapek, D., Chesley, S. R. and Ostro, S. J. (2005a). Yarkovsky detection opportunities. I. Solitary asteroids. *Icarus*, 173:166–184.

[Vokrouhlický et al., 2005b] Vokrouhlický, D., Čapek, D., Chesley, S. R. and Ostro, S. J. (2005b). Yarkovsky detection opportunities. *Icarus*, 179:128–138.

[Vokrouhlický et al., 2006a] Vokrouhlický, D., Brož, M., Bottke, W. F., Nesvorný, D., and Morbidelli, A. (2006a). Yarkovsky/YORP chronology of asteroid families. *Icarus*, 182:118–142.

[Vokrouhlický et al., 2006b] Vokrouhlický, D., Brož, M., Morbidelli, A., Bottke, W. F., Nesvorný, D., Lazzaro, D. and Rivkin, A. S. (2006b). Yarkovsky footprints in the Eos family. *Icarus*, 182:92–117.

[Vokrouhlický et al., 2007] Vokrouhlický, D., Breiter, S., Nesvorný, D. and Bottke, W. F. (2007). Generalized YORP evolution: onset of tumbling and new asymptotic states. *Icarus*, in press.

[Winter and Saari, 1969] Winter, D. F. and Saari, J. M. (1969). A particulate model of the lunar soil. *The Astrophysical Journal*, 156:1135–1151.

[Yomogida and Matsui, 1983] Yomogida, K. and Matsui, T. (1983). Physical properties of ordinary chondrites. *Journal of Geophysical Research*, 88:9513–9533.